

Validated leaf spring suspension models

by

Cor-Jacques Kat

Submitted in partial fulfilment of the requirements for the degree

Philosophiae Doctor (Mechanical Engineering)

in the

FACULTY OF ENGINEERING, THE BUILT ENVIRONMENT AND
INFORMATION TECHNOLOGY (EBIT)

UNIVERSITY OF PRETORIA
Pretoria

April 2012



UNIVERSITEIT VAN PRETORIA
UNIVERSITY OF PRETORIA
YUNIBESITHI YA PRETORIA

Denkleiers • Leading Minds • Dikgopolo tša Dihlalefi

© University of Pretoria

Summary of thesis

Title: Validated leaf spring suspension models

Author: Cor-Jacques Kat

Supervisor: Prof. P.S. Els

Department: Mechanical and Aeronautical Engineering, University of Pretoria

Degree: Philosophiae Doctor (Mechanical Engineering)

Mathematical and computer modelling have been playing an increasingly important role in the Computer Aided Engineering (CAE) process. Simulation offers great advantages in the development and analysis phase of products and offers a faster, better and more cost effective way than using physical prototypes alone. The ever increasing demand for new and improved products in the vehicle industry has decreased the time available for the development of new vehicles, but at the same time the demands on quality, reliability and mass that are set for the vehicle are becoming ever more stringent. These requirements have lead to the investigation of procedures and methodologies such as virtual prototyping that will reduce the development time of new vehicles without inhibiting the quality of the vehicle.

In order to perform effective and reliable simulations in the CAE process, accurate simulation models of the vehicle and its associated systems, subsystems and components are required. In the vehicle dynamics context simulation models of the tyres, suspension, springs, damper, etc, are needed. This study will look at creating a validated model of a leaf spring suspension system used on commercial vehicles. The primary goal set for the model is to be able to predict the forces at the points where the suspension system is attached to the vehicle chassis as the model is to be used in full vehicle durability simulations. The component which will receive a considerable amount of attention in this study is the leaf spring. Leaf springs have been used in vehicle suspensions for many years. Even though leaf springs are frequently used in practice they still hold great challenges in creating accurate mathematical models. It is needless to say that an accurate model of a leaf spring is required if accurate full vehicle models are to be created.

As all simulation models in this study are required to be validated against experimental measurements a thorough experimental characterisation of the suspension system of interest, as well as two different leaf springs, are performed. In order to measure the forces between

the suspension attachment points and the chassis, two six component load cells were developed, calibrated, verified and validated.

This study will primarily focus on the modelling of a multi-leaf spring as well as a parabolic leaf spring. The study starts with a literature study into the various existing modelling techniques for leaf springs. A novel leaf spring model, which is based on a macro modelling view point similar to that used for modelling material behaviour, is developed. One of the modelling techniques found in the literature, i.e. neural networks, is also used to model the leaf spring. The use of neural networks is applied and some of the challenges associated with the method are indicated. The accuracy and efficiency of the physics-based elasto-plastic leaf spring model and the non physics-based neural network model are compared. The modified percentage relative error metric is compared to two other quantitative validation metrics that were identified from the literature study. It is concluded that the modified percentage relative error has certain limitations but that it is able to give an accurate and representative account of the agreement/disagreement between two periodic signals around zero. The modified percentage relative error is used to obtain the accuracies of the elasto-plastic leaf spring models and the neural network model. Both models give good results with the neural network being almost 3 times more computationally efficient.

The elasto-plastic leaf spring model, for the multi-leaf spring, is further extended to model the behaviour of a parabolic leaf spring. Qualitative validation using experimental data shows that the elasto-plastic leaf spring model is able to accurately predict the vertical behaviour of both the multi-leaf spring as well as the parabolic leaf spring. The elasto-plastic leaf spring model was also combined with a method that is able to capture the effect of changes in the spring stiffness due to changes in the loaded length. Quantitative validation shows that the method proposed for accounting for the change in stiffness due to changes in the loaded length is able to capture this characteristic of the physical leaf spring.

Following a systematic modelling approach the elasto-plastic multi-leaf spring model is incorporated into a model of a simplified version of the physical suspension system. The qualitative validation results from this model show that the model is able to accurately predict the forces that are transmitted from the suspension system to the chassis. The models created in this study can be used in future work and, with the addition of more detail the models, can be extended to create a model of the complete suspension system.

Opsomming van proefskrif

Titel:	Gevalideerde bladveersuspensie modelle
Outeur:	Cor-Jacques Kat
Studieleier:	Prof. P.S. Els
Departement:	Meganiese en Lugvaartkundige Ingenieurswese, Universiteit van Pretoria
Graad:	Philosophiae Doktor (Meganiese Ingenieurswese)

Wiskundige- en rekenaargesteunde modellering se rol in die Rekenaargesteunde Ingenieursproses word al meer belangrik. Simulasie hou baie voordele in wanneer dit korrek gebruik word in die ontwikkeling en analise fase van produkte aangesien dit 'n vinniger, beter en meer koste effektiewe manier is as slegs die gebruik van fisiese prototipes. Die toenemende aanvraag vir nuwe en beter produkte in die voertuigindustrie het die tyd wat beskikbaar is vir die ontwikkeling van nuwe voertuie verminder maar terselfdertyd het die vereistes t.o.v. kwaliteit, betroubaarheid en massa wat gestel word vir die voertuig, deurlopend strenger geword. Hierdie vereistes het gelei tot die ondersoek na prosedures en metodieke, soos virtuele prototipes, wat die ontwikkelings tyd van nuwe voertuie verminder sonder om die kwaliteit van die voertuig in te te boet.

Om effektiewe en betroubare simulasies in die rekenaargesteunde ingenieursproses te kan doen, word akkurate simulasiemodelle van die voertuig en sy geassosieerde stelsels, substelsels, en komponente benodig. In die voertuigkonteks word simulasiemodelle van die bande, suspensie, vere, dempers, ens., benodig. Hierdie studie is gemik op die skep van gevalideerde modelle van die bladveer suspensiesisteme soos gebruik op kommersiële voertuie. Die primêre doelwit wat gestel word vir die modelle is dat hul in staat moet wees om die kragte te voorspel wat inwerk op die bakwerk waar die suspensie vasgeheg word aangesien die modelle gebruik gaan word in duursaamheidsimulasies. Die komponent wat 'n noemenswaardige hoeveelheid aandag sal kry in die studie is die bladveer. Bladvere word al vir baie jare lank in voertuigsuspensies gebruik. Selfs al word bladvere gereeld gebruik in die praktyk, is daar nog steeds verskeie uitdagings om akkurate modelle van bladvere te skep. Dit is vanselfsprekend dat 'n akkurate model van die bladveer benodig word indien 'n akkurate volvoertuig model geskep wil word.

Aangesien alle simulasiemodelle wat in hierdie studie ontwikkel word, gevalideer word teen eksperimentele metings, is daar 'n deeglike eksperimentele karakteriseringoefening uitgevoer. Die suspensiestelsel sowel as twee verskillende bladvere is gekarakteriseer. Om dit moontlik te maak om die kragte tussen die suspensiestelsel en die onderstel te kan meet is twee ses komponent lasselle ontwikkel, gekalibreer, geverifieer en gevalideer.

Hierdie studie fokus hoofsaaklik op die modellering van 'n multi-blad bladveer sowel as 'n paraboliese bladveer. Die studie begin met 'n deeglike literatuurstudie wat ondersoek instel na die verskeie modelleringstegnieke wat tans bestaan vir bladvere. 'n Unieke bladveer model, wat gebaseer is op 'n makro modelleringsoogpunt, soortgelyk aan die tegniek wat gebruik word om materiaalgedrag te modelleer, is ontwikkel. Een van die modelleringstegnieke wat uit die literatuur geïdentifiseer is, nl. neurale netwerke, is ook gebruik om die bladveer te modelleer. 'n Neurale netwerk is gebruik en van die uitdagings geassosieer met die metode word uitgewys. Die akkuraatheid en effektiwiteit van die fisika gebaseerde elasto-plastiese bladveer model en die nie-fisika gebaseerde neurale netwerk model is vergelyk. Die akkuraatheid is bereken deur 'n nuwe kwantitatiewe validasiemaatstaf te gebruik wat 'n intuitiewe en verteenwoordigende aanduiding gee van die fout tussen twee seine. Die kwantitatiewe validasiemaatstaf is gebaseer op die bekende, en algemeen gebruikte, relatiewe fout. Die aangepaste persentasie relatiewe fout maatstaf wat ontwikkel is neem die uitdagings wat geassosieer is met die gebruik van die relatiewe fout, op seine met periodiese gedrag om nul, in ag. Die gemodifiseerde persentasie relatiewe fout word vergelyk met twee ander kwantitatiewe validasiemaatstawwe wat geïdentifiseer is uit die literatuurstudie. Die gevolgtrekking word gemaak dat die persentasie relatiewe fout sekere beperkings het maar dat dit 'n akkurate en verteenwoordigende aanduiding van die ooreenkoms tussen twee periodiese seine om nul gee. Die gemodifiseerde persentasie relatiewe fout is gebruik om die akkuraatheid van die elasto-plastiese model en die neurale netwerk model te bepaal. Beide modelle gee goeie resultate, maar die neurale netwerk is omtrent drie keer meer berekeningseffektief.

Die elasto-plastiese bladveer model is ook gebruik om 'n paraboliese bladveer se gedrag te modelleer. Kwalitatiewe validasie, met die gebruik van eksperimentele data, wys dat die elasto-plastiese bladveer model wel in staat is om die vertikale gedrag van beide die multi-blad bladveer sowel as die paraboliese bladveer te voorspel. Die elasto-plastiese bladveermodel is ook gekombineer met 'n metode wat in staat is om die effek van die verandering in die veerstyfheid, as gevolg van veranderinge in die belaaide lengte, vas te vang. Kwantitatiewe validasie toon dat die metode wel die veranderinge in die veerstyfheid as gevolg van verandering in die belaaide lengte vasvang.

Volgens die sistematiese modelleringaanslag wat gevolg is, is die elasto-plastiese bladveer model van die multi-blad bladveer geïnkorporeer in 'n model van 'n vereenvoudigde weergawe van die suspensiestelsel. Die kwalitatiewe validasie resultate van die model toon dat die model in staat is om die kragte, wat van die suspensiestelsel na die onderstel oorgedra word, akkuraat kan voorspel. Die model wat in die studie geskep is kan in toekomstige werk gebruik word en met die byvoeging van addisionele detail kan die modelle uitgebrei word om modelle te skep van die volledige suspensiestelsel.

Acknowledgements

This research was made possible through the support and funding received from Afrit and the Department of trade and industry's Technology and Human Resources for Industry Programme (THRIP) initiative.

The following people's contribution added to the successful completion of this research and I would like to extend my gratitude to:

- Gerrit van de Wetering, for his supportive role from Afrit and for the hours he generously spent in proof reading reports and articles.
- Schalk Els, for his friendship, mentorship and his guidance throughout my studies.

I will be forever grateful to the following people as they taught me the virtues that have helped formed me into the man I am today. Without them it would have been impossible to achieve success and meaning in life:

- To my mother, for teaching me courage, determination and perseverance.
- To my grandfather, for teaching me integrity and to be just.
- To my brother Tjaart, for teaching me loyalty.
- To my brother Arné, for teaching me patience.
- To my grandmother, for teaching me commitment and consideration
- To my friend Tjaart van der Walt, for teaching me the importance of dependability.
- To my girlfriend Somarié, for strengthening my believes and principles

I can do everything through Him who gives me strength

Philippians 4:13

Table of contents

Summary of thesis	III
Opsomming van proefskrif	V
Acknowledgements	VII
List of symbols	XV
List of abbreviations	XXI
List of figures	XXIII
List of tables	XXXI
Chapter 1 – Introduction	1
1. Problem statement	3
2. Introduction to suspension system of interest	3
3. Literature study	6
3.1. Leaf spring models in previous studies	7
3.1.1. Analytical/Empirical models	7
3.1.2. Equivalent models	8
3.1.3. Discrete methods (or finite segment methods)	9
3.1.4. Finite element methods	11
3.1.5. Neural network models	13
3.2. Summary of leaf spring modelling techniques	14
3.3. Conclusion	18
4. Overview of study	19
Chapter 2 – Experimental characterisation	21
1. Six component load cell (6clc)	21
2. Characterisation of the suspension system using the multi-leaf spring	23

2.1. Force-displacement characteristic	24
2.1.1. In-service setup	27
2.1.1.1. Effect of U-bolt preload on the force-displacement characteristic	30
2.1.2. Spring only setup	31
2.1.2.1. Effect of longitudinal spacing of hangers	33
2.1.2.2. Deflection shape of the multi-leaf spring	34
3. Characterisation of the suspension system using the parabolic leaf spring	36
3.1. Force-displacement characteristic	36
3.1.1. In-service setup	37
3.1.1.1. Effect of U-bolt preload on force-displacement characteristics	38
3.1.2. Spring only setup	39
3.1.2.1. Effect of longitudinal spacing of hangers	40
3.1.2.2. Deflection shape of the parabolic leaf spring	41
4. Conclusion	42
Chapter 3 – Leaf spring modelling	43
1. Introduction	43
2. Elasto-plastic leaf spring model	44
2.1. The behaviour of materials and leaf springs	44
2.1.1. Deformation behaviour and models of materials	45
2.1.2. Mechanisms in crystalline materials vs. mechanisms in multi-leaf springs	46
2.1.2.1. Mechanisms in crystalline materials	46
2.1.2.2. Mechanisms in multi-leaf springs	47
2.1.2.3. Solid-solid contact (Tribological process)	49
2.1.2.4. Conclusion	51
2.2. Mechanical properties of a multi-leaf spring	51
2.3. Elasto-plastic leaf spring models	54
2.3.1. Elastic-linear model	54
2.3.2. Elastic-nonlinear model	55
2.4. Validation of the elasto-plastic leaf spring model	57
2.4.1. Elastic-linear model	57
2.4.2. Elastic-nonlinear model	59
2.5. Conclusion	60
3. Elasto-plastic leaf spring model applied to the parabolic leaf spring	60
3.1. Extracting mechanical properties for the elastic-linear parabolic leaf spring model	61

3.2.	Validation of elastic-linear leaf spring model emulating the parabolic leaf spring	62
3.3.	Conclusion	64
4.	Loaded length changes of a simply supported leaf spring	64
4.1.	Method to account for loaded length changes	64
4.2.	Validation of loaded length calculation combined with EPLS model	66
4.2.1.	Multi-leaf spring	67
4.2.2.	Parabolic leaf spring	67
4.3.	Conclusion	68
5.	Artificial neural networks	69
5.1.	Neural network model	70
5.1.1.	Reducing noise on neural network predictions	72
5.1.2.	Generalization	73
6.	Conclusion	80
 Chapter 4 – Multi-leaf spring suspension system model		81
1.	Introduction	82
2.	Modelling of the spring only setup	83
2.1.	ADAMS/Car leaf spring model	83
2.1.1.	ADAMS/Car leaf spring Model 1	84
2.1.2.	ADAMS/Car leaf spring Model 2	84
3.	Validation of the spring only model	87
3.1.	Validation of the spring only model using Model 1	87
3.2.	Validation of the spring only model using Model 2	89
4.	Conclusion	92
 Chapter 5 – Verification and Validation		93
1.	Introduction	93
2.	Qualitative validation metrics	97
2.1.	Literature survey	98
2.1.1.	Russell’s error measure	101
2.1.2.	Sprague & Geers’ metric	101
2.2.	Validation metric based on relative error	102
2.2.1.	Relative error (<i>RE</i>)	102
2.2.2.	Challenges in using the % <i>RE</i> as validation metric	103
2.2.3.	Summary of the modified % <i>RE</i> validation metric	111



3.	Comparison of validation metrics	112
3.1.	Analytical functions	113
3.1.1.	Ability to rank models and identify the best model	114
3.1.2.	Reliability and usefulness of validation metrics	116
3.1.3.	Combination of S&G and the modified %RE	117
3.2.	Case studies	118
3.2.1.	Case study 1: Known error between signals	119
3.2.2.	Case study 2: Elasto-plastic leaf spring model	120
3.2.3.	Case study 3: Comparison of accuracy and efficiency of leaf spring modelling methods	122
4.	Conclusion	124
Chapter 6 – Conclusions and Recommendations		127
1.	Conclusions	127
2.	Recommendations	128
2.1.	Chapter 2	128
2.2.	Chapter 3	129
2.2.1.	Elasto-plastic leaf spring model	129
2.2.2.	Neural network model	130
2.3.	Chapter 4	130
2.4.	Chapter 5	131
Bibliography		133
Appendix A – Six component load cell (6clc)		139
A.1.	Calibration of uni-axial load cells	139
A.2.	Verification and Validation of the physical and virtual 6clc	144
A.2.1.	Verification of 6clc	145
A.2.1.1.	Derivation of analytical equations	145
A.2.1.2.	Verification of 6clc concept	149
A.2.1.3.	Verification of the 6clc ADAMS/Car model	150
A.2.2.	Validation of 6clc models	153
A.2.2.1.	Load case 1 and Load case 2	154
A.2.2.2.	Load case 3	157
A.2.2.3.	Load case 4	158



A.2.3. Model refinement	160
A.2.3.1. Orientation of applied force	161
A.2.3.2. Application point of applied force	162
A.2.4. Validation results for the rear 6clc	167
A.3. Conclusion	171

Appendix B – Theoretical stiffness of the multi-leaf spring

B.1. Calculating the theoretical stiffness	173
B.1.1. Principle of superposition	174
B.1.2. SAE spring design manual	176
B.1.3. Calculating equivalent spring stiffness	177
B.1.3.1. Symmetrical loading	178
B.1.3.2. Asymmetrical loading	179
B.1.3.3. Conclusion	181
B.1.3.4. Neglecting the initial angle of the cantilevers	182
B.1.4. Validation of theoretical stiffness calculation	183
B.2. Effect of the clamping assumption on the theoretical stiffness	184
B.3. Additional validation tests	187
B.3.1. Test 1: 3 blade, clamped length = 0.076m	187
B.3.2. Test 2: 3 blade, clamped length = 0.22m	188
B.3.3. Test 3: 3 blade, clamped length = 0m	191
B.4. Conclusion	192

List of symbols

English symbols:

A	Cross-sectional area	$[\text{m}^2]$
a	Length between applied force and the front support	$[\text{m}]$
b	Length between applied force and the rear support	$[\text{m}]$
C_R	Russell's comprehensive error	
$C_{S\&G}$	Sprague & Geers' comprehensive error	
d_{X1y}	Distance in y-direction from the centre of volume of the 6clc to the line of action of the 1 st uni-axial load cell in the longitudinal direction (X_1)	$[\text{m}]$
d_{X2y}	Distance in y-direction from the centre of volume of the 6clc to the line of action of the 2 nd uni-axial load cell in the longitudinal direction (X_2)	$[\text{m}]$
d_{X12z}	Distance in z-direction from the centre of volume of the 6clc to the line of action of both uni-axial load cells in the longitudinal direction (X_1 and X_2)	$[\text{m}]$
d_x	Distance in x-direction from centre of volume to the application point of the applied force (F_A)	$[\text{m}]$
d_{Yx}	Distance in x-direction from the centre of volume of the 6clc to the line of action of the uni-axial load cell in the lateral direction (Y)	$[\text{m}]$
d_{Yz}	Distance in z-direction from the centre of volume of the 6clc to the line of action of the uni-axial load cell in the lateral direction (Y)	$[\text{m}]$
d_y	Distance in y-direction from centre of volume to the application point of the applied force (F_A)	$[\text{m}]$
d_{Z1x}	Distance in x-direction from the centre of volume of the 6clc to the line of action of the 1 st uni-axial load cell in the vertical direction (Z_1)	$[\text{m}]$

d_{z23x}	Distance in x-direction from the centre of volume of the 6clc to the line of action of the 2 nd and 3 rd uni-axial load cell in the vertical direction (Z_2 and Z_3)	[m]
d_{z2y}	Distance in y-direction from the centre of volume of the 6clc to the line of action of the 2 nd uni-axial load cell in the vertical direction (Z_2)	[m]
d_{z3y}	Distance in y-direction from the centre of volume of the 6clc to the line of action of the 3 rd uni-axial load cell in the vertical direction (Z_3)	[m]
d_z	Distance in z-direction from centre of volume to the application point of the applied force (F_A)	[m]
E	Young's modulus	[Pa]
F	Force	[N]
F_A	Force applied to 6clc	[N]
F_{Ax}	Component of force applied to 6clc in x-direction	[N]
F_{Ay}	Component of force applied to 6clc in y-direction	[N]
F_{Az}	Component of force applied to 6clc in z-direction	[N]
$F_{applied}$	Applied force	[N]
F_x	Equivalent force in x-direction that acts on the centre of volume of the 6clc	[N]
F_{xF}	Force in longitudinal direction at front hanger	[N]
F_{xR}	Force in longitudinal direction at rear hanger	[N]
F_y	Equivalent force in y-direction that acts on the centre of volume of the 6clc	[N]
F_z	Equivalent force in z-direction that acts on the centre of volume of the 6clc	[N]
$F_{y,elaslin}$	Elastic-linear frictional yield force	[N]
$F_{y,elaslin,L}$	Elastic-linear frictional yield force when leaf spring is loaded	[N]
$F_{y,elaslin,UL}$	Elastic-linear frictional yield force when leaf spring is unloaded	[N]
$F_{y,L}$	Frictional yield force when leaf spring is loaded	[N]
$F_{y,UL}$	Frictional yield force when leaf spring is unloaded	[N]

F_u	Ultimate frictional yield force	[N]
$F_{u,L}$	Ultimate frictional yield force when leaf spring is loaded	[N]
$F_{u,UL}$	Ultimate frictional yield force when leaf spring is unloaded	[N]
$F_{preload}$	Force due to preload in U-bolts	[N]
F_s	Spring force	[N]
F_{zF}	Force in vertical direction at front hanger	[N]
F_{zR}	Force in vertical direction at rear hanger	[N]
f_y	Yield fraction	[Dimensionless]
$f_{y,L}$	Yield fraction when leaf spring is loaded	[Dimensionless]
$f_{y,UL}$	Yield fraction when leaf spring is unloaded	[Dimensionless]
I	Area moment of inertia	[m ⁴]
k_a	Stiffness of front cantilever beam	[N/m]
k_b	Stiffness of rear cantilever beam	[N/m]
k_{eq}	Equivalent stiffness of cantilever beams in parallel	[N/m]
k_L	Stiffness of the layered beam during loading	[N/m]
k_{UL}	Stiffness of the layered beam during unloading	[N/m]
δk	Incremental change in stiffness	[N/m]
δk_1	1 st incrementally changes stiffness	[N/m]
δk_2	2 nd incrementally changes stiffness	[N/m]
L	Loaded length	[m]
l	length	[m]
l_f	Length between axle seat and front hanger	[m]
l_r	Length between axle seat and rear hanger	[m]
M_x	Equivalent moment about the x-axis that acts on the centre of volume of the 6clc	[N.m]
M_y	Equivalent moment about the y-axis that acts on the centre of volume of the 6clc	[N.m]

M_z	Equivalent moment about the z-axis that acts on the centre of volume of the 6clc	[N.m]
M_R	Russell's magnitude error	
$M_{S\&G}$	Sprague & Geers' magnitude error	
m	Measured signal	
N	Number of data point is signal	
n	Value in neuron that is sent to transfer function	
P	Probability	
P	Applied force	[N]
P_R	Russell's phase error	
$P_{S\&G}$	Sprague & Geers' phase error	
p	Predicted signal	
TP_L	Turning point which indicates the change from unloading to loading	[N]
TP_{UL}	Turning point which indicates the change from loading to unloading	[N]
V	Relative error bounded by the tanh function	
X_1	Force measured in 1 st uni-axial load cell orientated in longitudinal direction	[N]
X_2	Force measured in 2 nd uni-axial load cell orientated in longitudinal direction	[N]
x	Displacement (or deflection)	[m]
Y	Force measured in uni-axial load cell orientated in lateral direction	[N]
Z_1	Force measure by the 1 st uni-axial load cell orientated in vertical direction	[N]
Z_2	Force measure by the 2 nd uni-axial load cell orientated in vertical direction	[N]
Z_3	Force measure by the 3 rd uni-axial load cell orientated in vertical direction	[N]



Greek symbols:

α	Angle of slope at contact points between leaf spring and hanger	[°]
α_f	Angle of slope at contact points between leaf spring and front hanger	[°]
α_r	Angle of slope at contact points between leaf spring and rear hanger	[°]
ε	Strain	[Dimensionless]
ε_e	Elastic strain	[Dimensionless]
ε_p	Plastic strain	[Dimensionless]
σ_y	Yield stress	[Pa]
σ	Stress	[Pa]
θ	Angle between resultant force and horizontal line that goes through the contact point	[°]
v	Deflection of beam at applied force	[m]
v'_F	Slope of beam at applied force	

List of abbreviations

acar	ADAMS/Car
ADAMS	Automatic Dynamic Analysis of Mechanical Systems
ASTM	American Society for Testing and Materials
CAD	Computer Aided Design
CAE	Computer Aided Engineering
cv	centre of volume
DTW	Dynamic Time Warping
EPLS	Elasto-Plastic Leaf Spring
HRC	Rockwell hardness, C-scale
HV	Vickers hardness
HB	Brinell hardness
IEEE	Institute of Electrical and Electronics Engineers
Inf	Infinite
MBS	Multi-Body Simulation
m%RE	modified percentage relative error
m%RE ^m	modified percentage relative error defined by the mean of the percentage relative error
m%RE ^s	modified percentage relative error defined by a specific percentage relative error
NaN	Not-a-Number
NISE	Normalized Integral Square Error



NN	Neural Network
RE	Relative Error
%RE	Percentage relative error
rme	relative magnitude error
<i>SF</i>	Stiffening Factor
SME	Subject Matter Expert
SRQ	System Response Quantity
SRQ ^m	Measured system response quantity (obtained from physical system)
SRQ ^p	Predicted system response quantity (obtained from simulation model)
V&V	Verification and Validation
6clc	Six component load cell

List of tables

Chapter 1 – Introduction

Table 1.1. Summary of leaf spring modelling techniques	15
---	----

Chapter 2 – Experimental characterisation

Table 2.1. Spacing of hangers	34
--------------------------------------	----

Chapter 3 – Leaf Spring Modelling

Table 3.1. Elastic-linear equations	55
Table 3.2. Turning point force, frictional yield force and yield fraction	56
Table 3.3. Elastic-nonlinear equations	57
Table 3.4. Dimensions of layouts (see Figure 3.24)	67

Chapter 4 – Multi-leaf spring suspension system model

Table 4.1. Angle of slope at front contact point	86
Table 4.2. Angle of slope at rear contact point	86

Chapter 5 – Verification and Validation

Table 5.1. Summary of Error Measures and Metrics	99
Table 5.2. Effect of $\%RE$ not being bounded on the results of the $m\%RE^m$ (Not bounded)	108
Table 5.3. Effect of $\%RE$ not being bounded on the results of the $m\%RE$ (Bounded)	109
Table 5.4. Known $\%RE$ between true and approximate data	110
Table 5.5. Results for the $m\%RE^m$ using different $\%RE$ threshold values	110
Table 5.6. Summary of the two formulations of the modified $\%RE$ validation metric	112
Table 5.7. Equation for the various analytical functions	113
Table 5.8. Ranking of comparisons by different validation metrics (Functions 1 to 8)	114
Table 5.9. Ranking of comparisons by SME's (Functions 1 to 8)	114
Table 5.10. Ranking of comparisons by different validation metrics (Functions 9 to 15)	115
Table 5.11. Ranking of comparisons by SMEs (Functions 9 to 15)	115
Table 5.12. Comparison between the error measures' ability to quantify the accuracy (Function 21(a) and 21(b))	116

Table 5.13. Comparison between the error measures' ability to quantify the accuracy (Function 22(a) and 22(b))	117
Table 5.14. Comparison between error measures for models with same phase shift but different magnitudes	118
Table 5.15. Relative error between Model 1, Model 2 and the measured data	119
Table 5.16. Comparison between error measures for known %RE	120
Table 5.17. Results with noise on measured data around zero	121
Table 5.18. Results with noise on measured data around zero removed	122
Table 5.19. Results with noise on measured data around zero removed and Model 1 refined	122
Table 5.20. Accuracy of elastic-nonlinear and neural network model	123
Table 5.21. Accuracy of elastic-nonlinear and neural network model for the inner loop only	124

Chapter 6 – Conclusions and Recommendations

No tables in this chapter

Appendix A – Six component load cell (6clc)

Table A.1. Cross-sectional area of the uni-axial load cells	140
Table A.2. Results of harness tests	141
Table A.3. Calibrated Young's modules	144
Table A.4. Load cases used in verification process	145
Table A.5. Results from analysis with no load applied to 6clc	151
Table A.6. Maximum difference between analytical results and ADAMS/Car results (Load case 1)	152
Table A.7. Maximum difference between analytical results and ADAMS/Car results (Load case 2 to 4)	153
Table A.8. Application point	164
Table A.9. Application point (Rear 6clc)	168

Appendix B – Theoretical stiffness of the multi-leaf spring

Table B.1. Equation for calculating stiffness of prismatic and non-prismatic cantilever beams	176
Table B.2. Results from two cantilevers compared with results from simply supported beam	181
Table B.3. Equations for calculating stiffness of cantilevers (Neglecting initial angle of rotation)	182
Table B.4. Results from two cantilevers (initial angle of rotation neglected) compared with results from simply supported beam	183
Table B.5. Blade thickness measurements	185

Chapter 1

Introduction

Mathematical and computer modelling have been playing an increasingly important role in the Computer Aided Engineering (CAE) process of many products in the last 60 years. Simulation offers great advantages in the development and analysis phase of products and offers a faster, better and more cost effective way than using physical prototypes alone. The ever increasing demand for new and improved products in the vehicle industry has decreased the time available for the development of new vehicles, but at the same time the demands on quality, reliability and mass that are set for the vehicle, by both the client and the manufacturer, are becoming ever more stringent. These requirements have led to the investigation of procedures and methodologies that will reduce the development time of new vehicles without inhibiting the quality of the vehicle.

A high level layout of a typical product development life cycle is shown in Figure 1.1. The product development cycle will start with a set of user requirements for the product. The user requirements are then translated into a set of design parameters which can be used by the designers to generate concept designs for the product. After the various concepts have been evaluated a single concept will result from the concept selection process. A detail design of the conceptual product is then performed which will result in a set of drawings which can be used to manufacture a prototype of the product. The product can then undergo various tests to verify whether the product meets the user and design requirements set out at the start of the product development process. If the prototype satisfies all requirements, mass production of the product can commence. However, if the prototype does not satisfy all requirements the shortcomings have to be identified and the process will either return to the conceptualization phase, the design phase or the manufacturing phase. Having gone through the entire product development process up to where a physical prototype has been built and then realizing that there is a conceptual or design flaw has great cost and time implications.

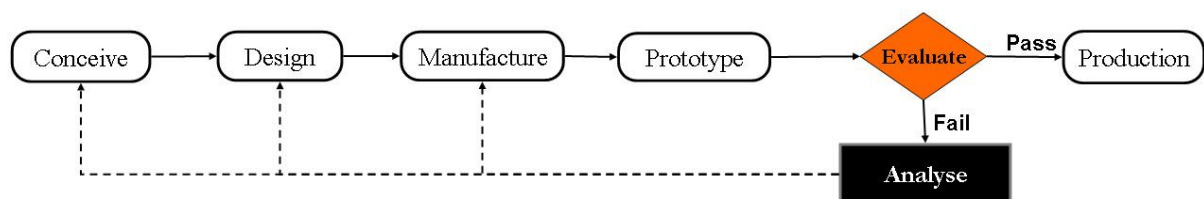


Figure 1.1. Typical product development life cycle

Figure 1.2 shows the cost as the development process of the product continues. It is clear from this figure that great savings in cost, and time, can be realised if the evaluation of the product

can be performed as early as possible in the development cycle. This is where a well founded CAE process holds exceptional benefits.

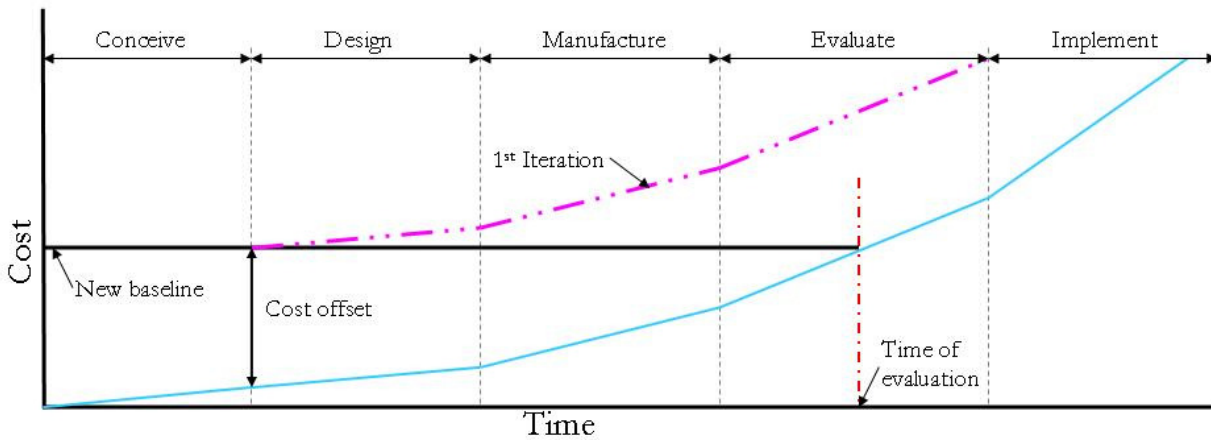


Figure 1.2. Typical product development life cycle cost

A CAE process with validated simulation models enables early evaluation of the product. Having the simulation models available implies that the evaluation of the product can be performed early on in the development process as the evaluation can be performed without the need for a physical prototype. Figure 1.3 indicates a product development cycle with numerous evaluation checkpoints. At each check point different aspects of the product can be evaluated. Take for example the development of a new vehicle. Various concepts have been generated for the suspension system and a concept selected. The suspension system’s kinematics is evaluated in order to check for bump steer, suspension travel, etc. If the concept conforms to the design requirements the concept suspension moves to the design phase. After the various subsystems of the vehicle, such as the suspension system, has gone through a detail design the subsystems can be modelled by the analysts and integrated into a full vehicle simulation model that can be used to evaluate, for example, the durability of the vehicle. Again, the results will be that the product satisfies the durability requirements and it can go into production, or it has unsatisfactory performance and requires refinement. It is not advocated that the product development process is purely based on simulation. It is therefore recommended that a physical prototype still be manufactured and tested.

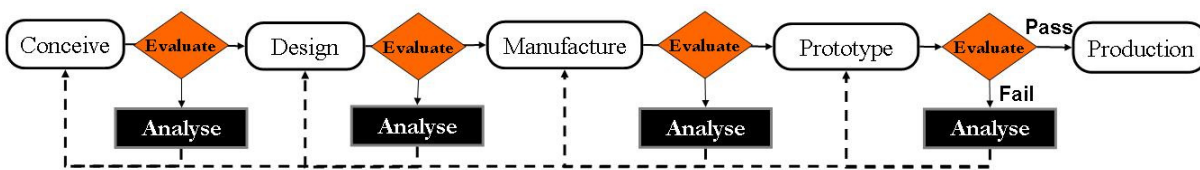


Figure 1.3. Product development life cycle with continuous evaluation

Even though the systematic evaluation of the product throughout its development process, as proposed in Figure 1.3, may lead to an increase in development cost and time, this methodology, if properly executed, has the potential to offer greater overall savings in time and cost and at the same time ensures that the product delivered to the client meets all the requirements and is of exceptional quality and design.

1. Problem statement

The development life cycle presented in Figure 1.3 requires a CAE process with validated simulation models of components, subsystems and systems. In the context of this study, components are elements such as the leaf springs, with the subsystems being the suspension system, and the system the full vehicle. This study forms part of a larger project that is concerned with obtaining a library that contains simulation models of components and subsystems that can be used to create full vehicle simulation models that can be used in the CAE process. Accurate full vehicle multi-body simulation (MBS) models are heavily dependent on the accuracy at which the subsystems, and more fundamentally, the different components that make up the subsystems, are modelled. In the commercial trailer market, at which this study is aimed, a relatively small number of “standard” suspension systems are used, which makes it feasible to develop detailed mathematical models for these and use them as building blocks in the design of new trailers. It is needless to say that an accurate model of a leaf spring is needed if an accurate subsystem model is to be created of the suspension system.

A validated model of the suspension system shown in Figure 1.4 has to be created. The primary goal set for the model is to be able to predict the forces at the attachment points where the suspension system is attached to the vehicle chassis. The model has to be validated by comparing the predicted and measured forces at the suspension attachments as the ultimate goal is to use the suspension model in full vehicle durability simulations.

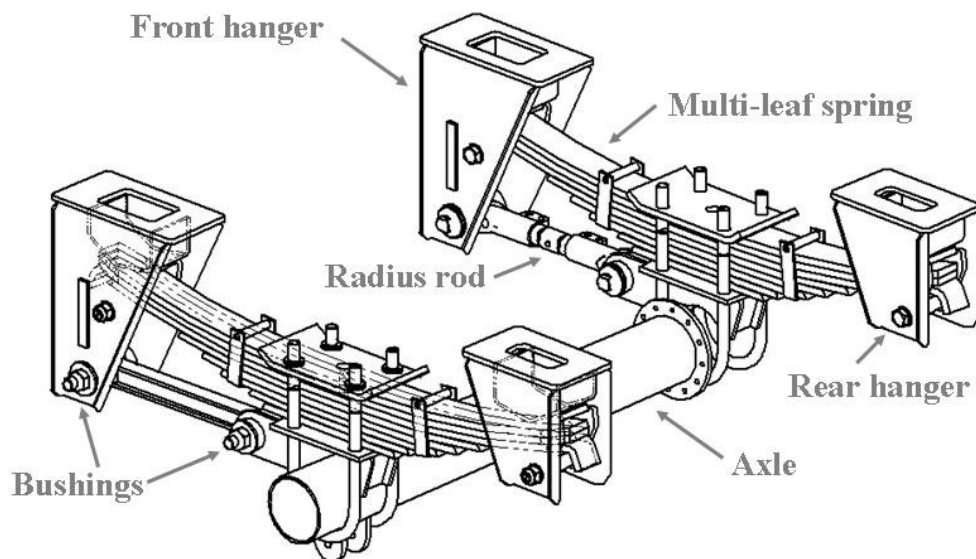


Figure 1.4. Suspension system of interest

2. Introduction to suspension system of interest

Figure 1.4 shows the suspension system that will be considered in this study. The figure shows the suspension system with a multi-leaf spring consisting of 8 blades (or leaves) having a uniform cross-section through the length of the blade. The leaf spring and radius rod constrains the axle in the vertical, longitudinal and lateral directions. The suspension system is attached to the chassis via the hangers. In this configuration the leaf spring is supported by the front and rear hangers instead of a fixed-shackled end configuration (see Figure 1.5 for an example of a fixed-shackled end configuration). In addition to the suspension system in

Figure 1.4 with the multi-leaf spring, another leaf spring will be considered that has a parabolic thickness profile along the length of the blade. This leaf spring will be referred to as a parabolic leaf spring.

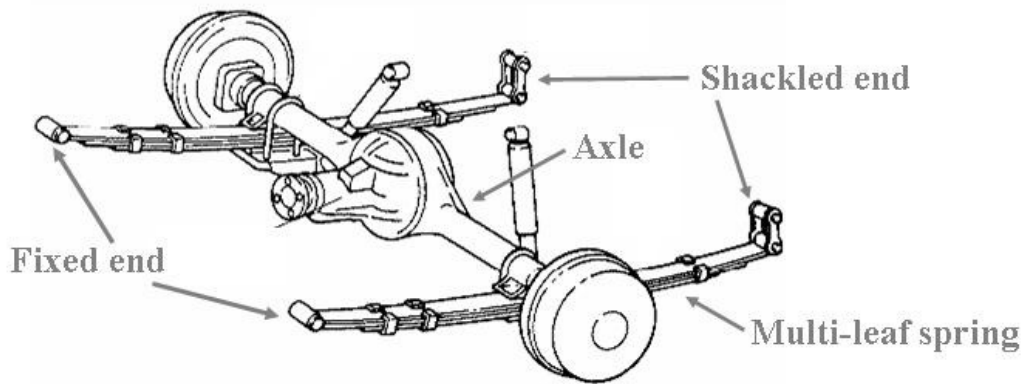


Figure 1.5. Suspension system with leaf spring in fixed-shackled end configuration (Adopted from Monroe (2011))

A systematic approach will be followed in creating a validated model of the suspension system, shown in Figure 1.4, which can be used in durability simulations. This systematic approach entails that the suspension system be broken down into smaller subsystems and the subsystems broken down into the various components (shown in Figure 1.6). Models of the components are then created and validated and then integrated into subsystems which are again validated. The subsystems are then integrated such that a model of the complete suspension is created and once again goes through a model validation process before it is used in full vehicle simulations.

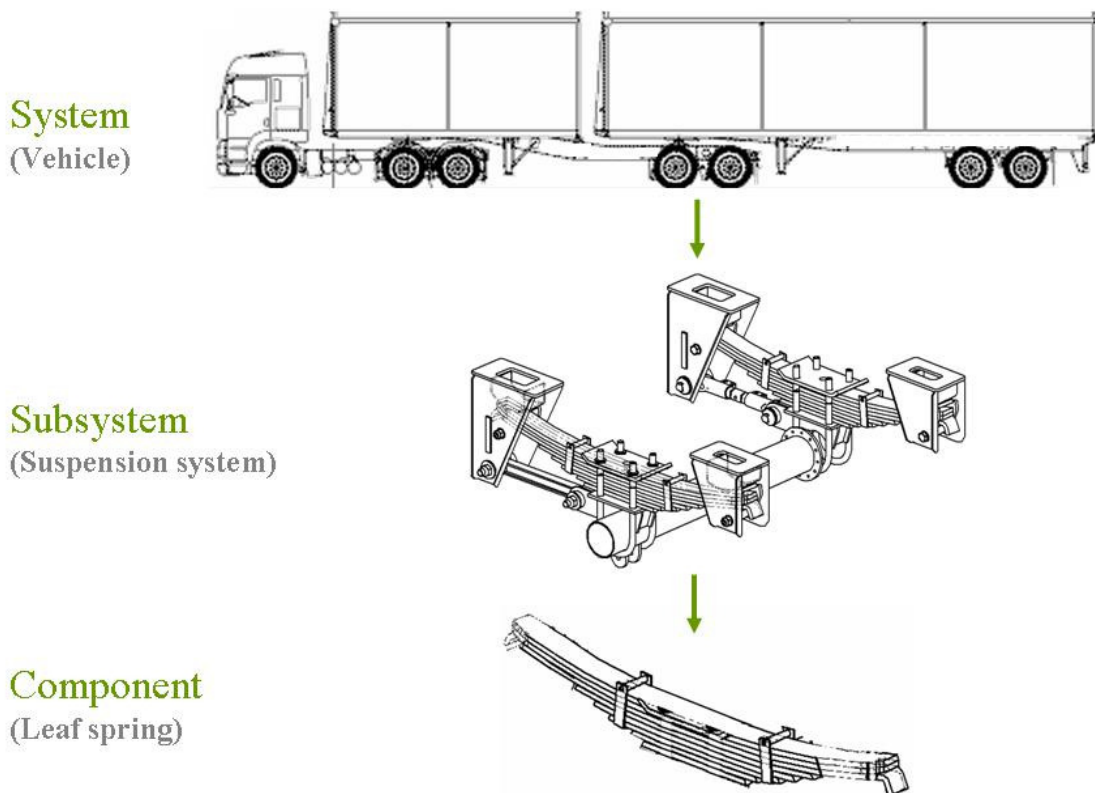


Figure 1.6. Systematic modelling approach

The component of greatest importance, when considering the vertical behaviour of the suspension system, is the leaf spring. The leaf spring has been used in vehicle suspensions for many years. It is particularly popular in commercial vehicles as it is robust, reliable and cost effective. Leaf springs are nonlinear devices which dissipate energy through inter-leaf friction and have force developing characteristics that are dependent on the static load and the amplitude of the imposed displacements. Leaf springs can exhibit highly nonlinear behaviour with hysteresis. High fidelity suspension models require that the nonlinear behaviour of the components, such as the leaf spring, be captured. Fancher *et al.* (1980) state that “since truck leaf springs are complicated nonlinear devices, involving hysteretic damping, their representation in detailed analyses of vehicle dynamic studies of ride, braking or handling is not easily accomplished using linear approximations or simplified models.” With any mathematical model it is ideally the aim to develop a model that is as simple (computationally efficient) as possible and as complex (accurate) as necessary. It will obviously be the goal in this study to obtain accurate simulation models that are also computationally efficient.

In order to obtain an accurate model of the vertical behaviour of the leaf spring the model should be able to capture important aspects of the behaviour of the physical leaf spring. The force-displacement characteristic in Figure 1.7 shows the typical aspects that are present in the behaviour of the multi-leaf spring when it is compressed and extended (in tension). Note that the following convention is used concerning compression and tension: when the spring is compressed the displacement and the force is taken as negative. This convention will be used throughout the study. In general, the multi-leaf spring will seldom be in tension as this occurs only when the wheels loose contact with the road. This situation may have a higher possibility of occurring under off-road and very rough road conditions than under smooth on-road conditions. The focus will be on the compressive behaviour of the spring in this study.

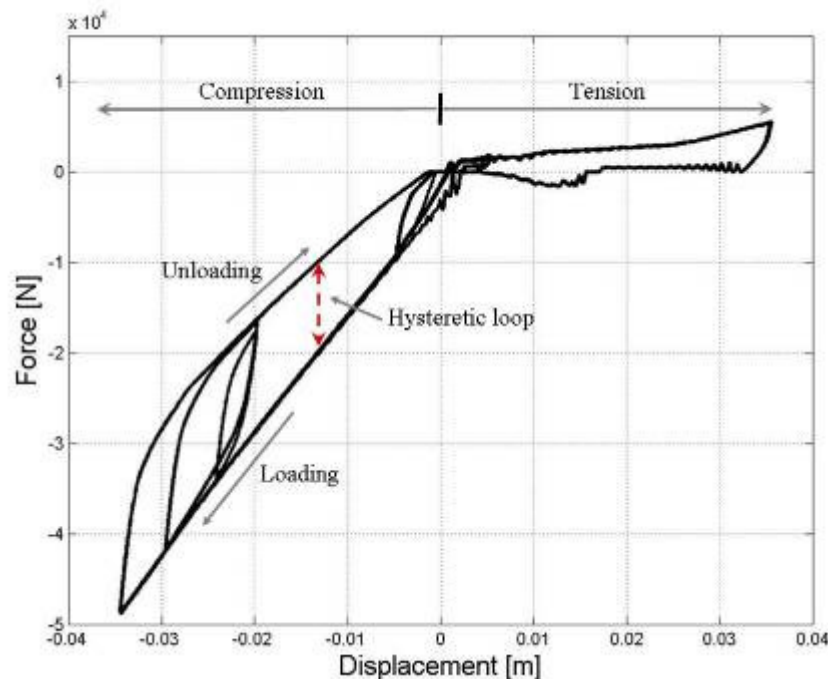


Figure 1.7. Typical force-displacement characteristic of a multi-leaf spring

From Figure 1.7, which shows the force-displacement characteristic of the multi-leaf spring, the two major aspects that a leaf spring model has to capture are identified as:

- the spring stiffness and,
- the hysteresis loop

These two aspects are dependent on the configuration of the leaf spring as well as the contact and friction processes that exists between the individual blades of the leaf spring. The stiffness of the leaf spring is affected by the configuration of the leaf spring (i.e. number of blades, geometry of blades, and loaded length of the leaf spring). The hysteresis loop is mainly governed by the friction and contact processes that exist between the individual blades. Therefore the number of blades, and the way the individual blades make contact with each other, will affect the size of the hysteresis loop. The leaf spring model should be able to capture the stiffness of the leaf spring as well as the hysteretic behaviour of the leaf spring.

After a validated model of the leaf spring has been created this component model can then be integrated into a subsystem representing the suspension system. The main requirement that is put to the leaf spring suspension model in this study is that it should be able to predict not only the spring characteristic, but also the vertical forces, which are transmitted to the chassis at the attachment points, accurately. This requirement is set, as it is required to obtain a leaf spring suspension model that can be used in full vehicle simulation models to perform durability analysis on the vehicle's structure. It is therefore essential to be able to predict the loads that act onto the chassis at the suspension attachment points. The fact that the vertical forces are the focus of this study does not mean that the lateral and longitudinal forces are not important but only that manoeuvres such as handling and performance (braking and acceleration) simulations are not the driving factors. Capturing the vertical behaviour will be the starting point from which the models can then be extended to capture longitudinal and lateral behaviour as well.

The result of a literature study, performed on the leaf spring models that exists and their use in vehicle simulations, is discussed in the next paragraph.

3. Literature study

A literature study was conducted to obtain an idea of the leaf spring models that have been developed and whether they are able to give accurate predictions of the force-displacement behaviour of the leaf spring as well as reaction forces on the vehicle attachment points. The application of the different leaf spring modelling methods in vehicle simulations is noted along with whether they were validated and for which parameters.

Sugiyama *et al.* (2006) suggests that existing leaf spring models can roughly be classified into three categories; (1) a lumped spring model, (2) a discretized model, where a number of rigid links, connected by springs and dampers, are used to account for the structural flexibility of the spring blades and (3) finite element models. Omar *et al.* (2004) reviews several techniques for modelling leaf springs. These include the use of empirical formulae and experimental testing, equivalent lumped systems, simple beam theory and finite-element methods. From the literature it would seem that there are various different leaf spring models that have been developed using different methods. The different approaches used to model leaf springs can be classified into the following broad categories:

- Beam theory,
- Analytical/Empirical models,
- Equivalent models,
- Discrete methods (or Finite segment method),
- Finite element methods (includes beam element models),
- Neural Network models,

- Lumped mass spring models (Equivalent lumped system),
- Graphical techniques and,
- Kinematic models.

Each of the different models have their own advantages and disadvantages, therefore it is expected that not all the models will give the same accuracy in different applications. In the following paragraph we will look at the use of the different leaf spring modelling approaches in various studies.

3.1 Leaf spring models in previous studies

A short review of the application of some of the different leaf spring models in previous studies will be given in this paragraph. The studies will be arranged according to the approach used to model the leaf spring.

3.1.1. Analytical/Empirical models

The analytical models use algebraic equations that are able to fit the experimentally obtained force-displacement characteristics of a leaf spring.

The objective of the research reported in the study by Fancher *et al.* (1980), was to 1) measure the force-producing characteristics of several different types of leaf springs while exciting them at various amplitudes and frequencies of oscillation about nominal loading conditions and 2) develop a means for representing the force-deflection characteristics of leaf springs in a form suitable for use in simulations of commercial vehicles. The test results showed that the leaf springs have rather unique force-deflection characteristics. Therefore, a model suitable for representing their characteristics over wide ranges of loading, deflection amplitudes, and random reversals of velocity is needed for use in vehicle dynamic simulations. Accordingly, they devised an equation to represent the characteristics of the leaf spring. They compare the predictions from this equation with test data and it shows that the model is indeed capable of representing the characteristics of the leaf spring, capturing the stiffness as well as the hysteresis loop. The model by Fancher *et al.*(1980) uses equations to represent the spring force which consist of a linear and exponential term. These equations are merely a fit to the envelope of the force-deflection characteristic of the leaf spring.

Cebon (1986) describes an experimental investigation into the behaviour of some typical leaf springs for realistic operation conditions. The accuracy of three alternative analytical spring models, suitable for use in vehicle vibration simulation, are also examined. The equation presented by Fancher *et al.* (1980) formed the basis of Cebon's (1986) fitting procedure. The measured responses of the leaf springs are compared to simulations which use empirical descriptions of their low frequency (quasi-static) behaviour. Cebon (1986) concludes that two different empirical descriptions can be used for accurately predicting the force developed by typical road vehicle leaf springs.

Application in vehicle simulations

In a study by Cole & Cebon (1994), they describe both a 2D and 3D model of a four-axle articulated vehicle. They summarize that a 2D model may be satisfactory for predicting the tyre forces of a heavy vehicle if: (1) the vehicle speed is high enough to prevent excitation of sprung mass roll modes, and (2) the contribution of the unsprung mass roll modes to the tire

forces are small. Attention is also given to modelling the tandem-axle, leaf-sprung trailer suspension. The hysteresis of the leaf spring element is modelled using the method of Francher *et al.* (1980) and Cebon (1986). The radius arms (or radius rods) were found to have a significant effect on the behaviour of the suspension. The model used in this study was validated by comparing the predicted tire forces with the measured tire forces (at the tire/road interface) and showed good correlation. The results suggest that further refinement of the trailer suspension model is needed to simulate its complex behaviour accurately.

Conclusion

The analytical model presented by Fancher *et al.* (1980) and Cebon (1986) show that it can model the stiffness and the hysteresis loop of the leaf spring accurately. However, the use of these analytical models in durability analyses are limited by the assumptions that the vertical force, that is developed by the spring, is divided equally between the front and the rear supports. This assumption may become invalid during non-symmetric loading or due to suspension configuration effects that causes the reaction forces between the front and rear not being equal.

3.1.2. Equivalent models

With this type of model the leaf spring is modelled as an equivalent system using a vertical spring (or a combination of series and parallel springs) with a damper and/or friction element. Figure 1.8 shows an example of such an equivalent model. The equivalent model aims at emulating the leaf spring by accounting for the different physical phenomena individually. For example, the stiffness of the spring is modelled by the spring and the hysteresis by the damper. An example of this modelling approach can be found in the study by Hoyle (2004) who models the leaf spring by using two springs in series, with a friction model between the two that would represent the two stiffness regimes of the leaf spring (see Figure 1.8)

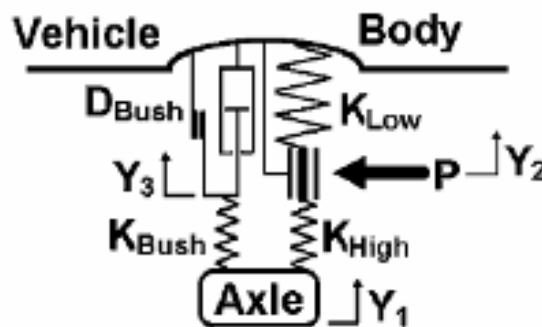


Figure 1.8. Equivalent leaf spring suspension model (Hoyle (2004))

Application in vehicle simulations

Hoyle (2004) extended his leaf spring model to include the relaxation and recovery regimes generated by the rubber bushes used in the suspension system. This was modelled as a spring in series with a damper/coulomb friction element. The study establishes the principle characteristics of the truck suspension and goes on to describe the linear and nonlinear models created to simulate the frequency response characteristics of the vehicle suspension. Comparison of the frequency response predictions with those of the actual vehicle revealed that the predictions of the nonlinear model were far better than the linear damped 5 DoF model. The model of Hoyle (2004) gives good results when the acceleration transmissibility

frequency response of the suspension is analysed, giving good comparison between the sprung mass and unsprung mass natural frequencies.

The dynamic interaction between an articulated vehicle and surface undulations is investigated by ElMadany (1987) using the equivalent technique to model the leaf spring. The effects of the frictional force generated in the laminated springs, bump-stops, wheel hop, road characteristics, loading condition and vehicle speed on the ride comfort and the road safety are discussed and evaluated. ElMadany (1987) models the friction in the suspension in one of two ways: 1) A linear spring and friction damper acting in parallel (directly coupled friction damping). 2) A linear spring in parallel with an elastically friction damper (elastically coupled friction damping). No validation was done to verify that their models can indeed capture the behaviour of the suspension accurately.

Conclusion

The equivalent model may give good results when used in ride analysis, but this model would not give good results when used in durability analysis, as its load path is not correct.

3.1.3. Discrete methods (or Finite segment methods)

This method discretizes the leaf spring into rigid elements. The rigid elements are then connected by, for example, a torsion spring and damper. The characteristics of the torsion springs and dampers are then adjusted until the leaf spring model's force-displacement characteristic is the same, or within some acceptable accuracy, to the physical leaf spring's force-displacement characteristic. Figure 1.9 shows a three link model of a leaf spring with two torsion springs (the number of links refer to the amount of links used to represent the leaf spring and does not include the other links such as for the shackle).

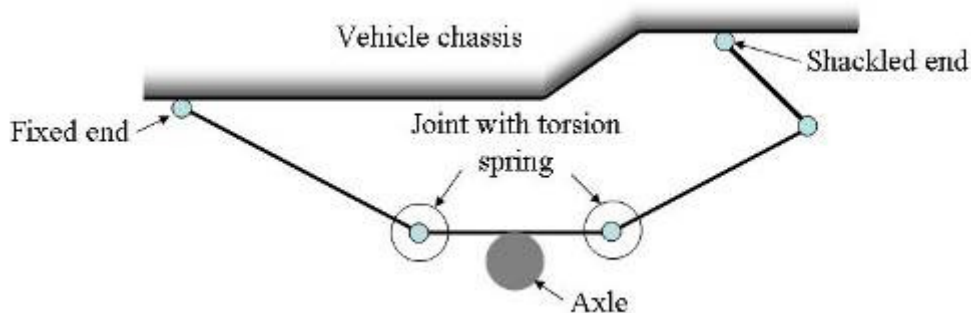


Figure 1.9. Discretized model of a leaf spring (Adapted from Huhtala *et al.*(1994))

Application in vehicle simulations

In the study by Huhtala *et al.* (1994) the aim was basically the same as that of Cole & Cebon (1994), being the prediction of the tire-road interaction forces. However, in the study by Huhtala *et al.* (1994) they model the multi-leaf spring as four links with two torsional springs, two bushings and a revolute joint. They state that when modelled in this way the model can represent the behaviour of a multi-leaf spring even when a braking force is applied to the wheel. They model the parabolic leaf spring in a similar manner. They show that the dynamic axle loads are much larger when multi-leaf springs are used compared to parabolic springs with dampers. Neither the model nor the sub-models were validated.

Yang *et al.* (2007) report a systematic methodology which is used to evaluate and improve vehicle ride comfort. The vehicle dynamics model of a tractor with tandem suspension is modelled and simulated in ADAMS. The modelling methods of nonlinear characteristic components and various road excitation inputs are introduced. These components include leaf springs, dampers and rubber bushes. In modelling the leaf spring they make the following assumptions in order to better reflect the damping characteristic of the leaf spring; (1) “Because each piece of leaf spring is a continuous flexible body, the discrete method can be used here to divide each spring into a number of quality modules, each of which can be regarded as a rigid quality and linked together with Timoshenko beams.” (2) “Adjacent leaves are clamped under normal working conditions, and only tangential direction friction happen because of the relative movement along the tangential direction”. (3) “The centres of all leaves are clamped by central bolts, so certain length of the central leaf spring can be treated as invalid length.” They showed correlation between the PSD weighted RMS of the seat acceleration, for laden and unladen cases, for different speeds. Simulation results show good agreement with the trends of experimental results but does not predict the values accurately.

Jayakumar *et al.* (2005) present a leaf spring model that can be used in road load simulations. They model the leaf spring in a similar way to the model shown in Figure 1.9. The model parameters are identified from static force-deflection test data. The advantage of this modelling method is that a simple model can be easily constructed to reproduce the kinematic and compliance properties of the actual leaf spring. They show correlation results for a static vertical test, a static longitudinal test and vertical random vibration. They also measure the vertical reaction force at the hanger bracket and shackle attachment points over severe proving ground durability events. The leaf spring model show good correlation compared to the test data even though the hysteresis loop could not be captured by the model. It may be that this spring has a very small hysteresis loop and therefore does not have an influence on the results.

Ekici (2005) compares the results of the three-link leaf spring model to test results. The geometry of this model consists of three rigid links with the leaf-spring compliance incorporated in the model through two nonlinear torsional springs at the centre-link joints. The model does not seem to be able to capture the hysteresis behaviour. They show the results of the acceleration obtained from experiments and simulation, but it is not clear from the paper where on the vehicle this acceleration measurement was taken.

Prasade *et al.* (2006) state that their experience with the 3 link leaf spring model is that it has difficulty predicting the lateral loads accurately. One of the reasons they contribute the lack of accuracy to, is that the 3 link leaf spring model cannot represent the roll behaviour of the actual suspension very well. However, Jayakumar *et al* (2005) suggests that the three-link leaf spring model can be used in durability simulations.

Conclusion

The studies that have been mentioned above, all used the discrete method to model the leaf spring. In all these studies the leaf spring had one fixed end and one shackled end. The applicability of the discrete segment method to model a leaf spring, configured as the suspension system of interest shown in Figure 1.4, is unknown and has to be investigated.

3.1.4. Finite element methods

The finite element and discrete methods are very similar. The distinction is made as the discrete method can be used directly in many rigid body dynamic software packages, whereas the finite element method requires additional software. The formulation of how the different elements are connected also differs between the two methods. Depending on the type of elements and the number of elements used the finite element method can become very computationally expensive. For details on the finite element method itself the reader is referred to the studies mentioned in the following paragraph.

Application in vehicle simulations

Often a combination of physical testing and analytical methods is used to obtain the load histories. This method is commonly called the hybrid load analysis method. Prasade *et al.* (2006) state that one of the important requirements of this method is an accurate mathematical representation of the suspension. They have a 3 link leaf spring model that has been used in various simulations. They however found that this modelling approach has difficulty predicting the lateral loads accurately. One of the reasons they contribute the lack of accuracy to, is that the SAE 3 link leaf spring model cannot represent the roll behaviour of the actual suspension very well. They use a beam element leaf spring model to address some of the limitations of the 3 link model. The 3 link and beam element model was subjected to various combinations of vertical, longitudinal and lateral loads. The two models give almost identical loads in the vertical and fore/aft direction, but the behaviour in the lateral direction is totally different. They show that the beam element model represents the roll stiffness of the actual suspension better than the 3 link model. The beam element was compared to measured forces and showed good correlation in the vertical direction and for braking events, but did not have the same good correlation for the acceleration events. They also show correlation for reaction forces in the vertical and lateral directions at the spring eye and shackle to frame attachments. It should be noted that no evidence is shown that this beam model can indeed predict the hysteresis loop correctly.

In the investigation of Sugiyama *et al.* (2006), a nonlinear elastic model of a leaf spring is developed for use in the simulation of multi-body vehicle systems. They develop a nonlinear finite element model of the leaf spring based on the floating frame of reference approach. They discuss the pre-stresses as well as the contact and friction that govern the nonlinear behaviour of the leaf spring. They conclude that their proposed leaf spring model, that includes the effect of windup, contact and friction between the spring blades, can effectively be used for assessing the dynamic stability of sports utility vehicles. No experimental model validation was performed to justify their conclusion.

Moon *et al.* (2007) developed a flexible multi-body dynamic model which can emulate the hysteretic characteristic and analyze the dynamic stress within a taper leaf spring. A finite element model of each leaf was created in MSC.Nastran which was then used to create a modal neutral file to create a flexible body of the leaf spring in ADAMS. Rigid dummy parts were attached at the places where the flexible bodies of the individual blades were in contact with one another in order to apply the contact model. This had to be done as contact could not be defined between two flexible bodies in the version of ADAMS used at the time of their study. Friction was defined in the contact model to represent the hysteretic characteristics of the leaf spring. They validated the leaf spring model by comparing the force-deflection curves for different excitation amplitudes. The results show good correlation.

Omar *et al.* (2004) state that accurate modelling of the leaf spring is necessary in evaluating ride comfort, braking performance, vibration characteristics and stability. They discuss two finite element methods that take into account the effect of the distributed inertia and elasticity, and use them to model the dynamic behaviour of leaf springs. They compare the predicted spring stiffness of their proposed model using the floating frame of reference formulation with the predictions of several other models: Equivalent lumped mass spring, equivalent beam cross-section, beam theory and the finite-element method. They state that the different techniques used to calculate the spring stiffness do not lead to the same results because different assumptions are used in each model. The assumptions made in their proposed model are as follows:

- The effect of the pre-strain due to bending of the blades during the assembly process of the spring is neglected. They believe that the pre-strains have the effect of increasing the stiffness of the leaf spring.
- The effect of the spring eyes, shackle arm, and the bushing elements are neglected.

They also discuss the importance of the number of modes that are included in the finite element model on the computational time and accuracy. Great effort was put into the model, but it was only compared to the results of other mathematical models. The ability of the proposed model to accurately represent, not only the spring stiffness, but also the hysteresis loop is not known as it was not validated against experimental data or data other than the stiffness values. Thus, there is not sufficient proof that the proposed model can indeed predict the hysteresis loop, accurately.

The paper by Li & Li (2004) presents a finite element algorithm to address the contact problem encountered in multi-leaf springs. According to them, “the most challenging part of stress analysis for the multi-leaf spring is perhaps to determine the contact status and pressure distributions between the contact faces of any two consecutive leaves”. To model the contact, a special type of interfacial element needs to be placed between adjacent blades. They state that the traditional analysis of leaf springs is based on classical beam theory due to its simplicity. However, the classic beam theory itself does not directly offer an analytical solution to the contact problems of layered members such as encountered in multi-leaf springs. They state that various approximations must be introduced to beam theory to address the contact problem. These include assumptions of concentrated load and continuous contact. The purpose of the work by Li & Li (2004) is to attempt to bridge the gap between the classical beam theory and the contact problem. As a preliminary study they ignore any frictional effects and concentrate on the distributions of the normal contact stresses. They validate their algorithm by comparing the predictions of their model with experimental results of the bending stress and the vertical load vs. deflection of the leaf spring. Good correlation was obtained for the bending stresses and the loading part of the vertical load vs. deflection results, but the model is not yet able to capture the hysteresis behaviour of the spring. Their study takes the full structure of the leaf spring into account and models it as a simply supported beam (pin and roller at the two supports respectively). It should be investigated whether the simply supported model of the leaf spring can indeed account for non-symmetric springs and more importantly for non-symmetric loads (e.g braking). Furthermore, it is unknown whether their model can account for leaf spring assemblies where the effective length changes.

Qin *et al.* (2002) presents detailed finite element modelling and analysis of a two-stage multi-leaf spring, a leaf spring assembly, and a Hotchkiss suspension using ABAQUS. Included in their models were the nonlinearities due to large deformations, the interleaf contact as well as friction. The spring and suspension characteristics such as spring rate, windup rate, roll rate,

and roll steer were analyzed. The validation was done by comparing the force-deflection and strain-deflection results from experimental measurements and simulations by loading the spring in 15 steps. For the leaf spring assembly they compare the roll moment vs. roll angle and the steer angle vs. roll angle. All the comparisons showed good correlation. They did analyse the leaf spring assembly windup but did not validate it against experimental results.

Conclusion

All the studies mentioned here was concerned with modelling a leaf spring that was fixed at one end and shackled at the other end except for Li & Li (2004) who had it supported by a pin and roller. This however is equivalent to the fix and shackled end configuration. Prasade *et al* (2006) showed results indicating that the beam element model can be used in durability analysis.

3.1.5. Neural network models

Neural networks are computationally efficient mathematical models that can be trained, through input-output data sets, to emulate smooth nonlinear functions. A neural network consists of neurons that can be connected to form various types of networks. Figure 1.10 shows a simple neuron. A network of a number of these interconnected neurons is shown in Figure 1.11. The network shown is known as a feedforward neural network. A neural network is trained during which the adjustable variable weights (w) and biases (b) are adjusted until the neural network is able give the correct output for a specific input. After training, the neural network can be used to emulate the function which it has been trained with. More detail on neural networks will be given in Chapter 3.

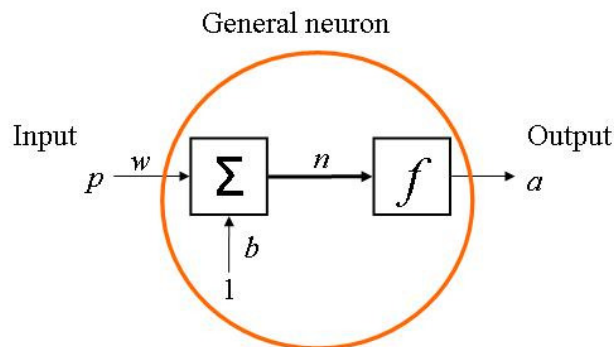


Figure 1.10. Simple neuron

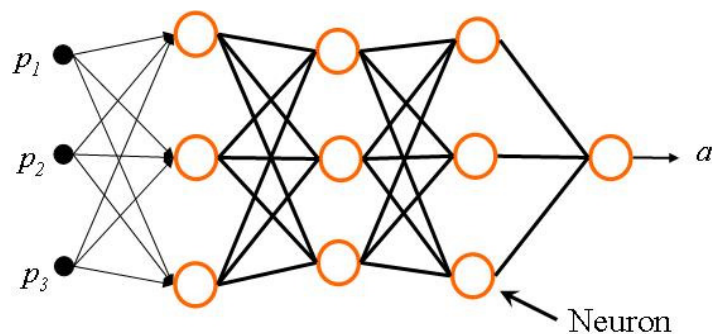


Figure 1.11. Feed forward neural network

Application in vehicle simulations

Leaf springs are known to have nonlinear and hysteresis behaviour. Ghazi Zadeh *et al.* (2000) state that this makes their mathematical modelling difficult and susceptible to a considerable amount of estimation errors. Ghazi Zadeh *et al.* (2000) state that the force-deflection curves that characterizes a leaf spring is very difficult to emulate using neural networks. They state that a neural network approach is successful when a smooth function is emulated and when a set of data points, that are evenly scattered over the entire working space of the function variables, are available. This set of data points are required to construct a set of input-output data points which can be used to train the neural network with. They show that the recurrent neural network is able to emulate the leaf spring behaviour accurately after it is taught with a set of input-output data points. They showed that the neural network emulates the leaf spring well by comparing the neural network and their analytical model's results in both the time and frequency domains. They compared the force-displacement and the spectral density functions of the tire force, spring force and acceleration of the unsprung mass with the results obtained from an analytical model.

Conclusion

The study of Ghazi Zadeh *et al.* (2000) showed that a neural network can be trained to accurately emulate a leaf spring. It should be noted that in order for the neural network to accurately emulate the leaf spring a comprehensive set of data is required to train the neural network. This has to be kept in mind when the neural network is to be used but limited data is available on the leaf spring.

3.2. Summary of leaf spring modelling techniques

A summary of the different approaches that exists to model the leaf spring along with some of the advantages and disadvantages of each method as well as an indication of the validation that have been done for the particular approach, is given in Table 1.1.

Table1.1. Summary of leaf spring modelling techniques

Approach	Variations on approach	Advantages	Disadvantages	Validation
Discrete method	<ul style="list-style-type: none"> Connect elements with Timoshenko beams (Yang <i>et al.</i>, 2007) 			<ul style="list-style-type: none"> Correlation between the PSD weighted RMS of the seat accelerations for laden and unladen for 4 different speeds shows good agreement in trend but does not predict the values accurately. (Yang <i>et al.</i>, 2007)
	<ul style="list-style-type: none"> Connect segments with springs and dampers (Rill <i>et al.</i>, 2003), (Milliken and Milliken, 2002), (Huhtala <i>et al.</i>, 1994) 	<ul style="list-style-type: none"> Able to predict behaviour under braking conditions (Huhtala <i>et al.</i>, 1994) 		
	<ul style="list-style-type: none"> SAE three-link model (Jayakumar <i>et al.</i>, 2005) 	<ul style="list-style-type: none"> Most common model according to Prasade <i>et al.</i> (2006) Three-link leaf-spring model is easy to construct (Jayakumar <i>et al.</i>, 2005) Three-link model accurately represents the kinematic and kinetic behaviour of the physical leaf-spring (Jayakumar <i>et al.</i>, 2005) Three-link model is very simple and has fewer degrees-of-freedom (Jayakumar <i>et al.</i>, 2005) Three-link model simulations are very efficient and easy to perform without encountering any numerical difficulties by the ADAMS solver. (Jayakumar <i>et al.</i>, 2005) 	<ul style="list-style-type: none"> Lateral loads very inaccurate (Prasade <i>et al.</i>, 2006) Cannot represent the roll behaviour very well (Prasade <i>et al.</i>, 2006) Inter-leaf friction not always included 	<ul style="list-style-type: none"> Correlation for static vertical test, a static longitudinal test and random vibration. Also measure the vertical reaction force at the hanger bracket and shackle attachment points. All these tests show good correlation. (Jayakumar <i>et al.</i>, 2005)
	<ul style="list-style-type: none"> Extension of the SAE three-link model is to use nonlinear vertical spring in parallel to account for the nonlinear force-deflection behaviour in the vertical direction (Jayakumar <i>et al.</i>, 2005), (Ekici, 2005) 		<ul style="list-style-type: none"> Introduces spurious load path (Jayakumar <i>et al.</i>, 2005), (Ekici, 2005) Likely misrepresentation of longitudinal behaviour makes this model unsuitable for application in road load simulation (Jayakumar <i>et al.</i>, 2005), (Ekici, 2005) 	
		<ul style="list-style-type: none"> Requires only rigid body modelling capabilities that are available in most existing general-purpose multi-body computer codes (Sugiyama <i>et al.</i>, 2006) 	<ul style="list-style-type: none"> Large number of discretized bodies in order to achieve accurate solutions. Leads to a large number of degrees of freedom (Sugiyama <i>et al.</i>, 2006) 	
			<ul style="list-style-type: none"> No systematic and generally acceptable procedure for determining the number and properties of the discrete bodies, springs and dampers (Sugiyama <i>et al.</i>, 2006) 	
Finite Element Method	<ul style="list-style-type: none"> Full FEM model with contact and friction 		<ul style="list-style-type: none"> Computationally expensive Use of these models impractical in multi-body vehicle simulations (Sugiyama <i>et al.</i>, 2006) 	

Approach	Variations on approach	Advantages	Disadvantages	Validation
	<ul style="list-style-type: none"> Floating frame of reference (to model stiff leaf springs that experience small elastic deformations) (Omar <i>et al.</i>, 2004) 	<ul style="list-style-type: none"> Leads to a reduced order model that includes all significant deformation modes (Sugiyama <i>et al.</i>, 2006) and (Omar <i>et al.</i>, 2004) 		
	<ul style="list-style-type: none"> Absolute nodal coordinate formulation (to model soft leaf springs that experience large deformations) (Omar <i>et al.</i>, 2004) 	<ul style="list-style-type: none"> Enables more detailed finite-element models for the large deformation of very flexible leaf springs (Omar <i>et al.</i>, 2004) 		
	<ul style="list-style-type: none"> Beam element models 	<ul style="list-style-type: none"> Considered state-of-the-art (Jayakumar <i>et al.</i>, 2005), (Ekici, 2005) Model gives good results in all directions (exception see disadvantages) (Prasade <i>et al.</i>, 2006) 	<ul style="list-style-type: none"> In situations where it is subjected to high fore/aft acceleration on high reverse braking events results not good (Prasade <i>et al.</i>, 2006) Results in a very large, and extremely nonlinear model with a high number of degrees-of-freedom (Jayakumar <i>et al.</i>, 2005). It showed accurate prediction in jounce condition but not in roll condition. (Tavakkoli, 1996) 	<ul style="list-style-type: none"> Shows correlation of vertical and lateral reaction forces at the spring eye and shackle attachment points (Prasade <i>et al.</i>, 2006)
	<ul style="list-style-type: none"> FlexBody in Adams 		<ul style="list-style-type: none"> Contact can not be applied between flexible bodies in ADAMS (Moon <i>et al.</i>, 2007). Have to add dummy parts 	<ul style="list-style-type: none"> Compare force deflection curves for different excitation amplitudes. Show good correlation. (Moon <i>et al.</i>, 2007)
Simple Beam theory	<ul style="list-style-type: none"> Simple beam theory has been extended to include large deflections, dual rate springs, stiffness modification due to shackles, initial camber and constant cross section (single leaf) design. (Cebon, 1986) 	<ul style="list-style-type: none"> Provide designers with estimates of large deflection spring rates 	<ul style="list-style-type: none"> Neglect interleaf friction 	
Lumped Mass Spring Model			<ul style="list-style-type: none"> This approach is too simple to take into account the effect of different deformation modes of the leaf spring in vehicle suspensions since all the spring characteristics are modelled by an equivalent spring constant (Sugiyama <i>et al.</i>, 2006) The effect of the distributed inertia and stiffness of leaf springs are neglected (Sugiyama <i>et al.</i>, 2006) The nonlinear characteristics of leaf springs due to contact and friction between blades cannot be captured (Sugiyama <i>et al.</i>, 2006) 	

Approach	Variations on approach	Advantages	Disadvantages	Validation
Analytical model (Empirical model)		<ul style="list-style-type: none"> • Easy to implement • Can capture stiffness and hysteresis loop (Fancher <i>et al.</i>, 1980) 	<ul style="list-style-type: none"> • Parameter values for the closest fit are strongly sensitive to the displacement amplitude. Not possible to fit equation to all hysteresis loops using single set of parameters. (Cebon, 1986) • Assumes reaction forces are equally divided between the front and rear supports 	<ul style="list-style-type: none"> • Compared to experimental force-displacement data Fancher <i>et al.</i>, 1980) • Used in model to predict tire forces. Showed good correlation (Cole & Cebon, 1994)
Equivalent model			<ul style="list-style-type: none"> • Spurious load path 	<ul style="list-style-type: none"> • Frequency response predictions showed good correlation with experimental data (Hoyle, 2004)
Neural Network models		<ul style="list-style-type: none"> • No need to model complex physical phenomenon's (for example friction or contact) 	<ul style="list-style-type: none"> • Non-physics based model 	

3.3. Conclusion

From the literature study it can be concluded that there is not a clear best leaf spring model. Different models exist and various studies have shown that these models can indeed represent aspects of the leaf spring accurately and give good results when used in simulations. It would seem that the type of model that can be used to give accurate predictions depend on the kind of parameters that are to be predicted. Thus, these models are very particular to the problem they are used in, and they may not give the same results in a different application, or when other sets of parameters are to be predicted.

Take for instance the model developed in the study by Hoyle (2004). They derive a model for the leaf spring that can take into account the different stiffness regimes, hysteresis, as well as the rubber bush relaxation. This model gives good results when the acceleration transmissibility frequency response of the suspension is analysed giving good comparison between the sprung mass and unsprung mass natural frequencies. However, this model is not adequate for predicting the forces that are transmitted to the chassis through the leaf spring suspension as this model does not have the same load path as the real leaf spring. Thus, this model is adequate when looking at the frequency response of the vehicle but when the forces between the suspension and the chassis need to be analysed the model becomes inadequate. This implies that there may be a number of ways to model a leaf spring but that only some of them may be useful in certain cases, thus making the leaf spring models problem dependent (see Figure 1.12). However, it should be kept in mind that a model should be as simple as possible and as complex as necessary, implying that the model be able to predict the forces acting on the chassis may be too complex to be used for predicting the frequency response of the vehicle, or vice versa. This may imply that it would be better to use one model for a specific problem and another for a different problem. This has the advantage that a model can be selected for a specific problem that gives the best computational efficiency and accuracy.

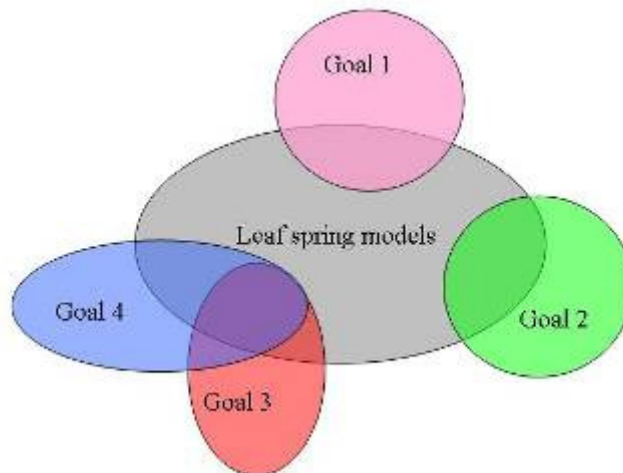


Figure 1.12. Applicability of models to simulation goals

The minimum requirements that are set for the leaf spring model in this study are that it has to be able to capture the spring stiffness and hysteresis loop of the leaf spring. In addition to these requirements, the model should preferably be able to account for changes in the load length of the leaf spring which affects the stiffness of the leaf spring (the loaded length and its effect on the stiffness of the leaf spring will be discussed in Chapter 2). As already stated the model of the leaf spring should be accurate yet computationally efficient. Unfortunately, the accuracy and computational efficiency of each model is not known and a modelling technique

cannot be selected according to these two criteria. It is however expected that the finite element method might be the least computationally efficient model. The majority of the leaf spring models in the literature study considered the leaf spring configuration where the leaf spring is attached to the vehicle chassis using the fixed-shackled end configuration. The suspension system used in this study does not use the fixed-shackled end configuration to attach the leaf spring to the chassis, instead the leaf spring is supported by the hangers, as was shown in Figure 1.4. The ability of the models used to model a leaf spring in the fixed-shackled end configuration might not be able to capture the load length change effect. Chapter 3 will address the modelling of the leaf spring in detail.

4. Overview of study

A brief overview of the study is given here with the layout of the study shown in Figure 1.13.

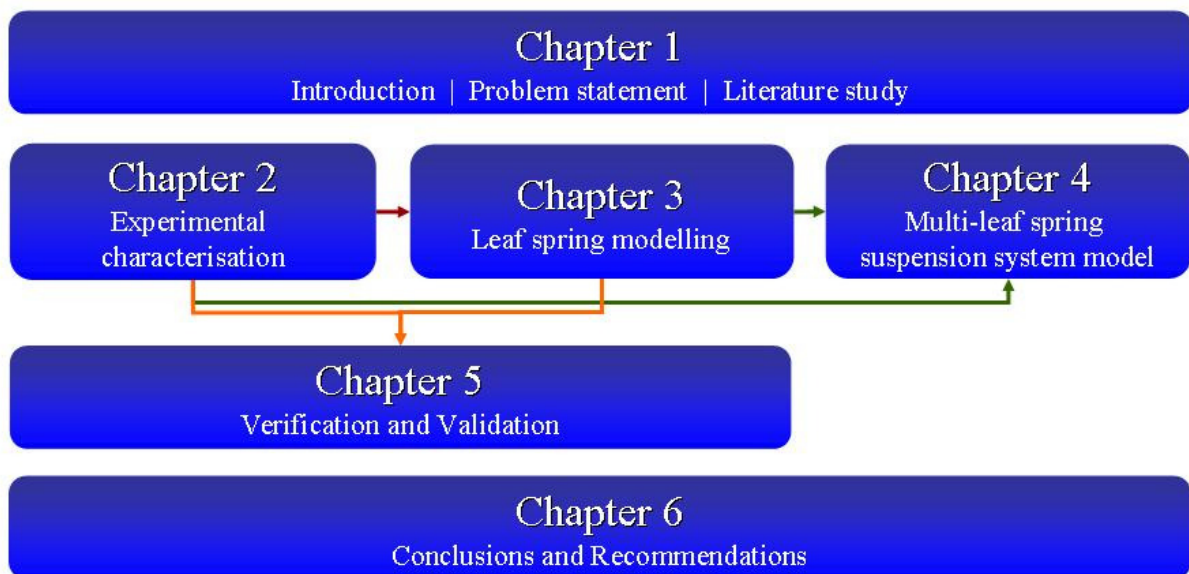


Figure 1.13. Overview of study

In this chapter, Chapter 1, the reader was introduced to the problem. A literature study was conducted that showed that many different modelling techniques exist that can be used to model a leaf spring. Because this study is concerned with obtaining a validated model of the leaf spring and of the suspension system, two primary elements are of concern i.e. the physical system of interest and the simulation model. The process of obtaining a validated model implies that the mathematical model has to be created and the experimental data gathered which is then used to parameterise and validate the model. The experimental characterisation that was performed to collect the required experimental data for model validation is presented and discussed in Chapter 2.

Chapter 3 is concerned with leaf spring modelling. Two fundamentally different modelling approaches is used i.e. a physics-based and non physics-based modelling approach. For the physics based model a novel model was developed that uses a macro modelling approach. Two formulations are presented for the elasto-plastic leaf spring model that are parameterised by merely extracting three or four parameters from experimental data depending on the formulation used. The elasto-plastic leaf spring model is used to model both the multi-leaf spring and the parabolic leaf spring. A method is also proposed that can account for the changes in the stiffness of the leaf spring due to changes in the loaded length. This method

can be used together with the elasto-plastic leaf spring model which results in a model that can capture the stiffness, the hysteresis as well as the changes in loaded length of the leaf spring. In addition to the physics-based elasto-plastic leaf spring model a non physics-based method was used that uses neural networks to emulate the leaf spring. The neural network was only used to emulate the multi-leaf spring in this study but can be used to emulate the parabolic leaf spring and is expected to give similar results.

The validated elasto-plastic leaf spring model is used to model a simplified version of the suspension system in Chapter 4. This model of the simplified suspension system is created to verify whether the subsystem model using the elasto-plastic leaf spring model is able to predict the forces that act onto the chassis. This subsystem model is validated using the experimental data obtained during the experimental characterisation performed in Chapter 2.

Chapter 5 discusses the verification and validation process and presents a new validation metric that can be used in a quantitative validation process. The validation metric is then used to calculate the accuracy of the elastic-nonlinear formulation of the elasto-plastic leaf spring model and the neural network model. The accuracy as well as the efficiency of the two modelling techniques are presented and compared. The study is concluded in Chapter 6 with the final conclusions and recommendations for future work.

Chapter 2

Experimental characterisation

Experimental data forms an integral part of many engineering endeavours. Among these are studies concerned with the development of mathematical models of a particular physical system of interest. Experimental data is of critical importance as it supplies the necessary input data to the mathematical models. The experimental data required as input to the models range from simple geometrical information to complex non-linear, hysteretic characteristics of force elements. Furthermore, experimental data is a prerequisite for model validation.

This study is concerned with the development of a validated mathematical model which is able to simulate the vertical behaviour of a leaf spring suspension system used on commercial vehicles. In order to create a validated model of the suspension system introduced in Chapter 1, various aspects need to be characterised experimentally in order to obtain the experimental data that will be required in the validation process. One of the required parameters is the forces between the suspension attachment points (i.e the hangers) and the chassis. In order to measure these forces a six component load cell was manufactured, calibrated, verified and validated. This process is briefly discussed in this chapter in paragraph 1 with a detailed discussion given in Appendix A. This chapter then continues with the experimental characterisation of the multi-leaf spring and parabolic leaf spring as well as the characterisation of the suspension system using the two different leaf springs. The characterisation of the multi-leaf spring and suspension system using the multi-leaf spring are discussed in paragraph 2. Paragraph 3 discusses the characterisation of the parabolic leaf spring and the suspension system using the parabolic leaf spring.

1. Six component load cell (6clc)

At the start of the experimental work it was clear that the reaction forces between the suspension attachment points and the chassis had to be measured. This requirement came from the aim of creating a validated suspension model for use in chassis durability analysis. In order to measure these forces, a six component load cell (6clc) was developed. The 6clc had to be able to measure the forces in all three directions and the moments about all three axis. With this information it is possible to obtain a complete picture of how the suspension system transmits the forces from the axle to the chassis and validate whether the suspension models can indeed predict these forces accurately.

The 6clc that was developed is shown in Figure 2.1. The 6clc consists of two parts that are connected to each other via six uni-axial load cells. One of the uni-axial load cells is shown in Figure 2.2. The six uni-axial load cells are connected between the two parts in such a way that all the degrees of freedom between the two parts are removed and so that each of the uni-axial

load cells measures only tension-compression forces. The two parts of the 6clc are attached between the two bodies where the forces need to be measured. The use of two six component load cells will also make it possible to measure how the forces are distributed between the front and rear suspension attachment points. It is expected that without the radius rod and with the front and rear hanger having equal distance from the centre of the axle a vertical force on the leaf spring will divide equally between the front and rear hanger attachment points. However, this 50/50 force distribution will change when the front and rear hanger spacing is not equal. The 50/50 distribution may also be affected by the radius rod as well as combined loading that may act on the axle.

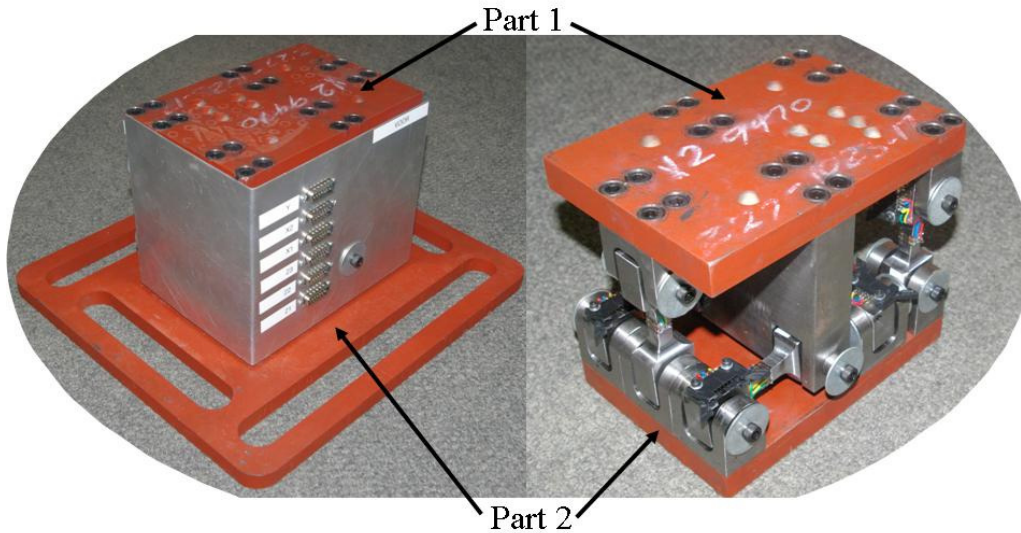


Figure 2.1. Six component load cell



Figure 2.2. Uni-axial load cell used in the six component load cell

The 6clc shown in Figure 2.1 uses six of the uni-axial load cells shown in Figure 2.2. After 12 uni-axial load cells were calibrated they were incorporated into two 6clcs one being the front 6clc and the other one the rear 6clc. Appendix A gives a detailed discussion of the calibration of the uni-axial load cells. The verification of the concept of the 6clc as well as the verification of the ADAMS/Car model using analytical equations are also shown in detail in Appendix A. The model in ADAMS/Car was created to measure the equivalent forces and moments in the simulation environment in order to compare the virtual measurements to the physical measurements. The virtual 6clc will be used in Chapter 4 to compare the modelling results to the physical measurements. The derivation of the analytical equations and the modelling of the 6clc is discussed in detail in Appendix A. Appendix A also presents the validation of both the analytical equations and the ADAMS/Car model using experimental

measurements. From the verification and validation results it was concluded that the physical and virtual 6clc is able to measure the forces that are transmitted from the suspension to the chassis. Figure 2.3 shows the use of the front and rear 6clcs in an experimental setup.

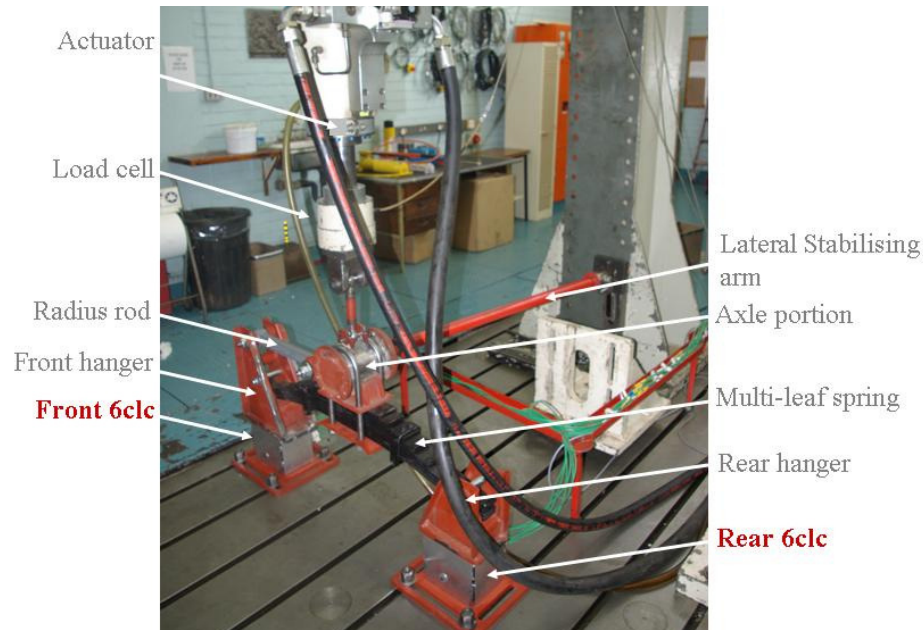


Figure 2.3. Use of front and rear 6clc in experimental setup

2. Characterisation of the suspension system using the multi-leaf spring

The various aspects of the suspension system that were characterised using the multi-leaf spring are shown in Figure 2.4. The tests are categorised into three major categories i.e. **vertical**, **lateral** and **longitudinal** characteristic. The vertical characteristics were considered the most important as the primary aim of the study is to obtain a validated mathematical model of the suspension system that could be used in durability analysis. The vertical characterisation was sub divided into three aspects i.e. the **force-displacement characteristic**, **roll stiffness** and the **complete** suspension. Only the force-displacement characteristics are relevant for this study and will therefore be presented. The characterisation of the roll stiffness and the characterisation of the complete suspension system as well as the lateral and longitudinal characterisation was done to have the experimental data available when the model is extended in future work. The experimental characterisation of interest to this study is shown in green in Figure 2.4 and will be presented in further detail in this chapter.

The force-displacement characterisation of the multi-leaf spring was done using two setups namely, the in-service setup and spring only setup. Details of the two setups will be given in paragraph 2.1.1 and paragraph 2.1.2. The effect of the U-bolt preload and the longitudinal spacing of the hangers on the force-displacement characteristic will be presented. The deflection shape of the leaf spring subjected to different loading and with different hanger spacings were also obtained. As indicated in Figure 2.4 three multi-leaf springs were used in the force-displacement characterisation. Two of them (New 1 and New 2) were brand new leaf springs that have not been used prior to the characterisation tests. The third leaf spring (Old) was taken from a commercial trailer that had done approximately 500 000 km.

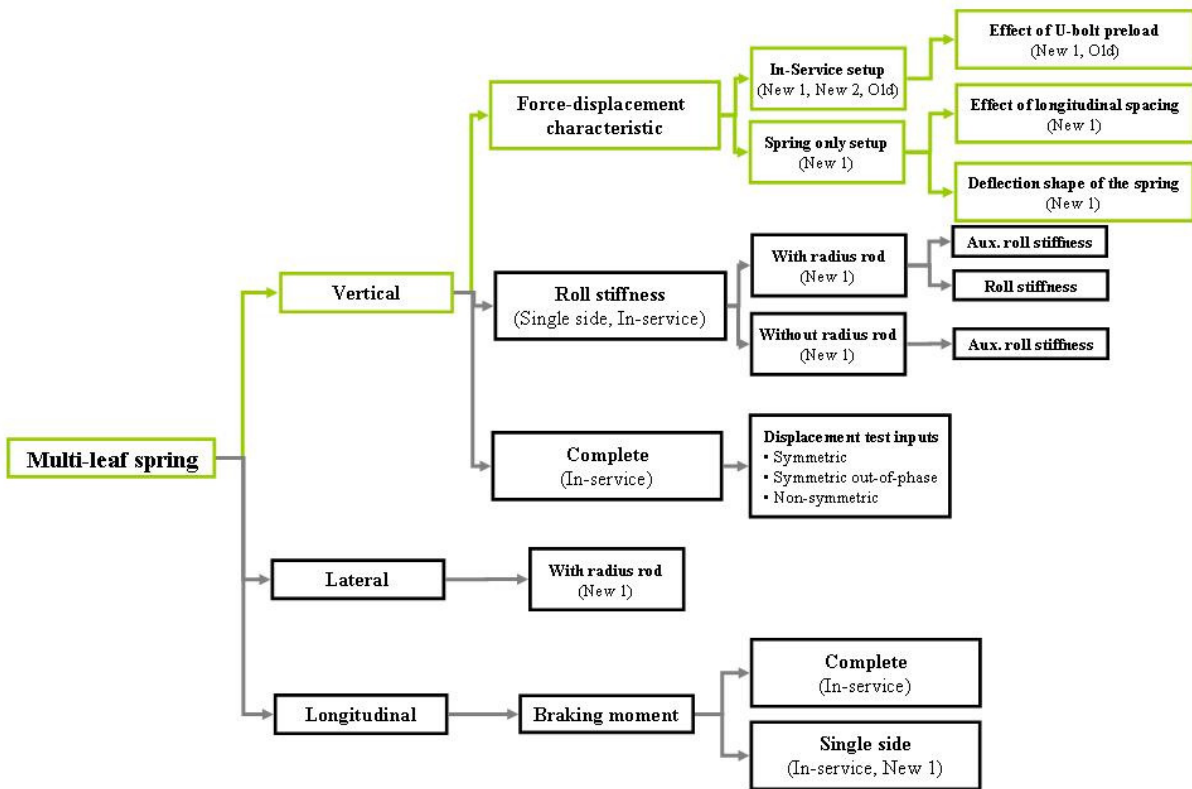


Figure 2.4. Overview of characterisation using the multi-leaf spring

2.1. Force-displacement characteristics

The force exerted by the leaf spring when deflected, is a function of the static load and the amplitude of the imposed displacement. Cebon (1986) and Fancher *et al.* (1980) found that the spring force is not dependent on the frequency of the imposed displacement. This would imply that the force-displacement characteristic does not need to be obtained at different input frequencies. To verify this, two displacement input signals were used that had frequencies of 0.05 Hz and 0.5 Hz, respectively. The force-displacement characteristics of the multi-leaf spring subjected to these two input signals are shown in Figure 2.5. Figure 2.6 shows the force-displacement characteristics when the amplitude is kept the same but the excitation frequency is swept from 0.05 Hz to 4 Hz. From Figure 2.5 and Figure 2.6 it can be observed that the force-displacement characteristic stays essentially the same irrespective of the excitation frequency. This seems to confirm that the force-displacement characteristic of the leaf spring is not dependent on the frequency of the displacement input. The experimental force-displacement characteristics shown in Figure 2.5 and Figure 2.6 were obtained with the multi-leaf spring in the in-service setup which is discussed in paragraph 2.1.1.

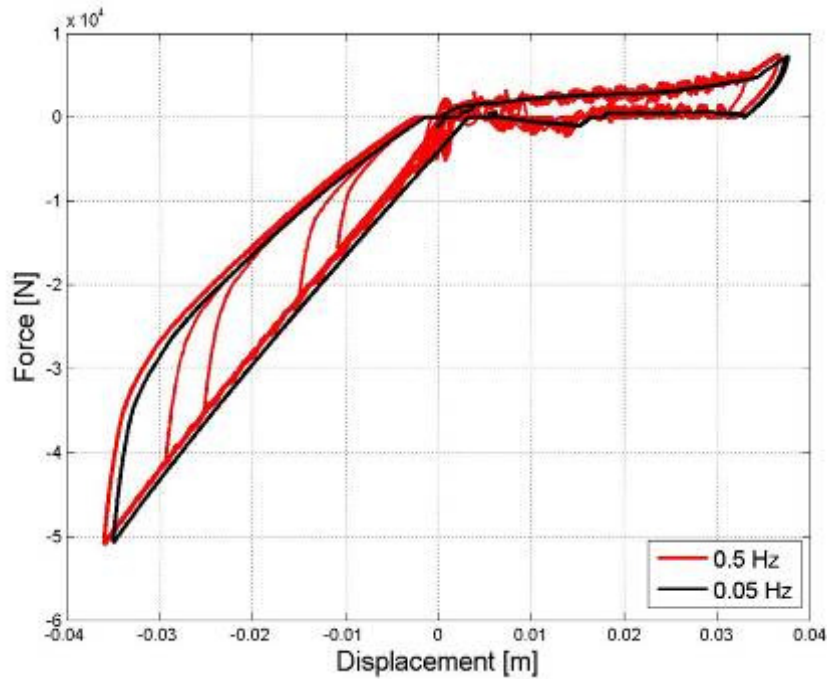


Figure 2.5. Compare force-displacement characteristics for different excitation frequencies

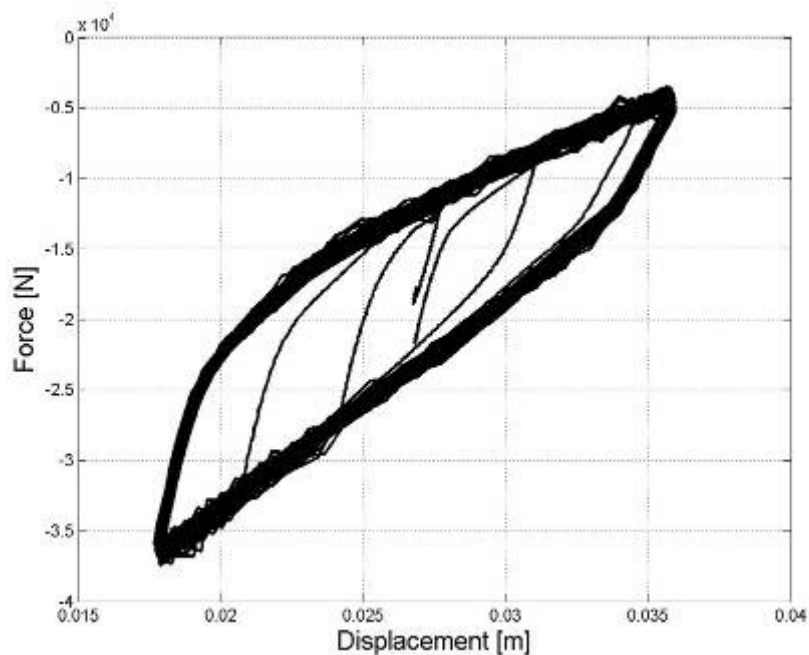


Figure 2.6. Force-displacement characteristic for sine sweep with frequencies ranging from 0.05 Hz to 4 Hz

From the results above and the findings of Cebon (1986) and Fancher *et al.* (1980) the spring force of the multi-leaf spring is therefore a function of the static load and the amplitude of the imposed displacement on the leaf spring:

$$\text{Leaf spring force} = f(\text{static load, amplitude of imposed displacement})$$

The force-displacement characteristic from the spring supplier is usually obtained from a test in which the spring is monotonically loaded. Therefore the supplier's force-displacement characteristic is not able to capture the hysteretic behaviour of the multi-leaf spring. For the

purpose of this study a more comprehensive force-displacement characteristic of the leaf spring is required which should include the hysteretic behaviour.

The force-displacement characteristic for the multi-leaf spring is obtained using two different setups i.e. an in-service setup and a spring only setup. These two setups are discussed in paragraph 2.1.1 and 2.1.2. In order to characterise the dependency of the spring force on the static load and the amplitude of the imposed displacement, five displacement inputs were used in the force-displacement characterisation. The five displacement inputs can be categorised into two groups. The first group of signals consist of sinusoidal waves with a frequency of 0.25 Hz and varying static loads with different amplitudes. The two signals used in this group are shown in Figure 2.7. The second group consists of three random signals with their input frequency having a bandwidth of 0.6 Hz. Figure 2.8 shows the three random signals used. The random signal in Figure 2.8(a) only compresses the spring and has a rms amplitude of 19.2 mm. The random signal in Figure 2.8(b) compresses and extends the leaf spring and has a rms amplitude of 16.9 mm. The third random signal, shown in Figure 2.8(c) only extends the spring and has a rms amplitude of 23 mm. These displacement signals will be referred to as follows:

- Input displacement signal 1 - Figure 2.7(a)
- Input displacement signal 2 - Figure 2.7(b)
- Input displacement signal 3 - Figure 2.8(a)
- Input displacement signal 4 - Figure 2.8(b)
- Input displacement signal 5 - Figure 2.8(c)

Most of the force-displacement characteristics shown in this study were obtained using either Input displacement signal 1 or Input displacement signal 3.

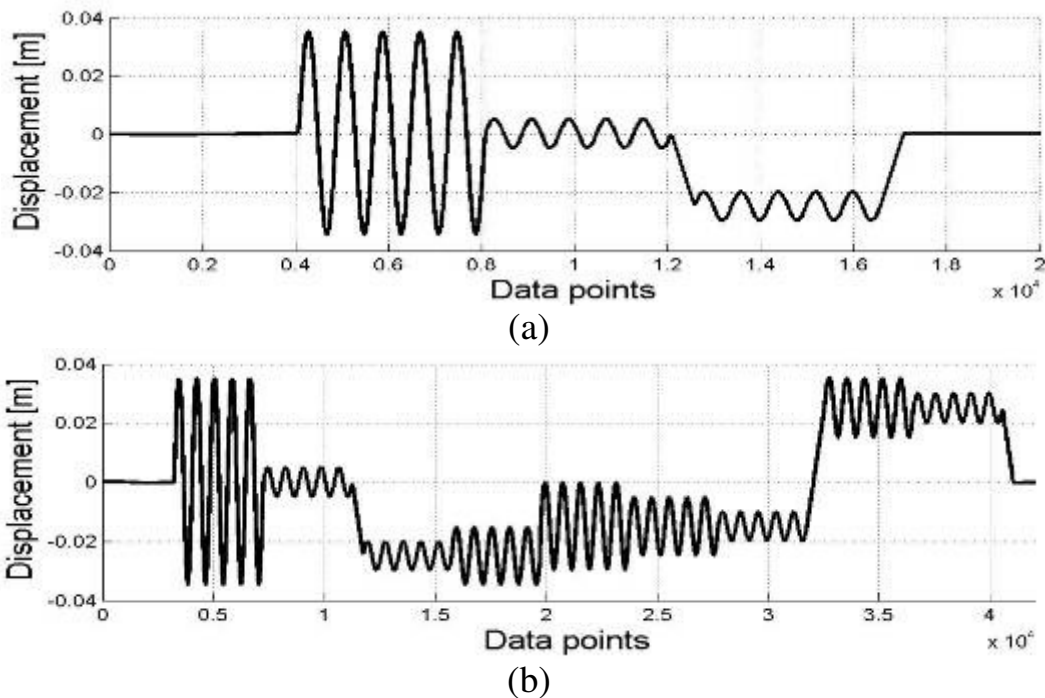


Figure 2.7. Sinusoidal input signals with constant frequency but varying static loads and amplitudes

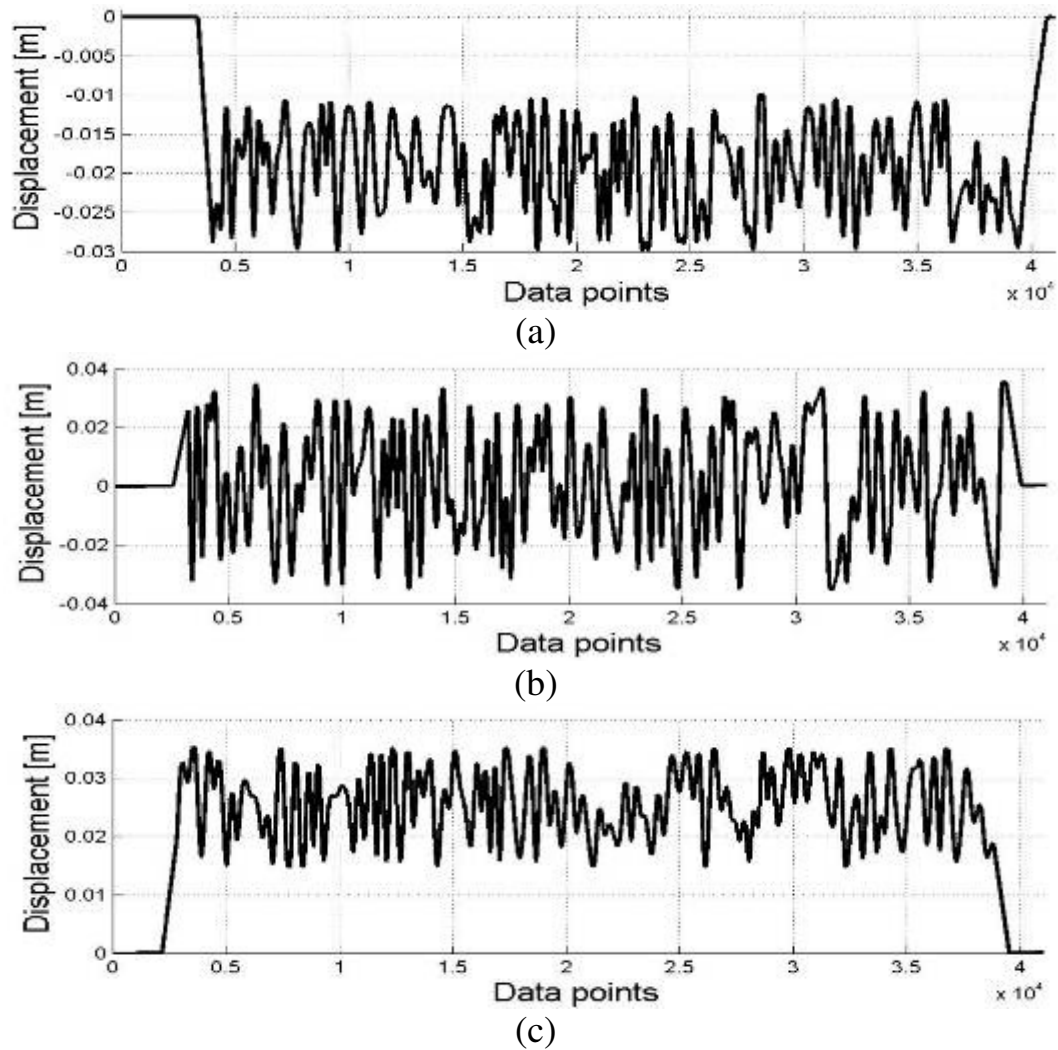


Figure 2.8. Random input signals. (a) Spring only compressed. (b) Spring compressed and extended. (c) Spring only extended

2.1.1. In-service setup

The in-service experimental setup is shown in Figure 2.9. The spring is constrained exactly as it would be when on the vehicle, meaning that the multi-leaf spring is supported by the front and rear hangers and the radius rod is connected between the front hanger and the axle. It should be noted that this setup only considers the one side of the suspension. In other words there is no coupling between the left and right hand springs as would be the case on the vehicle. A lateral stabilising arm is needed to prevent the single sided setup from tipping over when the actuator compresses the spring. The experimental setup includes the two six component lead cells (6clc) that are placed between the hangers and the laboratory floor (which represents the chassis of the vehicle). The measurements taken with the 6clcs enables the quantification of the input forces into the chassis of the vehicle. They also make it possible to check how the vertical force that the leaf spring develops is distributed between the front and rear attachment points.

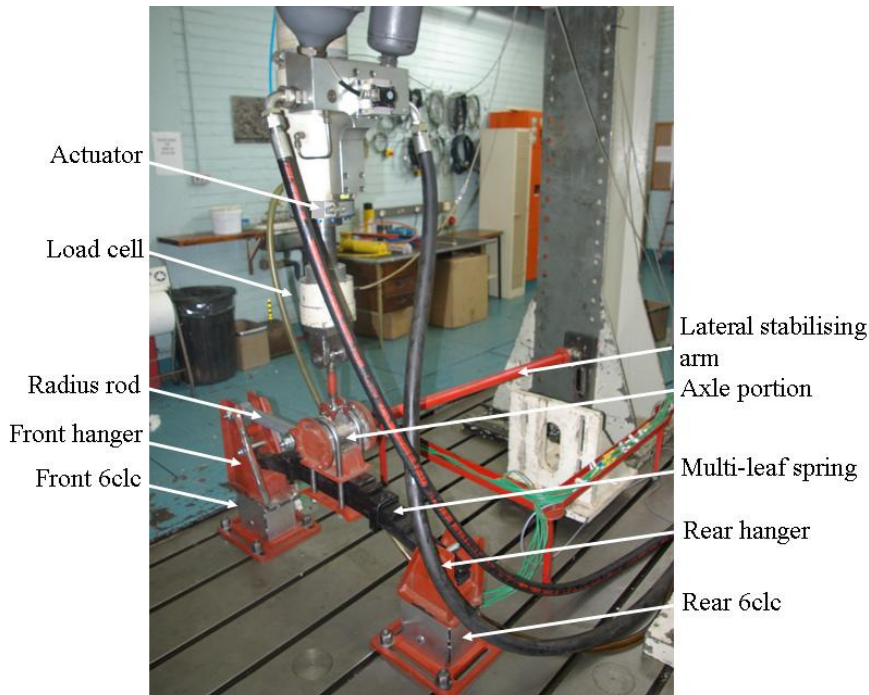
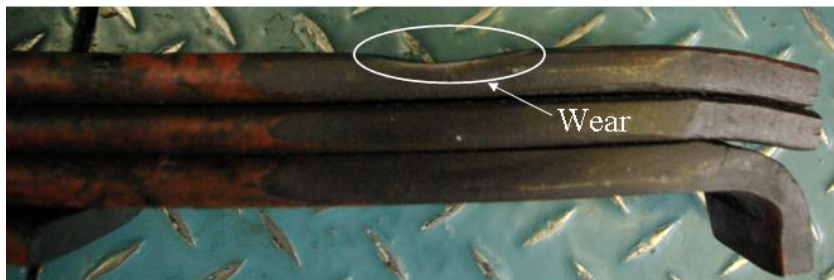


Figure 2.9. Experimental in-service setup of single sided suspension with the multi-leaf spring

The force-displacement characteristics were obtained for three multi-leaf springs. The leaf springs were all similar in that they all consisted of 8 blades, of which three were full length blades, with all of the blades having a uniform cross-section with a width of 76 mm and a thickness of 14 mm. Two of the leaf springs were new (New 1 and New 2) and the third leaf spring had been used on a vehicle and had done approximately 500 000 km (reference will be made to this spring as the old spring). Figure 2.10(b) shows the wear on the blade, of the old leaf spring, that was in contact with the wear plates in the hangers.



(a)



(b)

Figure 2.10. (a) New and old multi-leaf springs. (b) Wear on old multi-leaf spring

Figure 2.11 shows the force-displacement characteristics of the three multi-leaf springs. The characteristics obtained from the two new leaf springs are similar. It is interesting to note that the old spring's characteristics show a smaller hysteresis loop. The repeatability of the test is shown in Figure 2.12. One of the new multi-leaf springs (i.e. New 2) were characterised 7 times and it can be seen from Figure 2.12 that the characteristics obtained from run 2 and run 3 is similar with a small deviation between them and the other four runs (run 4 to 7) which again gave similar results. From this it can be seen that the experiment gives good repeatability.

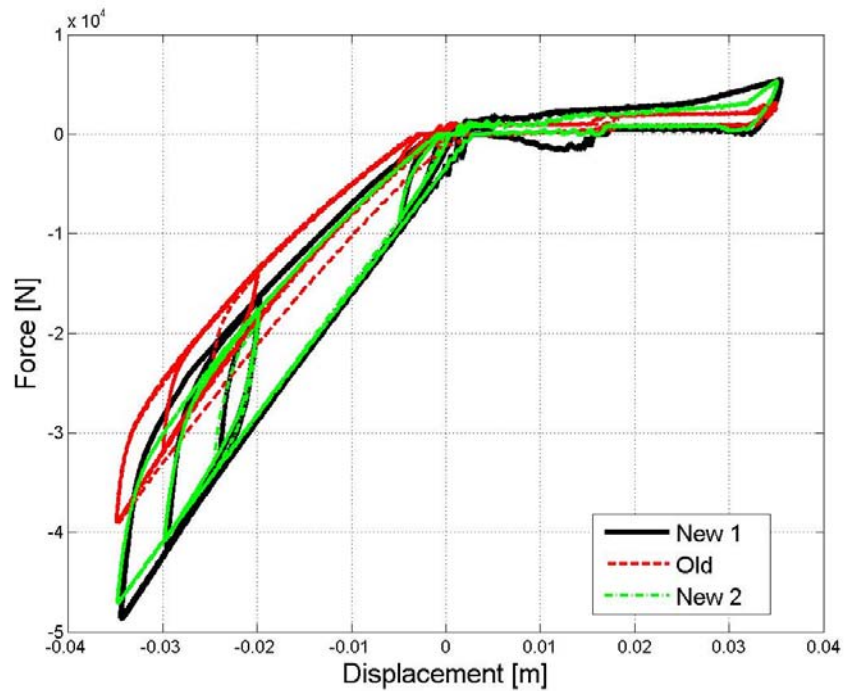


Figure 2.11. Comparison between the characteristics of the two new springs and the old spring

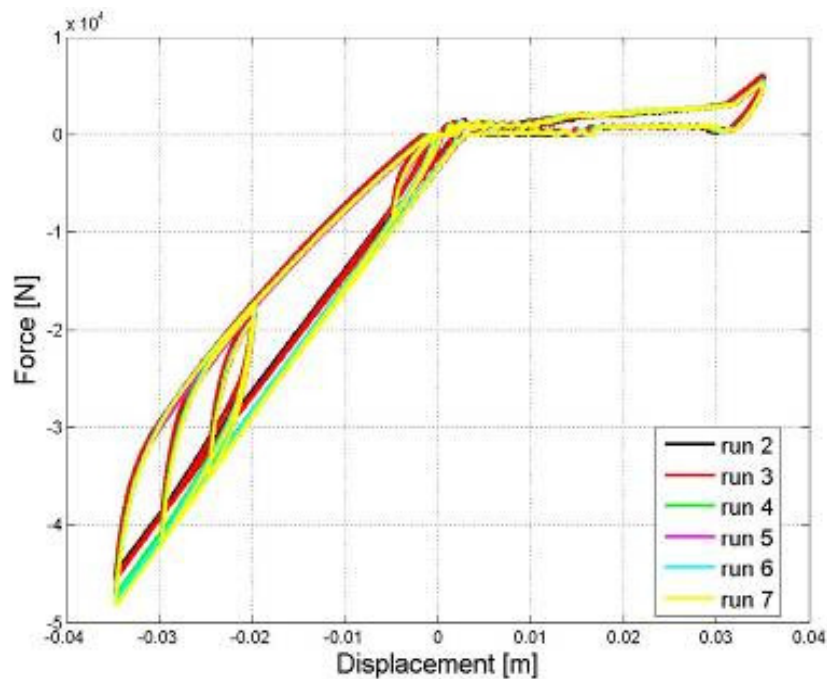


Figure 2.12. Comparison of seven separate measurements of the force-displacement characteristic of the same multi-leaf spring (New 2)

2.1.1.1. Effect of U-bolt preload on the force-displacement characteristic

An interesting and important observation was made concerning the effect of the U-bolt's preload on the force-displacement characteristic of the multi-leaf spring. The U-bolts are used to attach the axle to the leaf springs by looping the U-bolts around the axle and using a clamp plate to secure the axle via the U-bolts to the leaf spring (see Figure 2.13). This configuration constrains the multi-leaf spring and has an affect on the force-displacement characteristic of the multi-leaf spring.

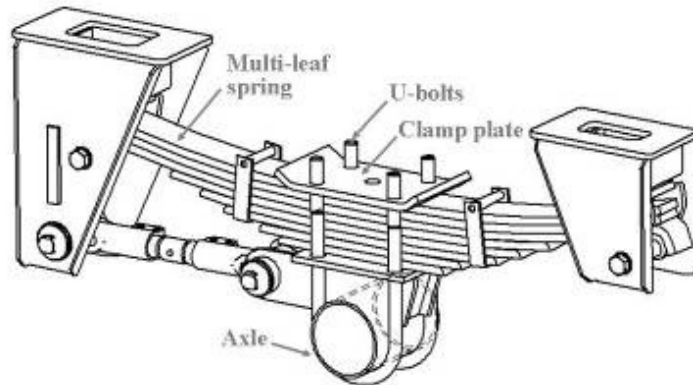


Figure 2.13. Attachment of axle to multi-leaf spring via U-bolts

Figure 2.14 shows the characteristics of the multi-leaf spring when the U-bolts are torqued to different values. The original characteristic shown in Figure 2.14 was obtained with the bolts torqued to the specified 450 N.m (Van De Wetering Engineering, 2001). The U-bolts were then completely loosened and torqued to a third of the specified value i.e. 150 N.m. After this the bolts were again torqued to the specified value of 450 N.m. The force-displacement characteristic of the spring was measured twice at each of the above mentioned values. From Figure 2.14 it can be observed that the multi-leaf spring's stiffness increases when the preload of the U-bolts are increased. The same trend is seen for the old spring which is shown in Figure 2.15. The effect is considerable and thus needs to be taken into account during suspension assembly.

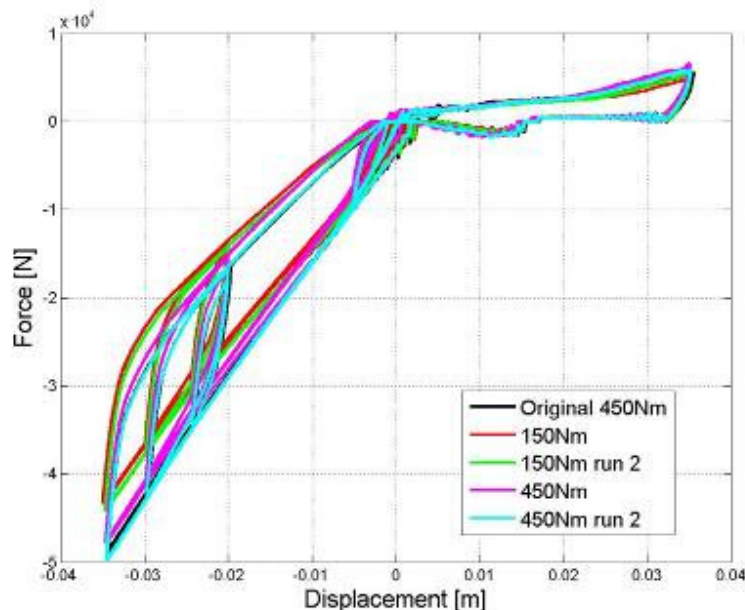


Figure 2.14. Effect of U-bolt preload on force-displacement characteristics of the multi-leaf spring New 1

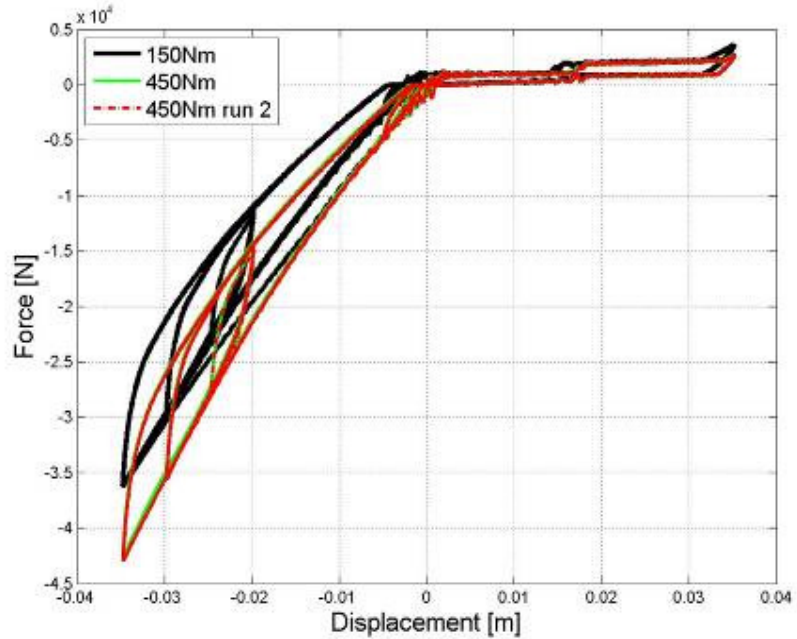


Figure 2.15. Effect of U-bolt preload on force-displacement characteristics of the old multi-leaf spring

2.1.2. Spring only setup

The experimental spring only setup is shown in Figure 2.16. The spring only setup of the multi-leaf spring differs from the in-service setup as the leaf spring in this setup is simply supported on bearings instead of the normal wear plates that are located in the front and rear hangers.

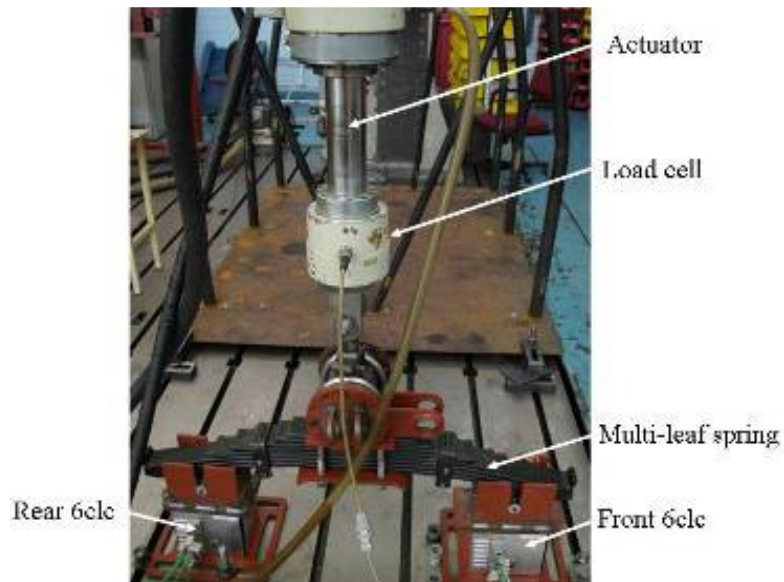


Figure 2.16. Experimental spring only setup of multi-leaf spring

The spring only setup uses bearing supports for two reasons. Firstly, the effect of friction between the leaf spring and the wear plates are eliminated. Secondly, with the spring only setup one has better control over the loaded length of the leaf spring. Also, any varying stiffness due to a change in the loaded length, which may be induced by the profile of the wear plates, is avoided. Figure 2.17 shows how the profile of the supports (in this case the profile of the wear plates) may affect the loaded length as the leaf spring is deflected.

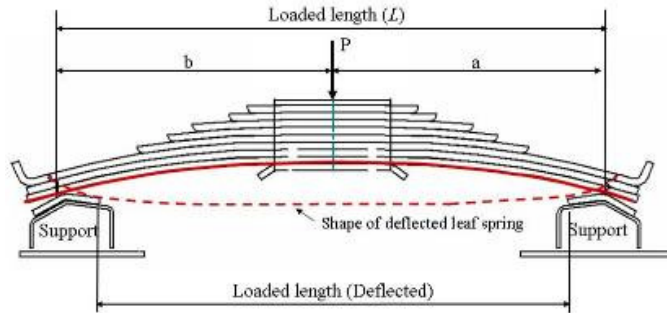


Figure 2.17. Changes in loaded length of the multi-leaf spring due to profile of the supports

With the use of bearings as supports for the leaf spring, the point of contact between the leaf spring and the bearing does not vary greatly as the leaf spring is deflected. This makes it possible to change the longitudinal hanger spacing, which changes the loaded length, and enables the effect of changes in the loaded length on the force-displacement characteristic to be investigated. The spring only setup only determines the characteristics of the multi-leaf spring and, unlike the in-service setup, ignores effects from other components such as for example the radius rod. The SAE spring design manual (1996) gives a guideline for measuring the load and rate of a leaf spring. This procedure is however not followed here because we would like to obtain the characteristic of the leaf spring for the configuration shown in Figure 2.16 which includes the attachment of the axle to the leaf spring via the U-bolts.

A comparison between the characteristics of the in-service and spring only force displacement characteristics, using the multi-leaf spring New 1, is shown in Figure 2.18 and Figure 2.19. The characteristics shown in these two figures were obtained with the input displacement signals 1 and 3 discussed in paragraph 2.1, respectively. Input displacement signal 1 had to be modified such that the spring is never extended. This is because with the spring only setup it was not possible to exert a force on the spring in the tensile direction. From the two figures it can be observed that the hysteresis loop differs slightly between the force-displacement characteristic obtained using the spring only and in-service setups. It can be concluded that the major contributor to the hysteresis loop is the inter-leaf friction with the friction between the spring and the wear plate having a smaller contribution. This also shows that the radius rod and its bushings has a negligible effect on the vertical force-displacement behaviour of the leaf spring.

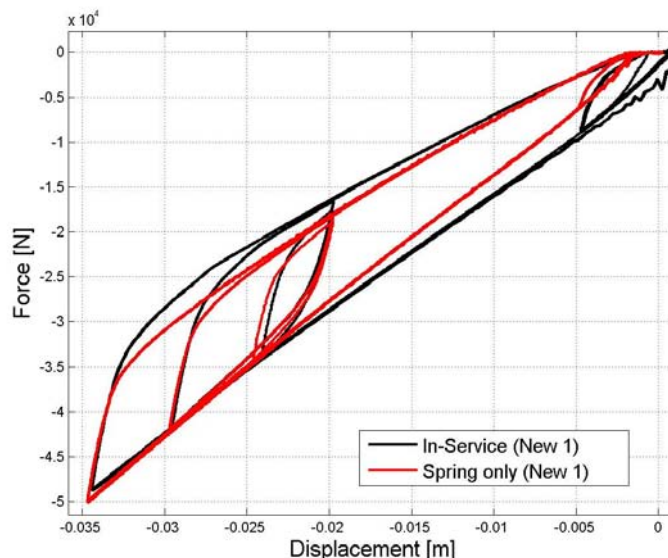


Figure 2.18. Comparison of in-service and spring only characteristics (input displacement signal 1 - modified)

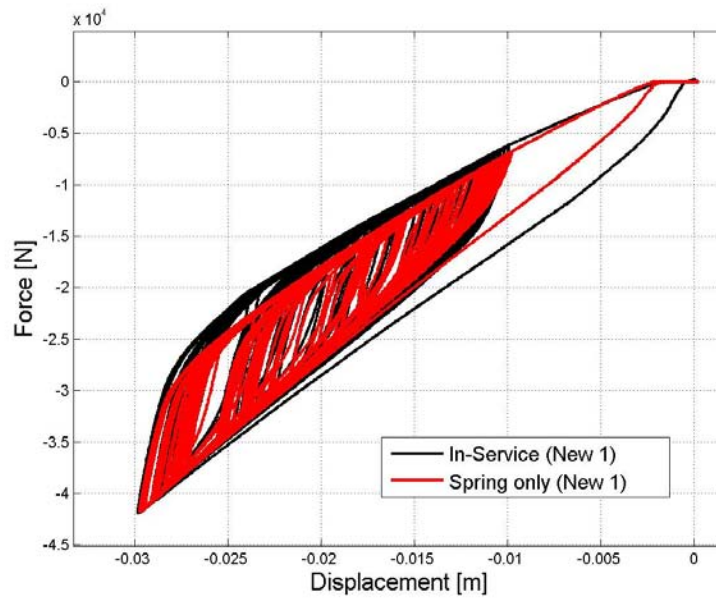


Figure 2.19. Comparison of in-service and spring only characteristics (input displacement signal 3)

2.1.2.1. Effect of longitudinal spacing of hangers

From simple beam theory it is known that the stiffness (k) of a simple beam is inversely proportional to the length (l) cubed ($k \propto \frac{1}{l^3}$). The stiffness of a multi-leaf spring is expected to have this same sensitivity with respect to the loaded length of the leaf spring. The loaded length was defined in Figure 2.17. The spacing of the front and rear hangers (see Figure 2.20) was changed to investigate the effect of different loaded lengths on the force-displacement characteristic of the leaf spring. Table 2.1 shows the different spacing values that were used. The centre spacing used for the Normal position given in Table 2.1, corresponds to the centre spacing between the hangers as used in the in-service setup when installed in the vehicle.

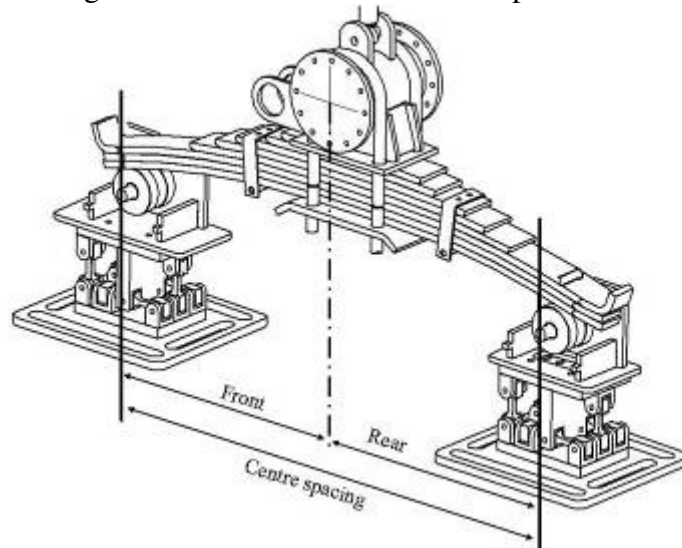
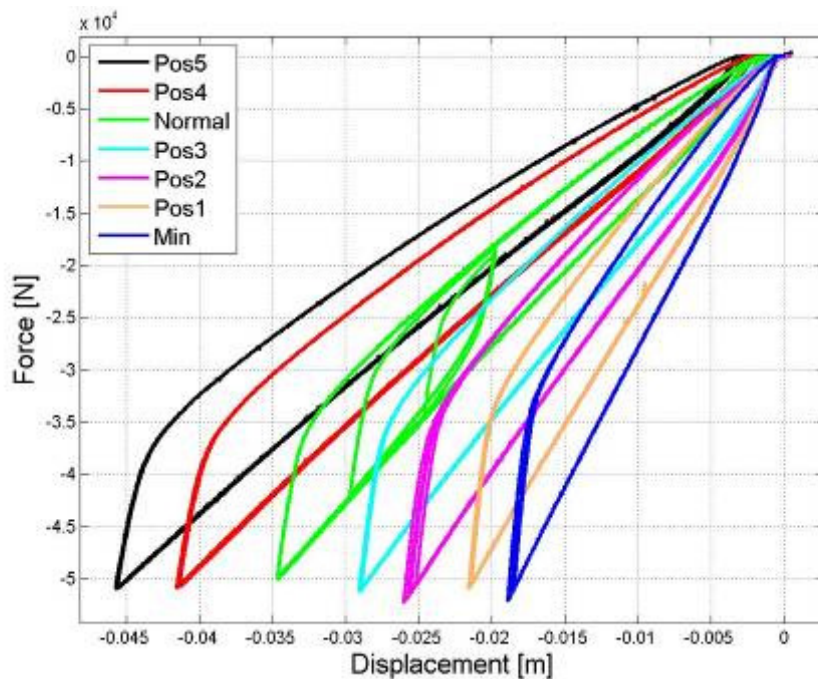


Figure 2.20. Centre spacing of hangers

Table 2.1. Spacing of hangers

Position	Centre spacing	
	Front [mm]	Rear [mm]
Min	430	398
Pos1	450	418
Pos2	470	438
Pos3	490	458
Normal	510	478
Pos4	530	498
Pos5	530	518

Figure 2.21 shows the effect of the longitudinal centre spacing of the hangers (or loaded length) on the force-displacement characteristic of the leaf spring. Using the loading section of the force displacement characteristic to calculate the stiffness of the leaf spring at the minimum spacing (Min) and the maximum spacing (Pos5), it is calculated that the leaf spring is approximately twice as stiff at the minimum position than at the maximum position. This indicates the significant change in spring stiffness that can be achieved, for the same spring, when the centre spacing (or loaded length) is changed.


Figure 2.21. Effect of the longitudinal centre spacing of hangers on the force-displacement characteristic of the multi-leaf spring

2.1.2.2. Deflection shape of the multi-leaf spring

The deflection shape of the leaf spring was measured at three different loads for two of the positions given in Table 2.1 namely the Normal position and Pos5. The experimental setup for measuring the deflection shape is shown in Figure 2.22. The deflection shapes of the multi-leaf spring for both centre spacings used were obtained at three vertical loads i.e. 0 N, 25.9 kN and 51.9 kN. Figure 2.23 shows the deflection shapes of the spring at the three vertical loads for Pos5 and Figure 2.24 shows the deflection shapes of the spring for the normal position.



Figure 2.22. Experimental setup for measuring the deflection shape of the multi-leaf spring

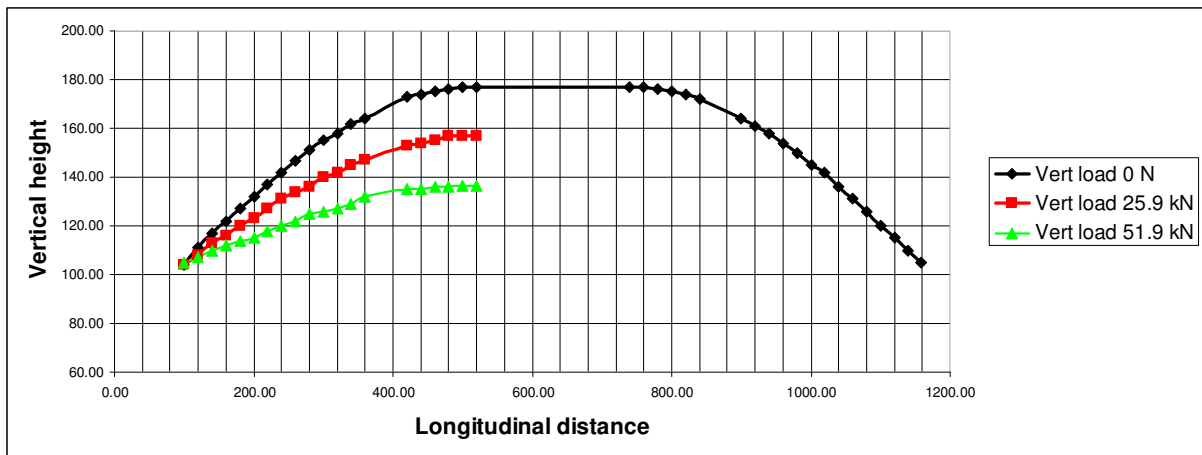


Figure 2.23. Deflection shape of the spring for Pos5

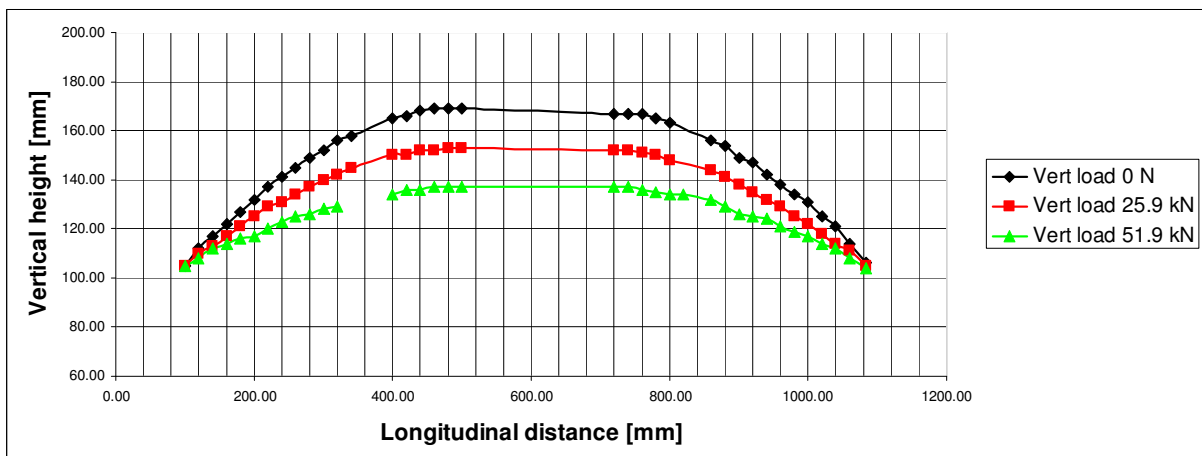


Figure 2.24. Deflection shape of the spring for the normal position

3. Characterisation of the suspension system using the parabolic leaf spring

The various aspects of the suspension system, using the parabolic leaf spring, that were characterised are shown in Figure 2.25. As already stated, the vertical characteristics were considered to be the most important. As can be seen from Figure 2.25 the lateral characterisation of the suspension system using the parabolic leaf spring was not performed as it was expected that the data obtained from the lateral characterisation done using the multi-leaf spring would give sufficient information. Furthermore, it was expected that the lateral characteristics of the suspension system would depend more on the radius rod than on the type of leaf spring used. For the parabolic leaf spring the aspects considered under the vertical characteristics of the suspension system did not include the complete suspension setup. The experimental characterisation of interest to this study is shown in green in Figure 2.25.

A similar process to that used to obtain the force-displacement characteristics of the multi-leaf spring will be followed to obtain the force-displacement characteristics of the parabolic leaf spring. The force-displacement characterisation of the parabolic leaf spring was done using the same two setups used for the multi-leaf spring namely, the in-service setup and spring only setup. Details of the two setups were given in paragraph 2.1.1 and 2.1.2. Unlike the characterisation of three multi-leaf springs only one parabolic leaf spring was characterised.

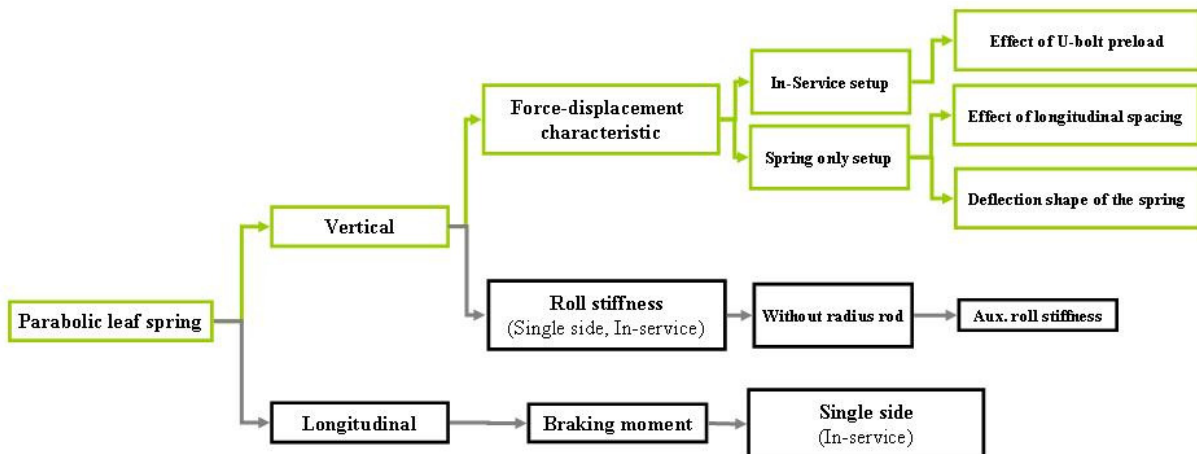


Figure 2.25. Overview of characterisation using the parabolic leaf spring

3.1. Force-displacement characteristic

As stated in paragraph 2.1, the force the leaf spring exerts when deflected is a function of the static load and the amplitude of the imposed displacement. The statements of Cebon (1986) and Fancher *et al.* (1980), that the force-displacement characteristic of a leaf spring does not depend on the input frequency, was confirmed to be true for the multi-leaf spring used in paragraph 2. The dependency of the force-displacement characteristic on the input frequency is also checked for the parabolic leaf spring. The same displacement input signals, which was used for the multi-leaf spring, are used as input to the parabolic leaf spring. The force-displacement characteristics of the parabolic leaf spring subjected to these input signals are shown in Figure 2.26 and Figure 2.27. Similar to the results obtained for the multi-leaf spring, the results for the parabolic leaf spring seem to indicate that its force-displacement characteristic is also not dependent on the excitation frequency. The experimental force-displacement characteristics shown in Figure 2.26 and Figure 2.27 were obtained using the in-

service setup which was discussed in paragraph 2.1.1. The in-service setup using the parabolic leaf spring is shown in Figure 2.28.

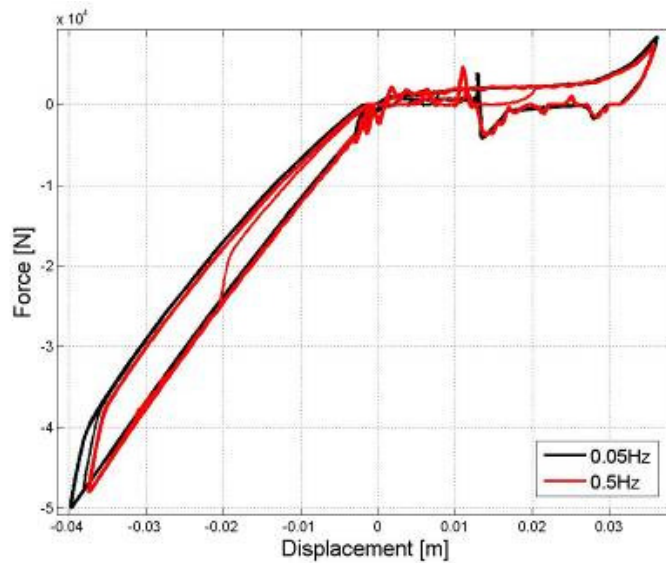


Figure 2.26. Compare force-displacement characteristics for different excitation frequencies

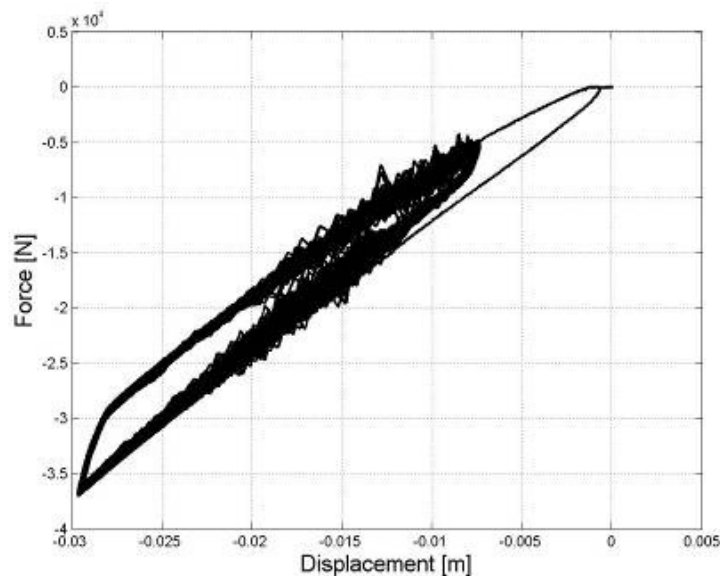


Figure 2.27. Force-displacement characteristic for sine sweep with frequencies ranging from 0.05 Hz to 4 Hz

From the above results it can be concluded that the spring force of the parabolic leaf spring, similarly to that of the multi-leaf spring, is a function of the static load and the amplitude of the imposed displacement on the leaf spring. The force-displacement characteristic of the parabolic leaf spring is obtained using two setups i.e. an in-service setup and a spring only setup. These two setups are the same as the setups used for characterising the multi-leaf spring and the reader is referred to paragraph 2.1.1 and 2.1.2 for the details of these setups. The force-displacement characteristic of the parabolic leaf spring is obtained using the same five displacement inputs as was used for the multi-leaf spring and presented in paragraph 2.1.

3.1.1. In-service setup

The in-service setup used to characterise the force-displacement characteristic of the parabolic leaf spring, shown in Figure 2.28, is exactly the same as the in-service setup used for

characterising the multi-leaf spring in paragraph 2.1.1. The force-displacement characteristic of the parabolic leaf spring using input displacement signal 1 is shown in Figure 2.29.

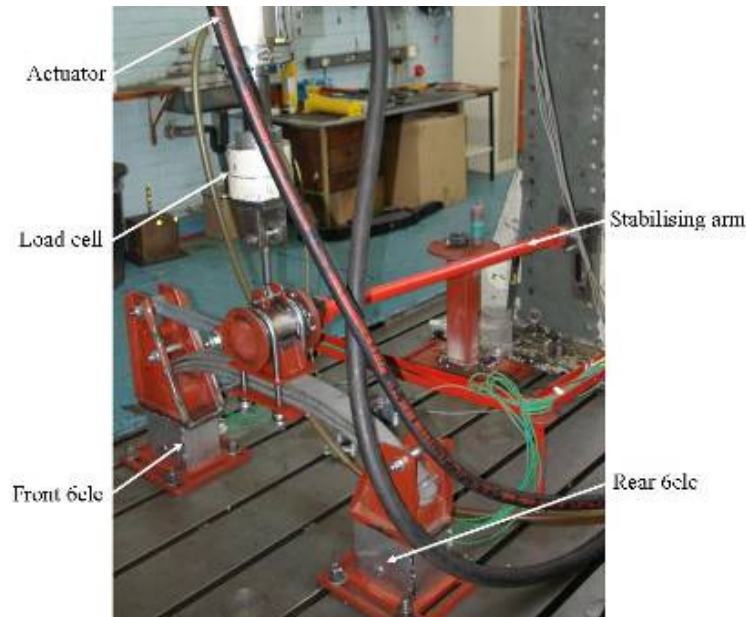


Figure 2.28. Experimental in-service setup of single sided suspension with parabolic leaf spring

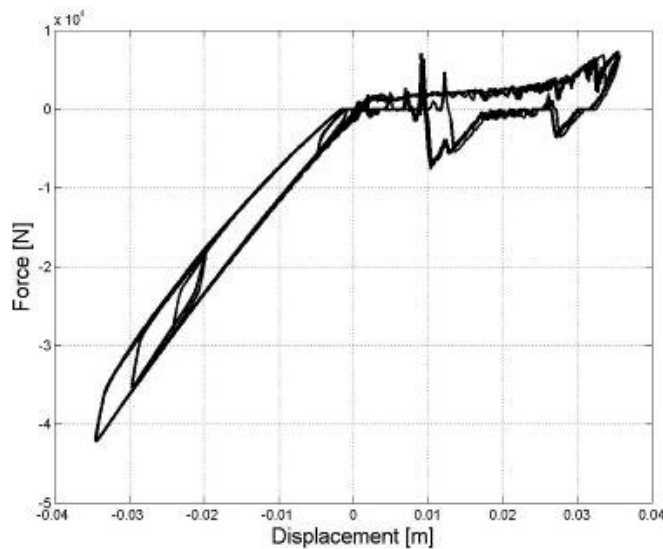


Figure 2.29. Force-displacement characteristic of parabolic leaf spring

3.1.1.1. Effect of U-bolt preload on force-displacement characteristics

An interesting observation was made with regards to the effect that the preload of the U-bolts has on the force displacement characteristic of the multi-leaf spring. The same observation is made with respect to the force-displacement characteristic of the parabolic leaf spring. Figure 2.30 shows the force-displacement characteristics of the parabolic leaf spring when the U-bolts are torqued to different values. The U-bolts were torqued to 150N.m and characterised twice. After this the U-bolts were torqued to 450N.m and again two characteristics were obtained. From Figure 2.30 it can be observed that the parabolic leaf spring's stiffness increases when the preload of the U-bolts is increased. This is similar to the results obtained for the multi-leaf spring.

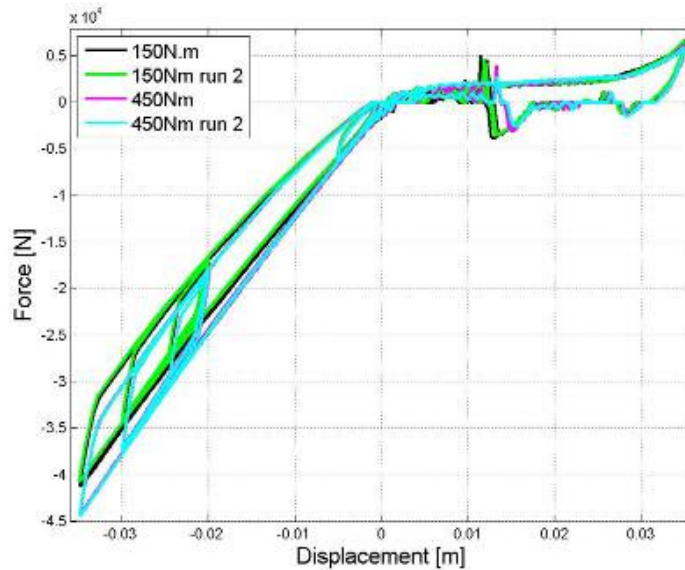


Figure 2.30. Effect of U-bolt preload on force-displacement characteristics of the parabolic leaf spring

3.1.2. Spring only setup

The spring only setup used in Figure 2.31 is exactly the same as the spring only setup used to obtain the force-displacement characteristic of the multi-leaf spring, obviously, except for the use of the parabolic leaf spring instead of the multi-leaf spring.



Figure 2.31. Experimental spring only setup of parabolic leaf spring

A comparison between the force-displacement characteristics of the parabolic leaf spring using the in-service and spring only setups is shown in Figure 2.32. Input displacement signal 1 was used to obtain the characteristics shown in Figure 2.32 but had to be modified such that the spring is never extended. This is because with the spring only setup it was not possible to exert a force on the spring in the tensile direction. From Figure 2.32 it can be observed that the hysteresis loop differs between the force-displacement characteristic obtained using the spring only and in-service setups. It can be concluded that the major contributor to the hysteresis loop is the inter-leaf friction with the friction between the spring and the wear plate having a smaller contribution. This is similar to the observation that was made when comparing the force-displacement characteristic of the multi-leaf spring using the spring only and in-service setups.

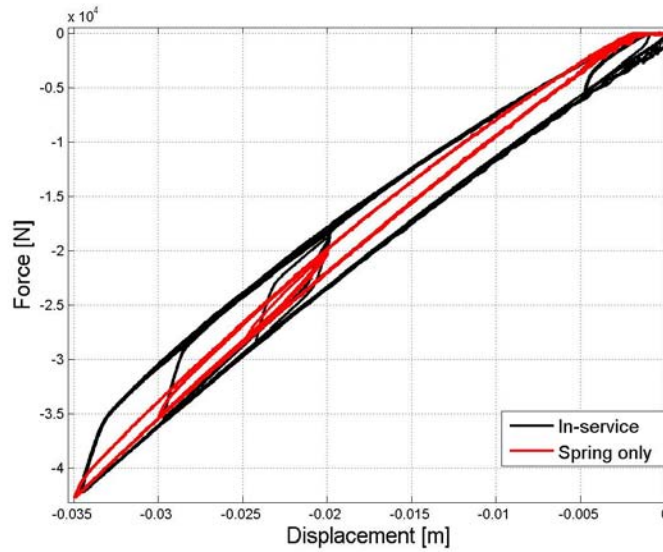


Figure 2.32. Comparison of in-service and spring only characteristics (input displacement signal 1 - modified)

3.1.2.1. Effect of longitudinal spacing of hangers

As with the multi-leaf spring in the spring only setup, the longitudinal spacing of the hangers was changed to investigate the effect the loaded length of the parabolic leaf spring has on its force-displacement characteristic. The spacing of the front and rear hangers (see Figure 2.20) was changed to investigate the effect it has on the force-displacement characteristic of the leaf spring. The same hanger spacing as was used for the multi-leaf spring shown in Table 2.1, is used for the parabolic leaf spring.

Figure 2.33 shows the effect the longitudinal centre spacing of the hangers (or loaded length) has on the force-displacement characteristic of the spring. Using the loading section of the force-displacement characteristic to calculate the stiffness of the parabolic leaf spring at the minimum spacing (Min) and the maximum spacing (Pos5), it is calculated that the parabolic leaf spring is approximately twice as stiff at the minimum position than at the maximum position. This indicates the significant change in spring stiffness that can be achieved, for the same spring, when the centre spacing (or loaded length) is changed. This shows the same increase in stiffness between the maximum and minimum hanger spacing as was obtained for the multi-leaf spring.

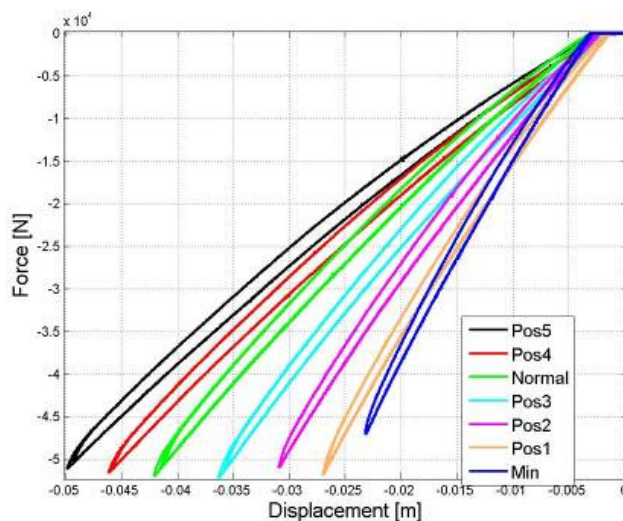


Figure 2.33. Effect of the longitudinal centre spacing of hangers on the force-displacement characteristic of the parabolic leaf spring

3.1.2.2. Deflection shape of the parabolic leaf spring

The deflection shape of the parabolic leaf spring was measured at three different loads for two of the positions given in Table 2.1. The two positions used were the Normal position and Pos5. The experimental setup for measuring the deflection shape of the parabolic leaf spring was similar to the setup used to measure the deflection shape of the multi-leaf spring (see Figure 2.22). The deflection shape of the parabolic leaf spring was obtained at three vertical loads i.e. 0 N, 25.9 kN and 51.9 kN. Figure 2.34 shows the deflection shapes of the parabolic leaf spring at the three vertical loads using the centre spacing of Pos5. Figure 2.35 shows the deflection shapes of the parabolic leaf spring for the Normal centre spacing.

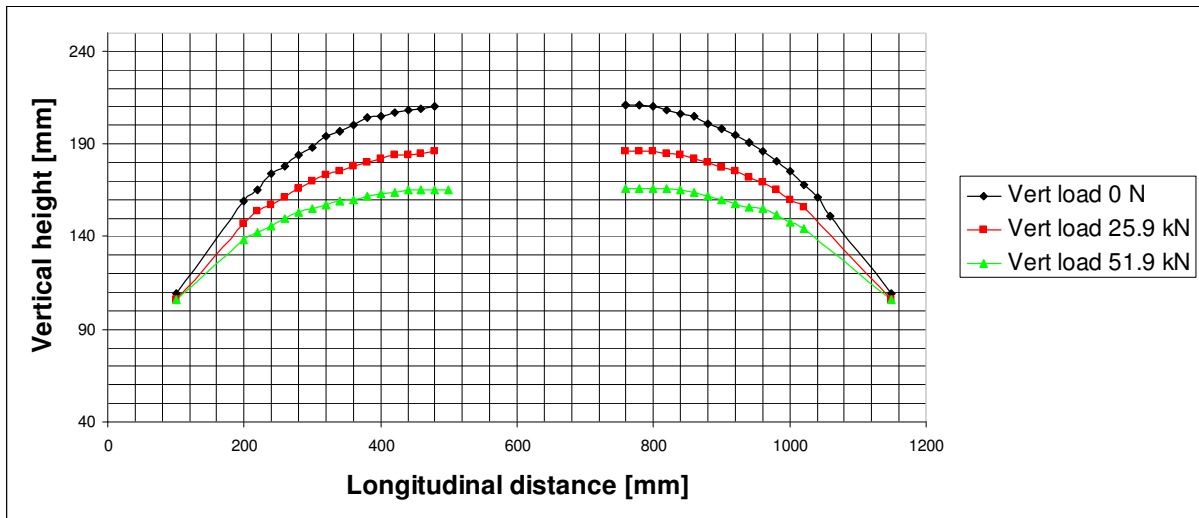


Figure 2.34. Deflection shape of the parabolic leaf spring for Pos5

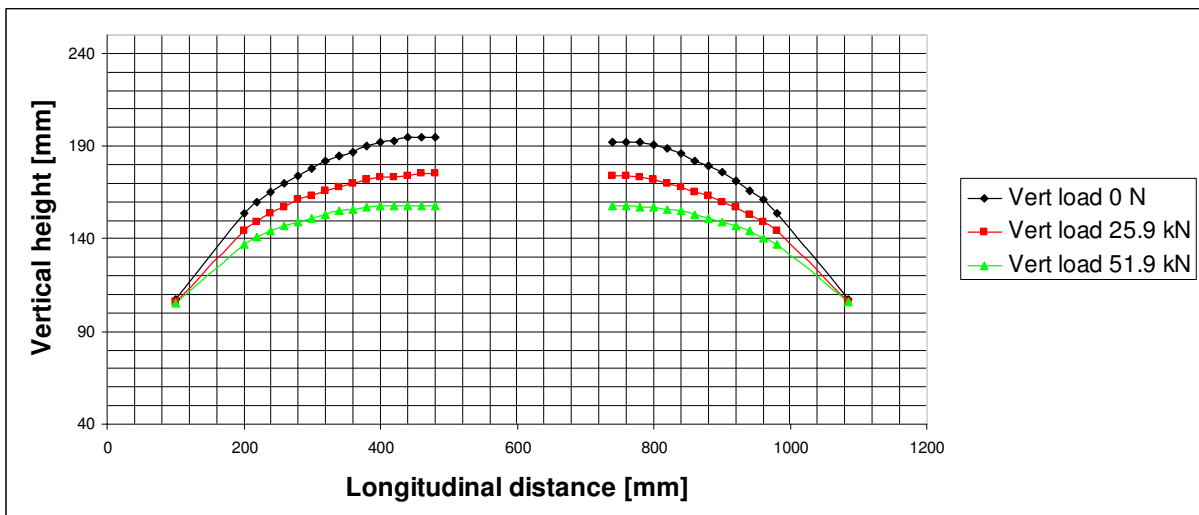


Figure 2.35. Deflection shape of the parabolic leaf spring for the Normal centre spacing

4. Conclusion

Various experimental characterisations were performed in order to obtain the required experimental data that is needed to validate the simulation models according to the goals set out in Chapter 1.

Figure 2.36 shows the comparison between the force-displacement characteristic of the multi-leaf and parabolic leaf spring. The difference in the force-displacement characteristic of the multi-leaf spring and parabolic leaf spring can be seen in this figure. The multi-leaf spring has a bigger hysteresis loop than the parabolic leaf spring. This implies that the multi-leaf spring will dissipate more energy than the parabolic leaf spring. It was shown that the force-displacement characteristics of both leaf springs react the same to changes in the preload of the U-bolts and to changes in the loaded length. It was also shown that the force-displacement of both leaf springs is independent of the excitation frequency.

The experimental data obtained in this chapter will be used to validate the mathematical models that are created in the chapters that follow.

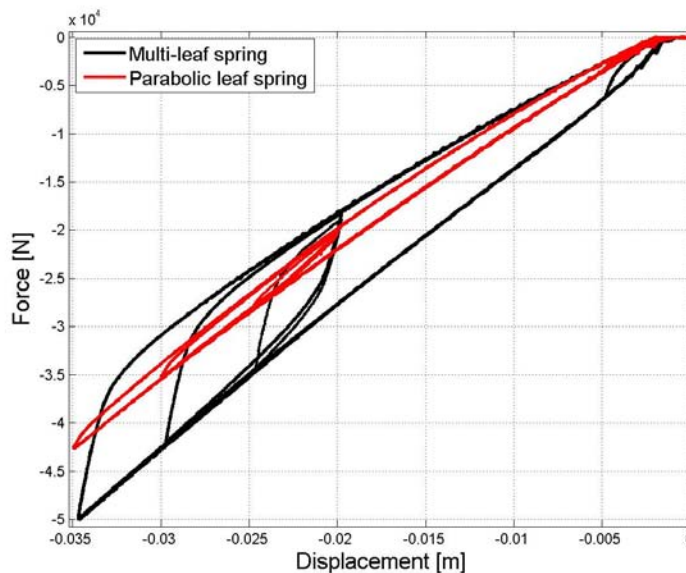


Figure 2.36. Force-displacement characteristic of the multi-leaf spring and parabolic leaf spring

Chapter 3

Leaf spring modelling

Accurate full vehicle multi-body simulation models are heavily dependent on the accuracy at which the subsystems, and more fundamentally, the different components that make up the subsystems, are modelled. It is needless to say that an accurate model of a leaf spring is needed if accurate suspension models, and eventually, full vehicle simulation models are to be created. The leaf spring has been used in vehicle suspensions for many years. It is particularly popular in commercial vehicles as it is robust, reliable and cost effective. Even though leaf springs are frequently used in practice they still hold great challenges in creating accurate mathematical models.

This chapter investigates the modelling of the leaf spring in the spring only configuration as described in Chapter 2.

1. Introduction

As concluded in Chapter 1, the majority of the leaf spring models in literature considers the leaf spring configuration where the leaf spring is attached to the vehicle using the fixed-shackled end configuration, whereas the suspension under investigation in this study has the leaf spring supported by the hangers, as was shown in Figure 1.4 in Chapter 1. The minimum requirements set for the leaf spring model are that it has to be able to capture the spring stiffness and hysteresis loop of the leaf spring. In addition to these requirements, the model should preferably be able to account for changes in the load length of the leaf spring. It was shown in Chapter 2 that the stiffness of leaf springs is very sensitive to changes in the loaded length.

From the literature study conducted in Chapter 1 it was shown that many methods exist that can be used to model leaf springs with varying success depending on the application. The methods have different advantages and disadvantages, with some being more computationally efficient than others. It would be ideal if all the modelling techniques could be evaluated against each other, comparing accuracy and efficiency. This is however not the goal of this study, rather a novel leaf spring model will be proposed and compared to one of the modelling methods from literature namely, neural networks. The aim with the proposed model is not to add just another modelling method but to try and obtain a model that is able to emulate the complex behaviour of the multi-leaf spring accurately and still be computationally efficient as well as being physically meaningful. The proposed elasto-plastic leaf spring model and the neural network leaf spring model are fundamentally two different techniques. The elasto-plastic leaf spring model is a physics-based model whereas the neural network model is a non-physics based model. Physics based models have certain advantages over non-physics based models. The main advantage of a physics based model, especially in the context of this study, is that the model has parameters that are associated with certain aspects of the behaviour of

the system. This makes it possible to use the physics based model in situations where the parameters can be optimized as well as performing sensitivity analysis. On the other hand the non-physics based neural network model has the potential to have a better computational efficiency than the other leaf spring models including the elasto-plastic leaf spring model. This computational efficiency can be utilized in the situations mentioned above by using the neural network in a gray-box or semi-physical approach as mentioned in Dreyfus (2005). The physics based and non-physics based models each have their advantages and therefore both are investigated in this chapter. The elasto-plastic leaf spring model will be presented first after which the neural network approach to modelling the leaf spring will be discussed.

2. Elasto-plastic leaf spring model

Some of the physical phenomena that gives multi-leaf springs their unique characteristics are the contact and friction processes that are present between the individual blades. These processes are responsible for the hysteretic behaviour of the leaf spring. The contact and friction processes are complex phenomena and modelling them are computationally expensive. Additional complexity is added to the contact and friction process as adjacent blades may have varying pressure distributions between them (Li and Li, 2004 and Omar *et al.*, 2004). This paragraph presents the elasto-plastic leaf spring model that is able to emulate the nonlinear, hysteretic behaviour of a leaf spring without needing to explicitly model the complex microscopic physical phenomena such as contact and friction. The elasto-plastic leaf spring model will first be used to model the multi-leaf spring. After the feasibility of the elasto-plastic leaf spring model has been determined it will then be applied to the parabolic leaf spring.

The following paragraph serves as an introduction to the elasto-plastic leaf spring model by stating the origin of the idea for the model.

2.1. The behaviour of materials and leaf springs

Comparing the force-displacement characteristics of the multi-leaf spring to the stress-strain behaviour of engineering materials, several similarities can be observed of which the most notable is the two stiffness regimes that are present (see Figure 3.1). Figure 3.1(a) shows the stress-strain curve for the elastic, linear hardening material model. From this curve two stiffness regimes can clearly be observed. Regime 1 coincides with the elastic deformation of the material and regime 2 with plastic deformation. Figure 3.1(b) presents a typical force-displacement characteristic of a multi-leaf spring. On the force-displacement characteristic two stiffness regimes can also be observed. Figure 3.1(c) shows the stress-strain curve of materials and the force-displacement characteristic of a multi leaf spring superimposed. From this figure it is concluded that it might be possible to use models, similar to material models, to emulate the behaviour of multi-leaf springs. This led to the investigation of developing a leaf spring model that was based on the approach used to model material behaviour.

Understanding the behaviour of engineering materials, and multi-leaf springs, requires that the microscopic mechanisms be considered. A brief summary of the deformation behaviour of materials and the models used to describe them will be given in the following paragraph. The similarities between the microscopic mechanisms involved in materials and in leaf springs will also be noted before presenting the elasto-plastic leaf spring models.

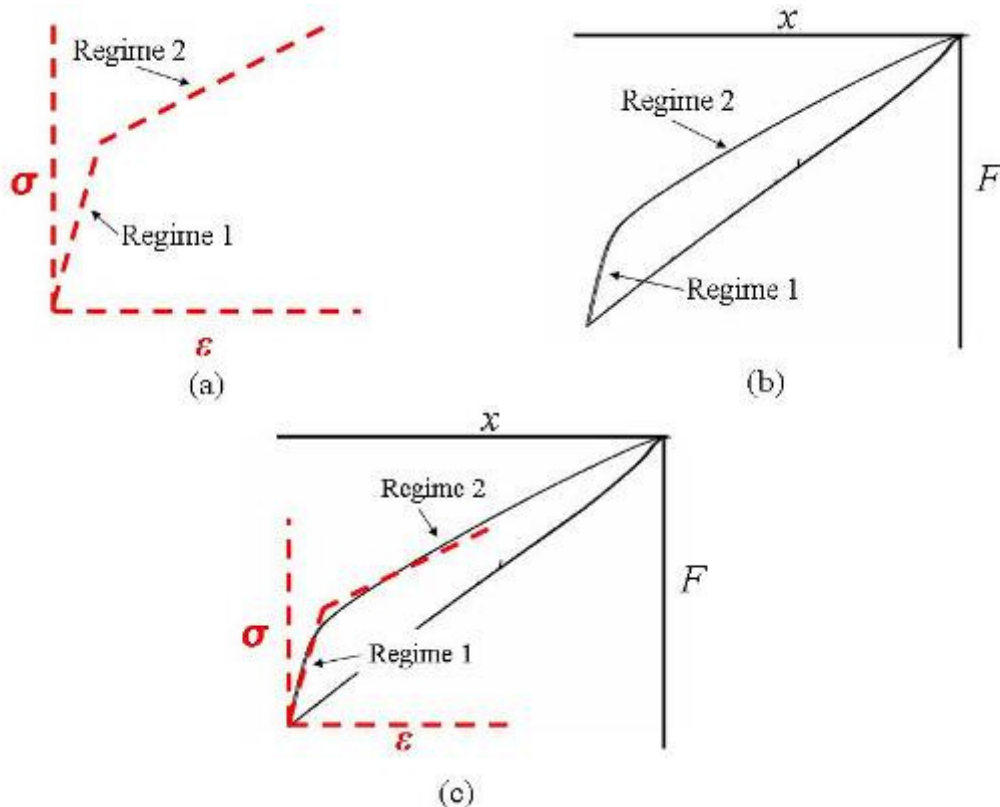


Figure 3.1. Similarities between the behaviour of leaf springs and engineering materials. (a) Stress-strain curve of elastic, linear-hardening material model. (b) Multi-leaf spring force-displacement characteristic. (c) Superposition of force-displacement characteristic of a multi-leaf spring and the stress-strain curve of the elastic, linear-hardening material model.

2.1.1. Deformation behaviour and models of materials

Materials may experience two kinds of deformation: elastic and inelastic (plastic or creep). Elastic deformation is non-permanent and is associated with the stretching, but not breaking, of inter-atomic bonds. In contrast, the two types of inelastic deformation involve processes where bonds with original atom neighbours are broken and new bonds are formed with the new neighbours as large numbers of atoms or molecules move relative to one another. If the inelastic deformation is time dependent, it is classed as creep, as distinguished from plastic deformation, which is not time dependent. The mechanism of plastic deformation is different for crystalline and non-crystalline (amorphous) materials. For crystalline solids, deformation is accomplished by means of a process called slip, which involves the motion of dislocations. Whereas, plastic deformation in non-crystalline solids occur by a viscous flow mechanism. Refer to Callister (2003) and Dowling (1999) for a more detailed discussion.

Several models that exist to describe the deformation behaviour of materials are shown in Figure 3.2. This figure shows the elasto-plastic stress-strain curves of the models subjected to a monotonic loading. All the curves have an elastic portion until the material starts yielding after which the stress and strains are no longer linearly proportional i.e. does not follow Hooke's law. This region is associated with plastic deformation.

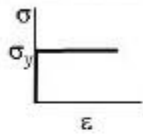
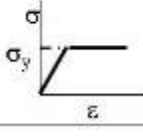
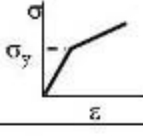
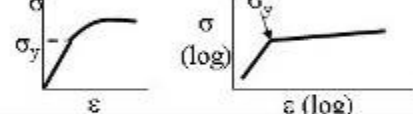
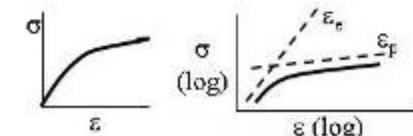
Model	Stress-strain response
(a) Rigid, perfectly plastic	
(b) Elastic, perfectly plastic	
(c) Elastic, linear-hardening	
(d) Elastic, power-hardening	
(e) Ramberg-Osgood	

Figure 3.2. Elasto-plastic material models

2.1.2. Mechanisms in crystalline materials vs. mechanisms in multi-leaf springs

In this paragraph we will consider some of the mechanisms present in crystalline materials that are responsible for their behaviour when subjected to a stress field. We will also discuss the mechanisms present in the multi-leaf spring to show the similarities between the two.

2.1.2.1. Mechanisms in crystalline materials

The previous paragraph gave a brief discussion of material deformation behaviour and the models used to represent this behaviour. We will take a step back and consider the microscopic mechanisms that govern the behaviour of metals and are responsible for the mechanical properties.

Starting at the atomic level some of the important properties of solid materials depend on the geometrical atomic arrangements, and the interactions that exist among the atoms and molecules. An understanding of many of the physical properties of materials is based on the knowledge of the inter-atomic forces that bind the atoms together. Primary (ionic, covalent and metallic) and secondary (or van der Waals) bonds exist between atoms, with the secondary bonds being much weaker than the primary bonds. The next level pertains to the arrangement that atoms assume in a solid state. Solid materials are classified according to the regularity with which atoms or ions are arranged with respect to one another. The classification can then be made as either a crystalline or non-crystalline material. As with the inter-atomic bonding, the crystal structure of the material and the imperfections that exists throughout the crystal structure, influences the properties of the crystalline solid.

It was mentioned in paragraph 2.1.1 that elastic deformation is associated with the stretching, but not breaking, of inter-atomic bonds. Whereas, plastic deformation on a microscopic scale corresponds to the net movement of large numbers of atoms in response to an applied stress (Callister, 2003). During this process, inter-atomic bonds must be broken and then reformed. In crystalline solids, plastic deformation most often involves the motion of dislocations (linear imperfections in the atomic structure). Callister (2003) discusses the characteristics of dislocations and their involvement in plastic deformation in more detail. Only some of the basic concepts will be discussed here.

The process by which plastic deformation is produced by dislocation motion is termed slip, and the crystallographic plane along which the dislocation line traverses is the slip plane, as indicated in Figure 3.3. Macroscopic plastic deformation simply corresponds to permanent deformation that results from the movement of dislocations, or slip, in response to an applied shear stress. Callister (2003) gives the following explanation for the movement of an edge dislocation in response to a shear stress applied in a direction perpendicular to its line. Plane A represents an initial extra half-plane of atoms (see Figure 3.3). When a shear stress is applied, plane A is forced to the right. This then forces the top halves of the planes B, C, D, etc. in the same direction. If the applied shear stress is of sufficient magnitude, the inter-atomic bonds of plane B are severed along the shear plane, and the upper half of plane B becomes the extra half-plane as plane A links up with the bottom half of plane B (Figure 3.3(b)). This process is repeated resulting in the extra half-plane emerging from the right surface of the crystal, forming an edge that is one atomic distance wide (see Figure 3.3(c))

Dislocations do not move with the same degree of ease on all crystallographic planes and in all crystallographic directions. Usually there is a preferred plane, and in that plane there is a specific direction along which dislocation motion occurs. This plane is called the slip plane and the direction of movement is called the slip direction. This combination of the slip plane and the slip direction is termed the slip system. For further details on the slip system the interested reader is referred to Callister (2003).

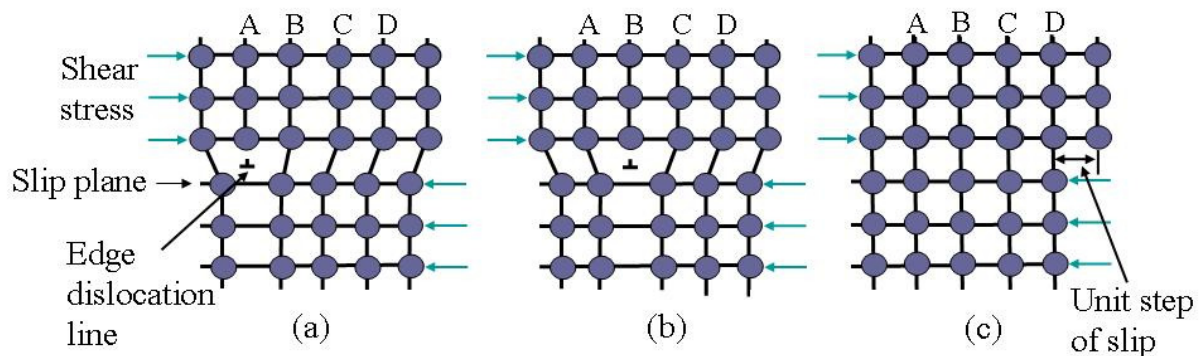


Figure 3.3. Atomic rearrangement that accompany the motion of an edge dislocation (Adapted from Callister (2003))

2.1.2.2. Mechanisms in multi-leaf springs

It is not difficult to imagine that the atomic interactions in a multi-leaf spring will have the same importance in understanding the behaviour of the multi-leaf spring as it has in materials. Let's investigate some of the microscopic mechanisms present in multi-leaf springs.

Consider a section, of an infinitesimally small distance dx , through all the blades of the multi-leaf spring (see Figure 3.4). We group the atoms in each leaf together and view this grouping

as a super-atom. This is done as it is assumed that the bonds which exist between the atoms in the crystalline structure of each individual leaf will be different from the bonds between the surfaces of two adjacent blades. This assumption is based on surfaces causing a discontinuity in the lattice structure of the material. Various factors (such as contaminants or lubricants) may cause the bonds between the atoms of two surfaces being different from the atomic bonds of the bulk material. The bonds between the surface atoms of two adjacent blades are called interfacial bonds. An atomic structure of the multi-leaf spring that is analogous to the structure of a crystalline material is shown in Figure 3.4. If a shear stress is applied to the micro-structure, the blades will start to move relative to one another (i.e. slip) once the shear stress exceeds the strength of the interfacial bonds. Slip will occur at the slip planes which exist between the super-atoms. The slip planes are assumed to exist where two adjacent super-atoms are in contact. This is based on the assumption that the interfacial bonds are weaker than the inter-atomic bonds within the super-atoms and thus causes the slip planes to exist between the surfaces of two super-atoms (or blades). This is the slip system of the multi-leaf spring.

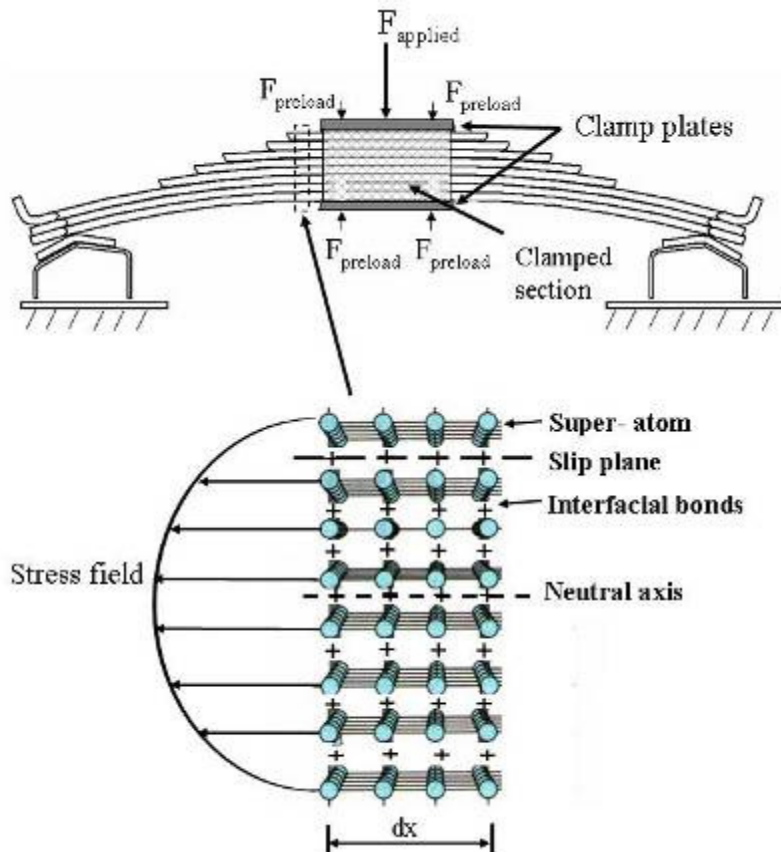


Figure 3.4. Multi-leaf spring micro-structure

The slip planes can easily be observed with a simple experiment. Figure 3.5 shows two pictures of a multi-leaf spring. The first is at a vertical load of 677 kg and the second picture has a vertical load of 4105 kg. Six vertical white lines are drawn over all the blades. When considering line 3 and 4 the relative motion between blades 2 and 3 can easily be observed. In Figure 3.5(a) no relative motion between the blades are observed, however, in Figure 3.5(b) the relative motion between the blades can be seen as the white lines on the different blades move relative to one another. This relative motion (or slip) occurs at the slip plane as discussed.

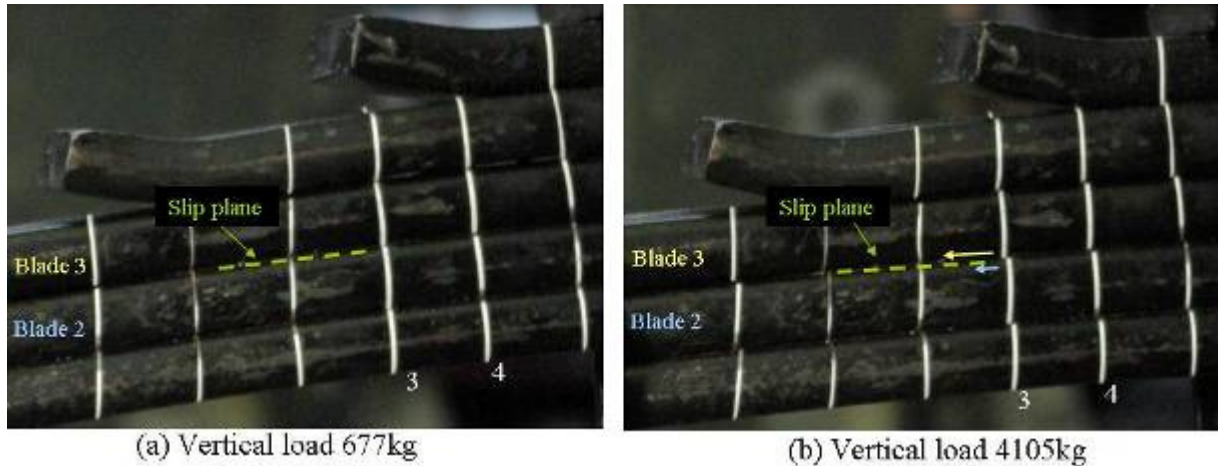


Figure 3.5. Multi-leaf spring slip planes

Similar to how the atomic bonds influence the physical properties of materials, the interfacial bonds will influence the behaviour of the multi-leaf spring. The interfacial bonds are a result of the contact process that exists between the surfaces of the leaf spring. The contact (and motion) between the surfaces of adjacent blades will be discussed in more detail in the following paragraph as it is an important process and contributes to the behaviour of the leaf spring.

2.1.2.3. Solid-solid contact (Tribological process)

An important physical phenomenon present in multi-leaf springs is the contact between two adjacent solid bodies (i.e. the contact between the individual blades). “The study of friction, wear and lubrication, and the science of interacting surfaces in relative motion” is termed tribology (Oxford Dictionaries, 2011). It incorporates the study of friction, lubrication and wear.

A feature associated with all processes involving motion is the occurrence of the resistance to motion due to friction of some kind. For the leaf spring the effects of friction are due to the interactions between the bodies moving relative to each other. As a consequence of friction, some part of the energy of motion is dissipated. The interfacial processes associated with the interaction of material surfaces in relative motion are termed tribological processes. Within the tribological process we need to consider the contact and friction processes.

The contact process

In the interfacial contact process, the forces and displacements of the interacting bodies (i.e. the contact mechanics), as well as the material interactions (i.e. the contact physics and chemistry) must be taken into account. In contact mechanics, a great variety of situations can be considered (Czichos, 1978) depending on:

- The number of bodies in the contact process,
- The macro-geometry of the bodies (2- or 3-dimensional problems),
- The surface topography (smooth or rough surfaces),
- The mechanical properties of the bodies,
- The deformation mode (elastic, plastic, elasto-plastic),
- The contact forces (normal forces, tangential forces),
- The type of relative motion (static contact, rolling, sliding, etc.)
- The velocity of relative motion.

Czichos (1978) gives reference to review articles on various aspects of contact mechanics. Some of the aspects with which the contact physics and chemistry are concerned with are the interfacial bonding and the generation of adhesive junctions.

The friction process

Whenever two solid bodies are in direct or indirect contact and made to slide relative to one another, there is always a resistance to the motion. This resistance to the motion is called friction and is energy consuming. Friction has long been the interest of many scientific studies and includes work done by Galileo, da Vinci, Amontons and Coulomb.

Different models have been developed in order to describe the macroscopic friction force between two sliding surfaces. Czichos (1978) state that based on the existing knowledge of the topography and the composition of solid surfaces, the following microscopic view of sliding friction is postulated: friction occurs through asperity (surface atom) interactions. In this model the macroscopic friction force can be expressed as the sum of microscopic friction forces at the individual micro-contacts. The energy dissipated can be calculated in a similar manner. The main processes involved in the different stages of the formation and separation of a micro-contact are shown in Figure 3.6:

- Elastic asperity deformation
- Plastic asperity deformation
- Ploughing
- Adhesion bonding
- Shearing of adhesive junctions
- Elastic recovery

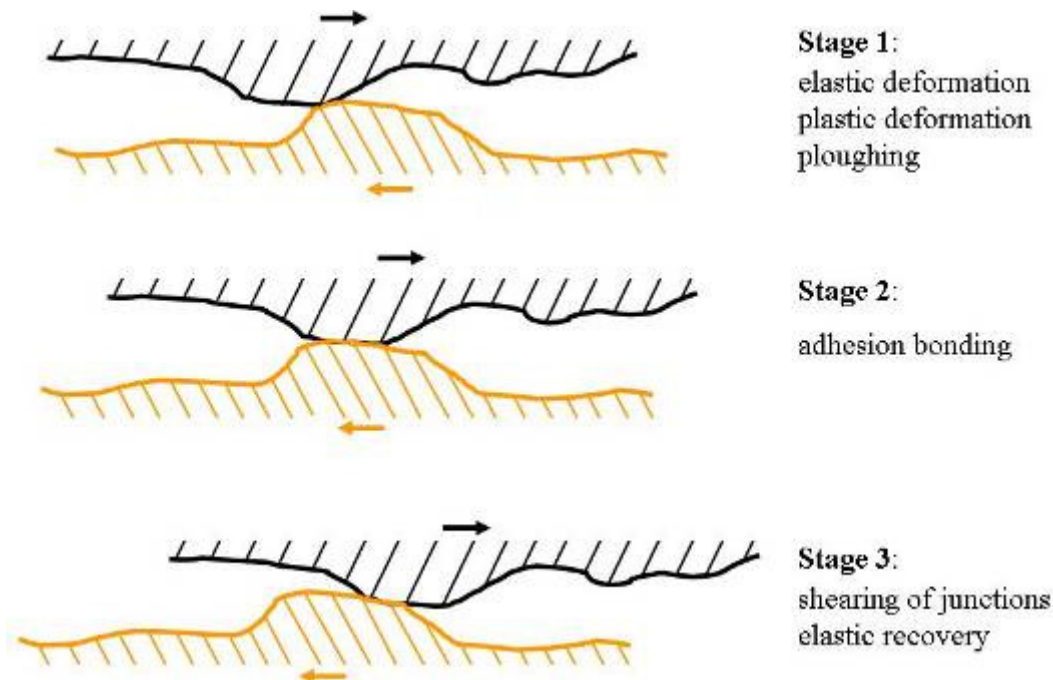


Figure 3.6. Schematic representation of a unit event in the friction process (Adapted from Czichos (1978))

It is however stated in Czichos (1978) that the friction force can only be understood qualitatively and that a quantitative calculation of friction forces or friction coefficients is only possible to very rough approximations under special simplified conditions. The main

reason for this is due to the incomplete knowledge of the surface properties of solids. In another study, Merkle and Marks (2007) describe the friction between crystalline bodies using a model that unifies elements of dislocation drag, contact mechanics and interface theory. Their model, as yet, is not able to explain all the frictional effects, but is able to give reasonable results for both the dynamic and static frictional coefficients.

2.1.2.4. Conclusion

From the brief discussion above, it was shown that there exist similarities between the mechanisms governing the behaviour of engineering materials and multi-leaf springs. It is clear that the mechanisms involved and the tribological processes associated with the multi-leaf spring are complex. Therefore, instead of trying to model it on a microscopic level we will rather try and quantify it on a macroscopic level. In material science, instead of modelling the inter-atomic bonds, dislocation, etc., the material is characterised on a macroscopic level by obtaining its mechanical properties. Similarly, the multi-leaf spring will be characterized on a macroscopic level by obtaining its mechanical properties.

2.2. Mechanical properties of a multi-leaf spring

From the mechanisms governing the behaviour of multi-leaf springs as discussed above, it is postulated that the multi-leaf spring will have two different stiffness regimes. In the study conducted by Hoyle (2004) the presence of two stiffness regimes were noted. He associated the first stiffness regime with small suspension deflections, which was significantly stiffer than the second stiffness regime, which was associated with larger suspension deflections. Hoyle (2004) attributed this to the fact that “if a certain load has to be applied to the suspension in order to overcome the friction between the blades, then until this load has been reached the blades will act like a solid beam. Implicit in this scenario is the possibility that for small deflections the locked blades will have a different, and probably higher, stiffness than the sum of the stiffnesses of the individual blades”. His suspicions are correct; the two stiffness regimes are due to the characteristic of the friction process that governs the characteristic of the interfacial bonds. Upon loading or unloading of the spring, the friction force will cause the individual blades to have no relative motion (i.e. no slip). As the load is increased (in the case of loading) or decreased (in the case of unloading) the friction force will reach a critical point at which point the individual blades will start to move relative to one another (i.e. slip along the slip planes). This causes the multi-leaf spring to act as either a solid beam (no slip between blades) or a layered beam (slip between blades).

For the postulate to hold it should be possible to observe two distinct stiffnesses on the multi-leaf spring's force-displacement characteristic. Figure 3.7 shows the experimentally measured force-displacement characteristic of the multi-leaf spring, and it seems to exhibit the presence of two stiffness regimes. Furthermore, it should be possible to calculate the stiffness of the solid and layered beam using beam theory. The multi-leaf spring can be viewed as two back-to-back non-prismatic cantilever beams. Using the theory of beams (Gere, 2004) we can calculate the deflection of the cantilever beam and infer the stiffness. The theoretical stiffness of the layered beam is also calculated by using the equation found in the SAE Spring Design Manual (1996). Both these approaches are discussed in detail in Appendix B. Figure 3.8 shows the theoretical stiffnesses for the two regimes superimposed on the measured force-displacement characteristic. From this figure it seems that the theory of beams can be used to calculate the stiffness of the two regimes. The equations presented in Appendix B, based on the method of superposition and the SAE Spring Design Manual (1996), can be used to

calculate the theoretical stiffness of the multi-leaf spring, given that the clamping in the clamped section is accounted for accordingly. The assumption made regarding the clamping and the clamp length has a considerable effect on the stiffness. The effect of the clamping assumption on the stiffness of the leaf spring is discussed in considerable detail in Appendix B. From Figure 3.7 and Figure 3.8 it would seem that the postulate concerning the behaviour of the multi-leaf spring holds true.

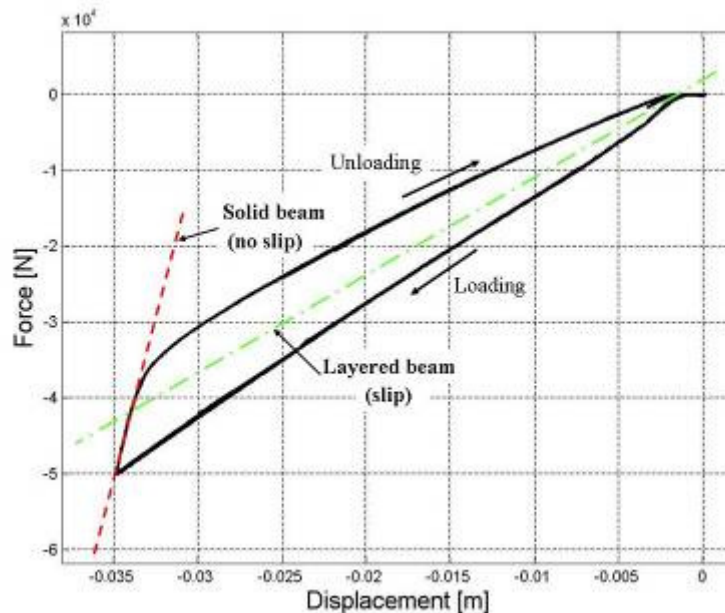


Figure 3.7. Two stiffness regimes present on the force-displacement characteristic

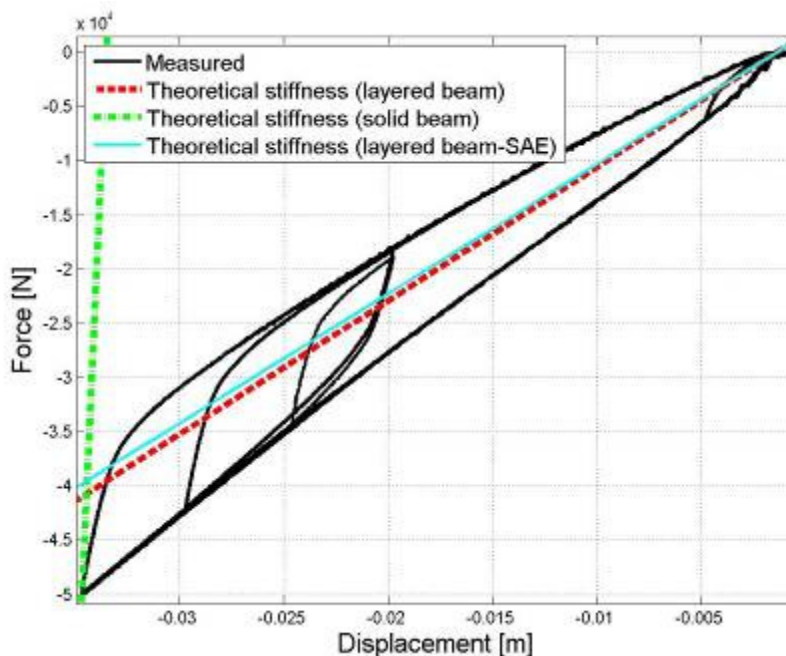


Figure 3.8. Theoretical calculation of the two stiffness regimes

As mentioned earlier, instead of modelling the complex microscopic phenomena, we will characterize it by means of the macroscopic behaviour of the multi-leaf spring (i.e. through the mechanical properties of the multi-leaf spring). In material science the mechanical properties of materials include strength, hardness, ductility, and stiffness. Some of the

parameters that are used in order to describe the mechanical behaviour of a material are Young's modulus, yield stress and ultimate stress. In the case of the multi-leaf spring, the stiffness of the solid beam and layered beam can be used as parameters to describe the mechanical behaviour of the multi-leaf spring. An obvious additional parameter that will be needed is a parameter that will indicate when the multi-leaf spring starts to behave as a layered beam as apposed to a solid beam. We call this parameter the frictional yield point. A further parameter that might be useful is one that indicates the point where the direction of loading is changed, termed the turning point. Thus, the parameters that we need to extract from test results in order to describe the mechanical behaviour of the leaf spring are summarized here and shown in Figure 3.9.

- k – stiffness of the solid beam,
- k_L – stiffness of the layered beam during loading,
- k_{UL} – stiffness of the layered beam during unloading,
- turning point – point where direction of loading is changed and,
- frictional yield point – point where spring starts to act as a layered beam.

Strictly speaking, both the turning point and the frictional yield point are not actually mechanical properties. However, these two parameters are used to calculate the fourth required mechanical property of the multi-leaf spring namely the yield fraction (The calculation of the yield fraction will be discussed in paragraph 2.3.2). Thus, four mechanical properties are proposed that will be able to characterize the behaviour of the multi-leaf spring:

- k - stiffness of the solid beam,
- k_L - stiffness of the layered beam during loading,
- k_{UL} - stiffness of the layered beam during unloading,
- f_y - yield fraction

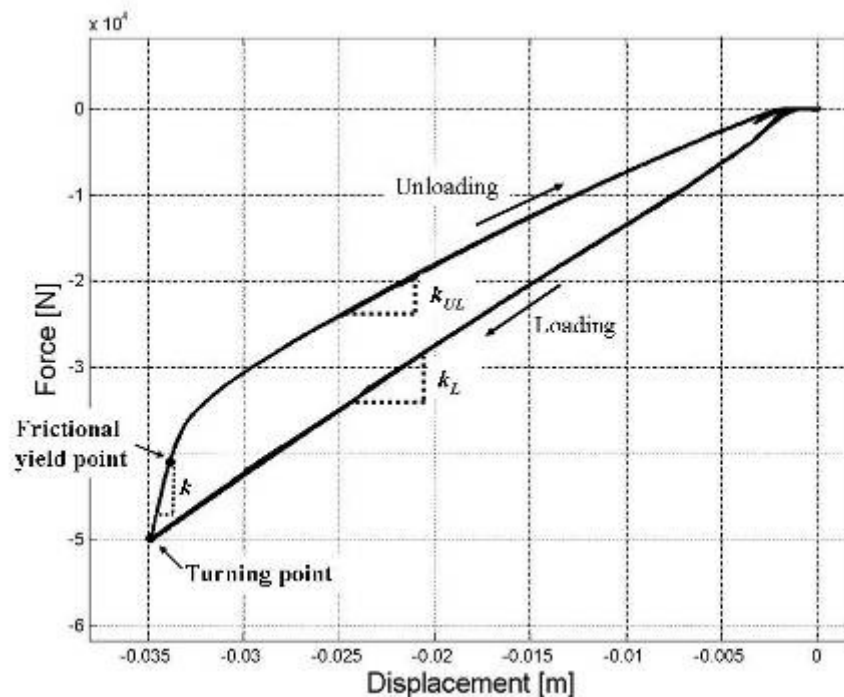


Figure 3.9. Mechanical properties of a multi-leaf spring

2.3. Elasto-plastic leaf spring models

In the previous paragraph we proposed four parameters that should enable us to describe the mechanical behaviour of the multi-leaf spring. When these parameters are used in combination with the elasto-plastic material models, mentioned in paragraph 2.1.1, they should be able to emulate the force-displacement behaviour of the leaf spring. Figure 3.10 shows the elasto-plastic leaf spring models. The models are given in this orientation (the 3rd quadrant) in order to coincide with the convention that was stated in Chapter 1: when the spring is compressed the displacement and the force is taken as negative. The following two paragraphs present the elastic-linear model and the elastic-nonlinear model.

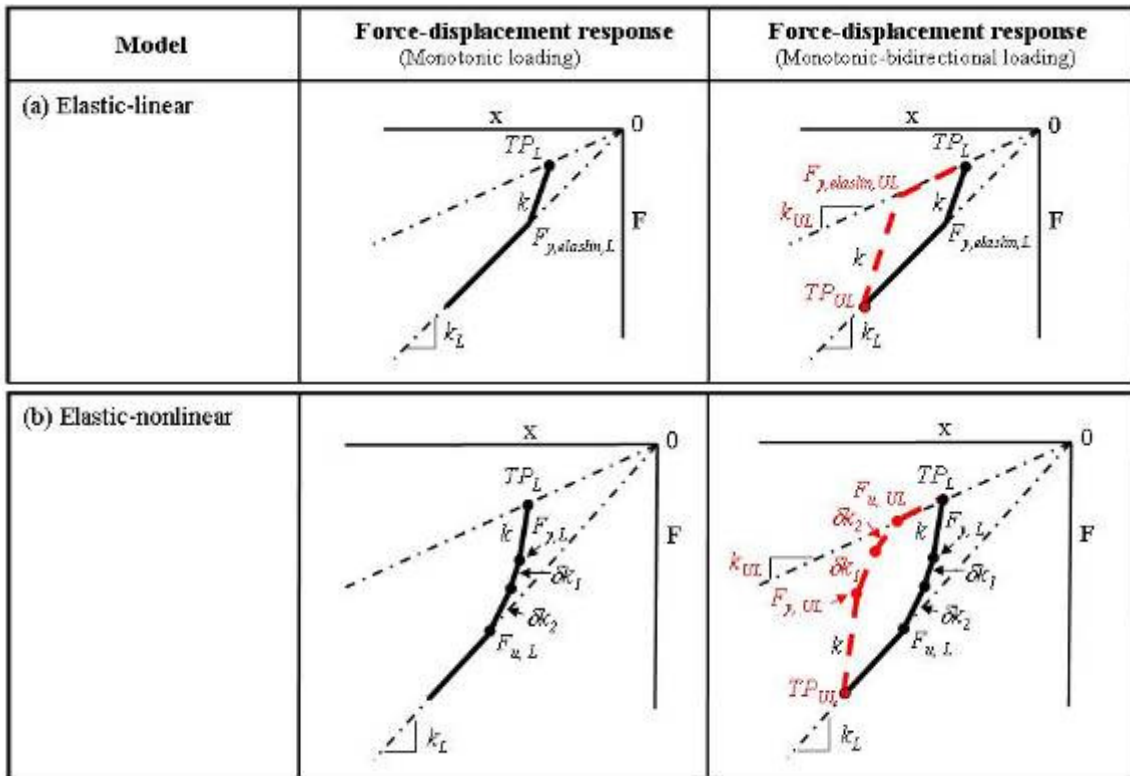


Figure 3.10. Elasto-plastic leaf spring models

2.3.1. Elastic-linear model

The elastic-linear model has two stiffness regimes representing the stiffness of the solid beam (k) and the layered beam. The layered beam is divided into two separate stiffnesses i.e. a layered beam stiffness during loading (k_L), and a layered beam stiffness during unloading (k_{UL}) (see Figure 3.10). The elastic-linear model assumes that the transition from the solid beam to the layered beam behaviour is at a discrete point and not a smooth transition between the two. This point of transition between the two stiffness regimes is termed the elastic-linear frictional yield force ($F_{y, elastin}$) and should not be confused with the frictional yield force (F_y) (see Figure 3.11). For the elastic-linear model it is not necessary to extract the yield fraction from the experimentally measured force-displacement characteristic, as the elastic-linear frictional yield force ($F_{y, elastin}$) will be used instead. The elastic-linear frictional yield force can be calculated using the stiffness of the solid beam (k), the stiffness of the layered beam during loading (k_L) and the turning point during loading (TP_L) (or the stiffness during unloading (k_{UL}) and the turning point (TP_{UL}) depending on the loading direction). Therefore either $F_{y,elastin,L}$ or $F_{y,elastin,UL}$ is calculated. Thus, after obtaining k , k_L and k_{UL} from the

experimental force-displacement characteristic, the model will be defined and should be able to calculate the force due to any given displacement using the equations in Table 3.1.

Table 3.1. Elastic-linear equations

Loading		Unloading	
$F = kx$	$(F \geq F_{y,elastin,L})$	$F = kx$	$(F \leq F_{y,elastin,UL})$
$F = k_L x$	$(F < F_{y,elastin,L})$	$F = k_{UL} x$	$(F > F_{y,elastin,UL})$

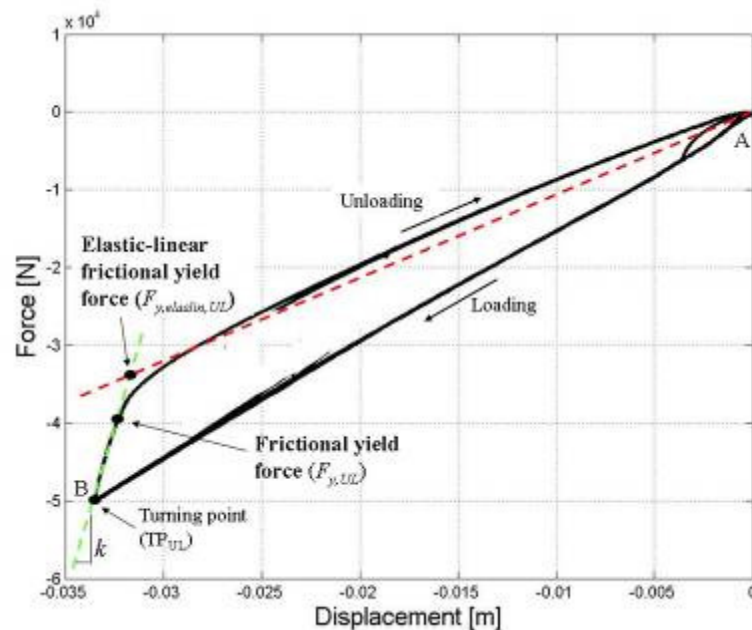


Figure 3.11. Elastic-linear frictional yield force and frictional yield force

Advantages and disadvantages

The elastic-linear leaf spring model only requires the stiffness of the solid beam (k) and the stiffness of the layered beam (during loading (k_L) and unloading (k_{UL})) in order to predict the force-displacement characteristic of the multi-leaf spring. Not needing to extract the yield fraction will be advantageous especially in scenarios where it may be difficult to observe the frictional yield force in the measured force-displacement characteristic. The way the transition between the solid beam and the layered beam is handled in the elastic-linear model, will result in the inability of this model to predict the smooth transition observed in the physical springs's characteristics.

2.3.2. Elastic-nonlinear model

Similar to the elastic-linear model, the elastic-nonlinear model also has two stiffness regimes - the stiffness of the solid beam (k) and the stiffness of the layered beam, with the stiffness of the layered beam consisting of the stiffnesses during loading (k_L) and unloading (k_{UL}). During the initial loading, or unloading of the multi-leaf spring, the model uses the stiffness of the solid beam in the force calculation until the frictional yield force is reached. After the frictional yield force is reached the model changes the stiffness incrementally from the solid beam to the stiffness of the layered beam (either k_{UL} or k_L depending on the direction of loading). This incremental change in stiffness (δk) is done in order to emulate the transition that is observed in the physical spring's behaviour. The point where the transition ends and

the spring again behaves as a layered beam is called the ultimate frictional yield force (F_u). Beyond the ultimate frictional yield force the stiffness of the layered beam is used.

In addition to the parameters k , k_{UL} and k_L that we needed to extract from the measured force-displacement characteristic for the elastic-linear model, we need to get the yield fraction for the elastic-nonlinear model. The yield fraction is calculated from the frictional yield force and turning point that is obtained from the force-displacement characteristic. Figure 3.12 shows a portion of a force-displacement characteristic containing two loops. The frictional yield points and turning points are also shown in the figure. The turning points are clearly defined on the graph and are easily extracted. In order to obtain the frictional yield point a line is constructed that goes through the turning point and has the stiffness of the solid beam as its slope. The frictional yield point is then the point where the force-displacement characteristic starts to deviate from this line. Table 3.2 gives the numerical values for the turning point force (TP_{UL}) and frictional yield force ($F_{y,UL}$) for the two loops. The yield fraction ($f_{y,UL}$) is calculated using Equation {3.4}.

$$f_{y,UL} = \frac{F_{y,UL}}{TP_{UL}} \quad \{3.4\}$$

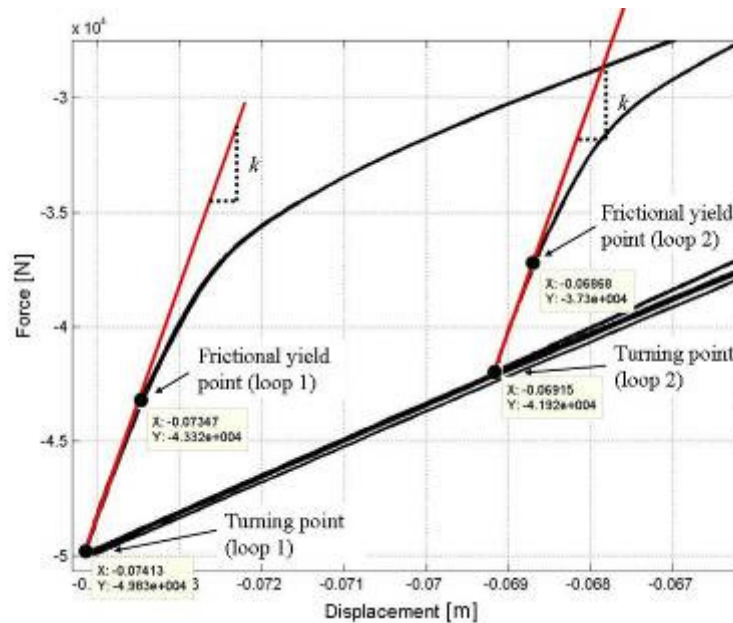


Figure 3.12. Frictional yield point and turning point on force-displacement characteristic

Table 3.2. Turning point force, frictional yield force and yield fraction

	Loop 1	Loop 2
Turning point [N]	-4.983e4	-4.192e4
Frictional yield force [N]	-4.332e4	-3.73e4
Yield fraction [dimensionless]	0.869	0.889

The yield fraction calculated in Table 3.2 was done for the case where the spring is being unloaded. When the yield fraction is used to calculate the frictional yield force during loading the reciprocal of the yield fraction during unloading ($f_{y,L} = \frac{1}{f_{y,UL}}$) should be used. From the

above the reason becomes clear why the yield fraction is used as the mechanical property instead of the frictional yield force. If the frictional yield force were to be used it could only

be applied to a single loop, whereas the yield fraction can be applied to all loops. Once the mechanical properties (k , k_{UL} , k_L and the yield fraction) have been obtained, the equations in Table 3.3 can be used to calculate the force for any given displacement.

Table 3.3. Elastic-nonlinear equations

	<u>Loading</u>	<u>Unloading</u>
Solid beam	$F = kx$ ($F \geq F_{y,L}$)	$F = kx$ ($F \leq F_{y,UL}$)
Transition	$F = \delta kx$ ($F < F_{y,L}$ AND $F \geq F_{u,L}$)	$F = \delta kx$ ($F > F_{y,UL}$ AND $F \leq F_{u,UL}$)
Layered beam	$F = k_L x$ ($F < F_{u,L}$)	$F = k_{UL} x$ ($F > F_{u,UL}$)

Advantages and disadvantages

The elastic-nonlinear leaf spring model will be able to give better predictions for the transition from the solid beam to the layered beam behaviour. However, there might be cases where it is difficult to obtain the frictional yield point from the force-displacement characteristic, and will therefore make it difficult to calculate the yield fraction. Furthermore, it has not yet been proven that the yield fraction will not change between loops and therefore it may occur that the yield fraction cannot be calculated in certain scenarios. Under these conditions the elastic-nonlinear model will not be able to accurately represent the transient behaviour.

2.4. Validation of the elasto-plastic leaf spring model

The proposed elasto-plastic leaf spring models will now be implemented and validated against measured data. The experimental data obtained using the spring only setup presented in paragraph 2.1.2 in Chapter 2 will be used. The data from the spring only setup is used as this setups isolates the leaf spring and does not include effects from other components.

2.4.1. Elastic-linear model

The predictions of the elastic-linear model and the measured data, subjected to the same displacement input, are compared in Figure 3.13 and Figure 3.14. Figure 3.13 shows the comparison of the force-displacement characteristic and Figure 3.14 shows the comparison of the spring force. The spring force was measured by the load cell situated between the actuator and the multi-leaf spring (see Figure 2.16 in Chapter 2). From both figures the error this model makes in predicting the transition between the solid and layered beam behaviour, can clearly be observed. It can also be observed that there is a deviation in the amplitude at the point at which the loading direction is changed (points B and D). Additionally, the model and the physical system were subjected to a random displacement input. Figure 3.15 shows the comparison of the spring force. The transitional error is shown in Figure 3.15(b). The errors that the model makes in the transitional phase are compounded in cycles that have small amplitudes. This compounding effect is shown in Figure 3.15(c). All the comparisons indicate that the elastic-linear model gives good predictions of the vertical behaviour of the leaf spring.

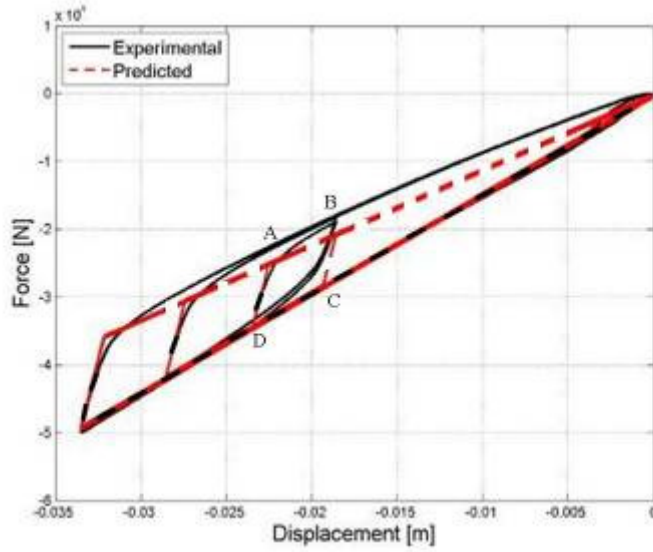


Figure 3.13. Comparison between experimental force-displacement characteristic and elastic-linear leaf spring model

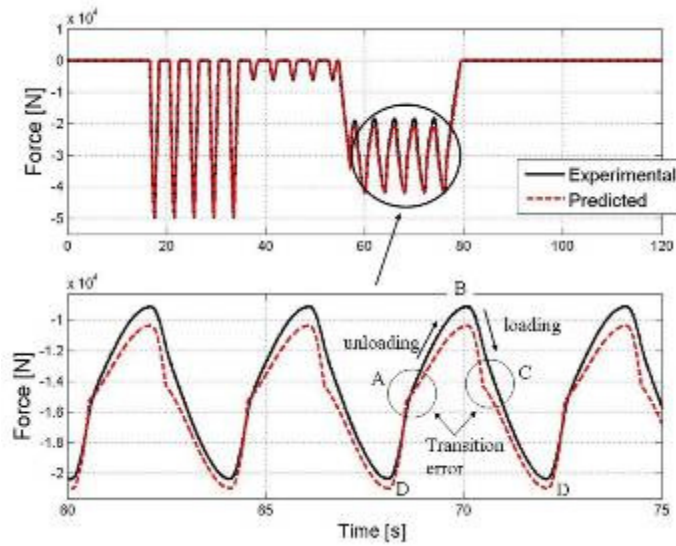


Figure 3.14. Transition error in prediction of elastic-linear leaf spring model

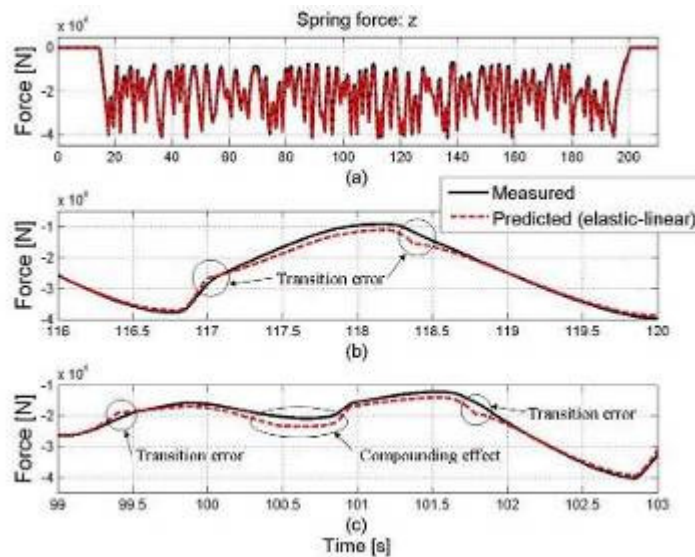


Figure 3.15. Transition error in prediction of elastic-linear leaf spring model (Random excitation)

2.4.2. Elastic-nonlinear model

The comparison between the spring force of the elastic-nonlinear model's predictions and measured data is shown in Figure 3.16. Figure 3.16(b) includes the predictions of the elastic-linear model in order to show the improvement in the predictions of the transitional behaviour of the elastic-nonlinear model. A further observation that is made from Figure 3.16(b) is that, except for the transitional phase, the elastic-linear and the elastic-nonlinear models give the same predictions.

Figure 3.17 shows the comparison of the spring force for a random displacement input. From Figure 3.17(b) we again observe that the elastic-linear and elastic-nonlinear model gives the same predictions except during the transitional phase. From Figure 3.17(c) we see the compounding effect and note that it is smaller for the elastic-nonlinear model than for the elastic-linear model.

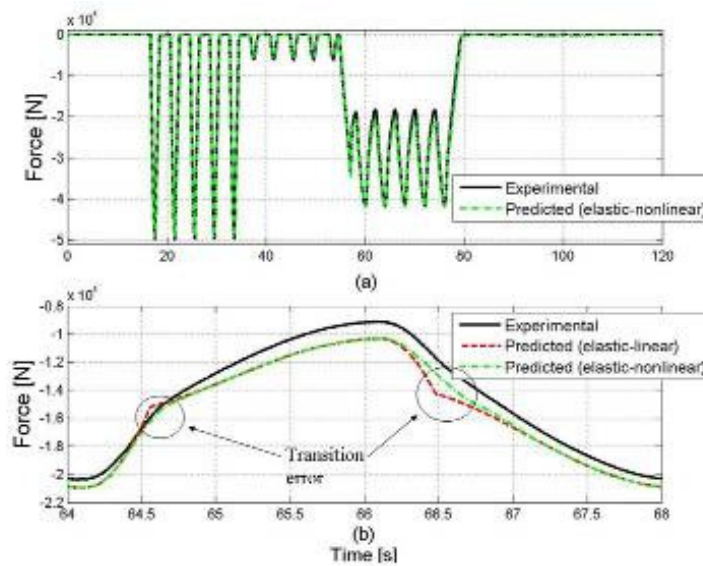


Figure 3.16. Transition error in predictions of elastic-nonlinear leaf spring model

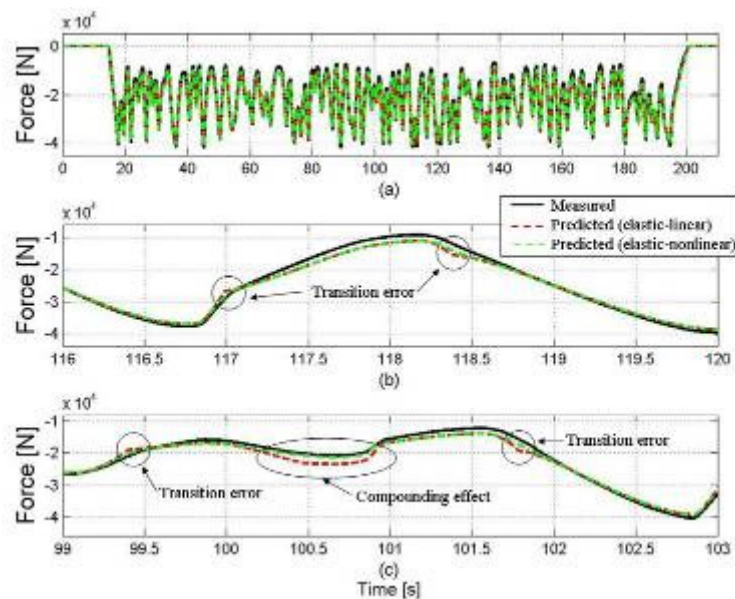


Figure 3.17. Transition error and compounding effect in predictions of elastic-nonlinear leaf spring model (Random excitation)

2.5. Conclusion

The proposed leaf-spring model is based on material behaviour and material models. The analogy implies that the leaf-spring should have two stiffness regimes that are associated with the no-slip and slip conditions, which corresponds to the elastic and inelastic deformation of engineering materials. It was shown that the leaf-spring does indeed have these two stiffness regimes present in its behaviour and that they can be estimated accurately by using beam theory.

The comparisons between the predictions of the elastic-linear and the elastic-nonlinear model, with the measured data, correlate well. Compared to the predictions of the elastic-linear model the elastic-nonlinear model gives better predictions especially during the transitional phase. The results show that the mechanical properties of the leaf spring, used with the elasto-plastic leaf spring models, are able to predict the behaviour of the leaf spring for both sinusoidal and random displacement inputs. From the qualitative results it can be concluded that the elasto-plastic leaf spring models can accurately predict the complex behaviour of the multi-leaf spring without needing to model the complex microscopic mechanisms. The elasto-plastic leaf spring model offers a simple and efficient mathematical representation of the multi-leaf spring, requiring only three parameters (when using the elastic-linear formulation) to accurately capture the behaviour of the multi-leaf spring.

3. Elasto-plastic leaf spring model applied to the parabolic leaf spring

In this paragraph the novel elasto-plastic leaf spring (EPLS) model, presented in the previous paragraph and used to model a multi-leaf spring, will now be applied to a parabolic leaf spring.

Figure 3.18 shows the force-displacement characteristic of the multi-leaf spring and the parabolic leaf spring that was obtained using the spring only setup. The difference in the two leaf spring's characteristics can be observed. The parabolic leaf spring has a much smaller hysteresis loop. This is due to the parabolic leaf spring having fewer blades and contact between blades only at the ends which implies that there is less friction. The elastic-linear formulation of the EPLS model, presented in paragraph 2.3.1, will be used to simulate the parabolic leaf spring. The elastic-linear model is used as the parabolic leaf spring has a more rapid transition between the solid and layered beam behaviour. This makes it difficult to extract the yield fraction required by the elastic-nonlinear model. Furthermore, because the transition from the solid beam to the layered beam behaviour takes place so rapidly the error the elastic-linear model will make in the area of transition is much smaller than when used to model the multi-leaf spring. Figure 3.19 shows the error the elastic-linear model will make when used to model the multi-leaf spring and the parabolic leaf spring.

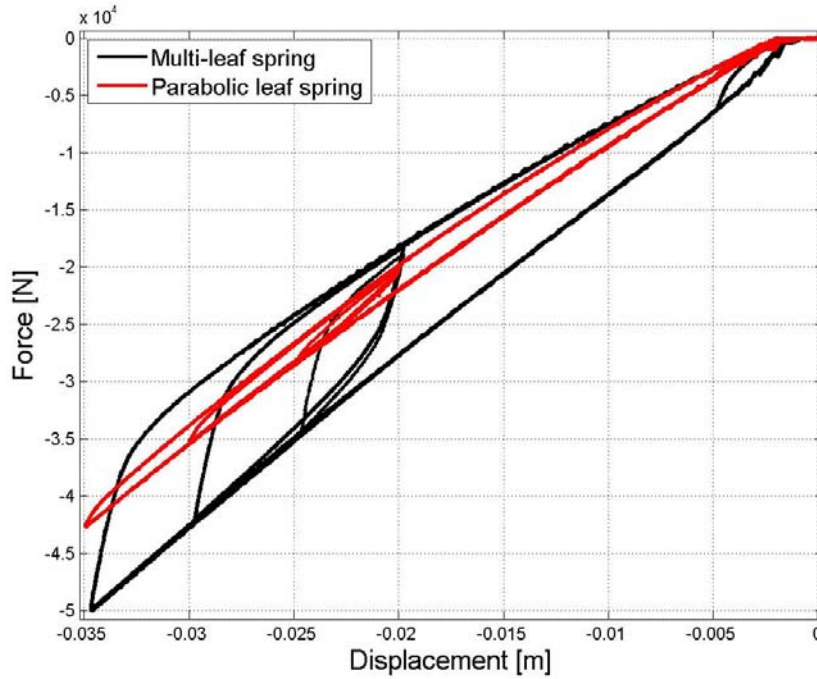


Figure 3.18. Force-displacement characteristic multi-leaf spring and parabolic leaf spring

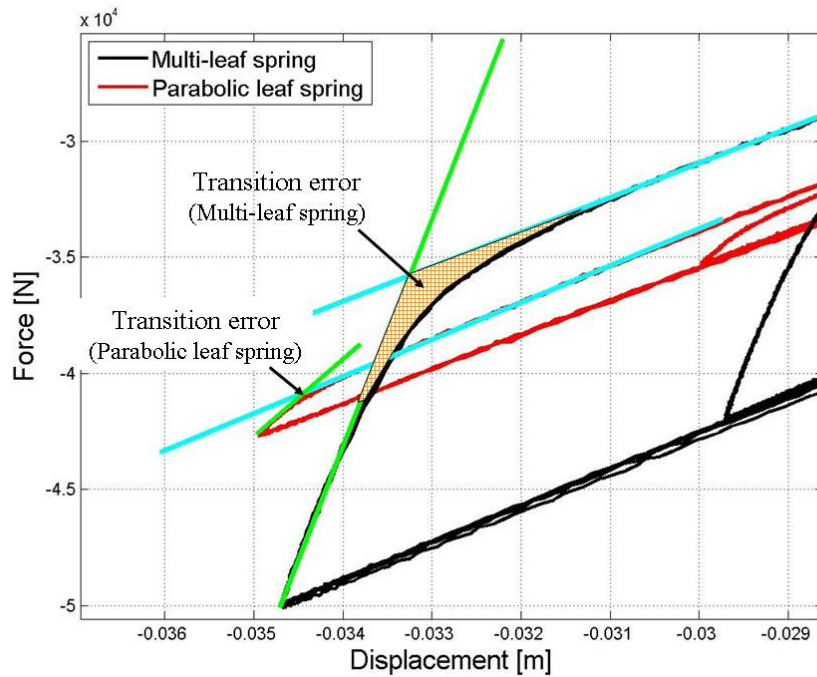


Figure 3.19. Transition error of using linear-elastic model on multi-leaf spring and parabolic leaf spring

3.1. Extracting mechanical properties for the elastic-linear parabolic leaf spring model

The parameters we need to extract from the experimental characteristic of the parabolic leaf spring in order to define the elastic-linear model are: the stiffness of the solid beam (k) and the stiffness of the layered beam during loading (k_L) and unloading (k_{UL}). Figure 3.20 indicates the extraction of the three parameters from the experimental characteristic of the parabolic leaf spring. The force-displacement characteristic shown in Figure 3.20 was obtained using the spring only setup discussed in paragraph 3.1.2 in Chapter 2.

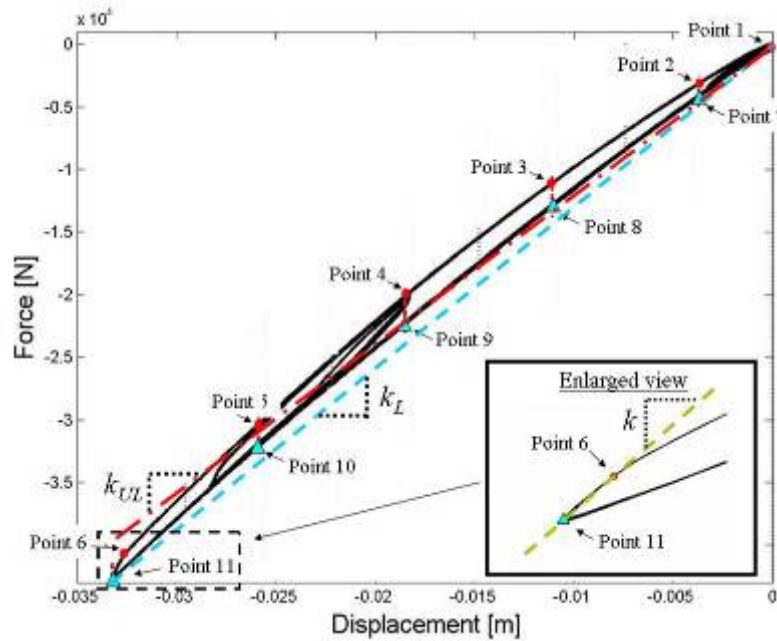


Figure 3.20. Extraction of mechanical properties for elastic-linear leaf spring model

The stiffness of the solid beam (k) is extracted by calculating the incline of the line that goes through point 6 and point 11. Point 11 is the starting point of the solid beam behaviour and point 6 is chosen such that it attempts to correspond to the point at which the beam stops to act like a solid beam and starts to act as a layered beam. In order to calculate the stiffness of the layered beam during loading (k_L) a straight line is fitted through the points 7 to 11. The incline of this line is then used as the stiffness of the layered beam during loading. The same procedure is used to calculate the stiffness of the layered beam during unloading (k_{UL}), except now points 1 to 6 are used. After calculating the three required parameters the model can now be used to predict the force for a given displacement input.

3.2. Validation of elastic-linear leaf spring model emulating the parabolic leaf spring

The predictions of the elastic-linear model and the measured data, both subjected to input displacement signal 1 presented in Chapter 2, are compared in Figure 3.21 and Figure 3.22. The experimental data used here in the validation process was obtained from the spring only setup of the parabolic leaf spring presented in Chapter 2. Figure 3.21 shows the comparison of the force-displacement characteristic and Figure 3.22 shows the comparison of the spring force. The spring force was measured by the load cell situated between the actuator and the multi-leaf spring (see Figure 2.31). Good correlation is observed from Figure 3.21 and Figure 3.22. The model and the physical system were also subjected to a random displacement input (Input displacement signal 3). Figure 3.23 shows the comparison of the spring force. All the comparisons indicate that the elastic-linear model gives accurate predictions of the vertical behaviour of the parabolic leaf spring. It should be noted from Figure 3.21 that the elasto-plastic leaf spring model is not able to capture the nonlinear behaviour that is observed in the experimental characteristic of the parabolic leaf spring when the leaf spring is in the layered beam regime. It is not exactly clear what the cause for the nonlinear behaviour is but it may be a result of the friction process. This should be investigated in future work to improve the predictions obtained from the elasto-plastic leaf spring models.

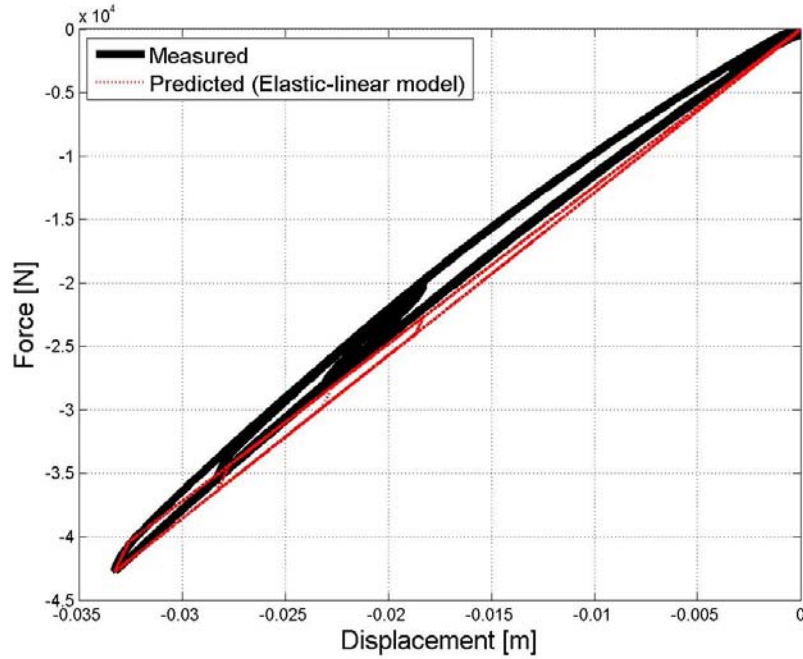


Figure 3.21. Comparison between measured force-displacement characteristic and elastic-linear leaf spring model of parabolic leaf spring

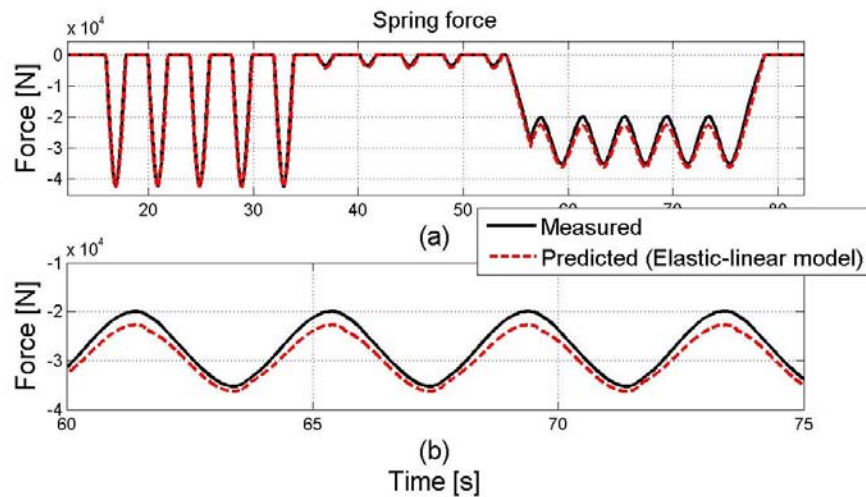


Figure 3.22. Comparison between measured and predicted spring force of parabolic leaf spring

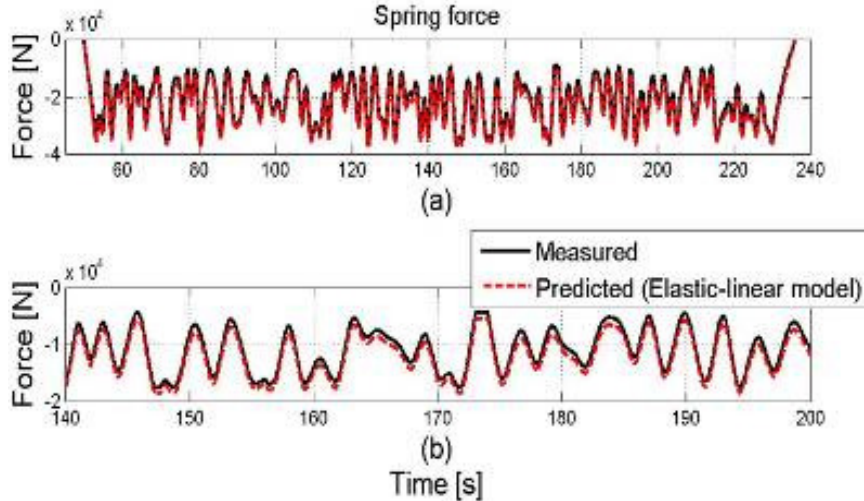


Figure 3.23. Comparison between measured and predicted spring force of parabolic leaf spring for random displacement input

3.3. Conclusion

The elastic-linear formulation of the EPLS model was used to emulate the parabolic leaf spring. After the required mechanical properties of the parabolic leaf spring were extracted, in order to parameterise the elastic-linear leaf spring model, the model was simulated. The result from the elastic-linear leaf spring model was compared to the measured data for which good correlation was obtained.

4. Loaded length changes of a simply supported leaf spring

In the multi-leaf spring setup shown in Figure 3.24 we have a leaf spring that is simply supported. A leaf spring in this layout is also referred to as a variable effective length spring (SAE spring design manual, 1996). Changing the length between the supports, or in other words, changing the loaded length of the leaf spring will constitute a change in the force-displacement characteristics of the leaf spring. This effect of the loaded length on the stiffness of the leaf spring was shown experimentally in Chapter 2. Changes in the loaded length of the leaf spring may also be induced by the shape of the supports. Figure 3.24 shows the difference in the loaded length between the deflected and undeflected leaf spring. Depending on the shape of the supports the changes in the loaded length, as the leaf spring is deflected, may be more severe in some cases than others. The loaded length is a parameter that has a significant effect on the force-displacement characteristic of the leaf spring as it changes the stiffness of the spring. This can offer interesting possibilities to change the characteristic of a leaf spring in a specific application by simply changing the shape of the supports. Considering a simple beam, the stiffness of the beam is inversely proportional to the length cubed ($k \propto \frac{1}{l^3}$).

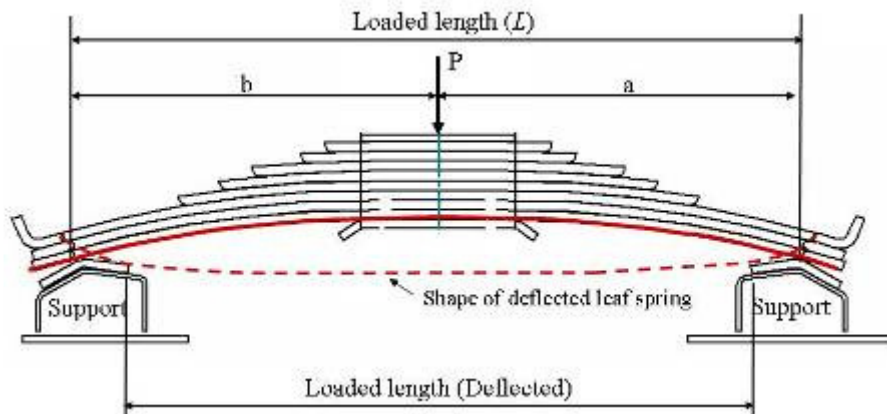


Figure 3.24. Variable effective length spring

4.1. Method to account for loaded length changes

The proposed method for accounting for the effect of changes in loaded length of the leaf spring is based on beam theory. Consider the beam shown in Figure 3.25. Gere (2004) gives Eq.{3.5} to calculate the deflection of the beam at the point where the force (P) is applied.

$$v = -\frac{Pbx}{6LEI}(L^2 - b^2 - x^2) \quad (0 \leq x \leq a) \quad \{3.5\}$$

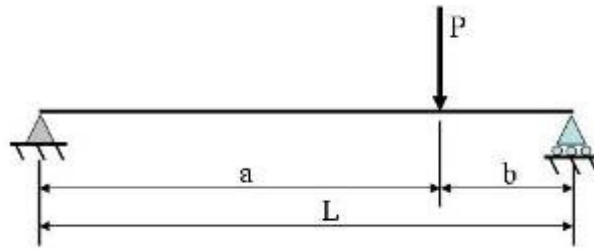


Figure 3.25. Simply supported beam

Eq.{3.5} can be rearranged and written as Eq.{3.6} which gives us the stiffness (k) of the beam.

$$k = \frac{P}{v} = \frac{6LEI}{ab(b^2 + a^2 - L^2)} \quad \{3.6\}$$

Assume we have two layouts of the simply supported beam shown in Figure 3.25. Both layouts have the same beam and the same force is applied to the beams in both layouts. This implies that E , I and P are the same for both layouts. The only difference in the two layouts is the distance between the supports and where P is applied. In other words for layout 1 we have E , I , a_1 , b_1 and L_1 and for layout 2 we have E , I , a_2 , b_2 and L_2 . Substituting the variables of the two respective layouts into Eq.{3.6}, and rearranging, we obtain Eq.{3.7}:

$$k_1 \frac{b_1 a_1 (b_1^2 + a_1^2 - L_1^2)}{L_1} = 6EI \quad \text{and} \quad k_2 \frac{b_2 a_2 (b_2^2 + a_2^2 - L_2^2)}{L_2} = 6EI$$

$$\therefore k_1 \frac{b_1 a_1 (b_1^2 + a_1^2 - L_1^2)}{L_1} = k_2 \frac{b_2 a_2 (b_2^2 + a_2^2 - L_2^2)}{L_2} \quad \{3.7\}$$

Rearranging this equation we obtain Eq. {3.8} which enables us to calculate the spring stiffness of a beam (k_2) for any loaded length (L_2) given the stiffness of the same beam (k_1) obtained at a different loaded length (L_1).

$$k_2 = k_1 \frac{b_1 a_1 L_2 (b_1^2 + a_1^2 - L_1^2)}{b_2 a_2 L_1 (b_2^2 + a_2^2 - L_2^2)} \quad \{3.8\}$$

The use of Eq.{3.8} to calculate the stiffness of a beam in one layout by using the stiffness of another layout is demonstrated and verified by the following example. Assume that we have two layouts with the values for their parameters given below. Using Eq.{3.6} we can calculate the stiffness of the beam in the two layouts.

Layout 1

Known: $a_1 = 2$
 $b_1 = 1$
 $L_1 = a_1 + b_1 = 3$
 E and I

$$k_1 = \frac{6 \times 3 \times EI}{1 \times 2 (1 + 4 - 9)}$$

$$= -\frac{18EI}{8}$$

$$= -2.25EI$$

Layout 2

Known: $a_2 = 4$
 $b_2 = 2$
 $L_2 = a_2 + b_2 = 6$
 E and I

$$k_2 = \frac{6 \times 6 \times EI}{2 \times 4 (4 + 16 - 36)}$$

$$= -\frac{36EI}{128}$$

$$= -0.28EI$$

Now let's approach this problem from a different angle. We would like to calculate the stiffness of the beam in layout 2 but we do not know the young's modulus (E) or the inertia (I) of the beam. However, we have the same beam in both layouts and we know the stiffness (k_1), and the length between the supports (L_1, L_2) and the application point (a_1, b_1, a_2, b_2) of the force (P) for both layouts. In this situation we cannot use Eq.{3.6} to calculate the stiffness of the beam as we do not know the young's modulus (E) of the material or the inertia (I) of the beam. However, the information that is known makes it possible to use Eq.{3.8} to calculate the stiffness of the beam in layout 2.

$$\begin{aligned} \text{Known: } k_1 &= -2.25EI \\ a_1 &= 2 \\ b_1 &= 1 \\ L_1 &= a_1 + b_1 = 3 \\ a_2 &= 4 \\ b_2 &= 2 \\ L_2 &= a_2 + b_2 = 6 \end{aligned}$$

Substituting the known values into Eq.{3.8} we obtain:

$$k_2 = -0.28EI$$

This is the same result as obtained when using Eq.{3.6}. Eq.{3.8} gives a simple method that relates the stiffness of the leaf spring to its loaded length. This method makes it possible to recalculate the experimentally extracted stiffnesses (k, k_{UL} and k_L), needed for the elasto-plastic leaf spring model, obtained from one layout to other layouts. This implies that the force-displacement characteristic only have to be obtained for one layout. To verify this the elasto-plastic leaf spring model is combined with Eq.{3.8} to check whether this combined model can indeed capture the change in stiffness for different loaded lengths. The predictions from the combined model for both the multi-leaf spring and parabolic leaf spring are compared to the experimental data obtained in Chapter 2. The validation results are presented in the following paragraph.

4.2. Validation of loaded length calculation combined with EPLS model

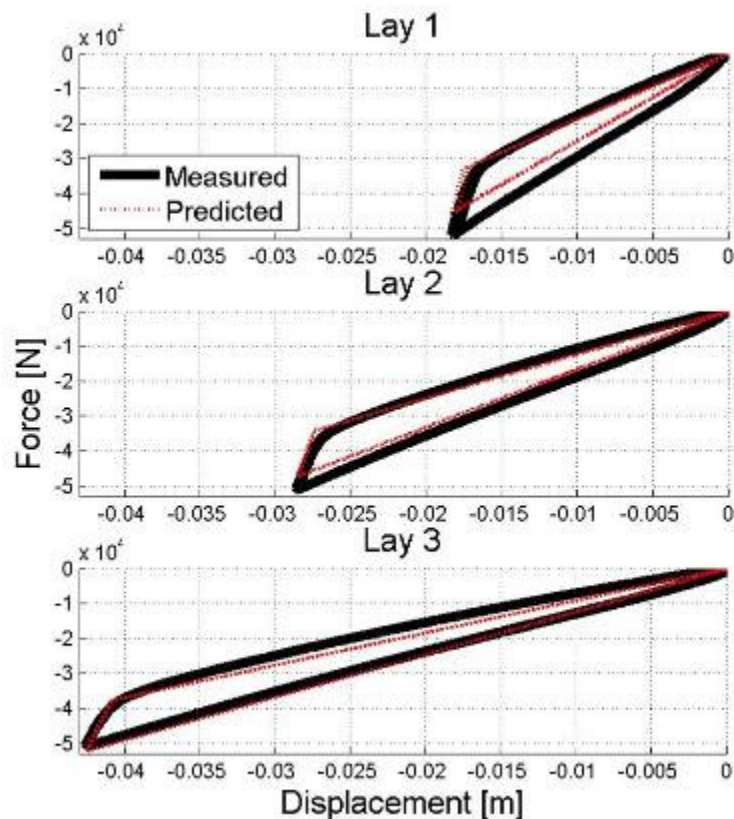
The combination of the proposed method for accounting for a change in loaded length and the elastic-linear version of the EPLS model will now be validated against measured data. The model will be used to predict the force-displacement characteristic of both the multi-leaf spring and the parabolic leaf spring's behaviour that was experimentally obtained in Chapter 2. The results from the model will be validated against these experimental measurements. The loaded length was changed in the experimental setup by changing the longitudinal spacing of the hangers. The experimental force-displacement characteristic, for both the multi-leaf spring and parabolic leaf spring, were obtained at seven different spacings as was shown in Chapter 2. Four of these seven layouts will be used to validate the combined model. Table 3.4 shows the dimensions of the four layouts that are used. The layout at the normal position is used to extract the stiffnesses (k, k_{UL} and k_L) of the spring as needed to define the elastic-plastic formulation of the EPLS model. These stiffnesses along with the loaded length of the other layouts are then given to the combined model. The results for the multi-leaf spring and the parabolic leaf spring are given in the following two paragraphs.

Table 3.4. Dimensions of layouts (see Figure 3.24)

Position	Layout	Front spacing (<i>a</i>) [mm]	Rear spacing (<i>b</i>) [mm]	Loaded length (<i>L</i>) [mm]
Normal	Original	510	478	988
Min	1	430	398	828
Pos3	2	490	458	908
Pos5	3	530	518	1048

4.2.1. Multi-leaf spring

Figure 3.26 shows the comparison between the predicted and measured force-displacement characteristic of the multi-leaf spring. From the figure the effect of the loaded length on the stiffness of the multi-leaf spring can clearly be observed. The stiffness decreases from Lay 1 to Lay 3 as the loaded length increases. From the comparisons it is evident that Eq. {3.8} combined with the linear-elastic formulation of the EPLS model gives accurate predictions of the multi-leaf spring's characteristics for different loaded lengths.


Figure 3.26. Comparison of measured and predicted force-displacement characteristics of multi-leaf spring for different loaded lengths

4.2.2. Parabolic leaf spring

Figure 3.27 shows the comparison between the predicted and measured force-displacement characteristic of the parabolic leaf spring. From the graphs shown in this figure we can again observe the effect of the loaded length on the stiffness of the leaf spring, with the stiffness decreasing from Lay 1 to Lay 3 as the loaded length is increased. From these comparisons it is again evident that Eq. {3.8} combined with the linear-elastic formulation of the EPLS

model gives accurate predictions of the parabolic leaf spring's characteristics for different loaded lengths.

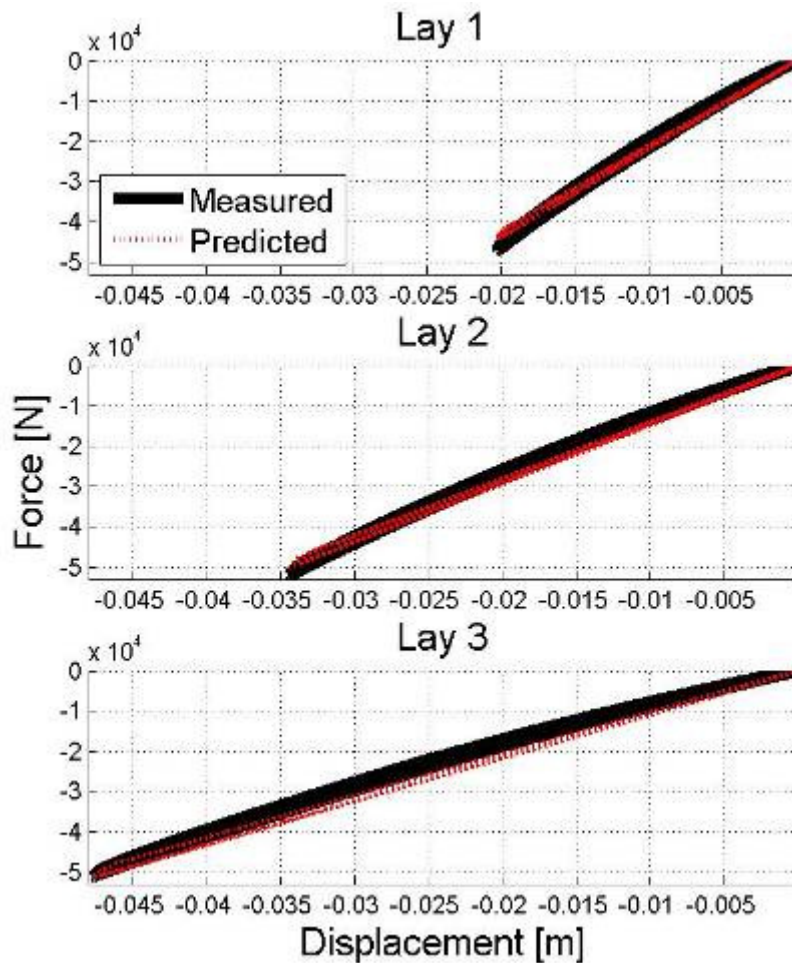


Figure 3.27. Comparison of measured and predicted force-displacement characteristics of parabolic leaf spring for different loaded lengths

4.3. Conclusion

The method that was proposed to account for changes in the loaded length was combined with the linear-elastic leaf spring model. This combination was used to predict the characteristics of different layouts of a multi-leaf spring as well as a parabolic leaf spring. The predicted characteristics were compared to measured characteristics and showed good correlation. The combined model was shown here to work for discrete changes in the loaded length. It should be confirmed that this combined model is also capable of predicting the force-displacement characteristic for a continuous change in the loaded length.

Up to this point we have shown that the physics-based EPLS model is able to emulate both the multi-leaf spring as well as the parabolic leaf spring. The EPLS model was combined with a method that is able to capture the sensitivity of the stiffness with respect to the loaded length. Attention will now be given to the non-physics based neural network approach and its ability to emulate the multi-leaf spring's vertical behaviour.

5. Artificial neural networks

Artificial neural networks are inspired by the biological networks found in the brain. Artificial neural networks are however extreme simplifications of their biological counterparts on which they are based. For details on biological neurons and the networks they form the reader is referred to the book by Müller *et al.* (1995). A simple artificial neuron model is shown in Figure 3.28 which has the following mathematical representation for the output of the neuron:

$$a = f(wp + b)$$

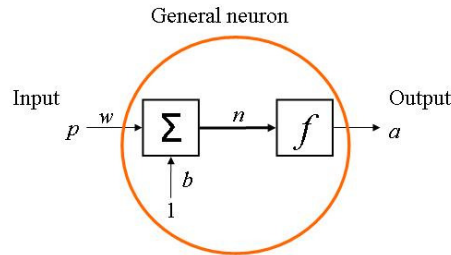


Figure 3.28. Simple artificial neuron

The neuron is the basic building block of neural networks. The neuron input p is multiplied by the weight w to form the term wp which is sent to the summer. The bias value, b , is also sent to the summer and added to the term wp to form the value n which is sent to the transfer function (or activation function) f and produces the neuron output a . For this neuron the parameters w , p and b are all scalar values. The parameters w and b are variables that are adjusted by some learning rule so that the neuron input/input relationship satisfies some specific goal. The transfer function (f) may be a linear or nonlinear function with the most common transfer functions being a hard limit transfer function, a linear transfer function and a log-sigmoid transfer function. Modelling nonlinear behaviour requires the use of nonlinear transfer functions. The neuron shown in Figure 3.28 is a single-input neuron and can be extended to have multiple inputs. These multiple input neurons can be connected to form various network architectures (Hagan *et al.* (1996)). The network architecture that will be used in this study is a feed forward multilayer network. Other networks include networks with feedback called recurrent networks. Figure 3.29 shows typical architectures of these two networks.

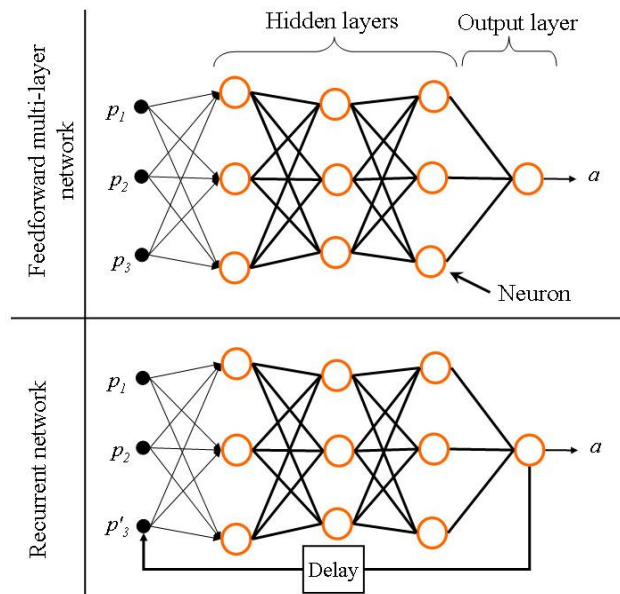


Figure 3.29. Feed forward and recurrent network architecture

5.1. Neural network model

This study will look at employing artificial neural networks in modelling the vertical behaviour of the multi-leaf spring. The literature study in Chapter 1 showed that neural networks have been used successfully to emulate the vertical behaviour of a leaf spring. Ghazi Zadeh *et al* (2000) used two similar recurrent neural networks with one emulating the loading behaviour and the other one the unloading behaviour of the leaf spring. A switching algorithm was used to determine which one of the networks should be used depending on whether the spring is loaded or unloaded. Each of the loading and unloading neural networks has architecture of $3 \times 10 \times 20 \times 1$. The three inputs to the neural network are the deflection at the current time step, the absolute value of the deflection change and the force at the previous time step (this is the recurrent terminal). The required training data was generated by an analytical model of the leaf spring.

Before going to a recurrent network architecture, such as used in the study by Ghazi Zadeh *et al.*(2000), a simple feed forward network architecture will be used to emulate the force-displacement characteristics of the multi-leaf spring. The advantage of using a feed forward network over a recurrent network is that the training of the feed forward network is faster. The feed forward neural network that is used in this study has two inputs being the displacement and the velocity of the spring with the output being the spring force. The architecture of the feed forward neural network is $2 \times 35 \times 1$. The hidden layer has 35 neurons with a tan-sigmoid (tansig) transfer function with the output layer having a linear (purelin) activation function. The network is shown in Figure 3.30.

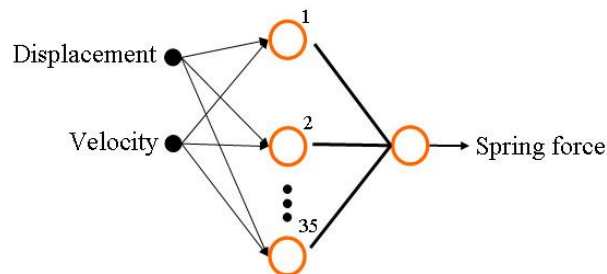


Figure 3.30. The 2-35-1 network

There is no clear method in which the architecture of a neural network can be determined. There are however some general guidelines which can be followed to obtain a good neural network. For instance, these guidelines give an indication of the amount of neurons that should be used in order to obtain good generalization from the neural network. The choice of the network architecture shown in Figure 3.30 was based on the following considerations. The choice in using the displacement as input is obvious as any spring develops a force due to it being deflected. The velocity is chosen as this will tell the neural network whether its being loaded or unloaded. The nonlinear function that will be required to model the force-displacement is not that complex and it is assumed that 35 neurons will be a good starting point.

The 2-35-1 neural network is a much simpler network than was used in the study of Ghazi Zadeh *et al.* (2000). Furthermore, instead of obtaining the training data from an analytical leaf spring model, as was the case in the study of Ghazi Zadeh *et al.* (2000), the training data is obtained from the experimental measurements on the leaf spring from Chapter 2. The multi-

leaf spring in the spring only setup will be used to evaluate whether the 2-35-1 neural network can emulate the multi-leaf spring.

Two training sets were constructed from the experimental data. The first training set used data that consisted of only the outer force-displacement loop. The second training set used data that consisted of all the loops in the force-displacement characteristic that are the result of different combinations of static loads and amplitudes. Figure 3.31 indicates the loops mentioned above.

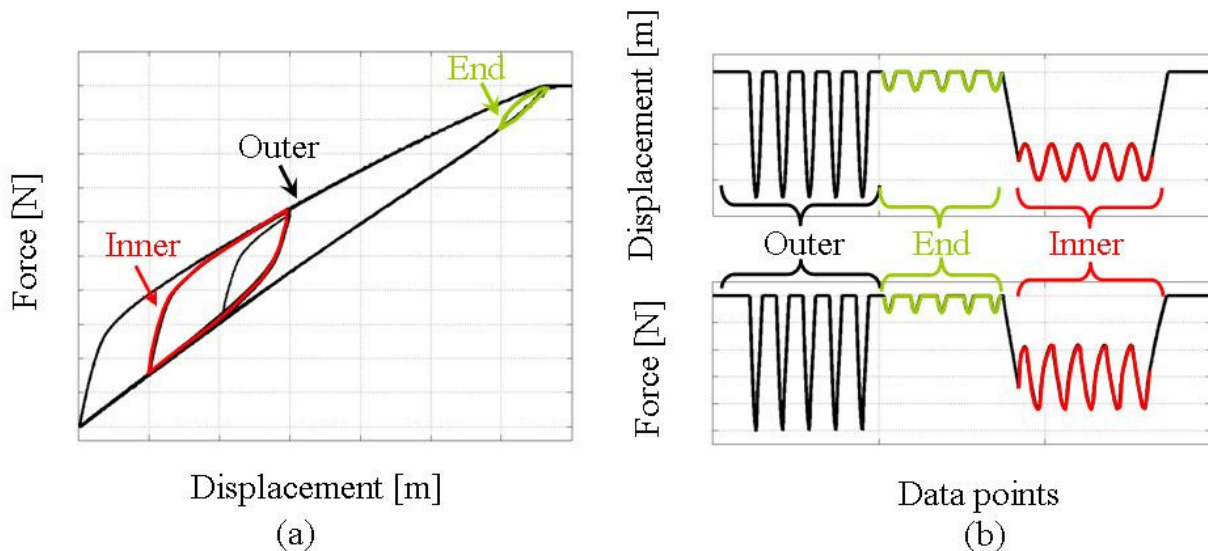


Figure 3.31. The different loops are shown on the force-displacement characteristic in (a) and, on the force and displacements versus data points in (b)

Two 2-35-1 neural networks were trained, one using the first training data set and the other using the second training data set. Both neural networks were then simulated by giving them the same displacement input signal. Figure 3.32 shows the results of the neural network compared to the experimental data when the first training set is used. From this figure it can be observed that the neural network emulates the leaf spring well for the outer loop, however, for the other loops it gives inaccurate predictions. The outer loop, for which good correlation is obtained, is the loop that was used in the training data. When we use the other neural network model which was trained using all the loops and compare its prediction to the experimentally measured force-displacement characteristic (see Figure 3.33), it can be observed that this neural network is able to correctly predict the force for all the loops. From the results in Figure 3.32 and Figure 3.33 it can be concluded that the neural network has difficulty in generalizing, in other words it is not able to correctly predict the force for displacements it was not trained for. Furthermore, the predictions from the neural network have a lot of noise present. These two aspects will be addressed in the following two paragraphs.

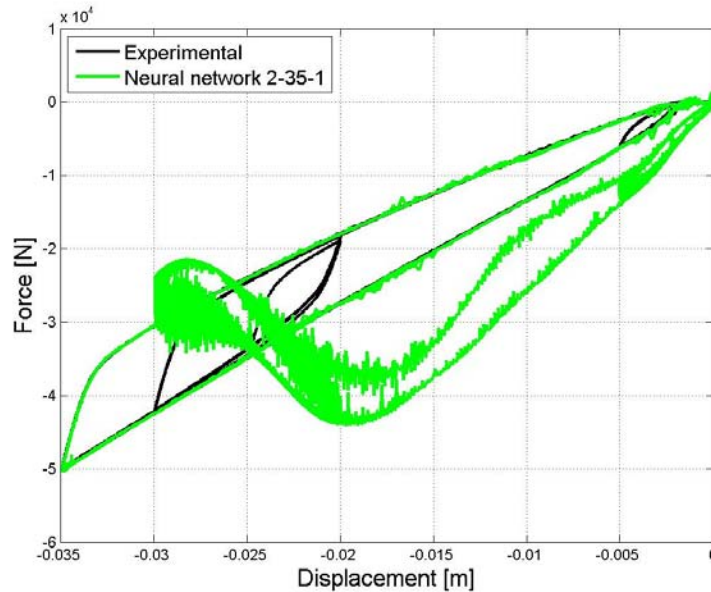


Figure 3.32. Comparison of neural network predictions and experimental data (neural network trained with outer loop)

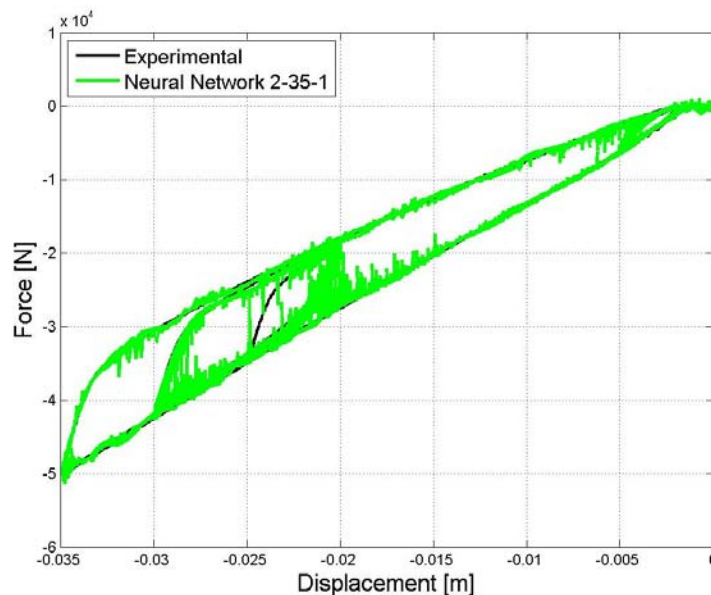


Figure 3.33. Comparison of neural network predictions and experimental data (neural network trained with all loops)

5.1.1. Reducing noise on neural network predictions

The results shown in Figure 3.33 showed that the neural network was able to predict the spring force due to a given displacement when it was trained with data that covered the entire working range of the function variables (in this case the displacement and velocity). The velocity is obtained by differentiating the displacement. When the velocity signal is viewed it is observed that the signal has a lot of noise present. This noise on the velocity seems to be the source of the noise observed on the predictions of the neural network in Figure 3.33. The velocity signal is smoothed by applying a four point moving average to the signal. Figure 3.34 shows the velocity signal before and after the four point moving average is applied. The smoothed velocity signal will now be used as input to the neural network.

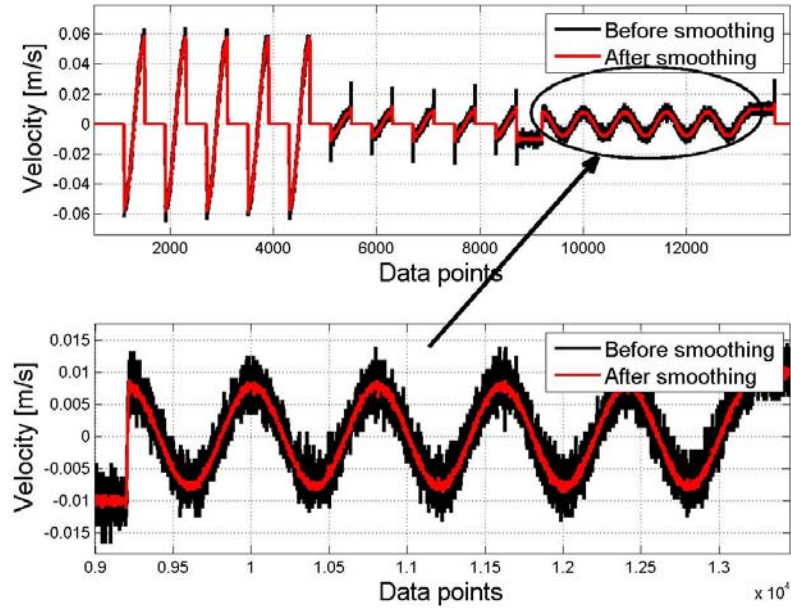


Figure 3.34. Velocity signal before and after smoothing

Figure 3.35 shows the results obtained from the neural network when the four point moving average is applied to the velocity signal. The prediction from the neural network has a lot less noise than were obtained in Figure 3.33.

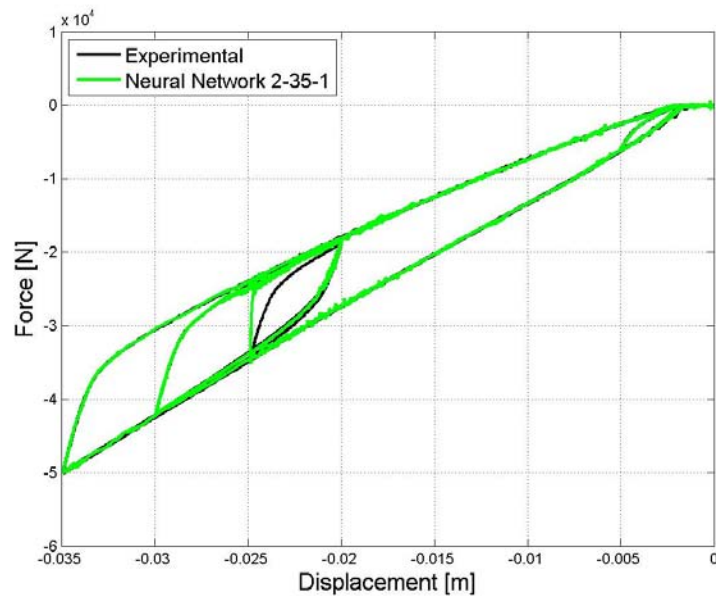


Figure 3.35. Comparison of neural network predictions and experimental data with smoothing applied to the velocity signal.

5.1.2. Generalization

Generalization refers to the ability of the neural network to give a satisfactory response to situations that were not present in the training data (Dreyfus, 2005). In Figure 3.32 it was shown that the neural network has difficulty in predicting the correct force for displacements and velocity inputs for which it was not trained with. This was referred to as an inability of the neural network to generalize. It should however be noted that generalization is often used to refer to the ability of the neural network to interpolate correctly between the supplied

training data, whereas, in the case shown in Figure 3.32 the neural network is actually trying to extrapolate.

The difference between the generalization ability of the neural network with respect to interpolation and extrapolation is discussed using an example similar to the one used in Hagan *et al.* (1996). Figure 3.36(a) shows a typical case where the neural network does not generalize well. The network used in Figure 3.36(a) has an architecture 1-9-1. This network architecture results in the neural network having more adjustable parameters (weights and biases) in comparison to the data points in the training set. To improve the generalization of the neural network the number of neurons can be reduced to give the simplest model that is able to adequately represent the training set (Hagan *et al.*, 1996 and Dreyfus, 2005). When the network architecture is reduced to one having two neurons (1-2-1), the generalization is improved as shown in Figure 3.36(b). Figure 3.36(b) shows that for any input(s) lying between the data points of the training set, the neural network will give good predictions. Using the 1-2-1 network, the ability of the neural network to extrapolate is shown in Figure 3.37. The 1-2-1 network was trained three separate times. From this figure it is clear that the network is not able to predict the correct response for data outside the range used for the variable(s) in the training set. It can be noted that for the region that the network has to extrapolate, the network predictions differ for each of the three training runs. This is because the training process results in different values for the weights and biases. For the inputs for which the network is interpolating the results stay similar but when the network is extrapolating, the network output differs greatly depending on the weights and biases. This example indicates that the model can generalize well when “unseen” inputs are given that lie within the range of the training set. The model is however not able to generalize to such an extent that the network is able to give the correct output for inputs that fall outside the range of the training set.

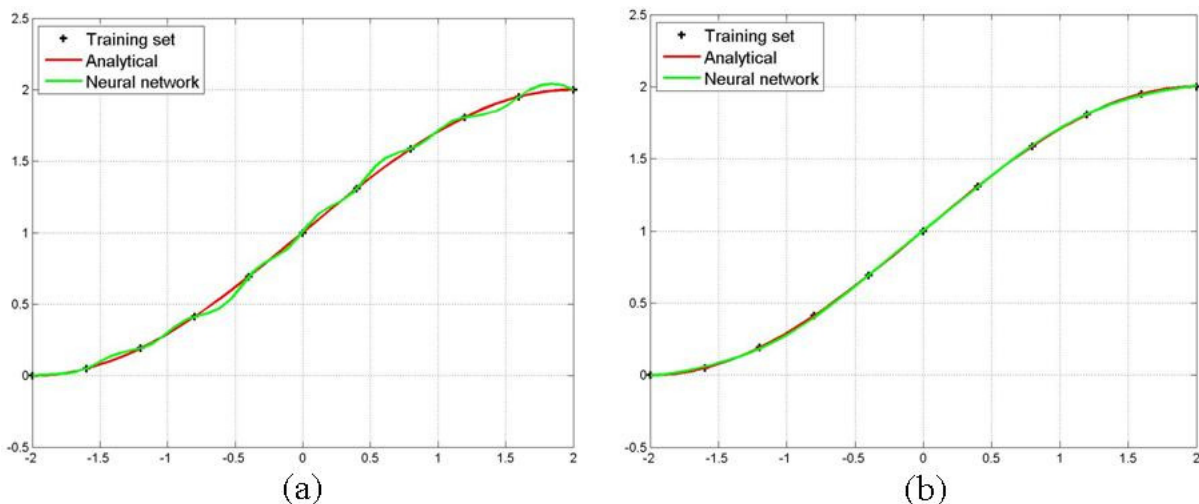


Figure 3.36. (a) 1-9-1 Network predictions. (b) 1-2-1 Network predictions.

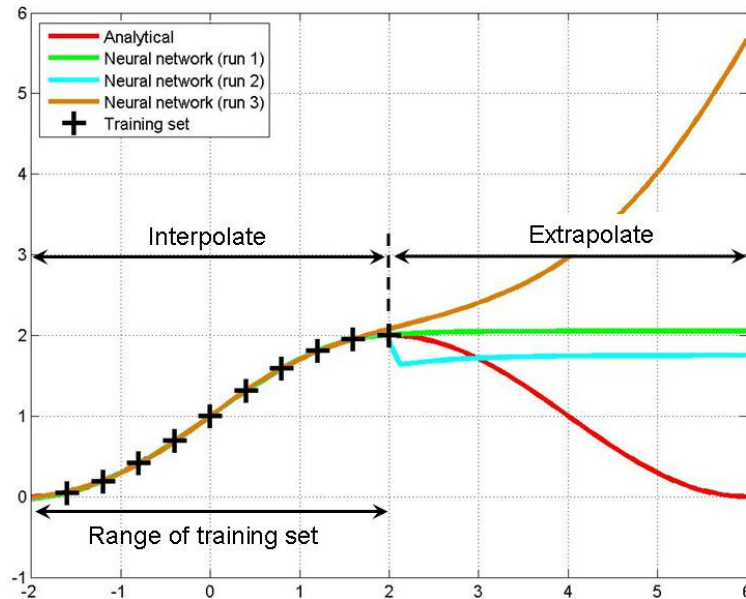


Figure 3.37. Results of 1-2-1 network when interpolating and extrapolating

The ability of the 2-35-1 network to generalize the behaviour of the leaf spring will now be investigated. Attention will be given to both the interpolation and extrapolation behaviour. As mentioned, generalization is improved when the network is as simple as possible while still being able to adequately represent the training set. Therefore, the 2-35-1 network's neurons are reduced. Figure 3.38 shows how the predictions of the neural network compare to the experimental data as the neurons are reduced. It can be seen that the neurons can be reduced until the network has nine neurons at which point the networks struggles to represent the training data. The network of 2-15-1 results in a simple network that is still able to represent the training data. This architecture should therefore give us a network that will be able to generalize. Figure 3.39 shows the results for the neural network that is simulated with a displacement signal that does not have any of the displacements used in the training set but does however fall within the range of the training set. The results from this figure show that the network does not have any problems with generalizing when the unseen inputs fall within the range of the training set, i.e. the network can interpolate.

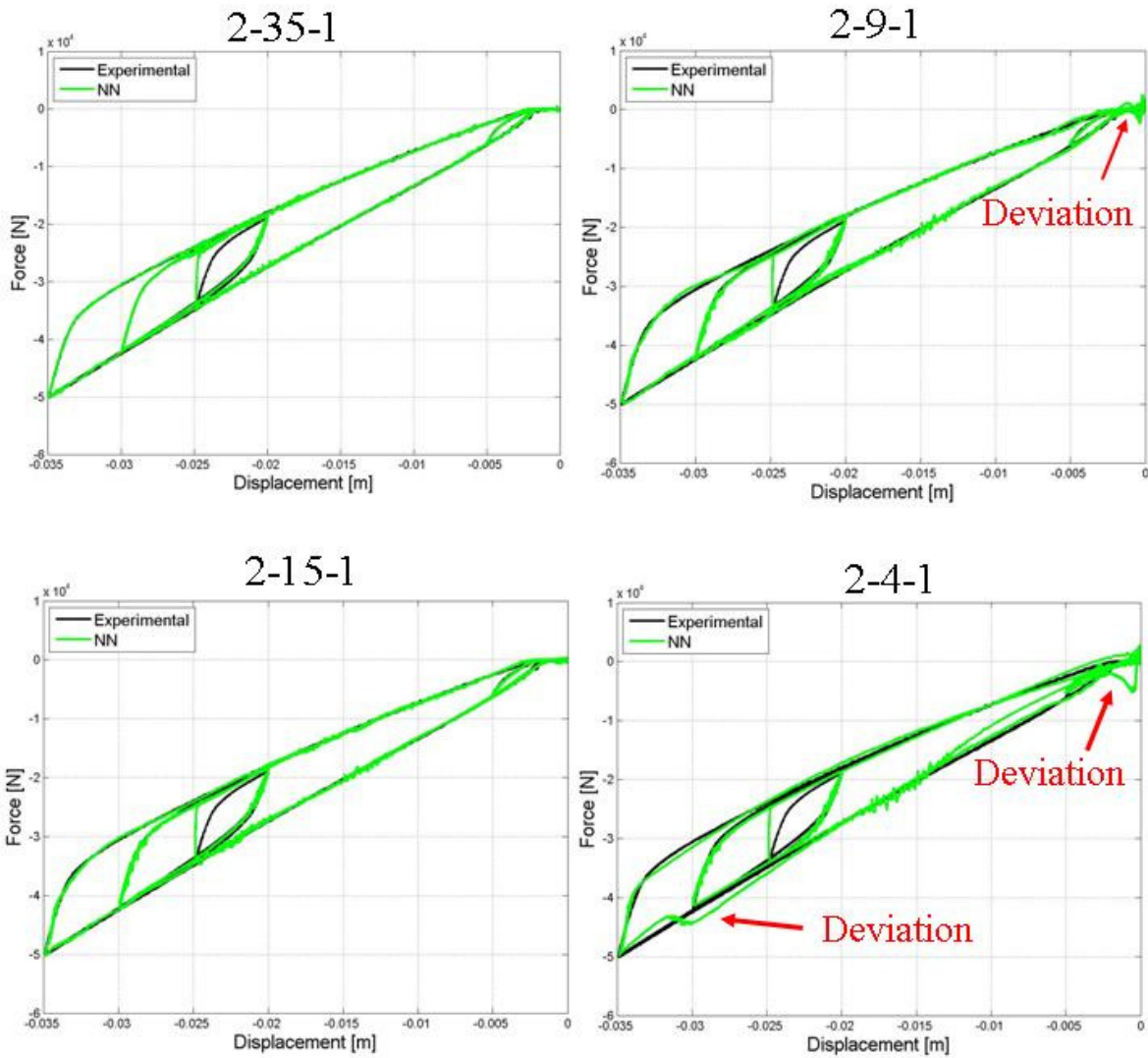


Figure 3.38. Effect of reducing neurons on the predictions of the network

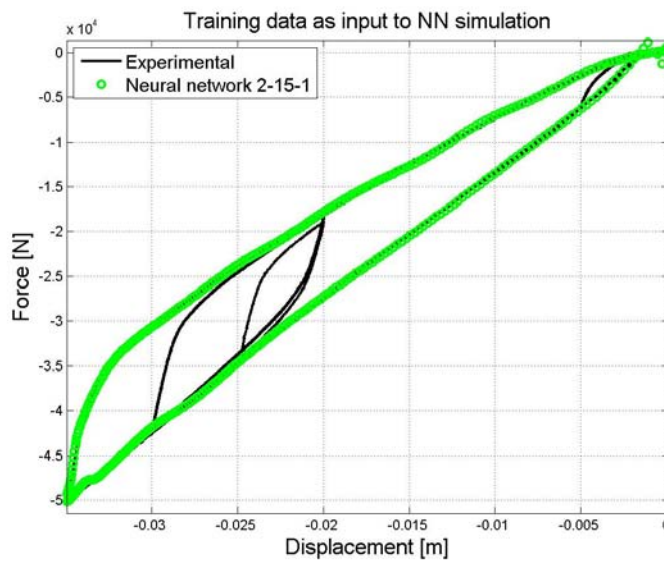


Figure 3.39. Ability of neural network to generalize (interpolate)

It was shown in Figure 3.37 that the neural network has some difficulty in generalizing when it has to extrapolate. In the case of the network that is used to emulate the leaf spring, the network will have to extrapolate when it is given displacements it was not trained with. It will

also have to extrapolate when the network is given displacements that it has been trained with but have a different excitation frequency. This dependency on frequency is present due to the velocity being one of the inputs to the neural network. Figure 3.32 showed the result of the 2-35-1 network when it has to extrapolate for displacements it was not trained with. The neurons in the network used in Figure 3.32 were reduced from 35 to 15 neurons. The 2-15-1 network was trained with the training set consisting of only the outer loop. The network was trained on three occasions and simulated. The results in Figure 3.40 are similar to what was observed in Figure 3.37. The network is able to give good predictions for the inputs that fall within the range of the training set but gives different force prediction for the input displacements that fall outside the range of the training set. With the neural network having the other input being the velocity, the same results is expected when the network is given a displacement input that fall within the range of the training set but with velocities that fall outside the range of the training set.

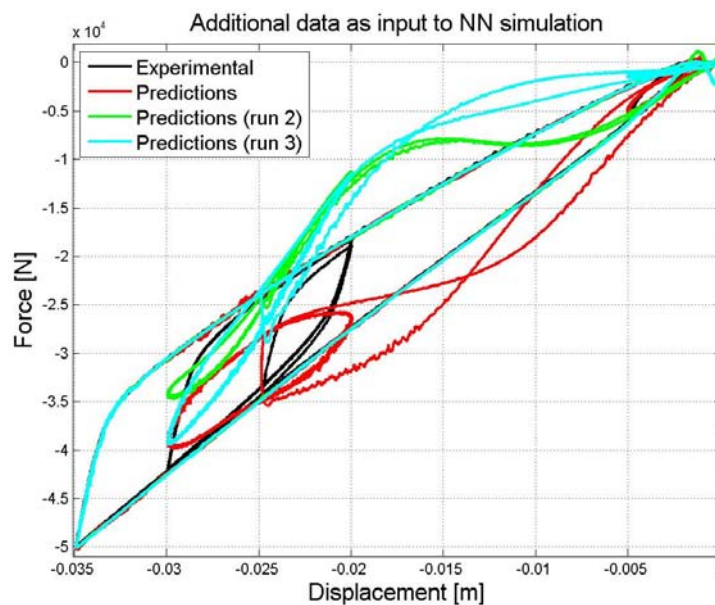


Figure 3.40. Results of 2-15-1 network when interpolating and extrapolating the input displacements

Figure 3.41 shows the results when the neural network is simulated with a displacement signal with a different frequency to that which was used during training. In this case the neural network has to extrapolate the excitation frequency. The dependency of the neural network on the excitation frequency seems to be due to the use of velocity as one of the inputs. Figure 3.42 shows the two inputs and the force output of the neural network. Note that the displacement, velocity and force time histories have been shifted such that the point where the loading direction on the spring changes from loading to unloading coincides. Figure 3.42(b) shows the difference between the velocities for the displacement signal having the same amplitude but different frequencies. It is interesting to note from Figure 3.42 that the force output from the neural network gives good results in the proximity where the time equals seven seconds. This is the moment where the loading on the leaf spring changes and the velocity is zero. At this point the velocity, for all the different excitation frequencies, is similar and therefore the force prediction of the network is good independent of the excitation frequency.

The results shown in Figure 3.41 clearly indicate the dependency of the neural network on the excitation frequency which is in contradiction to the behaviour of the physical leaf spring. It was shown in Chapter 2 that the force-displacement characteristic of the leaf spring is not

dependent on the excitation frequency. This observation seems to indicate that velocity may not be a good input to use in order to create a neural network that is able to emulate a multi-leaf spring.

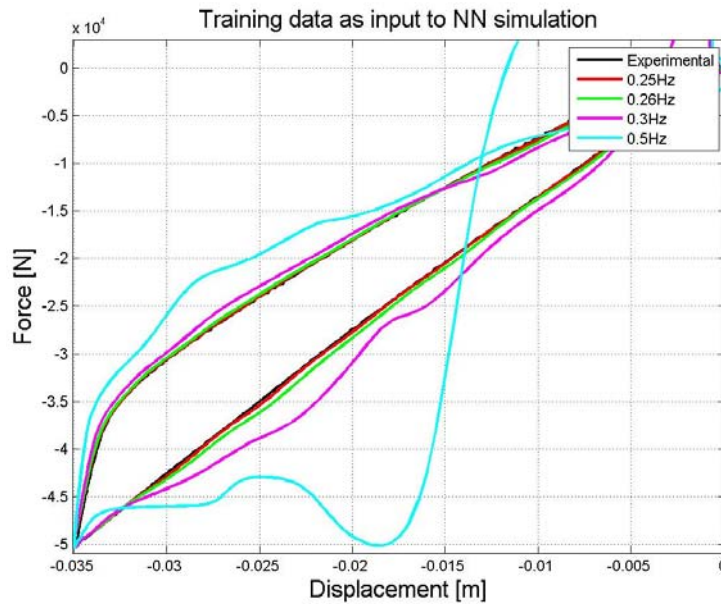


Figure 3.41. Results of 2-15-1 network when interpolating and extrapolating the input velocities

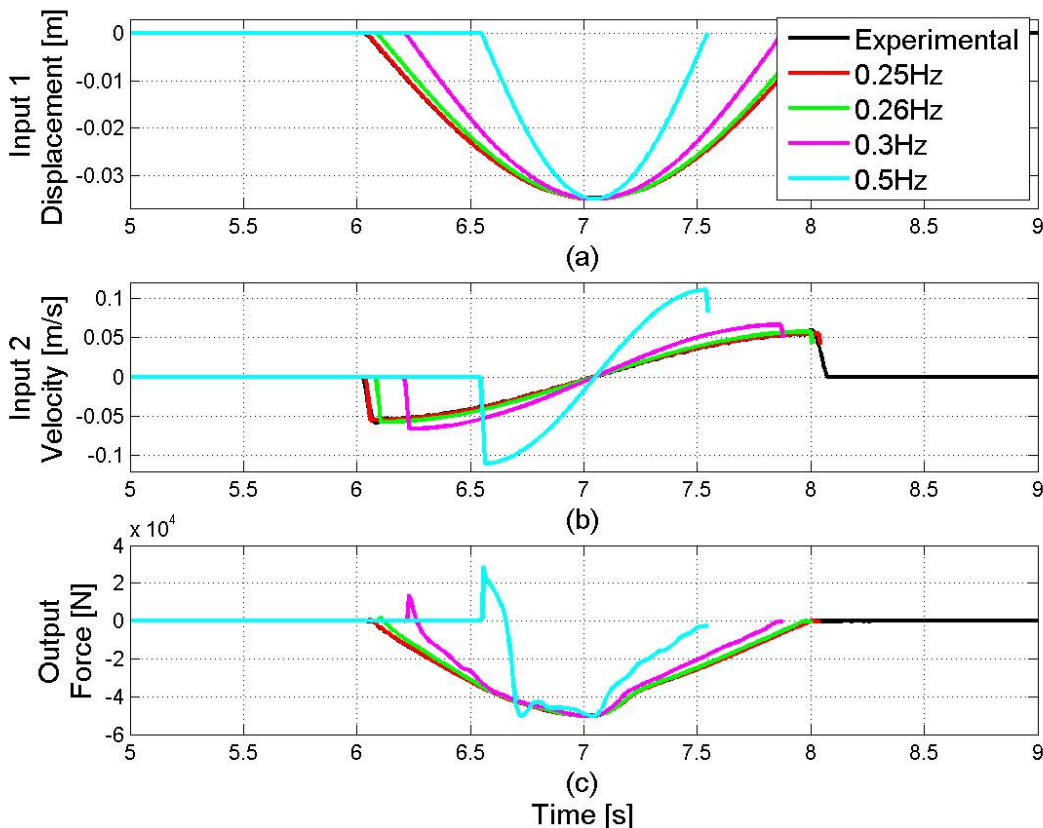


Figure 3.42. Inputs and Output of 2-15-1 network for displacement signal with different excitation frequencies

The results seem to indicate that the neural network model has difficulties in generalising the response of the leaf spring when given displacement and velocity inputs that are outside the range of the training set. Therefore, in order to train the neural network the characterisation of the leaf spring has to be done with displacement inputs consisting of all possible static load

and amplitude combinations at various frequencies. This will help to avoid the issues with generalisation. It may however not be economical to perform all the required experimental tests. Alternatively, the leaf spring can be characterised for the displacement and velocities that it will most probably encounter, or the neural network can be used as a gray-box instead of a black box. This implies that the neural network is used in conjunction with another model which generates all possible input-output data that could then be used to train the neural network. The elasto-plastic leaf spring model is one such model that can be used with the neural network. The elasto-plastic leaf spring model requires only the experimental data of the outer loop of the force-displacement characteristic to parameterise it. After it has been parameterised the elasto-plastic model can be used to generate the required training set which will ensure good generalization of the neural network.

The use of a neural network in emulating the leaf spring in Ghazi Zadeh *et al.* (2000) was mentioned earlier. They used a recurrent neural network with the displacement at the current time step, the deflection change and the force at the previous time step as inputs to network. They trained the neural network with a training set containing data over the entire working range of the variables which was generated by an analytical model. The neural network presented in this study is much simpler than the model they proposed with the network giving good predictions when trained with experimental data and simulated with inputs that fall within the range of the training set. The network can be used in a gray-box modelling approach, with the elasto-plastic model generating the required training data. Further investigation into the choice of inputs to the neural network and their effect on the ability of the neural network to generalize (interpolate and extrapolate) should be performed but lies outside the scope of this study. From the results obtained in this study it is postulated that the inputs to the neural network has the “intelligence” of the neural network and influences the generalization of the network. Well chosen inputs may improve the generalization of the neural network.

The 2-15-1 feed forward neural network is able to accurately emulate the vertical behaviour of the multi-leaf spring when using the four point moving average on the velocity input and a training set containing data over the entire working range of the inputs. The result of this network is shown in Figure 3.43 and shows good correlation with the experimental data. This neural network will be used further in this study.

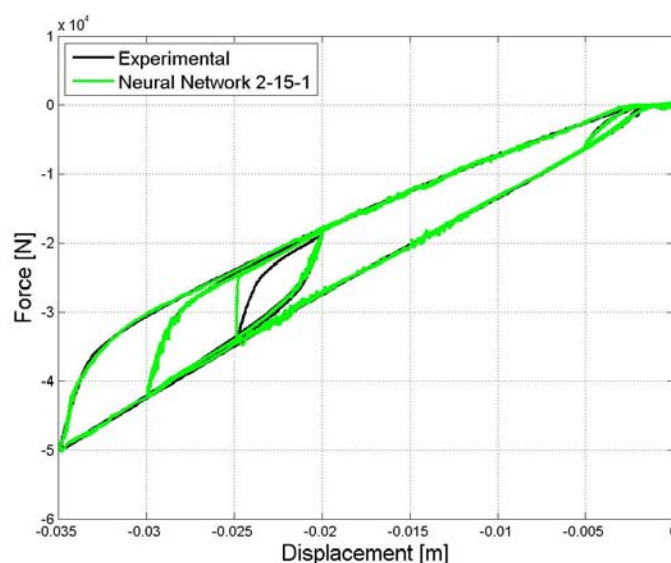


Figure 3.43. Results of the 2-15-1 feed forward neural network

6. Conclusion

This chapter was concerned with the modelling of the vertical behaviour of the leaf spring. A novel physics-based model was developed that is able to capture the complex nonlinear hysteric behaviour of the leaf spring. The capability of the elasto-plastic leaf spring model to represent both the multi-leaf spring and the parabolic leaf spring was shown. A simple modelling technique was also presented in order to capture the changes in stiffness of the leaf spring due to changes in the loaded length of the leaf spring. The non-physics based neural network approach was also investigated. It was found that the neural network was able to emulate the vertical behaviour of the leaf spring when trained with data over the entire range of the variables.

The next chapter will see the use of the elasto-plastic leaf spring model in creating a model of the simplified version of the suspension system used during the characterisation in Chapter 2. This is according to the systematic approach which sees an incremental increase in complexity of models with validation at each stage. A comparison between the accuracy and efficiency of the elasto-plastic and the neural network model of the multi-leaf spring will be shown in Chapter 5 after the modified percentage relative error validation metric has been introduced.

Chapter 4

Multi-leaf spring suspension system model

Following a systematic modelling approach the validated elasto-plastic leaf spring model from Chapter 3 will now be used to model the spring only setup. The spring only setup reduces the complexity of the suspension system of interest by reducing the number of components that may contribute in various ways. The spring only setup isolates the multi-leaf spring and by using this setup, as an initial check, it can be validated that the forces at the attachment points can be predicted accurately. After the spring only model has been validated additional detail can be added to the model by adding other components such as the radius rod and the hangers with the wear plates. This will result in the in-service setup used in Chapter 2 that considers the additional components but neglects the interaction between the left and right hand leaf springs. Once the model of the in-service setup has been validated the model can be extended to include the interaction between the left and right hand side to represent the complete suspension. The systematic modelling approach described above is shown in Figure 4.1. This chapter will consider the modelling and validation, with respect to the forces at the attachment points, of the spring only setup. The extension of the spring only model falls outside the scope of this study.

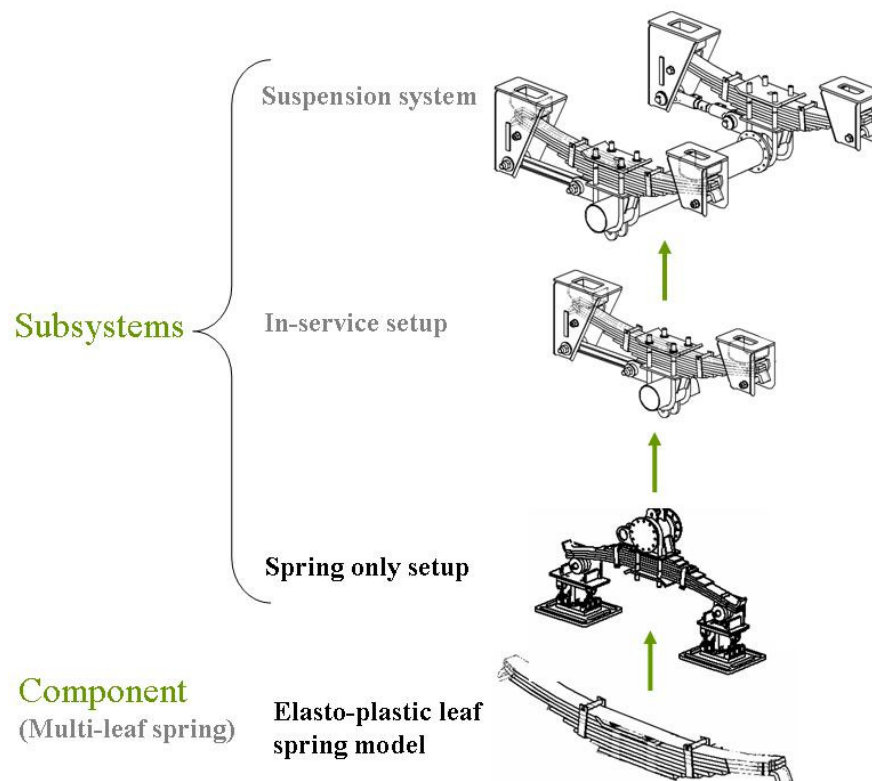


Figure 4.1. Systematic modelling approach

1. Introduction

Figure 4.2 shows the experimental spring only setup. The load cell between the actuator and the multi-leaf spring measures the spring force. The two 6clcs measure the forces that the leaf spring is transmitting to the chassis. These experimental measurements will be compared to the “measurements” taken on the simulation model which uses the 6clc model that was discussed in Appendix A. The model of the 6clc was created in ADAMS/Car to measure the equivalent forces and moments in the simulation environment in order to compare the virtual measurements to the physical measurements. The ADAMS/Car model of the 6clc was verified against analytical equations and both the analytical equations and the ADAMS/Car model was validated using experimental measurements. The verification and validation done on the 6clc is shown in detail in Appendix A. The validation results showed good correlation between the two models and the measured data when the experimentally calculated force orientation and application point was used as input to the two models. Four load cases were used to validate the 6clc models and good correlation was obtained for all the equivalent forces and for all four load cases used. From the results in Appendix A it was concluded that the ADAMS/Car model of the 6clc can be used to measure the equivalent forces and moments in the simulation environment and these virtual measurements can be compared to the physical measurements. Comparing the 6clc measurements from the experiment and from the model it can be validated whether the forces at the attachment points are accurately predicted.

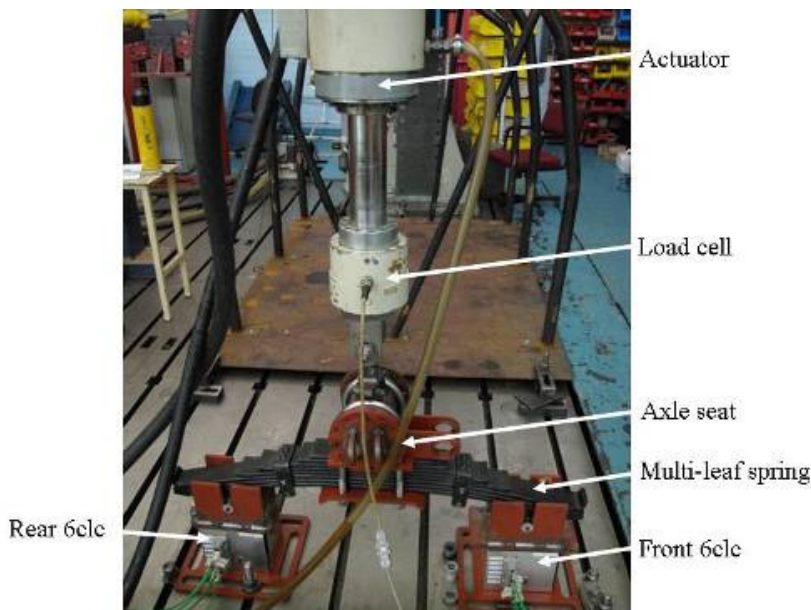


Figure 4.2. Spring only setup

The modelling approach that will be used to create a model of the spring only setup is indicated in Figure 4.3. The kinematics of the suspension system is solved in ADAMS which sends the displacement of the spring to the elasto-plastic leaf spring model in MATLAB via SIMULINK. SIMULINK is used to calculate the forces induced by the spring on the hangers. These forces are then applied to the model in ADAMS to determine the displacement at the next time step. This process is repeated for the duration of the displacement that is applied to the axle seat by the actuator. Paragraph two in this chapter will discuss the modelling of the spring only setup with the validation results presented in paragraph three.

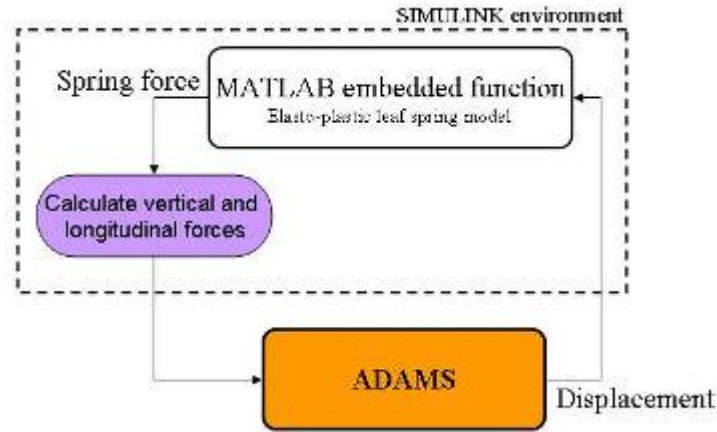


Figure 4.3. Co-simulation data flow between SIMULINK and ADAMS

2. Modelling of the spring only setup

The model of the spring only setup shown in Figure 4.4, with the exception of the multi-leaf spring, is simple. The modified hangers are connected to the front and rear 6clc with fixed joints. The modified hangers refer to the hangers having bearings that support the leaf spring instead of wear plates, found in the normal hangers. The 6clcs used in the model were modelled, verified and validated as discussed in Appendix A. The axle seat is connected via a link (geometry not included in Figure 4.4) and a revolute joint to the actuator. The axle seat is connected to the modified hangers via the ADAMS/Car leaf spring subsystem. This subsystem sends its displacement to SIMULINK and receives back the spring force (see Figure 4.3). It is also the ADAMS/Car subsystem of the leaf spring that regulates the motion between the axle seat and the modified hangers.

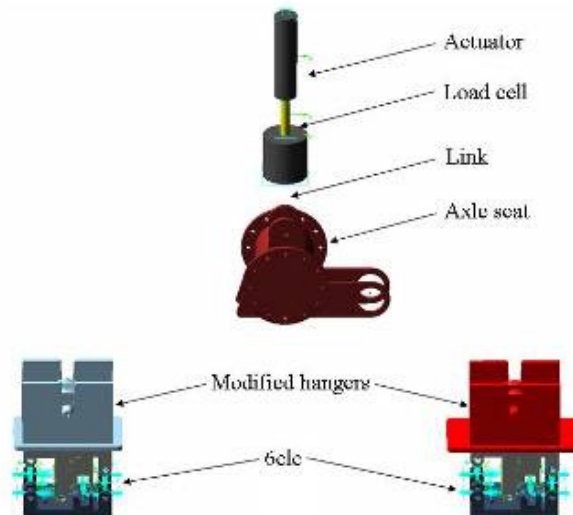


Figure 4.4. ADAMS/Car model of spring only setup

2.1. ADAMS/Car leaf spring model

The ADAMS/Car leaf spring model integrates the elasto-plastic leaf spring model into ADAMS/Car such that it can be used as a subsystem. Several of these subsystems can easily be included later in a vehicle model as required. Different models for the leaf spring was created in ADAMS/Car starting with the simplest one that calculates only the vertical force

acting on the supports which is induced by the leaf spring when it is deflected. The following paragraphs describe the different models of the ADAMS/Car leaf spring model.

2.1.1. ADAMS/Car leaf spring Model 1

This model only considers the vertical movement and the vertical forces of the spring. To achieve this motion, a translational joint is placed between the axle seat and the front modified hanger to allow only the vertical translational degree of freedom of the axle seat. It should be noted that the use of the translational joint when a longitudinal force acts on the axle seat becomes inaccurate. When this suspension model is to be used in simulations where a longitudinal force is imposed on the axle seat (such as in braking simulations or in durability simulation with high obstacles) the use of the translational joint has to be reconsidered. The ADAMS/Car leaf spring model calculates the displacement of the spring and sends this to the elasto-plastic leaf spring model which is implemented in SIMULINK as an embedded MATLAB function. The elasto-plastic leaf spring model then solves for the spring force (F_s). Before the spring force is send back to ADAMS, the vertical forces acting at the front (F_{zR}) and rear (F_{zF}) hanger interface points (see Figure 4.5) are calculated. F_{zR} and F_{zF} are calculated by using Equation {4.1} and Equation {4.2}. Equation {4.1} and Equation {4.2} are obtained by simultaneously solving the equation of the sum of forces in the z-direction and the sum of moments taken about the axle seat.

$$F_{zF} = -\frac{l_r F_s}{l_r + l_f} \quad \{4.1\}$$

$$F_{zR} = -\frac{l_f F_s}{l_r + l_f} \quad \{4.2\}$$

The ADAMS model uses two point-point actuators which are placed between the axle seat and the front and rear hangers. The two point-point actuators are controlled by the forces F_{zR} and F_{zF} , respectively. The resulting force on the axle seat is the spring force F_s .

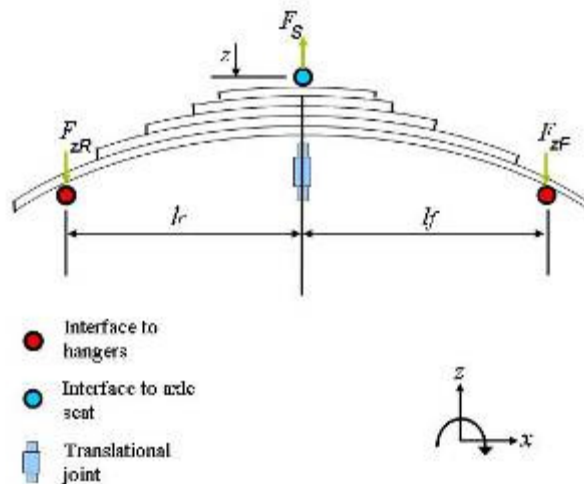


Figure 4.5. Schematic representation of ADAMS/Car leaf spring Model 1

2.1.2. ADAMS/Car leaf spring Model 2

This model includes both the vertical and longitudinal forces acting at the hanger interface points (see Fig. 4.6). The translational joint between the axle seat and front hanger limits the motion to only the vertical direction. As was mentioned in paragraph 2.1.1 the use of the

translation joint when longitudinal forces act onto the axle seat should be reconsidered as this may cause inaccuracies. This model calculates the vertical forces (F_{zR} , F_{zF} , F_s) in exactly the same way as Model 1. Due to the translational joint this model exerts no longitudinal force on the axle seat. The longitudinal forces acting on the front (F_{xR}) and rear (F_{xF}) hangers are sent to ADAMS from SIMULINK and implemented in ADAMS as two point-point actuators placed between ground and the front and rear hangers, respectively.

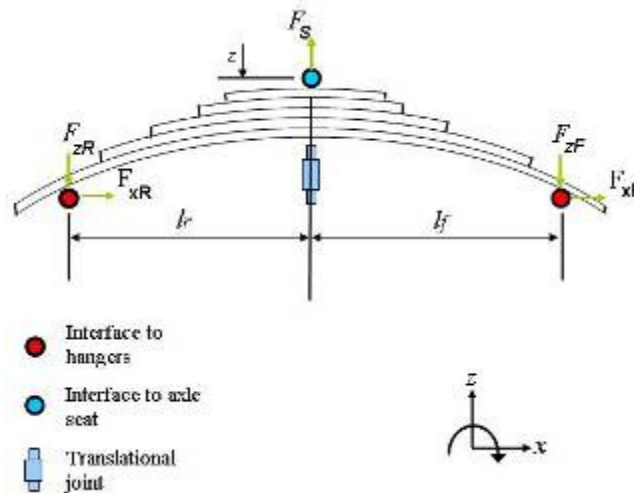


Figure 4.6. Schematic representation of ADAMS/Car leaf spring Model 2

The longitudinal forces F_{xR} and F_{xF} are simply calculated by taking the vertical forces (F_{zR} and F_{zF}) and relating them to the longitudinal forces (F_{xR} and F_{xF}) via the slope of the leaf spring at the point of contact between the leaf spring and the bearings. The assumption is made that the contact between the leaf spring and the bearing consists of a thin line. Figure 4.7 shows the forces acting at the point of contact between the leaf spring and the bearing. When we know the vertical forces (F_{zR} and F_{zF}) and the angle of the slope (α) we will be able to calculate the longitudinal forces (F_{xR} and F_{xF}). The vertical forces are obtained from the leaf spring model, whereas the angle of the slope is calculated by relating it to the deflection of the leaf spring.

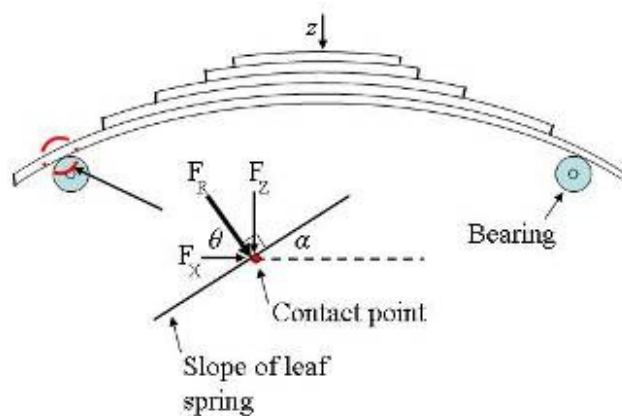


Figure 4.7. Forces at point of contact

The angle of the slope (α) of the leaf spring at the point of contact with the bearing is related to the deflection of the leaf spring (z) as follows. Table 4.1 and Table 4.2 shows the angles of the slope calculated from the experimentally measured deflection shapes of the leaf springs at three deflections for the front and rear contact points. The experimental setup and

measurements of the deflection shapes were given in paragraph 2.1.2.2, Chapter 2. The deflection shape of the leaf spring at the normal position is given again here in Figure 4.8. In the figure it is indicated where the deflection at the three vertical loads, shown in Table 4.1 and Table 4.2, were obtained from.

Table 4.1. Angle of slope at front contact point

Vertical load [N]	Deflection (z) [m]	Angle of slope (α) [deg]
0	0	19.3
25.9	-0.016	14
51.9	-0.032	8.5

Table 4.2. Angle of slope at rear contact point

Vertical load [N]	Deflection (z) [m]	Angle of slope (α) [deg]
0	0	18.4
25.9	-0.015	14
51.9	-0.030	9.46

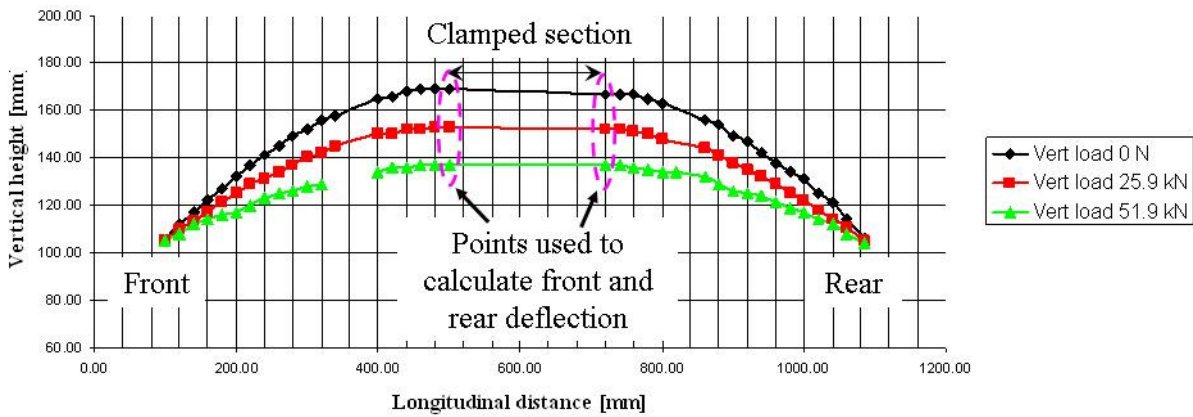


Figure 4.8. Deflection shape of the spring for the normal position

The values in Table 4.1 and Table 4.2 seem to have a linear relationship when viewed graphically. Therefore, the relationship between the angle of the slope and the deflection of the leaf spring can be given by Equation {4.3} and Equation {4.4} for the front and rear contact points, respectively.

$$\alpha_f = 337.5z + 19.3 \quad \{4.3\}$$

$$\alpha_r = 298z + 18.4 \quad \{4.4\}$$

The difference between the front and rear relationship between the angle of the slope and the deflection of the leaf spring may be due to the following possible cause. In this setup the lengths between the axle seat and the front and rear hangers (l_r and l_f) are not equal. Because the lengths (l_r and l_f) are different, the supports makes contact at a different longitudinal position on the leaf spring which means it is at a different part of the geometrical shape of the leaf spring. This implies that when the leaf spring has no vertical load on the leaf spring the clamped section of the spring will not be horizontal. As was observed in Figure 4.8. The front contact point is further away from the symmetry plane of the leaf spring than the rear contact point. This implies that the front and rear contact points are located on the leaf spring's geometrical shape such that it tends to tilt it clockwise (when viewing the spring in the

orientation in Figure 4.8). This leads to the rear points that are used to calculate the deflection of the leaf spring, as indicated in Figure 4.8, to seem more deflected than the points used at the front. It can also be noted that as the vertical load is increased the difference in deflection of the front and rear points decreases. The relationship between the angle of the slope, at the front and rear contact points, and the deflection of the leaf spring have been established and presented as Eq.{4.3} and Eq.{4.4}. With the relationship between the angle of the slope and the deflection of the leaf spring known the relationship between the longitudinal and vertical forces at the front and rear contact points can now be determined.

From $\theta = 90^\circ - \alpha$ and $\tan \theta = \frac{F_z}{F_x}$ we can obtain Equation {4.5} and Equation {4.6} which calculates the longitudinal force given the vertical force and deflection of the leaf spring.

$$F_{xF} = \frac{F_{zF}}{\tan(70.7^\circ - 337.5z)} \quad \{4.5\}$$

$$F_{xR} = -\frac{F_{zR}}{\tan(71.6^\circ - 298z)} \quad \{4.6\}$$

3. Validation of the spring only model

The model of the spring only model will now be validated against experimental measurements. The spring only model will be used with both ADAMS/Car leaf spring models that were discussed in the previous paragraph. The validation results using Model 1 and Model 2 of the ADAMS/Car leaf spring subsystem model is shown in the following two paragraphs.

3.1. Validation of the spring only model using Model 1

This paragraph presents the qualitative comparisons between the experimental measured data and the predicted data for the spring only setup using Model 1. Figure 4.9 shows the correlation between the measured and predicted spring force of the spring only setup. The correlation achieved is good and we could conclude that the model is an accurate representation of the physical system. However when we consider the equivalent forces and moments as measured by the two 6clcs it tells a different story. As expected the longitudinal and lateral forces measured by the 6clcs in the model measures zero (see Figure 4.10). This is due to the way this model was constructed. The vertical force shows good correlation when compared to the experimental data. It should be rather obvious that this should be the results for the forces at the attachment points, but it may have been neglected if the model was only validated against the spring force. This clearly shows the importance of correct model validation as discussed in Kat and Els (2011).

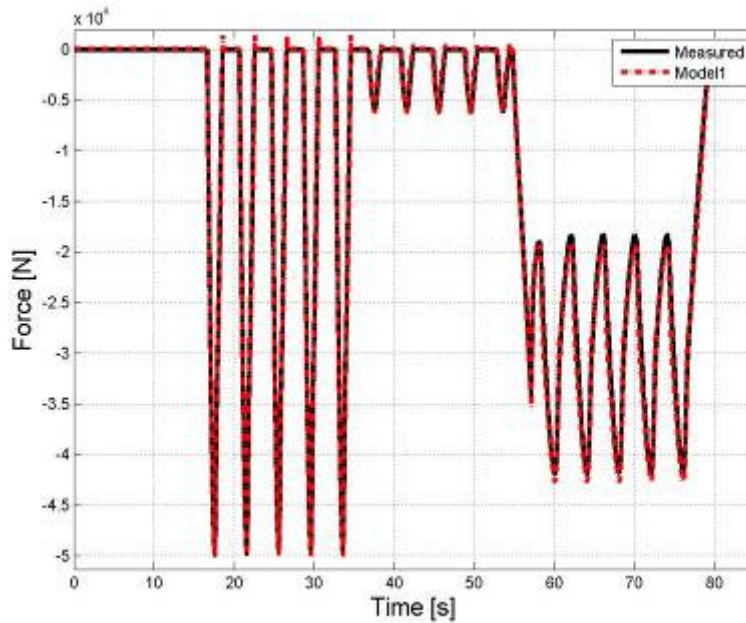


Figure 4.9. Comparison of measured and predicted spring force for the spring only setup using Model 1

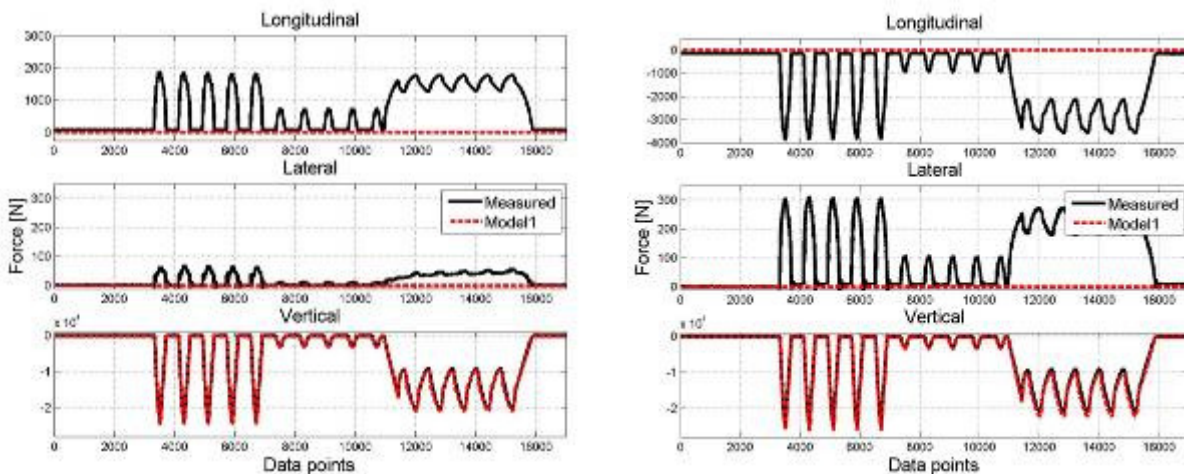


Figure 4.10. Equivalent forces measured by front (shown left) and rear (shown right) 6clcs

Figure 4.11 shows the correlation of the equivalent moments measured by the two 6clcs. It can be observed from this figure that all three moments from the model is zero. This is because the vertical force that the leaf spring imposes on the hanger acts at the centre of volume of the 6clc and thus does not induce any moments. However, the experimental measurement does indeed show that moments are induced, this is because in the experimental setup the vertical force from the leaf spring does not act exactly at the centre of volume. It is also true that in the experimental setup there is not only a vertical force imposed on the hanger but also longitudinal and lateral forces. Figure 4.11 may also indicate that there exists a discrepancy between the model and the experimental setup's points where the force acts on the hanger. The comparison of the equivalent vertical force in Figure 4.10 suggests that the vertical force is indeed predicted accurately, but the correlation of the equivalent moments (in Figure 4.11) and the correlation of the forces in the uni-axial load cells (in Figure 4.12) suggests that the application point of the vertical force, imposed by the leaf spring on the hanger, is not the same between the experimental setup and the model. Only the forces measured in the uni-axial load cells that are orientated in the vertical direction were shown (Figure 4.12). Due to the way this model was constructed the forces in the uni-axial load cells,

measured by the 6clc in the longitudinal and lateral direction, are zero and therefore was not presented.

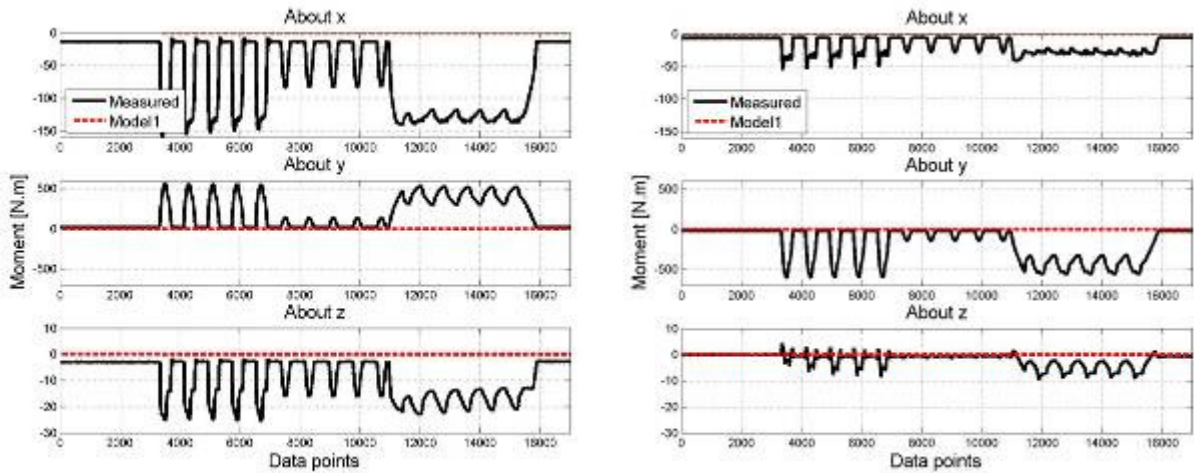


Figure 4.11. Equivalent moments measured by front (left) and rear (right) 6clcs

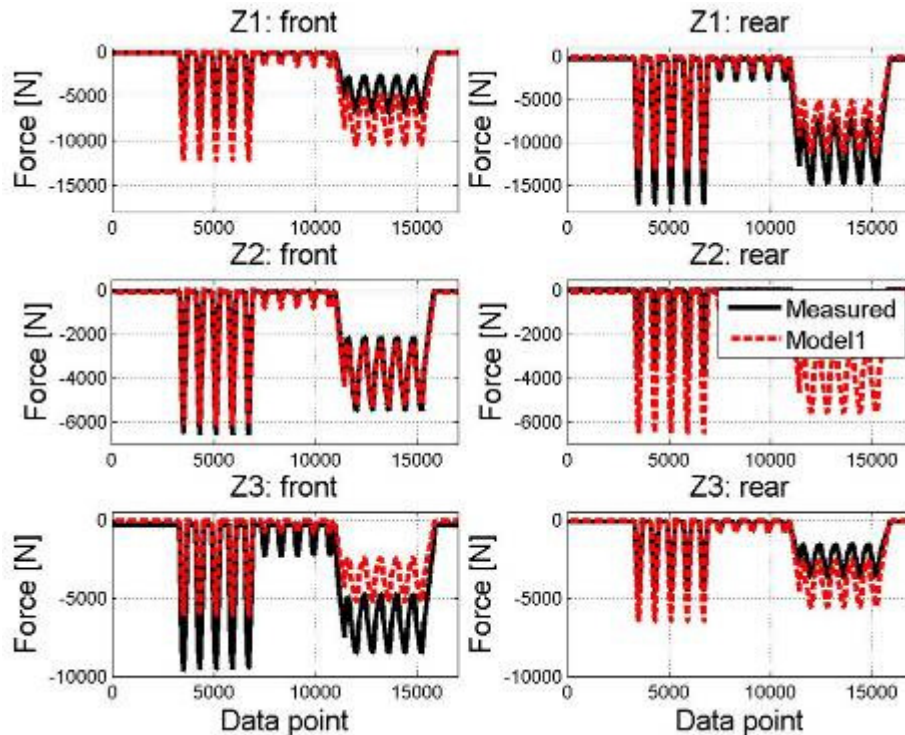


Figure 4.12. Reaction forces measured by front (left) and rear (right) 6clcs

3.2. Validation of the spring only model using Model 2

This paragraph presents the qualitative comparisons between the experimental data and the predicted data for the spring only setup using Model 2. From Figure 4.13 we observe a significant improvement in the longitudinal forces. The correlation of the longitudinal forces at the rear 6clc is good with the longitudinal forces of the front 6clc predicted by Model 2 being higher. Figure 4.14 shows the equivalent moments at the front and rear 6clcs. The model only predicts moments about the y-axis whereas the experimental measurements show moments about all three axis. This may be due to either the resultant force acting on the hanger being incorrect and/or that the application point is incorrect. From the comparisons of

the equivalent force, in Figure 4.13, and the longitudinal and vertical uni-axial load cell forces (Figure 4.15 and Figure 4.16) we can see that we have a discrepancy in the orientation and the application point of the resultant force. The discrepancy in the orientation of the resultant force can be observed from Figure 4.13. The discrepancy in the application points of the front and rear hangers are more difficult to observe. If the three equivalent forces were predicted accurately any difference between the measured and predicted equivalent moments and reaction forces will then indicate that the application point is not correct. In this case the equivalent forces are not predicted accurately, mainly because the lateral forces are ignored by the model, and the equivalent moments do not show good correlation and we therefore have the situation that the discrepancy is due to a combination of the orientation and application point of the resultant force not being entirely accurate.

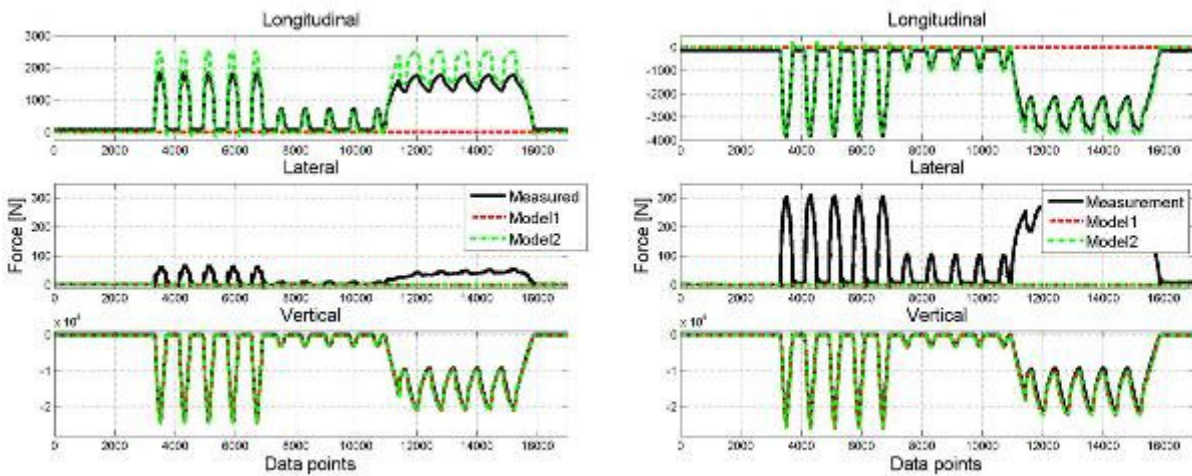


Figure 4.13. Equivalent forces measured by front (shown left) and rear (shown right) 6clcs

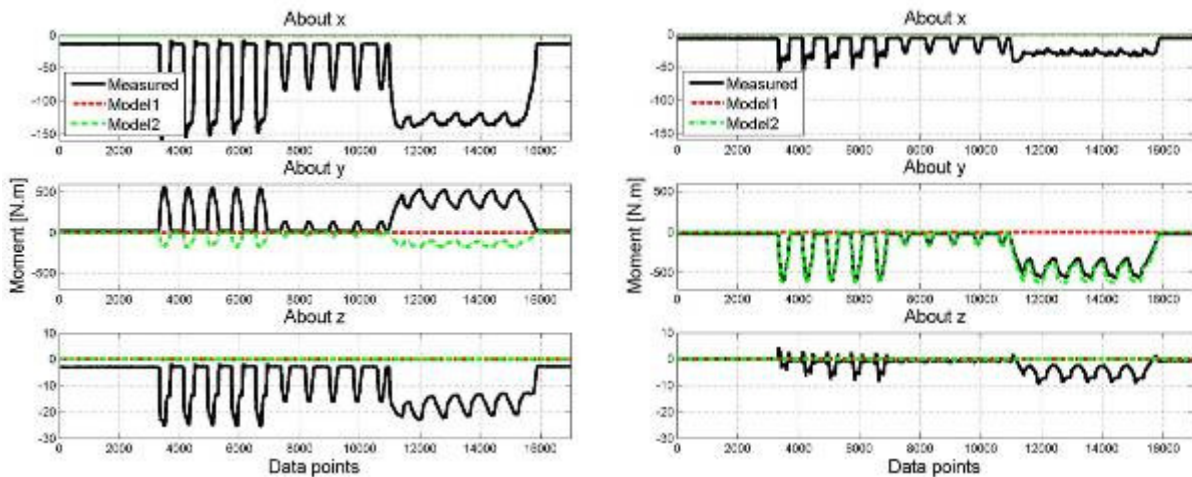


Figure 4.14. Equivalent moments measured by front (left) and rear (right) 6clcs

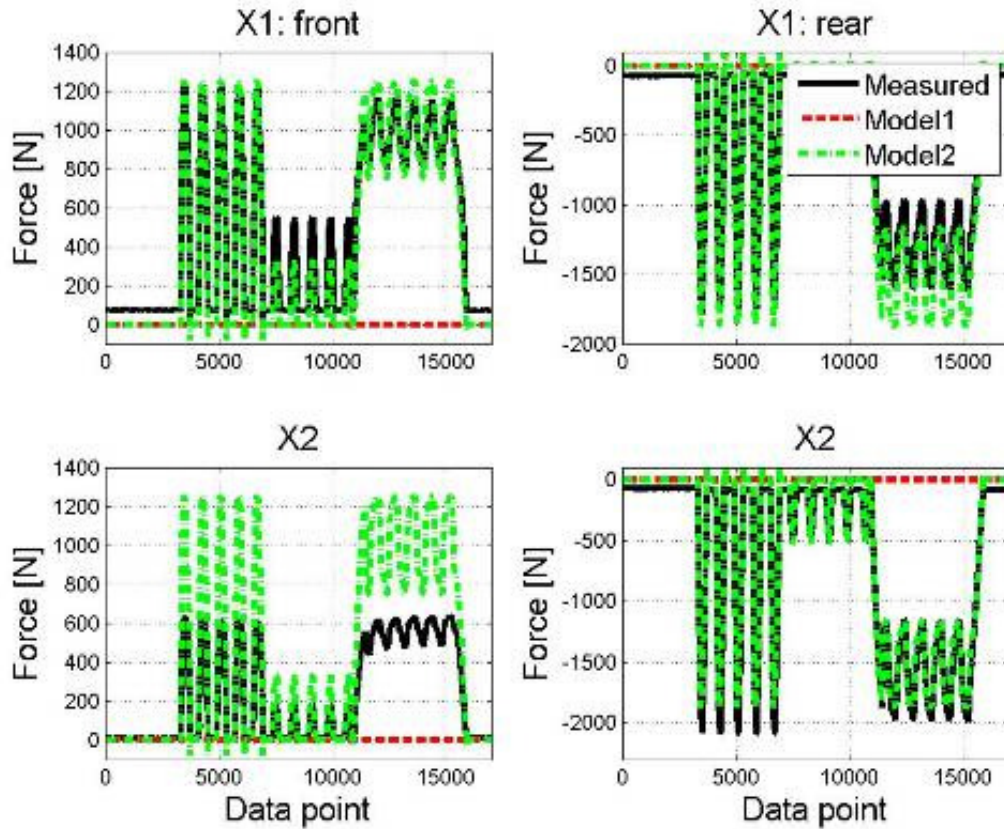


Figure 4.15. Reaction forces in longitudinal direction measured by front and rear 6clcs

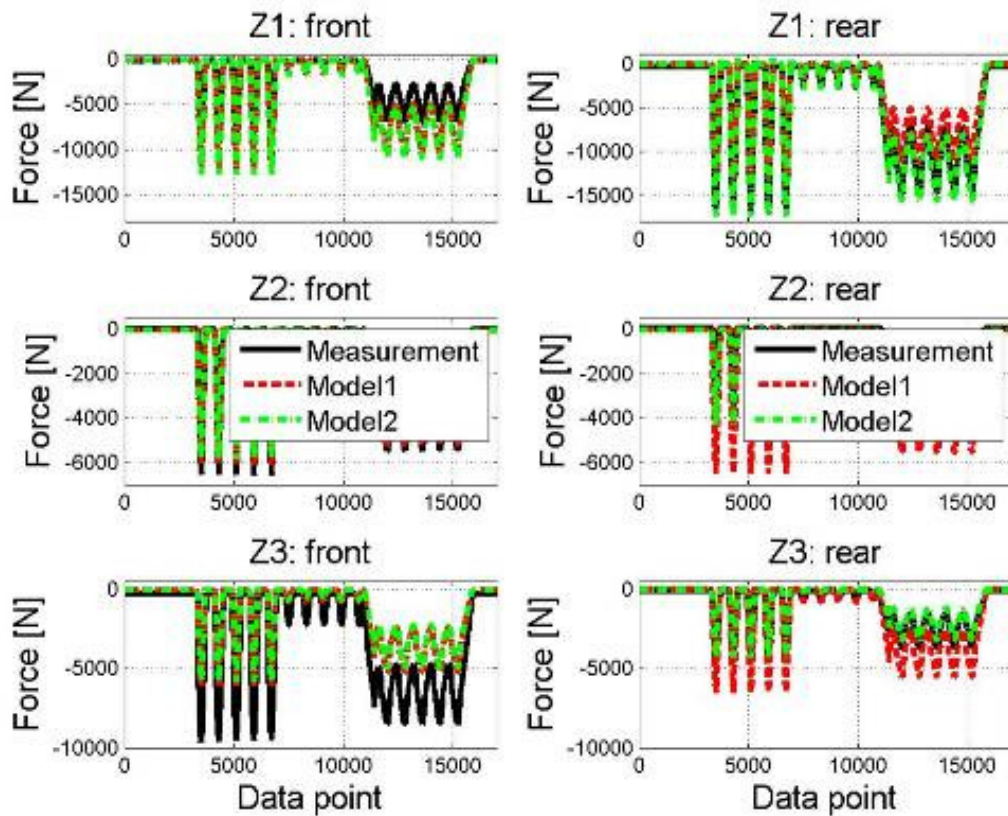


Figure 4.16. Reaction forces in vertical direction measured by front and rear 6clcs

4. Conclusion

The elasto-plastic leaf spring model from Chapter 3 was integrated into two ADAMS/Car models which were used to model the spring only setup. One of the two models only considered the vertical forces at the hanger attachment points (Model 1) with the other model considering both the vertical and longitudinal forces at the hanger attachment points (Model 2). The validation results indicate that Model 2 gives better predictions than Model 1. Both models give good predictions of the vertical equivalent force. The spring only model using Model 2, which included the longitudinal forces, is able to predict the longitudinal forces. The validation results showed good correlation for the longitudinal and vertical forces but it is clear from the validation results that the model of the spring only setup needs some refinement. The most probable cause for the discrepancies may be due to an incorrect application point of the resultant force to the two hangers. As mentioned, the use of the translational joint has to be reconsidered when this suspension model is to be used in simulations where a longitudinal force is imposed on the axle seat (such as in braking simulations or in durability simulation with high obstacles)

The validation results obtained for the spring only setup showed good correlation which can be improved by refining the model. The refinement of the spring only model as well as the extension of the model to include additional components in order to create an accurate model of the in-service setup, and ultimately, a model of the complete suspension system, will not be addressed in this study. The extension of the spring only model to the models shown in Figure 4.1 will be the subject of future work. Instead we will turn our focus to the verification and validation process in the next chapter. All the models that were created in this study were validated against experimental data. A qualitative validation procedure was followed by which superimposed graphical plots of the data were interpreted. The following chapter will discuss the verification and validation process as well as investigate the use of quantitative validation methods which are less subjective than the qualitative methods used.

Chapter 5

Verification and Validation

Engineers develop mathematical models to emulate various physical systems. The model can be as simple as a linear spring or as complex as a full vehicle. However simple or complex the mathematical model may be, the engineer needs to evaluate the mathematical model and decide whether the mathematical model does indeed emulate the physical system accurately. This is generally done by comparing the data qualitatively and/or quantitatively. The data consists of two sets i.e. the data containing the experimental measurements obtained from the physical system and the data predicted by the model emulating the physical system. Generally, the measured data is considered to be true and the predicted data considered to be an approximation. Measurement uncertainties are dealt with in different ways but will not be covered in this study. Qualitative comparisons are usually done by graphically comparing the superimposed plots of the two data sets. This qualitative method was used in the previous chapters to compare the predictions of the models to the experimental data. The conclusion drawn from a qualitative comparison is very subjective. A quantitative comparison aims at obtaining a conclusion that is more objective. This chapter will investigate the use of quantitative methods in order to perform more objective comparisons during the validation process. Although this study will focus more on the validation process, an overview of the verification and validation (V&V) process will briefly be discussed in order to understand the purpose of validation.

1. Introduction

As already mentioned, mathematical and computer modelling have been playing an increasingly important role in the computer aided engineering (CAE) process in the last 60 years. Simulation offers great advantages in the development and analysis phase of products and offers a faster, better and more cost effective way than using physical prototypes alone. Engineers develop mathematical models of varying complexity to emulate various physical systems. The engineer needs to evaluate the mathematical model and decide whether the model does indeed represent the physical system to an acceptable level of accuracy. Therefore, in order to obtain meaningful simulation models it is necessary to verify and validate them. The need for a formal validation method for quantifying the accuracy of simulation models emulating physical systems has become increasingly important with the greater reliance on the CAE process during product development. The drive for a formal validation method is fuelled by the need for obtaining simulation models which satisfy accuracy requirements, and can be used with confidence to base key engineering and business decisions on.

The verification and validation process is an important part of any model that is created to emulate physical events and engineering systems. Oberkampf and Barone (2006) state that

“the terms verification and validation have a wide variety of meanings in the various technical disciplines”. Similarly Babuska and Oden (2004) state that “the broad interest in V&V in many different scientific areas has led to a diverse and often incompatible list of definitions and concepts as it pertains to different disciplines. Moreover, despite the fact that modern views of the subject have been under development for nearly a decade, much remains to be done toward developing concrete approaches for implementing V&V procedures for particular applications”. Oberkampf and Barone (2006) refer to work that played a major role in attempting to standardize the terminology within the engineering community. Similarly, a committee was formed known as the ASME Committee for Verification and Validation in Computational Solid Mechanics whose purpose is to develop standards for assessing the correctness and credibility of modelling and simulation in computational solid mechanics. This committee released a guide for the verification and validation in computational solid mechanics (ASME standards, 2006). They give the following definitions for verification and validation:

- Verification* - The process of determining that a computational (or simulation) model accurately represents the underlying mathematical model and its solution.
- Validation* - The process of determining the degree to which a model is an accurate representation of the real world from the perspective of the intended uses of the model.

Figure 5.1 gives an overview of the V&V process and the tasks associated with the process. The two primary elements of a V&V process are 1) the physical system of interest and 2) the mathematical (or simulation) model that is created to emulate the physical system. An experimental setup of the physical system is constructed in task (a) from which the experimental data is obtained. In task (b) measurements or analysis (e.g. Computer Aided Design (CAD)) are made on the physical system in order to obtain the properties and parameters of the physical system, such as mass, mass moments of inertia, etc, which are required as inputs into the mathematical model. The path from the conceptual model to the simulation model is shown as well as the stages where the code and calculation verification is performed. With the simulation model verified it can be used to generate the simulation data. From the experimental data and the simulation data the system response quantity (SRQ) of interest can be obtained. The measured system response quantity (SRQ^m) is obtained from the measurements on the physical system and the predicted system response quantity (SRQ^p) is obtained from the predictions of the model. The measured and predicted SRQs are the required inputs into the validation process.

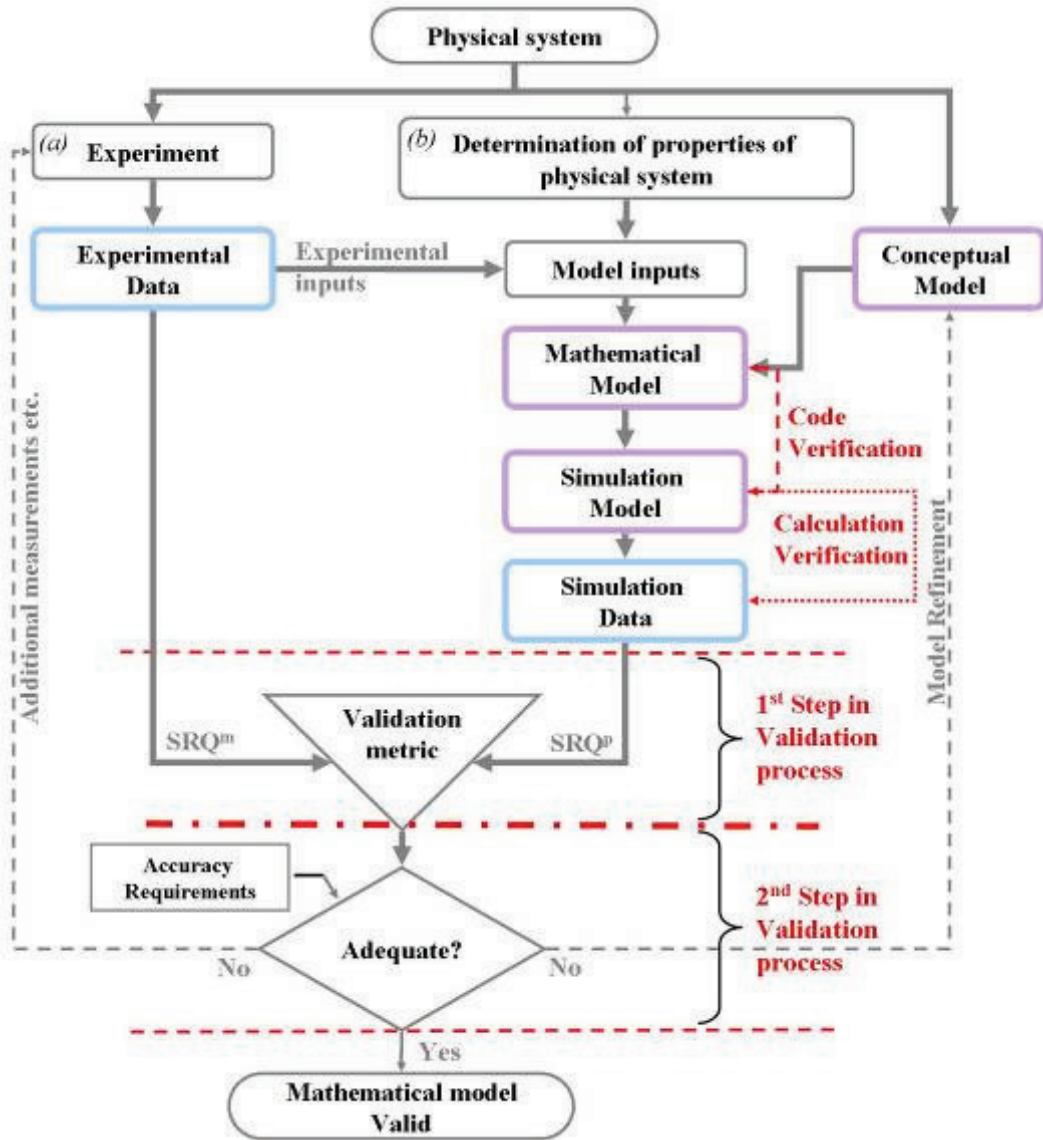


Figure 5.1. Overview of Verification and Validation process

Various uncertainties exist that will affect both the measured and predicted SRQs. Roy and Oberkampf (2011) categorizes the sources of uncertainty in the simulation model broadly into uncertainty occurring in the model inputs, in the numerical approximations or in the model form. Similarly, uncertainty may exist in the measurements taken during the experiment due to measurement errors. These measurement errors may arise from various elements such as for example the individual measuring instruments. The characterization of the numerical approximation errors associated with a simulation is called verification (Roy and Oberkampf, 2011). Verification is composed into two fundamental activities in the ASME standards (2006) i.e. code verification and calculation verification, and is indicated in Figure 5.1. Roy and Oberkampf (2011) state that the characterization of the model form uncertainty is estimated during the validation process. The uncertainty quantification in the experimental measurements and in the simulation model is outside the scope of this study. Therefore, both the measured and predicted SRQs considered in this study are deterministic. The reader is referred to Oberkampf and Barone (2006), Roy and Oberkampf (2011) and Figliola and Beasley (2006) for more detail on uncertainties.

With the SRQs from the experimental and simulation model obtained, the validation process can commence. The validation process can be divided into two steps (Oberkampf and Barone, 2006). The first step is the quantitative comparison of the measured and predicted SRQs. The measured and predicted data can however also be compared qualitatively by superimposing them on graphs but the subjective conclusions on the correlation of bad, good or excellent makes quantifying the accuracy very difficult. Qualitative validation may be useful in certain scenarios, especially in identifying possible causes of errors in the model, but its inability to give a quantitative measure of the agreement/disagreement between the experimental and simulated data makes it difficult to use in determining whether the accuracy requirements are satisfied (2nd step of the validation process). Quantitative comparisons attempt to circumvent the limitations of qualitative comparisons. Quantitative comparisons consist of comparing defined error measures or error metrics (validation metrics). Sarin *et al.* (2010) makes the following distinction between an error measure and an error metric: “An error measure provides a quantitative value associated with differences in a particular feature of time series. An error metric provides an overall quantitative value of the discrepancy between time series; it can be a single error measure or a combination of error measures”. The error measures to be used are chosen by the engineer and will vary depending on the data. Examples of error measures are steady state gains, response times, peak response times, percent overshoot for time domain data and peak frequency, peak amplitude ratio and phase angle for frequency domain data (Heydinger *et al.*, 1990). Heydinger *et al.* (1990) states however that certain data will not lend itself to the identification of such error measures. Instead of defining error measures of certain features of the data, the measured and predicted data can be compared by using error metrics (or validation metrics) which do not require the extraction of specific features in the data. The validation metric (or measure of comparison) attempts to give an overall measure of the comparison between the data being compared. Validation metrics will be discussed in paragraph 2. It is the author’s opinion that both quantitative and qualitative comparisons of measured and predicted responses are useful to employ. During model refinement and fault-finding, qualitative comparisons can supply the modeller with valuable information and may give much more insight into the possible causes for the deviation than a validation metric. However, in determining whether the model is valid or not, the qualitative comparisons should be substituted with a quantitative comparison method.

The second step of the validation process shown in Figure 5.1 is concerned with determining whether the results obtained from the quantitative validation metric satisfies the accuracy requirements. When the result of the validation metric satisfies the accuracy requirements the model can be considered to be valid. Alternatively, it may be that the validation metric gives results that do not satisfy the accuracy requirements. Depending on the reason for the accuracy requirements not being met one of the two dash-line paths shown in Figure 5.1 can be taken. Either better/more experimental data may be required or the model needs to be refined.

Although validation is essential in assuring that the model is valid, validation does have some shortfalls and the engineer should be aware of them and should try to avoid them. Various studies (Ferry *et al.* (2002), Edara *et al.* (2005) and Cosme *et al.* (1999)) validated models against certain parameters and then used them to predict others. For example, a vehicle model is developed for durability analysis but is only validated against accelerations. This approach may have certain risks involved such as stated in Bernard and Clover (1994). They use the example of a vehicle doing a severe J-turn with the assumption that the measured yaw rate and lateral acceleration are available from vehicle tests, but measured normal loads on the tyres are not. They compare the simulated yaw rate and lateral acceleration of two models of the same vehicle with the difference being that the centre of gravity height of one of the

models is 10% higher. Comparing the yaw rate and lateral acceleration the models seem to give similar results, but comparing the lateral load transfer it becomes clear that there is some discrepancy between the two models. The importance of validating the model for the correct parameters is also shown in Kat and Els (2011).

The focus in this study will be on the validation process and more specifically on the first step of the validation process concerned with the validation metric. The reader is referred to Babuska and Oden (2004), Oberkampf and Trucano (2002) and ASME standards (2006) for further details on the complete V&V process. The rest of this chapter will be concerned with the development and evaluation of a quantitative validation metric based on relative error for use in the first step of the validation process. Of primary interest will be quantifying the agreement/disagreement between SRQs that are periodic in nature with a combination of many frequencies that may or may not oscillate around zero. An example of a SRQ that exhibits behaviour as described above is an acceleration measurement on a vehicle driving over a discrete bump or the accelerometer measurements on a vibrating beam. In this study deterministic SRQs with time as the independent variable will be compared.

2. Quantitative validation metrics

A quantitative validation metric should be able to provide a measure that quantifies the overall error (or agreement/disagreement) between two sets of data, for example between measured and predicted data. In the context of the validation process we would like the validation metric to quantify the level of agreement/disagreement of the model with respect to the physical system in order to conclude whether the model satisfies the accuracy requirements and can be considered valid for the intended use. The validation metric's result should be an easily interpretable value that can be used to determine whether the agreement between the physical system and model satisfies the accuracy requirements.

Although many different error measures and validation metrics can be found in the literature for quantitatively comparing SRQs with time as the independent variable, not many studies concerning validation of simulation models make use of them. Rather the validation is done qualitatively with subjective conclusions such as the correlation is good, excellent or fair. This begs the question: Why are these measures not used? Do they give engineers physically meaningful and interpretable results? In an attempt to answer these questions, a literature survey was conducted in order to form an idea of the measures and metrics available, their capabilities, limitations and whether they give physically meaningful and easily interpretable results in order to determine whether or not the model satisfies the accuracy requirements.

2.1. Literature survey

Oberkampf and Barone (2006) divide traditional quantitative comparison approaches into three categories:

- i) Techniques developed by structural dynamists for assessing agreement between computational and experimental results as well as techniques for improving agreement. These techniques are known as parameter estimation, model parameter updating or system identification.
- ii) Hypothesis testing or significance testing.
- iii) Bayesian analysis or Bayesian statistical inference.

Oberkampf and Barone (2006) mentions the following on the approaches used in the three categories:

- i) “Although these techniques are used to compare computational and experimental results, their primary goal is to improve agreement based on newly obtained experimental data”.
- ii) “A validation metric is not specifically computed as a stand-alone measure that indicates the level of agreement or disagreement between computational and experimental results. The results of a hypothesis test is focused, instead, on obtaining a yes-no statement of computational-experimental consistency for a pre-specified level of significance”
- iii) “Much of the theoretical development in Bayesian estimation has been directed toward optimum methods for updating statistical models of uncertain parameters in the computational model. In validation metrics, however, the emphasis is on methods for assessing the fidelity of the physics of the *existing* computational model”.

They state that the primary goal of both parameter estimation and Bayesian inference is model updating and model calibration. This may be the goal in many situations but is different from the aim of the validation metric in the validation process. The purpose of a validation metric is to be able to assess the predictive capability of the mathematical model and not to optimize the agreement between the mathematical model and the experimental measurements. The functionality of the parameter estimation and Bayesian inference to optimize the agreement between the mathematical model and the physical system can be useful in the model refinement stage shown in Figure 5.1.

Oberkampf and Barone (2006) presents an approach that evaluates the accuracy of the model based on comparing deterministic computational results with the estimated mean of the experimental measurements. The primary difference between their approach from the three traditional quantitative comparison approaches they mention are that: (a) “a stand-alone validation metric is constructed to provide a compact, statistical measure of quantitative disagreement between computational and experimental results”, and (b) “a statistical confidence interval is computed that reflects the confidence in the accuracy of the experimental data“. They state however that their validation metric is applicable to SRQs that do not have a periodic character and do not have a complex mixture of many frequencies. They state that these types of SRQs require sophisticated time-series analysis and/or transformation into the frequency domain. They suggest using validation metrics constructed by Geers (Geers, 1984), Russell (Russell (1997a)) and Sprague and Geers (Sprague and Geers, 2003) for periodic systems or system responses with many frequencies.

Among the three validation metrics (Geers, Russell and Sprague and Geers) many other error measures and error metrics exist that can be used to quantify the agreement between two time histories. Table 5.1 attempts to summarize the various error measures and error metrics found in literature. For a detailed discussion on each error measure/metric the reader is referred to the study that treats them in detail.

Table 5.1. Summary of Error Measures and Metrics

Error measure/ Metric	Advantages	Disadvantages
Discussed in Sarin <i>et al.</i> (2010)¹		
Vector norms		Norm choice lead to different conclusions. Not capable of distinguishing error due to phase from error due to magnitude.
Average Residual and its standard deviation		Positive and negative differences at various points may cancel out. Results of Average Residual and its standard deviation are conflicting.
Coefficient of correlation		Sensitive to phase difference and cannot distinguish between error due to phase and error due to magnitude.
Cross-correlation		Can only measure difference in phase
Sprague & Geers Metric	Gives error due to magnitude and phase separately which is useful when more detailed investigation of the error source is necessary.	Not symmetric. Cannot consider shape of the time histories.
Russell's Error Measure	Symmetric	Same problem with respect to magnitude error as Sprague & Geers Metric.
Normalized Integral Square Error (NISE)		Magnitude error can be negative, which can decrease the combined error erroneously.
Dynamic Time Warping (DTW)	Effect of phase deviation on magnitude error can be minimized by using DTW.	
Discussed in Schwer (2007)		
Sprague & Geers Metric	Magnitude error – Insensitive to phase discrepancies Phase error – Uses error proposed by Russell. Insensitive to magnitude differences. Defines a Comprehensive error	
Discussed in Russell (1997b)		
Russell's Error Measure	Magnitude error is unbiased and signed.	
Geers'		May only be an appropriate choice when a high level of confidence exists in the test data
Whang's Inequality		No means for evaluating phase and magnitude errors
Theil's Inequality		No means for evaluating phase and magnitude errors
Zilliacus error		Incorrectly identifies the degree of error
RSS error factor		Incorrectly identifies the degree of error
Regression Coefficient		Incorrectly identifies the degree of error
Johansen's Magnitude		Should not be used in current state.
Johansen's Energy		Should not be used in current state.

¹ The comments made in Sarin *et al.* (2010) regarding the advantages and disadvantages are made in respect to their application to vehicle safety applications.

Russell (1997b) evaluated various measures in Table 5.1 and concluded that some error measures are very similar and other incorrectly identifies the error. He recommends using Geers', Whang's or Russell's error measure (Russell, 1997a), but state that Geers' error may only be an appropriate choice when a high level of confidence exists in the test data, and that Whang's Inequality is very sensitive to phase errors. Russell (1997a) developed a set of magnitude, phase and comprehensive error measures that can be used to evaluate the deviation between two general functions or test and analytical data. Russell's error measures address some of the issues associated with some of the existing measures given in Table 5.1. He states the following five deficiencies with existing error measures, which he claims that his proposed error measure resolves:

- 1) The value may not be well bounded and therefore may make it difficult to evaluate and compare results,
- 2) the physical interpretation of the results may not be intuitive,
- 3) the degree of error may not be correctly identified,
- 4) the results can not be used to identify the cause of the error
- 5) the basis of the error factor may not be understood, which can lead to false interpretations of the results.

Sarin *et al.* (2010) propose three error measures describing the error in magnitude, the error in phase and the error in slope by combining existing measures. The three measures are then combined into a single validation metric based on linear regression using Subject Matter Expert (SME) ratings. Much of the objectivity of the proposed validation metric is lost as the metric is based on the subjective opinions of SMEs. Before the validation metric can be used to validate a model, the validation metric has to be created by training it in order for it to be able to evaluate the model. This training is done by fitting the regression model to the SME ratings of the comparison between different data. This makes it highly dependent on the SMEs and it will therefore not be possible to compare the quantitative results of comparisons between two different models to a single set of "true" data (or test data) made using two different sets of SMEs, unless the SMEs' assessment is the same and given that the SME exists. The error measure proposed by Sarin *et al.* (2010) is not used further in this study as the metric is heavily dependent on SMEs. This causes it to lose a lot of the required objectivity of a quantitative validation metric. This metric may however be useful in certain applications.

From the above mentioned studies (Sarin *et al.* (2010), Russell (1997b)) in which various error measures/metrics were evaluated it would seem that the two most likely error measures/metrics to give the most reliable validation results are Russell's error measure and Sprague & Geers' metric. These two metrics will now be discussed in more detail.

2.1.1. Russell's error measure

The following equations are used to calculate the magnitude, phase and comprehensive error measures as presented in Russell (1997a).

For the magnitude error the following equation is used:

$$M_R = \text{sign}(rme) \text{Log}_{10}(1 + |rme|)$$

With the relative magnitude error (*rme*) computed by,

$$rme = \frac{\sum_{i=1}^N p_i^2 - \sum_{i=1}^N m_i^2}{\sqrt{\sum_{i=1}^N p_i^2 \sum_{i=1}^N m_i^2}}$$

p and m represent the two signals that are being compared. p represents the predicted data obtained from the simulation model and m is the measured data obtained from the experiment. N equals the number of data points in the measured (m) and predicted (p) data. The length of p and m should be the same.

For the phase error the following equation is used:

$$P_R = \frac{1}{\pi} \cos^{-1} \left(\frac{\sum_{i=1}^N p_i m_i}{\sqrt{\sum_{i=1}^N p_i^2 \sum_{i=1}^N m_i^2}} \right)$$

The magnitude and phase error are combined into a comprehensive error, C_R :

$$C_R = \sqrt{\frac{\pi}{4} (M_R^2 - P_R^2)}$$

2.1.2. Sprague & Geers' metric

The most recent version of Geers' error measure (Geers, 1984), presented in Sprague and Geers (2006), will be used. In this version the equation of the phase error has been updated.

The Sprague & Geers' (S&G) magnitude error is calculated by:

$$M_{S\&G} = \sqrt{\frac{\sum_{i=1}^N p_i^2}{\sum_{i=1}^N m_i^2} - 1}$$

The phase error is calculated by:

$$P_{S\&G} = \frac{1}{\pi} \cos^{-1} \left(\frac{\sum_{i=1}^N p_i m_i}{\sqrt{\sum_{i=1}^N p_i^2 \sum_{i=1}^N m_i^2}} \right)$$

The Sprague and Geers' comprehensive error measure is given by:

$$C_{S\&G} = \sqrt{M_{S\&G}^2 + P_{S\&G}^2}$$

From the above equations it can be observed that the phase error of both metrics is calculated in the same way. The calculation of the magnitude and comprehensive error differs between S&G's metric and Russell's error measure. Whether these two validation metrics are able to 1) give results for which the physical interpretation is intuitive and 2) identify the degree of

error correctly is not clear. A validation metric will be proposed in the next paragraph that will address these two aspects directly. This proposed validation metric will then be compared to Russell's error measure and to the Sprague & Geers (S&G) metric in paragraph 3.

2.2. Validation metric based on relative error

The validation metric that is proposed will use the simple and commonly used relative error to quantify the agreement/disagreement between two data sets. The data sets may be SRQs obtained from a physical system and a model. The use of the relative error as a validation metric has been employed in previous studies (Oberkampf and Trucano (2002) and Oberkampf and Barone (2006)). Oberkampf and Barone (2006) state that, as long as the measured data is not near zero, the relative error metric is a useful quantity. A similar remark is made by Schwer (2007) stating that "a simple metric such as relative error works well for point-to-point comparisons, e.g. maximum deflection of a cantilever beam. However when comparisons involve time or spatial variations, e.g. velocity history at a point or deflection along a beam, then the application of a simple metric like relative error becomes sensitive to inaccuracies in time and space dimensions as well as the system response quantity (SRQ)". As mentioned, this study will consider the comparison of SRQs with a periodic nature and which may have values at or near zero, which according to Oberkampf and Barone (2006) and Schwer (2007) will cause difficulties in using the relative error as a validation metric. Before discarding the use of the relative error as a validation metric on periodic systems where the measured data might be near or equal to zero, we'll investigate the characteristics of the relative error, its various challenges and suggest ways to circumvent them.

2.2.1. Relative error (*RE*)

The equation for the relative error between two values is given in Eq.{5.1}. Consider the two values as one being the measured (*m*) and the other the predicted (*p*) value, with the measured value taken as the true (or reference) value.

$$RE = \left| \frac{p - m}{m} \right| \quad \{5.1\}$$

The calculation of the relative error between a measured (*m*) and predicted (*p*) value is simple and when expressed as a percentage (see Eq.{5.2}) easy to interpret.

$$\%RE = \left| \frac{p - m}{m} \right| \times 100 \quad \{5.2\}$$

The relationship between the *RE* and the ratio *p/m*, which represents the respective over or under prediction of the measured value, is shown in Figure 5.2.

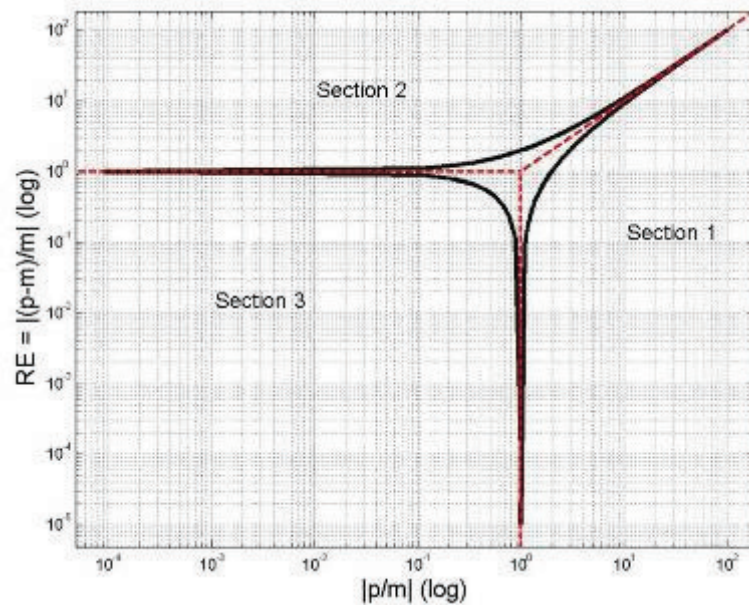


Figure 5.2. Relationship between the RE and the ratio p/m

From Figure 5.2 the following observations can be made:

- i. The first obvious observation is that in the limit of p approaching m , RE goes to zero ($\lim_{p \rightarrow m} RE = 0$).
- ii. When $\frac{p}{m} \gg 1$ the relative error goes to positive infinity (along the line in section 1),
- iii. Similarly, when $\frac{p}{m} \ll 1$ the relative error goes to negative infinity. However, because we plot the absolute values of the ratio p/m these large negative values instead goes to positive infinity (along the line in section 2)

The ratio of p/m indicates whether the predicted value p is an over or under prediction of the measured value m . The predicted value p is said to be an over prediction of m if p is a larger positive value when m is positive, or when p is a larger negative value when m is negative. Similarly, p is classified as an under prediction when p is a smaller positive value (or any negative value) when m is positive, or when p is a larger negative value (or any positive value) when m is negative. With this convention relative errors that fall in section 1 are over predictions and relative errors in either section 2 or 3 are under predictions.

From Figure 5.2 and Eq. {5.1} it is obvious that the relative error may result in infinite values and NaNs (Not-aNumber) due to the operations of $0/0$ and $1/0$, which may make further calculations on the relative error difficult. These challenges are discussed in the following paragraph.

2.2.2. Challenges in using the $\%RE$ as validation metric

The challenges concerning the use of the percentage relative error as a validation metric mainly arise when data has to be compared that have been obtained from a periodic system and the measured and/or predicted data has values equal to, or near, zero. Figure 5.3 shows an example of measured and predicted data obtained from a periodic system.

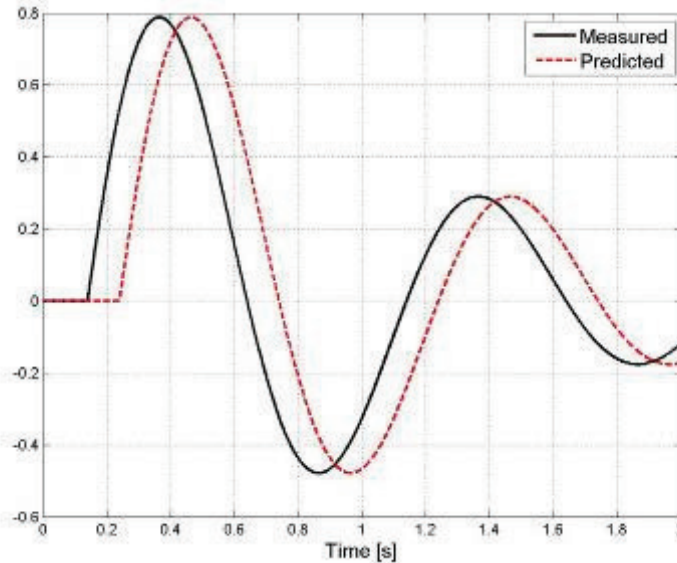


Figure 5.3. SRQs from experimental measurements and model simulations of a periodic system

The challenges associated with the $\%RE$ when periodic data, as shown in Figure 5.3, is compared are:

- i. Non-constant $\%RE$ over the independent variable (time in the case of Figure 5.3),
- ii. NaNs (Not-a-Number) present in the $\%RE$ s,
- iii. Inf (infinite) values present in the $\%RE$ s.

The first challenge faced when using the $\%RE$ in comparing two periodic SRQs, is that the $\%RE$ at each data point may not be the same. This makes it difficult to report a single representative result indicating the overall agreement/disagreement. Further challenges that are associated with using the $\%RE$ arise from comparing periodic SRQs that are near zero. When calculating the $\%RE$ of periodic SRQs near zero, NaNs and Inf values may be present in the $\%RE$. These values result from the operations $0/0$ and $1/0$, respectively, and make further calculations on the $\%RE$ difficult. These challenges are discussed in further detail in the following paragraphs and methods to overcome them are proposed.

Non-constant $\%RE$ over the independent variable

The $\%RE$ may not have a constant value over the entire range of the data. In other words the $\%RE$ may have different values for each data point. This makes it difficult to report on the agreement between the measured and predicted data using the $\%RE$. When the $\%RE$ does not have a constant value one of the following two methods can be used to report a single representative value for the $\%RE$. In the two methods the non-constant $\%RE$ will be represented by a modified $\%RE$ defined either by the mean of the $\%RE$ s or by a specific $\%RE$. In both methods a probability will be given that represents the percentage of $\%RE$ s that are below, or equal to, either the mean of the $\%RE$ s or the specific $\%RE$ that was chosen. When the mean of the $\%RE$ s is used to define the modified $\%RE$, it will be denoted as $m\%RE^m$ and by $m\%RE^s$ when it is defined by a specific $\%RE$.

In order to define the $m\%RE^m$ the mean and cumulative histogram of the $\%RE$ s are calculated. Using the cumulative histogram and the mean, the probability is calculated that the $\%RE$ s are at or below the mean $\%RE$. Figure 5.4(a) shows the histogram and the mean of the $\%RE$ s and Figure 5.4(b) the cumulative histogram and the mean of the $\%RE$ s for an arbitrary set of $\%RE$ s. Figure 5.4 illustrates that when we take the y-intercept (representing the frequency of a

specific $\%RE$) of the cumulative histogram where the mean value intersects the cumulative histogram, we can obtain the probability that the data is at, or below the mean value. Therefore, for the data in Figure 5.4 the result will be that 55% of the $\%RE$ s are at or below the mean $\%RE$ of 15% ($m\%RE^m = 15\% P(55\%)$).

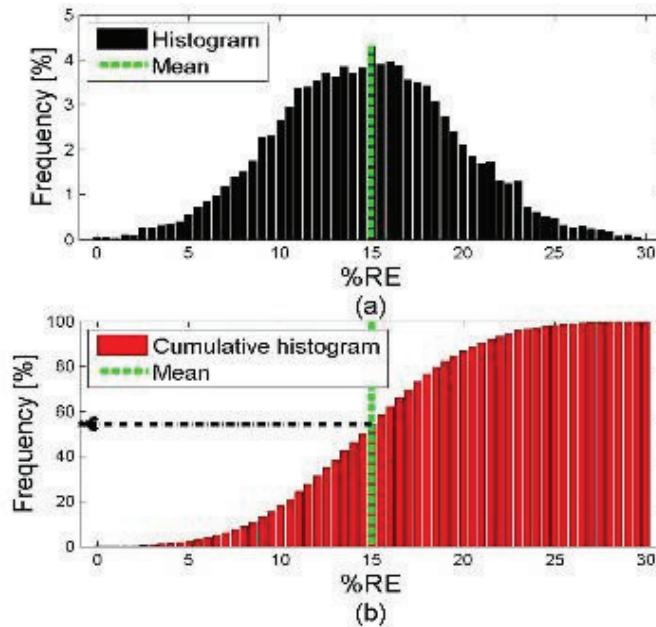


Figure 5.4. (a) Superimposed mean and histogram, and (b) superimposed mean and cumulative histogram of $\%RE$ with a normal distribution

Even if the $\%RE$ does not have a normal distribution (see Figure 5.5(a)) the mean $\%RE$ can still be used to define the $m\%RE^m$. Figure 5.5(a) shows the non-normal distribution of the $\%RE$ and Figure 5.5(b) presents the cumulative histogram with the mean $\%RE$ superimposed on it. For the example in Figure 5.5 we obtain that 57.6% of the $\%RE$ s are at or below the mean $\%RE$ of 48.5% ($m\%RE^m = 48.5\% P(57.6\%)$).

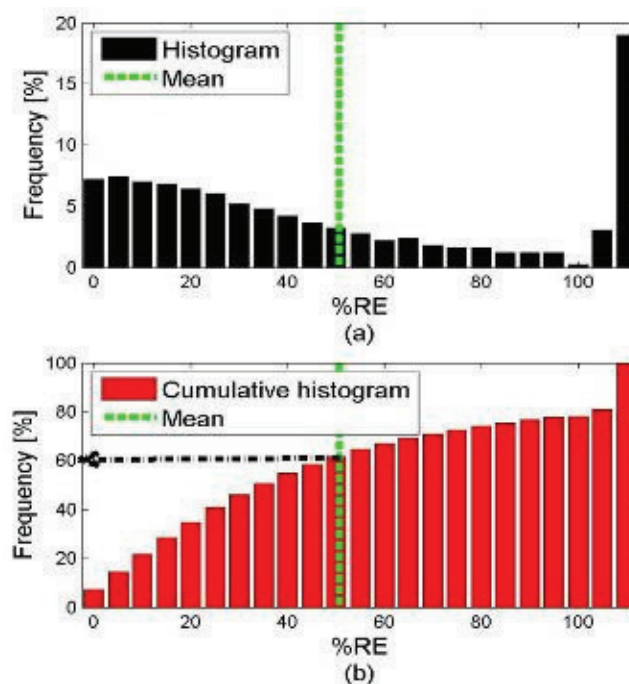


Figure 5.5. (a) Superimposed mean and histogram, and (b) superimposed mean and cumulative histogram of $\%RE$ with a non-normal distribution

In the second method, instead of defining the modified $\%RE$ by using the mean $\%RE$, a specific $\%RE$ can be chosen and the probability that the $\%REs$ are below, or equal to, this specific $\%RE$ can be calculated. However it may be that there is no $\%REs$ below this chosen $\%RE$ and the result will be that there is zero probability that the $\%REs$ are below this chosen $\%RE$ ($m\%RE^s = x\% P(0\%)$). This result will make comparing and selecting the best model from a group of models impossible if this is the result for all the models. In this situation it may be better to use the mean $\%RE$ to define the modified $\%RE$. However, in the situation where accuracy requirements are set for the model the result from the $m\%RE^s$ can easily be used to check whether the requirements are satisfied or not. It will therefore depend on the intended use of the validation metric whether the modified $\%RE$ is defined by a specific $\%RE^s$ or the mean $\%RE^m$.

NaNs present in the $\%REs$

The calculation of the $\%RE$ is subject to the operation $0/0$. This is one of the major problems encountered when using the relative error to quantify the agreement/disagreement between the measured and predicted SRQs obtained from periodic systems near zero. This occurs when the $\%RE$ is calculated at a point where the measured and predicted value equals zero. The IEEE floating point representation of $0/0$ is NaN (Not-a-Number). The presence of NaNs in the $\%RE$ makes it difficult to perform further calculations on it. It is proposed that any NaN is set equal to 0 as the operation $0/0$ implies that the $\%RE$ is equal to zero. The next step is now to use either the $m\%RE^m$ or the $m\%RE^s$ to report a single value for the $\%REs$ in order to quantify the overall agreement between two SRQs.

The following considerations should be kept in mind when using the $m\%RE^m$. Zeros in the $\%RE$ result in problems with the representation of the $m\%RE^m$. Consider the $\%RE$ between measured and predicted data having 10 data points. Nine of them are equal to 8% and one is a NaN. Assigning a zero to the NaN the mean of the $\%RE$ is 7.2%. Using the mean of 7.2% we will obtain a probability that 0.1% of the $\%REs$ are lower than 7.2% ($m\%RE^m = 7.2\% P(0.1\%)$). If we calculate the mean of the $\%RE$ but now ignoring any zero value we will obtain a mean of 8%. This will give us the result that 100% of the $\%REs$ are at, or below, 8% ($m\%RE^m = 8\% P(100\%)$). Ignoring the zeros gives a result that represents the agreement better. Consider the example shown in Figure 5.6 that reiterates this. We have a true time response and an approximation to the true response. We know that the amplitude of the approximate response deviates from the true response by 10%. If we calculate the modified $\%RE$ defined by the mean $\%RE$, including the zero values, the result is that there is a 0.2% probability that the $\%REs$ are smaller or equal to 9.98% ($m\%RE^m = 9.98\% P(0.2\%)$). Even though this is true, the results without including the zeros in the calculation of the mean $\%RE$, are considered more meaningful. Excluding the zeros when the mean of the $\%RE$ is calculated, the result is obtained that a 100% of the $\%REs$ are equal to, or below 10% ($m\%RE^m = 10\% P(100\%)$), which we know to be true. Therefore the mean of the $\%REs$, defining the $m\%RE^m$, will be calculated neglecting all the zero values in the $\%REs$. Zeros in the $\%REs$ do not have the same effect on the $m\%RE^s$ and does not need any special consideration.

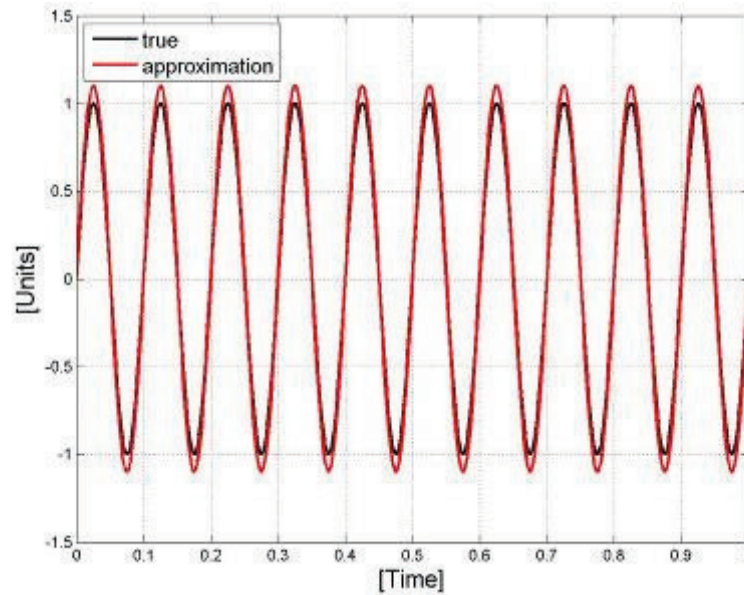


Figure 5.6. Example of time response histories of SRQs for the physical system (true) and computation model (approximation)

Inf values present in the %REs

We already looked at how to handle operations involving $0/0$ which the IEEE represents as NaNs. Another problem with using the relative error in comparing periodic signals is introduced by operations involving $1/0$. This occurs when the measured value is zero and the predicted value has a non-zero value. The IEEE uses Inf to represent these operations. The effects of operations involving $1/0$ on the modified %RE are discussed at the hand of an example.

In Figure 5.7, two mathematical models (approximation 1 and 2) are compared to the physical system (true). Approximation 1 has a 10% deviation and approximation 2 a 30% deviation from the true value. In Figure 5.7(a) the data of both approximations are perfectly in-phase with the true data, whereas in Figure 5.7(b) the approximations and true data have some phase difference. Table 5.2 shows the results for the modified %RE. For the in-phase case we obtain the expected $m\%RE^m$ of 10% P(100%) and 30% P(100%) respectively, however for the out-of-phase case we obtain the result that there is a 100% probability that the %REs are smaller than infinity ($m\%RE^m = \infty$ P(100%)), which has no meaning even though it is correct. The $m\%RE^s$ gives meaningful results for both the in-phase and out-of phase example.

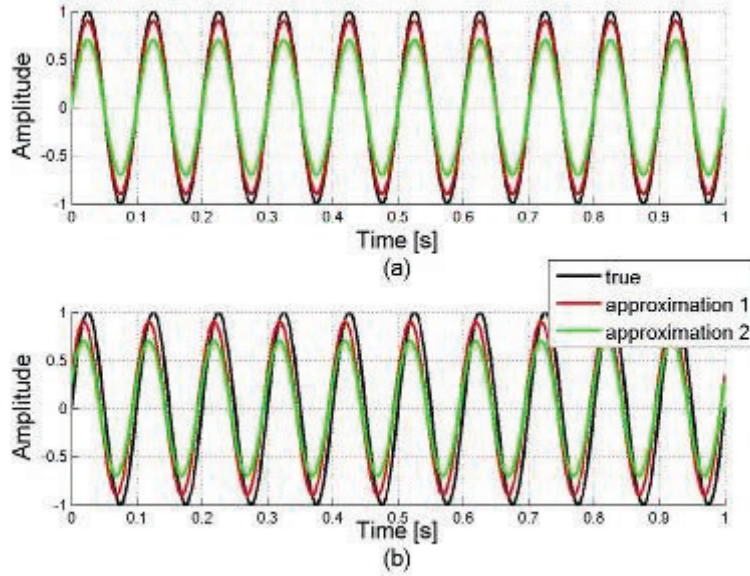


Figure 5.7. (a) Approximation 1 and 2 in-phase with true data. (b) Approximation 1 and 2 out-of-phase with true data

Table 5.2. Effect of %RE not being bounded on the results of the $m\%RE$ (Not bounded)

	(a) In-phase		(b) Out-of-phase	
	Approximation 1	Approximation 2	Approximation 1	Approximation 2
$m\%RE^m$	10% P(100%)	30% P(100%)	Inf P(100%)	Inf P(100%)
$m\%RE^s$	15% P(100%)	15% P(0.2%)	15% P(21.6%)	15% P(13.6%)

From the results in Table 5.2 it is clear that the presence of Inf values do not affect the results of $m\%RE^s$. However, the presence of Inf values in the %REs makes it difficult to compare the models using the $m\%RE^m$. There is one of two ways to deal with Inf values in the %REs when the $m\%RE^m$ is used namely:

- i. If $\%RE_i > \text{Inf}$, then remove Inf value from %RE data, or
- ii. Bound the %REs.

Completely removing the Inf values, as proposed in method (i), will imply that the %REs at these points are ignored. The implication of this is that when the $m\%RE^m$ is used, the mean of the %RE will be lower than it really is. In the case where both models have the same amount of values above the specified %RE threshold method (i) will not influence the results negatively. However, if only one model has values above the threshold that is removed this may lead to the incorrect model being chosen as the more accurate model. Bounding the %RE as proposed in method (ii) will be less likely to make an erroneous model choice. Oberkamp and Trucano (2001) presents a validation metric that uses the relative error combined with the hyperbolic tangent function which results in the relative error being bounded. Their equation is changed and presented here as Equation {5.3}. V is the bounded RE.

$$V = \tanh \left| \frac{p-m}{m} \right| \quad \{5.3\}$$

Plotting this equation on Figure 5.8 shows that the implementation of \tanh bounds the RE, for all ratios of p/m , to 1. However, using \tanh the “true” relative error is distorted. As can be seen from Figure 5.8, Eq.{5.3} deviates from the true relative error as it moves away from

$p/m = 1$. Therefore, for a ratio of $p/m = 2$ Equation {5.3} results in a relative error of 0.7616 instead of 1. This results in a 24% lower error than which truly exists. The use of \tanh in combination with the RE bounds the RE to 1, but has the implication that the true relative error is lost.

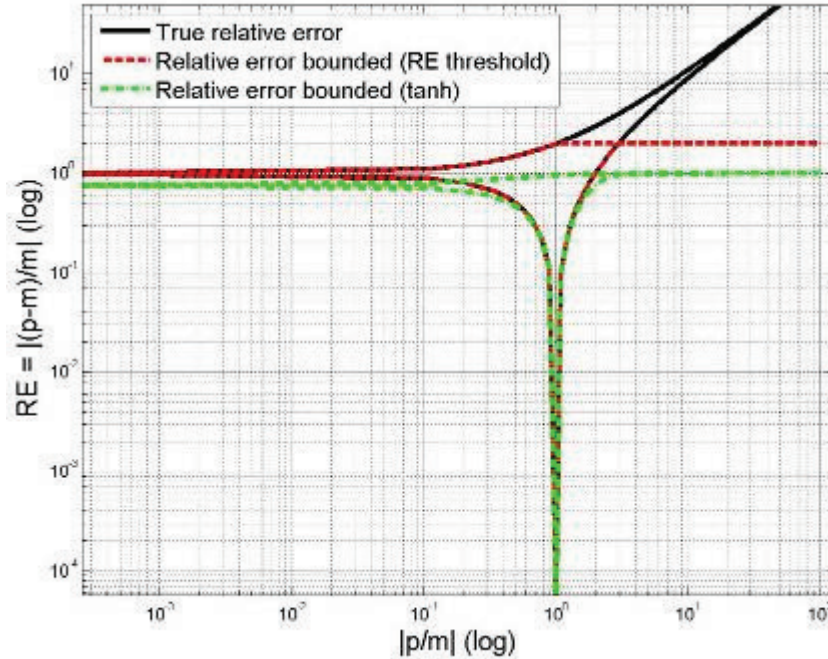


Figure 5.8. Relationship between the RE and the ratio p/m (relative error bounded)

The relative error can be bounded without distorting the true relative error by setting any RE that is greater than a chosen RE threshold equal to the RE threshold. This implies that the RE is now bounded but unlike Eq.{5.3} all the RE s below the RE threshold value are the true relative errors. The implementation of this and its effect on the relationship between the RE and the ratio p/m is also shown on Figure 5.8 as the graph *Relative error bounded (RE threshold)*. From the figure it can be observed that the true relative error is obtained until the RE threshold is reached. Above the RE threshold the true relative error is set equal to the RE threshold. In figure 5.8 the RE threshold was set equal to 2.

We again calculate the $\%RE$ between the measured and predicted data in Figure 5.7 but now using the bounded $\%RE$. The $\%RE$ threshold is set equal to a 100%. Using the bounded $\%RE$ we obtain results for the $m\%RE^m$ that can actually be interpreted (see Table 5.3). It is now possible to evaluate approximation 1 and approximation 2, using the $m\%RE^m$, in order to conclude that approximation 1 is more accurate than approximation 2. This is similar to the results obtained from the $m\%RE^s$ which also indicates that approximation 1 is better than approximation 2.

Table 5.3. Effect of $\%RE$ being bounded on the results of the $m\%RE$ (Bounded)

	(a) In-phase		(b) Out-of-phase	
	Approximation 1	Approximation 2	Approximation 1	Approximation 2
$m\%RE^m$	10% P(100%)	30% P(100%)	48.5% P(57.6%)	51.3% P(56.8%)
$m\%RE^s$	15% P(100%)	15% P(0.2%)	15% P(21.6%)	15% P(13.6%)

From the results in Table 5.2 and Table 5.3 it is clear that whether the $\%RE$ is bounded or not the $m\%RE^s$ is unaffected. Therefore unlike the $m\%RE^m$, the $m\%RE^s$ will not be affected by the choice of the $\%RE$ threshold. It is important that when the $m\%RE^s$ is used, that the specific $\%RE$ that is chosen to define the modified $\%RE$, is never above the $\%RE$ threshold. The effect of the choice of the $\%RE$ threshold on the $m\%RE^m$ will be discussed by considering three scenarios:

- i.) All $\%REs < \%RE$ threshold,
- ii.) Some $\%REs > \%RE$ threshold, and
- iii.) All $\%REs > \%RE$ threshold.

It is obvious that for scenario 1 the choice of the $\%RE$ threshold is irrelevant. With scenario 2 having some $\%RE$ greater than the $\%RE$ threshold the choice of the $\%RE$ threshold will affect the result of the $m\%RE^m$. Consider the example given in Table 5.4. We have a set of true values and their associated $\%RE$ between the true and approximate data. Table 5.5 presents the results for the $m\%RE^m$ for two $\%RE$ threshold values.

Table 5.4. Known $\%RE$ between true and approximate data

Data point	True	$\%RE$
1	0	0
2	0.5	90
3	0.8	80
4	1	60
5	1.2	50
6	0.8	4
7	0.7	6
8	0.6	8
9	0.5	10
10	0	1
11	-0.5	-20
12	-0.8	-30
13	-1	-55
14	-1.2	-35
15	-0.8	-25
16	-0.7	-20
17	-0.6	-15
18	-0.5	-10
19	1	200
20	1	200
21	1	200

Table 5.5. Results for the $m\%RE^m$ using different $\%RE$ threshold values

$\%RE$ threshold	110%	250%
$m\%RE^m$	44.6% P(61.9%)	58.8% P(71.4%)

Figure 5.9 shows the histogram, cumulative histogram and the mean of the $\%RE$ for both the $\%RE$ threshold equal to 110% and 250%. From this figure it can be observed that the $\%REs$ smaller than the $\%RE$ threshold is not affected by the choice of the $\%RE$ threshold. Therefore the histogram and cumulative histograms will be identical up until the $\%RE$ threshold after

which they will differ. This implies that both results in Table 5.5 are correct and it can be concluded that it does not matter what value is chosen for the $\%RE$ threshold, as long as the same $\%RE$ threshold is used when two models are compared.

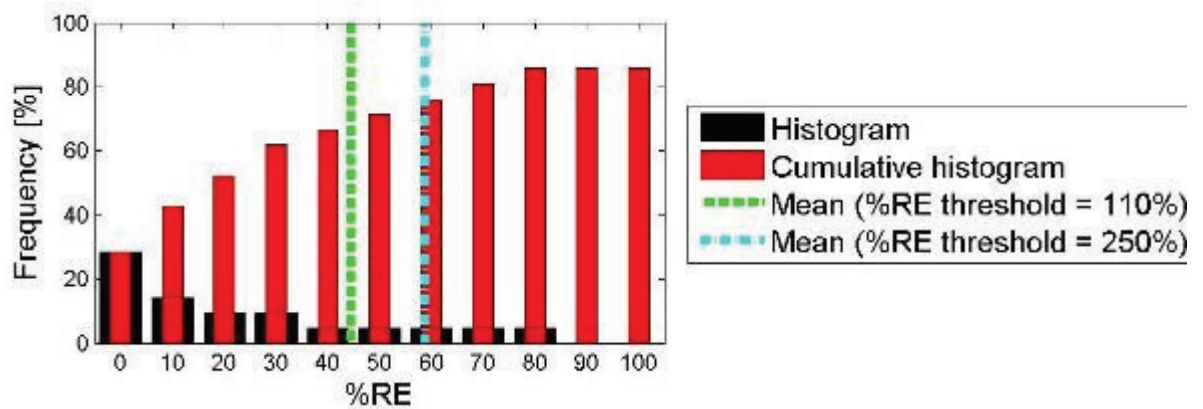


Figure 5.9. Superimposed histograms, cumulative histograms and means of $\%RE$ using different $\%RE$ threshold values

This brings us to the third scenario. If all the $\%RE$ s are above the $\%RE$ threshold, all the $\%RE$ s will be set equal to the $\%RE$ threshold. This implies that if the $\%RE$ threshold = 100% the results for both model 1 with a constant $\%RE = 200\%$ and model 2 with a constant $\%RE = 150\%$ will be that 100% of the $\%RE$ s are below a 100% ($m\%RE^m = 100\% P(100\%)$). This result is obtained because the percentage relative errors that are above the $\%RE$ threshold are bounded by the $\%RE$ threshold. Having two models with an accuracy worse than 100% may already make them invalid models, however if they need to be analysed the threshold value for the $\%RE$ can be adjusted. By adjusting the $\%RE$ threshold to 200% we get that 100% of the $\%RE$ s are below 200% for model 1 and that 100% of the $\%RE$ s are below 150% for model 2. Therefore model 2, although bad, is a better approximation to the measurements than model 1.

It is important to remember that because the $\%RE$ s greater than the $\%RE$ threshold is bounded to the $\%RE$ threshold, the $\%RE$ s above the $\%RE$ threshold are not the true $\%RE$ s. This is important especially when a specific $\%RE$ is chosen to define the modified $\%RE$. The specific $\%RE$ should always be below the $\%RE$ threshold. When the specific $\%RE$ is chosen below the $\%RE$ threshold both the $m\%RE^s$ and the $m\%RE^m$ will give the true relative error.

2.2.3. Summary of the modified $\%RE$ validation metric

The modified percentage relative error validation metric and its two formulations ($m\%RE^m$ and $m\%RE^s$) were presented. It should be realized that both formulations can be used to either compare (and rank) a set of models or to evaluate the model against accuracy requirements using either formulation of the modified $\%RE$. It is however suggested that the $m\%RE^m$ should be used for comparing a set of models and the $m\%RE^s$ used to evaluate the model against the accuracy requirements. Table 5.6 summarizes the two formulations of the modified percentage relative error validation metric.

Table 5.6. Summary of the two formulations of the modified %RE validation metric

	$m\%RE^m$	$m\%RE^s$
Defined by	The percentage of %REs (given as a probability) that are equal to, or below, the mean of the %REs: $m\%RE^m = \text{mean}(\%REs) P(\%)$ <p>Note: the mean of the %REs is calculated neglecting all zero values in the %REs</p>	The percentage of %REs (given as a probability) that are equal to, or below, the specified %RE (for example x%): $m\%RE^s = x\% P(\%)$ <p>Note: The specified %RE must always be below the %RE threshold</p>
Preprocessing of the %REs	NaNs (Not-a-Number)	
	Set NaNs = 0	Set NaNs = 0
	Inf (infinite) values	
	Bound %REs with %RE threshold <p>Note: Choice of %RE threshold influence result of the $m\%RE^m$. %RE threshold must be the same when comparing $m\%RE^m$ results</p>	None required <p>Note: If the %REs were bounded, x% must be below the %RE threshold</p>
Suggested uses	Primary use	
	Comparing and selecting the best model from a group of models	Evaluation of model against accuracy requirements
	Secondary use	
	Evaluation of model against accuracy requirements	Comparing and selecting the best model from a group of models

In the previous paragraph the use of the relative error as basis for a validation metric between two data sets was investigated. The relative error gives intuitive results, but has certain challenges. How these challenges can be overcome to still get useful intuitive results from the %RE when it is presented in the modified form (either $m\%RE^m$ or $m\%RE^s$) were discussed. Because the modified %RE includes both the error due to a magnitude difference, as well as the error due to a phase difference, it is considered to be a comprehensive error. The modified %RE validation metric will now be compared to the validation metrics of Russell (Russell, 1997a) and Sprague & Geers (Sprague and Geers, 2006).

3. Comparison of validation metrics

The modified %RE validation metric will now be compared to the Sprague & Geers metric (Sprague and Geers, 2006) and Russell's metric (Russell, 1997a) that were presented in paragraph 2.1 of this chapter. It should be noted that the magnitude, phase and comprehensive error measures of both S&G and Russell's metric is multiplied by a hundred in order to present them as a percentage. This is done to compare it directly to the modified %RE metric. The %RE threshold value that is used throughout this chapter is 100%.

From the comparison of the validation metrics we would like to conclude two things. Firstly, and most importantly, we would like to establish whether the validation metrics give a useful and reliable measure that quantifies the agreement between the experimental and simulated data. It is important that the validation metrics give a reliable and easily interpretable metric which can be used to determine whether the model satisfies the accuracy requirements. Secondly we would like to evaluate the ability of the validation metrics to rank models and select the best model from a group of models. Analytical functions will firstly be used to compare the capabilities of the validation metrics to rank models. The analytical functions will also aid in determining whether the validation metrics can indeed quantify the agreement

of the model and give a useful and reliable metric which will aid the engineer in deciding whether the model is valid or not. Case studies will then be used to further show the advantages and limitations of the different metrics.

3.1. Analytical functions

The analytical functions that we will use include the functions used in previous studies by Russell (1997b) and Schwer (2007) which are based on, and extensions of, the functions given in Geers (1984). The analytical functions that are used are given in Table 5.7.

The analytical functions 1 to 15, listed in Table 5.7, were used in Russell (1997b). Functions 1 to 8 represent the predicted data and are compared to the measured data given by $m(t) = e^{-t} \sin(2\pi t)$. Similarly, functions 9 to 15 represent the predicted data that uses the measured data given by $m(t) = 1 - e^{-t/0.1} - 0.6e^{-t/0.4} \sin(5\pi t) + 0.01 \sin(200\pi t)$. Functions 21(a), 22(a) and 22(b) are three additional functions used by Schwer (2007) that were not considered by either Russell (1997b) or Geers (1984). The reference function for function 21(a), 21(b), 22(a) and 22(b) is given by $m(t) = e^{-(t-0.14)} \sin 2\pi(t - 0.14)$.

Table 5.7. Equation for the various analytical functions

Function	Equation
Reference function for 1 to 8	$m(t) = e^{-t} \sin(2\pi t)$
1	$p(t) = 0.8e^{-t/0.8} \sin(2\pi t)$
2	$p(t) = e^{-t} \sin(1.6\pi t)$
3	$p(t) = 1.2e^{-t/1.2} \sin(1.6\pi t)$
4	$p(t) = 0.4e^{-t/1.2} \sin(1.6\pi t)$
5	$p(t) = 0.5e^{-t} \sin(1.6\pi t)$
6	$p(t) = 0.6e^{-t/1.2} \sin(1.6\pi t)$
7	$p(t) = e^{-t} \sin(2\pi t) + 0.1e^{-t} \sin(30\pi t)$
8	$p(t) = e^{-t} \sin(2\pi t) + 0.3e^{-t} \sin(30\pi t)$
Reference function for 9 to 15	$m(t) = 1 - e^{-t/0.1} - 0.6e^{-t/0.4} \sin(5\pi t) + 0.01 \sin(200\pi t)$
9	$p(t) = 1 - e^{-t/0.1} - 0.6e^{-t/0.3} \sin(5\pi t)$
10	$p(t) = 1 - e^{-t/0.1} - 0.6e^{-t/0.4} \sin(4\pi t)$
11	$p(t) = 0.6 - 0.6e^{-t/0.1} - 0.8e^{-t/0.3} \sin(4\pi t)$
12	$p(t) = 0.6 - 0.6e^{-t/0.3} - 0.3e^{-t/0.5} \sin(3\pi t)$
13	$p(t) = 0.3 - 0.3e^{-t/0.3} - 0.2e^{-t/0.5} \sin(3\pi t)$
14	$p(t) = 1 - e^{-t/0.1} - 0.5e^{-t/0.4} \sin(5\pi t) - 0.25t$
15	$p(t) = 1 - e^{-t/0.1} - 0.6e^{-t/0.4} \sin(4\pi t) - 0.5t$
Reference function for 21 to 22	$m(t) = e^{-(t-0.14)} \sin 2\pi(t - 0.14)$
21(a)	$p(t) = 1.2e^{-(t-0.14)} \sin 2\pi(t - 0.14)$
21(b)	$p(t) = 0.8e^{-(t-0.14)} \sin 2\pi(t - 0.14)$
22(a)	$p(t) = e^{-(t-0.24)} \sin 2\pi(t - 0.24)$
22(b)	$p(t) = e^{-(t-0.04)} \sin 2\pi(t - 0.04)$

3.1.1. Ability to rank models and identify the best model

We start by comparing the validation metrics using functions 1 to 8 given in Table 5.7. The analytical functions 1 to 8 are compared to the same reference function. Table 5.8 shows how each validation metric ranks the 8 examples. All the functions are ranked the same by the three validation metrics except for Function 1 and 2. This gives an average agreement of 91.7%. The $m\%RE^m$ ranks Function 8 in 2nd and Function 1 as 3rd. The $m\%RE^m$ gives a lower mean for Function 1 than for Function 8 but Function 8 has a higher amount of $\%RE$ s below the mean $\%RE$ and therefore Function 8 is ranked higher than Function 1. The ranking of the functions in this order is confirmed when the results for the $m\%RE^s$ is considered. The $m\%RE^s$ for Function 8 is 37% P(63.85) and Function 8 therefore has a higher amount of $\%RE$ s below the same $\%RE$ than Function 1. The same functions were given to subject matter experts (SMEs) and asked to rank the comparisons of the eight functions to the reference function. The SMEs ranked all the functions the same as the three validation metrics except for Function 2 and 3 (see Table 5.9). The overall average agreement between the seven SMEs is 64.3%, which is a lot lower than between the three validation metrics.

Table 5.8. Ranking of comparisons by different validation metrics (Functions 1 to 8)

Function	S&G	Rank	Russell	Rank	$m\%RE^m$	Rank	Overall Rank (%)
1	28.68	4	20.2	3	37 P(47.9)	3	3 (66.6)
2	23.4	3	20.7	4	68.9 P(40.1)	4	4 (66.6)
3	38.6	5	27.3	5	71.5 P(36.9)	5	5 (100)
4	61.9	8	46.2	8	76.8 P(44.2)	8	8 (100)
5	55.6	7	41.2	7	75 P(43.6)	7	7 (100)
6	42.9	6	32.9	6	72.4 P(43)	6	6 (100)
7	3.3	1	2.87	1	18.8 P(76.8)	1	1 (100)
8	10.4	2	8.9	2	39.2 P(66.2)	2	2 (100)

Table 5.9. Ranking of comparisons by SME's (Functions 1 to 8)

Function	SME #1	SME #2	SME #3	SME #4	SME #5	SME #6	SME #7	Overall rank (%)
1	2	3	5	3	3	3	3	3 (71.4)
2	3	5	3	2	5	5	4	5 (42.8)
3	4	6	4	4	4	4	5	4 (71.4)
4	8	8	7	6	8	8	8	8 (71.4)
5	6	4	8	7	7	6	7	7 (42.8)
6	7	7	6	8	6	7	6	6 (42.8)
7	1	1	1	1	1	1	1	1 (100)
8	5	2	2	5	2	2	2	2 (71.4)

The validation metrics were compared using another seven functions (Functions 9 to 15 given in Table 5.7). The results for the validation metrics and the SMEs are given in Table 5.10 and Table 5.11, respectively. The ranking by the three validation metrics and the seven SMEs are again the same for all but two Functions. For Function 13 and 15 the SMEs rank these two functions as either 6th or 7th. The three validation metrics again have a higher average agreement of 90.5% against the 71.4% of the SMEs.

Table 5.10. Ranking of comparisons by different validation metrics (Functions 9 to 15)

Example	S&G	Rank	Russell	Rank	m% RE	Rank	Overall rank (%)
9	0.91	1	0.8	1	5 P(85.5)	1	1 (100)
10	3.37	2	2.98	2	11.3 P(67.7)	2	2 (100)
11	40.1	4	28.2	4	45 P(77.6)	4	4 (100)
12	45.7	5	32.3	6	49.9 P(73.1)	5	5 (66.6)
13	72.89	7	57	7	75 P(72.5)	7	7 (100)
14	26.4	3	18.91	3	29.52 P(54.2)	3	3 (100)
15	50.1	6	36.4	5	54.6 P(48.5)	6	6 (66.6)

Table 5.11. Ranking of comparisons by SMEs (Functions 9 to 15)

Function	SME #1	SME #2	SME #3	SME #4	SME #5	SME #6	SME #7	Over all rank (%)
9	1	1	1	1	1	1	1	1 (100)
10	2	2	2	2	2	2	2	2 (100)
11	4	4	4	3	4	4	3	4 (71.4)
12	5	6	5	5	5	5	4	5 (71.4)
13	6	7	6	6	7	7	5	6 (42.8) 7 (42.8)
14	3	3	3	4	3	3	6	3 (71.4)
15	7	5	7	7	6	6	7	6 (42.8) 7 (42.8)

From the above results it was observed that the three validation metrics and the SMEs tend to rank models similarly. The ranking of the functions by the validation metrics were done with more coherence than the ranking by the SMEs. The results may be influenced having more SMEs or using different groups of SMEs. Having additional validation metrics may also influence the results of the overall ranking of the models. These effects are outside the scope of this study. The results obtained seem to indicate that the validation metrics are able to rank the models and indicate which model is the best model from a group of models. The question is now whether all the metrics are able to give a reliable and useful measure of the level of agreement between the experimental and the simulated data.

3.1.2. Reliability and usefulness of validation metrics

The following two examples, indicated in Figure 5.10 and Figure 5.11, discuss the reliability and usefulness of the quantitative measure of the agreement/disagreement between two SRQs given by the various validation metrics. The example we consider in Figure 5.10 uses function 21(a) and 21(b) given in Table 5.7. There is no phase difference between the function representing the measured data and the two sets of predicted data represented by Function 21(a) and 21(b). The magnitude of Function 21(a) is 20% larger than the magnitude of the measured response and Function 21(b) is 20% smaller. We therefore know the error in magnitude between the measured response and the two models. This makes it possible to evaluate which of the metrics can indeed give the agreement between the two data sets correctly. Table 5.12 shows the results for the various metrics. Only S&G and the $m\%RE^m$ give the correct percentage relative error between the two signals. S&G is also capable of stating whether the magnitude is smaller or larger than the measured magnitude.

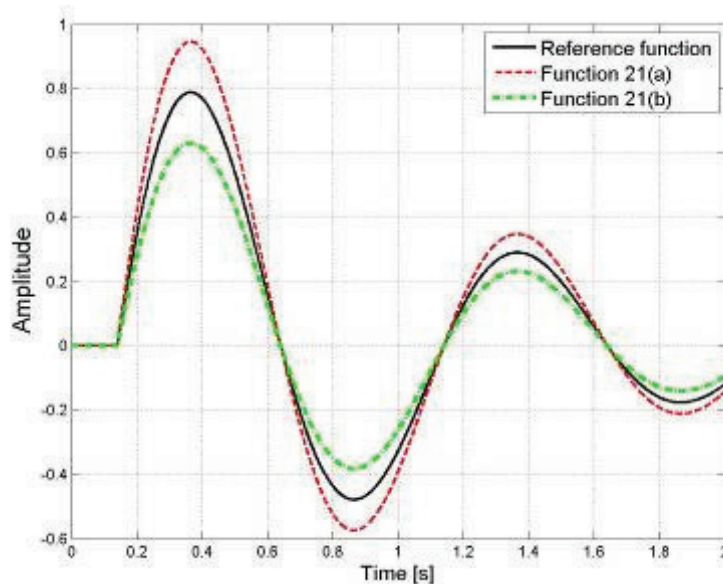


Figure 5.10. Comparison of function 21(a) and 21(b) to the reference function

Table 5.12. Comparison between the error measures' ability to quantify the accuracy (Function 21(a) and 21(b))

	Function 21(a)			Function 21(b)		
	S&G	Russell	$m\%RE^m$	S&G	Russell	$m\%RE^m$
Magnitude	20	13.57		-20	-16.14	
Phase	0	0		0	0	
Comprehensive	20	12	20 P(100)	20	14.3	20 P(100)

The comprehensive error of S&G and $m\%RE^m$, in the example where function 21(a) and 21(b) were used, is easy to interpret and captures the agreement of the two models. The magnitude and phase error of S&G provide additional information indicating that the error is due to a difference in the magnitude. However, when we consider two models with only a phase difference and no magnitude difference, as in Figure 5.11 for Function 22(a) and 22(b), the results of the validation metrics need more consideration to understand what they actually mean. Considering the magnitude and phase error obtained from S&G for Function 22(a) and 22(b), it is clear that there is little difference in the magnitude compared to the reference function and that there exist a phase difference of almost 20% (see Table 5.13). However, the meaning of the comprehensive errors is not as clear. The comprehensive error of S&G in the

comparisons of Functions 21(a) and (b) and Functions 22(a) and (b) are effectively equal. However, at time 0.4s the value that Function 21(a) had to predict is 20% higher than the reference function's value. At the same time (0.4s) the value that Function 22(a) had to predict is 30% lower than the reference function's value.

The $m\%RE^m$ gives a comprehensive error that is easier to interpret. In comparing Function 21(a) to the reference function the $m\%RE$ indicates that all the predicted values deviate less than 20% from the measured value. In comparing Function 22(a) to the reference function the $m\%RE^m$ indicates that 53.1% of the errors between the responses are smaller than 60.3%. The magnitude and phase error of S&G for Function 21(a) and (b) and 22(a) and (b) is easily interpretable, whereas its comprehensive error is not, as discussed above. Combining the magnitude and phase errors of S&G with the comprehensive error of the $m\%RE^m$, we obtain a validation metric that has a meaningful comprehensive error. Furthermore, this combination of S&G and the $m\%RE^m$ makes it possible to determine whether the error is in the magnitude and/or in the phase.

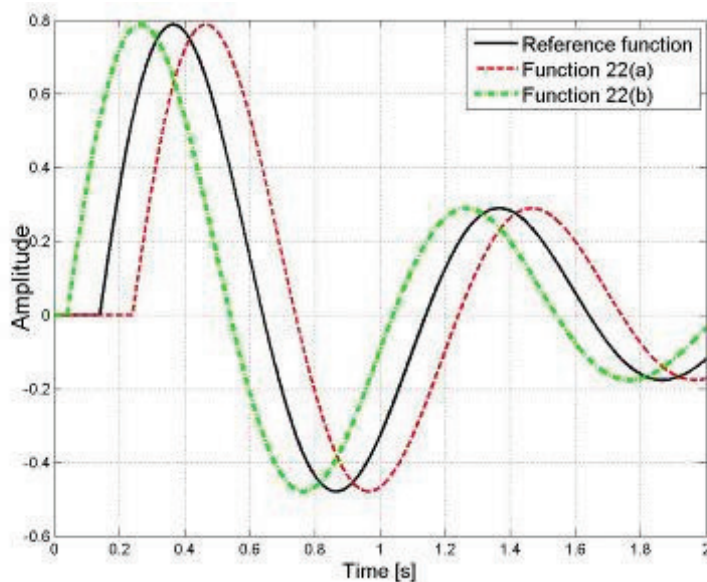


Figure 5.11. Comparison of functions 22(a) and 22(b) to the reference function

Table 5.13. Comparison between the error measures ability to quantify the accuracy (Function 22(a) and 22(b))

	Function 22(a)			Function 22(b)		
	S&G	Russell	$m\%RE^m$	S&G	Russell	$m\%RE^m$
Magnitude	-0.48	-0.41		0.14	0.122	
Phase	19.5	19.5		19.5	19.5	
Comprehensive	19.5	17.3	60.3 P(53.1)	19.5	17.3	59.4 P(51.9)

3.1.3. Combination of S&G and the modified $\%RE$

Figure 5.12 shows two approximations obtained from Model 1 and Model 2 both having the same deviation in phase from the true value. The amplitude of Model 1 is 10% higher than the measured value and Model 2 is 10% lower. The results for the different validation metrics are shown in Table 5.14. Analyzing the results of the different validation metrics on their own are not as insightful as combining them. When we combine the magnitude and phase error of S&G with the comprehensive error of the $m\%RE^m$ we can form the following conclusion. The agreement of both Model 1 and Model 2 is approximately similar with roughly 58% of the

$\%RE$ being below 51%. The deviation of both Model 1 and Model 2 is due to a difference in both phase and magnitude. Model 1 and Model 2 have the same difference in phase with the amplitude of model 1 being 10 % higher than the true signals amplitude and Model 2 10% lower. In the context of the validation procedure the magnitude error measure does not mean that Model 1 over predicts the true (measured) values and that Model 2 will under predict the values. If the phase difference between the two signals were zero then the magnitude error measured of S&G would have indicated that Model 1 over predicts the true data and Model 2 under predicts the data. In order to comment on Model 1 and Model 2 over or under predicting the values, the relationship between the relative error and the ratio of p/m, as discussed in paragraph 2.2.1, should be used to calculate whether the model is under or over predicting.

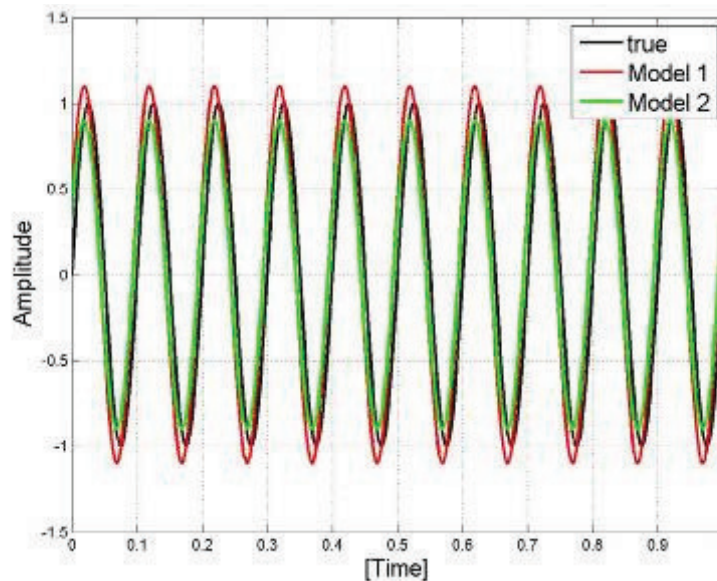


Figure 5.12. Model 1 and Model 2 with same phase shift but different magnitudes

Table 5.14. Comparison between error measures for models with same phase shift but different magnitudes

	Model 1			Model 2		
	S&G	Russell	$m\%RE^m$	S&G	Russell	$m\%RE^m$
Magnitude	10	7.6		-10	-8.3	
Phase	12.7	12.7		12.7	12.8	
Comprehensive	16.2	13.2	51.3 P(55.6)	16.2	13.5	48.5 P(57.6)

3.2. Case studies

Three case studies will now be used to further compare the validation metrics. The reliability and usefulness of the validation metric's results in quantifying the measure of agreement between the experimental and simulated data is investigated using these case studies.

The first case study will consider the comparison of two arbitrary models' predictions to measured data. The percentage relative error between the two models and the measured data is known. The second case study will compare both formulations of the elasto-plastic leaf spring model from Chapter 3 to the experimental data from Chapter 2. The final case study will use the validation metrics to compare the accuracies of the elasto-plastic leaf spring model and the neural network model of the multi-leaf spring. The two models' computational efficiencies will also be compared.

3.2.1. Case study 1: Known error between signals

Consider the two predicted SRQs obtained from Model 1 and Model 2 shown in Figure 5.13. The $\%RE$ between the two predicted SRQs and the measured SRQ are known and shown in Table 5.15. The results for the different metrics are shown in Table 5.16. Looking at the comprehensive errors of S&G and Russell, Model 1 seems to be a closer fit to the measured data than Model 2. However, when we consider the $\%RE$ between the models and the measured data, shown in Table 5.15, it is clear that Model 2 has the smaller $\%RE$ and is therefore closer to the measured data. The $m\%RE^m$ metric correctly shows that Model 2 is closer to the measured data stating that 60% of the errors are smaller than 35.2%. When the magnitude and phase errors of S&G are considered along with the results from the $m\%RE^m$ metric for Model 2 it can be seen that the difference in magnitude is the major contributor to the errors as the error in phase is small. For Model 1 the magnitude and phase errors of S&G give similar results and it is difficult to conclude whether the deviation is due to an error in the magnitude or an error in the phase. From Figure 5.13 it seems as if the deviation is largely due to an error in the magnitude.

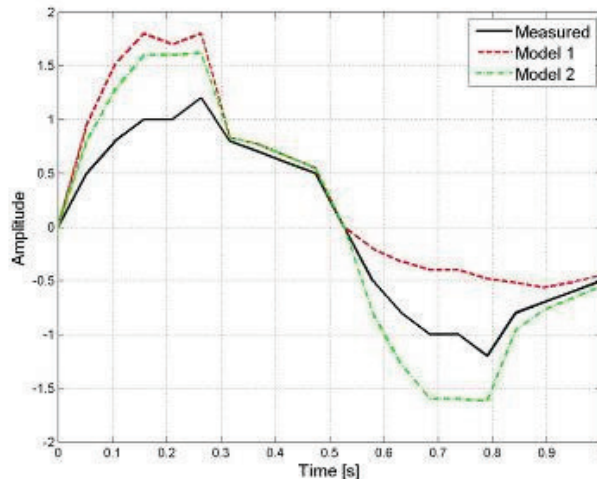


Figure 5.13. Two models with known $\%RE$ relative to the measured data

Table 5.15. Relative error between Model 1, Model 2 and the measured data

Data point	Model 1	Model 2
1	0	0
2	90	60
3	90	60
4	80	60
5	70	60
6	50	35
7	4	4
8	10	10
9	10	10
10	10	10
11	0	0
12	-60	60
13	-60	60
14	-60	60
15	-60	60
16	-60	35
17	-35	20

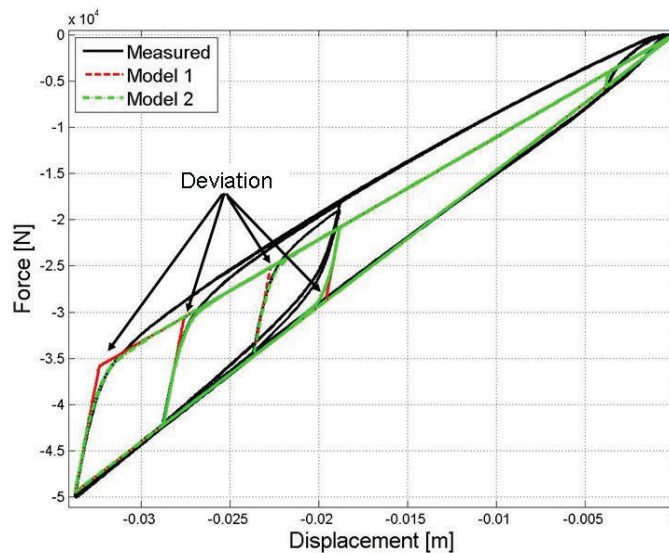
Data point	Model 1	Model 2
18	-20	10
19	-15	10
20	-10	10
mean($1\%REI$)	39.7	31.7
mean($1\%REI$) (without zero)	44.1	35.2

Table 5.16. Comparison between error measures for known $\%RE$

	Model 1			Model 2		
	S&G	Russell	$m\%RE^m$	S&G	Russell	$m\%RE^m$
Magnitude	16.28	11.3		41.8	23.3	
Phase	16.27	16.2		4.75	4.8	
Comprehensive	23	17.5	44.1 P(50)	42.1	21.1	35.2 P(60)

3.2.2. Case study 2: Elasto-plastic leaf spring model

In this case study the two formulations of the elasto-plastic leaf spring model, presented in Chapter 3, will be compared to the measured data taken on the physical multi-leaf spring using the quantitative validation metrics. Two models of the multi-leaf spring are created; Model 1 uses the elastic-linear formulation of the elasto-plastic leaf spring model and Model 2 the elastic-nonlinear formulation. Both models are given the same displacement input as was given to the physical spring during the experimental characterisation. Figure 5.14 shows the qualitative comparison of the two models against the measured data.


Figure 5.14. Qualitative comparison of predictions by leaf spring models and measured data

Both models give similar results except for the transition region where the two models' prediction deviate. Model 2, which uses the elastic-nonlinear formulation, gives better predictions in this transition region and should result in more accurate predictions than the elastic-linear model. Table 5.17 shows the quantitative results for the different validation metrics when comparing the prediction of Model 1 and Model 2 with the measured data. All the metrics indicate that Model 1 gives better predictions. The metrics of S&G and Russell gives very similar results for the two models. The result from the quantitative validation metrics seem to be in contradiction to the conclusion drawn from the qualitative comparison

in Figure 5.14. However, after closer inspection of the measured signal we see that there exists noise around zero which is shown in Figure 5.15. The actuators controller was such that the actuator was not very stable at zero load and resulted in the noise shown. Therefore, all the measurements below 25N were set equal to zero.

Table 5.17. Results with noise on measured data around zero

	Model 1				Model 2			
	S&G	Russell	$m\%RE^m$	$m\%RE^s$	S&G	Russell	$m\%RE^m$	$m\%RE^s$
Magnitude	2.46	2.06			2.6	2.17		
Phase	1.64	1.64			1.5	1.5		
Comprehensive	2.96	2.33	26.39 P(68)	10 P(39.07)	3.0	2.34	54.01 P(49.64)	10 P(31.43)

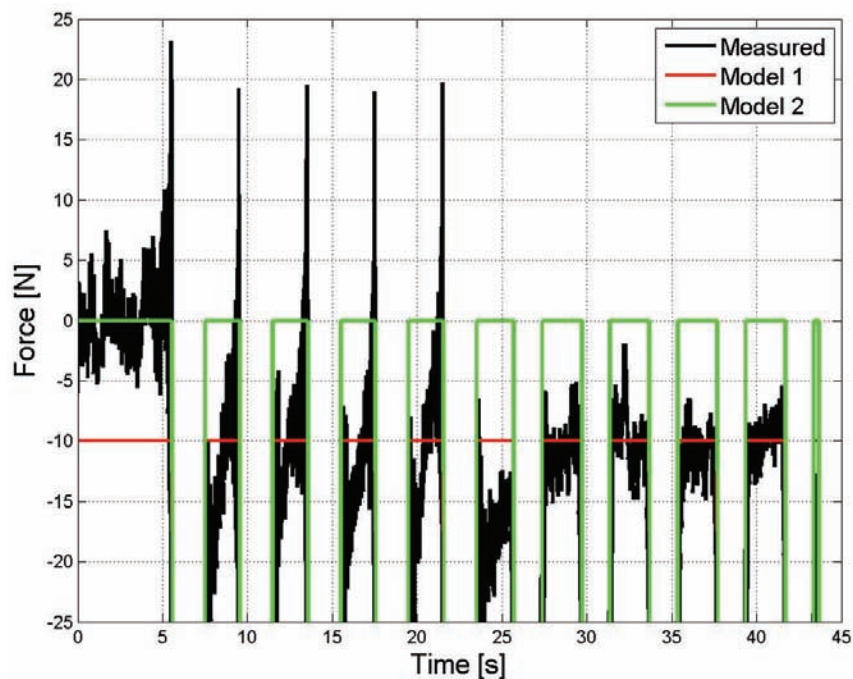


Figure 5.15. Noise on measurement signal around zero

Removing the noise on the measurement error around zero by reassigning all measurements lower than 25N to 0N, gave the results shown in Table 5.18. The results for S&G and Russell stay the same whereas the results from the modified $\%RE$ (for both the $m\%RE^m$ and the $m\%RE^s$) changes and show that Model 2 is significantly better than Model 1. When Figure 5.14 is viewed it would be expected that Model 2 would be more accurate than Model 1 but that the results would be very similar. After closer inspection of the prediction of Model 1, it was found that Model 1 had an error in predicting the zero values correctly (see Figure 5.15). The figure shows that Model 1 predicts a value of -10N instead of zero. After the cause for the error in the prediction of Model 1 had been identified and the model refined the results are obtained shown in Table 5.19. S&G and Russell still gives the same results, with the results from all the metrics now showing similar results with the modified percentage relative error indicating that Model 2 is slightly better than Model 1.

Table 5.18. Results with noise on measured data around zero removed

	Model 1				Model 2			
	S&G	Russell	$m\%RE^m$	$m\%RE^s$	S&G	Russell	$m\%RE^m$	$m\%RE^s$
Magnitude	2.46	2.06			2.6	2.17		
Phase	1.64	1.64			1.5	1.5		
Comprehensive	2.96	2.33	53.52 P(49.61)	10 P(31.13)	3.0	2.34	16.98 P(89.38)	10 P(76.04)

Table 5.19. Results with noise on measured data around zero removed and Model 1 refined

	Model 1				Model 2			
	S&G	Russell	$m\%RE^m$	$m\%RE^s$	S&G	Russell	$m\%RE^m$	$m\%RE^s$
Magnitude	2.46	2.06			2.6	2.17		
Phase	1.64	1.64			1.5	1.5		
Comprehensive	2.96	2.33	17.26 P(88.83)	10 P(75.72)	3.0	2.34	17.01 P(89.37)	10 P(76.01)

S&G and Russell indicated from the start that the difference between the models should not be far from each other but the use of the modified $\%RE$ metric showed that there were large errors between the SRQs and helped with identifying the error in Model 1. Both metrics from S&G and Russell stayed the same throughout the analysis. The removal of the noise around zero on the measurement signal and the error in the predictions of the zero values of Model 1 did not influence the metrics of S&G and Russell. This is due to these two metrics being insensitive to small absolute errors between the signals. This is as a result of the formulations of the magnitude errors. Both formulations of the modified $\%RE$ continually gave an accurate representation of the accuracy between the models. This example also shows that the modified $\%RE$ and especially the $m\%RE^s$ can easily be used to compare the validation measure's results to predefined accuracy requirements. An accuracy requirement of 10% or closer could have been defined and Model 2 having 76.01% of the model's predictions below 10% may indeed satisfy the requirements.

3.2.3. Case study 3: Comparison of accuracy and efficiency of leaf spring modelling methods

The two formulations of the elasto-plastic leaf spring model were compared to the measured data in paragraph 3.2.2. The two showed similar results with the elastic-nonlinear formulation giving slightly better predictions for the behaviour of the multi-leaf spring. The elastic-nonlinear formulation of the elasto-plastic leaf spring model will now be compared to the neural network model of the multi-leaf spring. Details of the two models used here to model the multi-leaf spring were given in Chapter 3.

The two main aspects of interest in this comparison are the accuracy and efficiency of each model. The same displacement input signal is given to both models. Figure 5.16 shows the force-displacement characteristics from the two models compared to the measured data. Table 5.20 shows the results for the various validation metrics. The validation metrics of S&G and Russell indicate that the neural network gives more accurate predictions. However, the modified $\%RE$ indicate that the accuracy of the neural network is not as good as the elastic-nonlinear model. From Figure 5.16 it can be seen that the neural network gives better predictions overall, however, the predictions of the neural network is not that good near zero. This can be seen more clearly on Figure 5.17 which shows the time history of the measured force as well as the forces predicted by the two models. Figure 5.17(a) and (b) shows the error the neural network makes in predicting the force around zero. The validation metrics of S&G and Russell is able to show that the neural network model give overall better predictions with

the modified %RE indicating that the accuracy is not that good due to the error the neural network makes in the force predictions near zero. This again shows that the metrics from S&G and Russell are not sensitive to the small absolute errors and that the modified percentage relative error gives the true agreement/disagreement between the two signals.

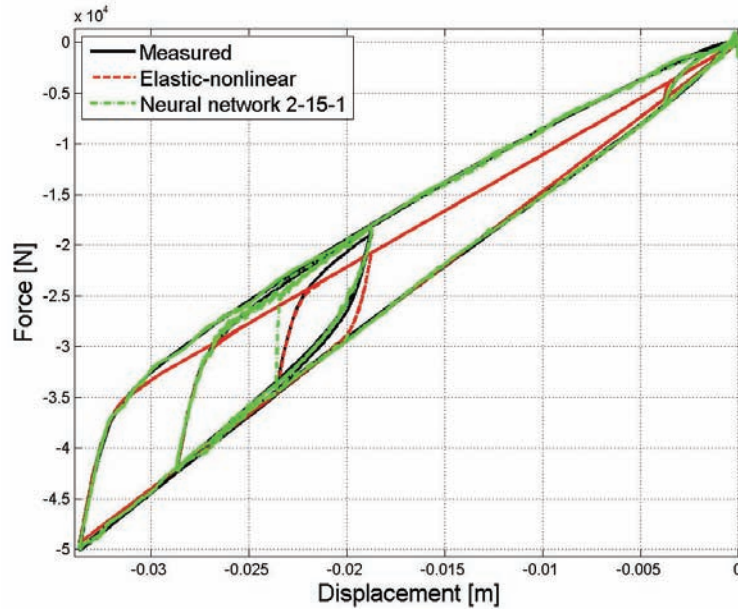


Figure 5.16. Comparison of force-displacement characteristics between the measured data and the elastic-nonlinear and neural network model

Table 5.20. Accuracy of elastic-nonlinear and neural network model

	Elastic-nonlinear model				Neural network model			
	S&G	Russell	$m\%RE^m$	$m\%RE^s$	S&G	Russell	$m\%RE^m$	$m\%RE^s$
Magnitude	2.6	2.17			-0.025	-0.021		
Phase	1.5	1.5			0.5	0.5		
Comprehensive	3.0	2.34	17.01 P(89.37)	10 P(76.01)	0.5	0.44	49.27 P(51.52)	10 P(49.67)

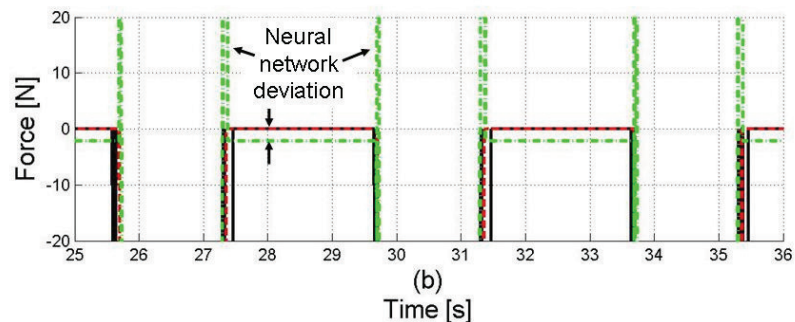
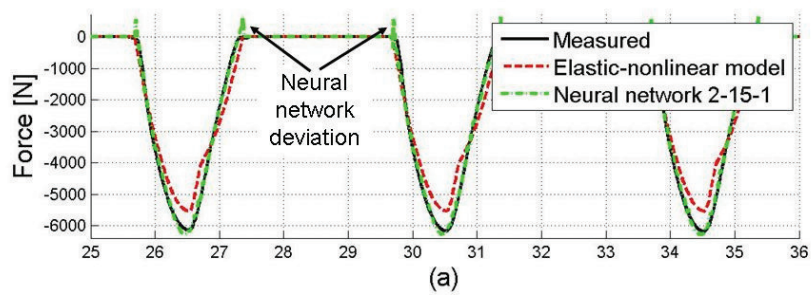


Figure 5.17. Error that neural network makes in predicting zero force

The results in Table 5.20 were for the evaluation of the entire force signal shown in Figure 5.18. It was shown that the neural network has an error in the forces it predicts near zero. When evaluating the section of the force signal which is not near zero, and therefore does not include these errors, the accuracy of the neural network model can be seen to be better than the elastic-nonlinear model. The results of the various validation metrics applied only to the inner loop, as shown in Figure 5.18, are given in Table 5.21. The results from Table 5.21 show that the predictions from the neural network are better than the elastic-nonlinear model.

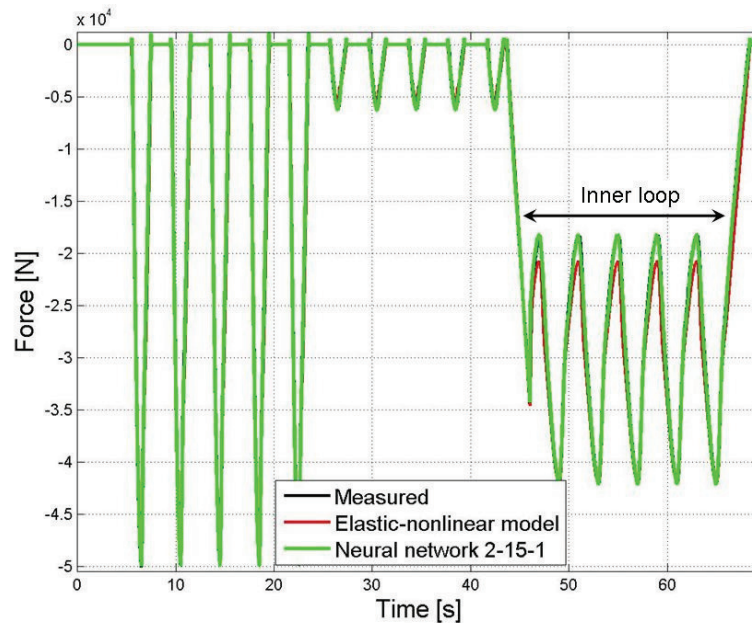


Figure 5.18. Time histories of the measured force and predicted force from the elastic-nonlinear and neural network model

Table 5.21. Accuracy of elastic-nonlinear and neural network model for the inner loop only

	Elastic-nonlinear model				Neural network model			
	S&G	Russell	$m\%RE^m$	$m\%RE^s$	S&G	Russell	$m\%RE^m$	$m\%RE^s$
Magnitude	3.42	2.82			-0.035	-0.03		
Phase	1.32	1.32			0.59	0.59		
Comprehensive	3.66	2.76	5.62 P(55.69)	10 P(72.85)	0.59	0.53	1.2 P(67.16)	10 P(99.3)

The results from Table 5.20 and Table 5.21 seem to indicate that when the predictions of the neural network around zero are improved it will be the more accurate model to use. It will also be the most computationally efficient. The elastic-nonlinear model took 0.2429s to solve for the spring force for the given displacement input whereas the neural network model took 0.0792s. The neural network is three times faster than the elastic-plastic leaf spring model.

4. Conclusion

An overview of the V&V process was presented and briefly discussed. From literature two validation metrics were identified and compared to the validation metric that is based on relative error. The challenges associated with using the $\%RE$ as a validation metric was discussed and techniques were presented to circumvent these challenges. From the comparisons of the three validation metrics it was found that the validation metrics give similar results when ranking models and in selecting the best model. It was shown that the

comprehensive error of the modified $\%RE$ validation metric is the most reliable in providing a representative measure of the agreement/disagreement between two SRQs. Furthermore, when used in combination with the magnitude and phase errors of other measures such as S&G it gives information that enables the ranking of models, selecting the best model, fault finding and refinement, and ultimately validation of the model.

The modified $\%RE$ validation metric gives a comprehensive error and can not distinguish between an error in phase or an error in magnitude. It is suggested that when comparing analytical functions that the modified $\%RE$ be used together with the magnitude and phase error measures such as presented by S&G. When SRQs are compared that are obtained from a simulation model and a physical system, the modified $\%RE$ should rather be used with qualitative comparisons methods as this might give the analyst a holistic view and make the identification of the possible causes for the deviation more likely.

It was shown that the modified $\%RE$ validation metric gives a reliable and easily interpretable metric that will enable the quantification of the agreement of the simulation model's predictions against the measurements on the physical system and comparison to the accuracy requirements. The modified $\%RE$ can also be used on analytical functions and on deterministic SRQs with an independent variable other than time.

Chapter 6

Conclusions and Recommendations

This chapter presents the final conclusions and the recommendations for future work. The recommendations are done such that it corresponds to the chapter the work was presented in the study.

1. Conclusions

The aim with this study was to obtain a validated simulation model of a leaf spring suspension system that can be used in durability simulations. A systematic approach was followed by starting at component level, obtaining the necessary validated models and then proceeding by including more detail to the model, continuously validating the model until a model of the complete suspension system is obtained. In order to validate the models created in this study extensive experimental characterisation was performed to obtain the necessary data that would be required in the parameterisation and validation of the various models.

The study started at component level with the modelling of two leaf springs. Validated models, able to represent the multi-leaf and parabolic leaf spring, was developed in Chapter 3. A novel elasto-plastic leaf spring model was proposed that could emulate the complex behaviour of both leaf springs without requiring the microscopic modelling of complex physical phenomena such as the tribological processes. The elasto-plastic leaf spring model gives accurate predictions of the behaviour of both the multi-leaf spring as well as the parabolic leaf spring. In addition to the physics based elasto-plastic leaf spring model a non physics-based neural network model was also used to model the multi-leaf spring. A simple feed forward neural network was constructed that was able to emulate the vertical behaviour of the multi-leaf spring. It was however shown that the neural network model is not able to predict the correct response for inputs that fall outside the range of the training data used. Therefore, it is required that a comprehensive set of experimental data be available in order to construct a training data set that covers the entire working range of the inputs to the neural network. Alternatively, the neural network can be used as a gray-box by using the elasto-plastic leaf spring model to generate the required training data as the elasto-plastic leaf spring model required a lot less experimental data in order to parameterise it.

The elasto-plastic leaf spring model was integrated into an ADAMS/Car subsystem and was used to model the spring only setup in Chapter 4 using ADAMS-SIMULINK co-simulation. The results showed that the model of the spring only setup is able to predict the vertical and longitudinal forces acting at the suspension attachment points. The results obtained indicated that the elasto-plastic leaf spring model can be integrated into a suspension model in order to

predict the forces that are transmitted on to the chassis. The spring only setup can now be extended to include more detail.

Chapter 5 discussed the verification and validation process. A quantitative validation metric was proposed that is able to give an accurate representation of the agreement/disagreement between two signals. The modified percentage relative error validation metric that was proposed is based on the well-known relative error. The challenges associated with using a simple metric such as the relative error when comparing periodic signals around zero was addressed and was compared to two other validation metrics. The three validation metrics were compared by applying them to various signals and it was shown that the modified percentage relative error always gives a true representation of the agreement/disagreement between two signals. The modified percentage relative error was used to compare the accuracies of the two formulations of the elasto-plastic leaf spring model as well as the neural network model. It was shown that the elastic-linear formulation of the elasto-plastic leaf spring model was slightly more accurate than the elastic-linear formulation. The comparison between the elastic-nonlinear formulation and the neural network model showed that the neural network model, after some refinement, will be more accurate. Along with the comparison of the two modelling techniques' accuracies their computational efficiencies were also compared. The neural network showed a computational efficiency that is three times faster than the elasto-plastic leaf spring model.

The elasto-plastic leaf spring and neural network leaf springs can now be used in further studies to obtain more detailed models of the suspension system. The recommendations for future work are given next.

2. Recommendations

This study addressed various aspects concerning the physical suspension system, its components and the various models that were created. From the work done in this study the following recommendations can be made for future work concerning the physical systems and models concerned.

2.1. Chapter 2

Chapter 2 looked at the experimental characterisation of the multi-leaf spring and parabolic leaf spring. The suspension system was also characterised using either the multi-leaf spring or the parabolic leaf spring. Two 6clcs were manufactured, calibrated, verified and validated. It was concluded that the most probable cause for the discrepancy between the virtual measurements and physical measurements of the 6clc was due to the uncertainties of the exact size of the resultant force applied to the 6clc and the exact point of application. It is recommended that a more precise experimental setup be used to obtain the experimental data to validate the 6clc model. In this setup attention should be given especially to the measurement of the applied force's orientation as well as its point of application.

In the experimental characterisation two setups were used namely, the spring only setup and the in-service setup. The two setups were used to show the dependency of the force-displacement characteristics of the two leaf springs on certain parameters (such as the loaded length). In future work the force-displacement characteristics of both the multi-leaf spring as well as the parabolic leaf spring should be obtained using a support profile that induces a continuous loaded length change of the leaf spring. This data can then be used to validate the

leaf spring model that attempts to replicate the observed behaviour. This property may give the vehicle designer significant scope for fine-tuning the suspension characteristics by simply modifying the profile of the spring supports.

2.2. Chapter 3

In this chapter attention was given to the modelling of the multi-leaf spring and the parabolic leaf spring. Two models were used to model the vertical behaviour of the multi-leaf spring i.e. the elasto-plastic leaf spring model and a neural network model. Only the elasto-plastic leaf spring model was used to model the parabolic leaf spring. The recommendations for future work on the two modelling techniques are given in the following two paragraphs.

2.2.1. Elasto-plastic leaf spring model

Future work on this model should include:

- **Ramberg-Osgood formulation**
 Two formulations were presented for the elasto-plastic leaf spring model namely the elastic-linear and elastic-nonlinear formulations. The development and feasibility of another formulation that is based on the the Ramberg-Osgood relations (Dowling, 1999) should be investigated. The Ramberg-Osgood relationship may give a hybrid method between the elastic-linear model and the elastic-nonlinear model. It is postulated that this formulation will only require knowledge of stiffness of the solid beam (k), and the stiffness of the layered beam during loading and unloading (k_{UL} and k_L) but will be able to predict the smooth transition between the solid beam stiffness and the layered beam stiffness.
- **Investigate alternative methods for handling the friction.**
 The elasto-plastic leaf spring model does not handle the friction as a separate quantity but includes it in the two parameters of the layered beam stiffnesses (k_L and k_{UL}). This is the reason why the layered beam has two stiffnesses in the elasto-plastic leaf spring model. If the friction can be accurately captured by a parameter specific to the friction it would imply that a single value may be obtained for the layered beam stiffness. This may then enable the friction and the layered beam stiffness to be calculated theoretically. It was already shown that the solid and layered beam stiffnesses can be calculated theoretically, it should however be investigated whether it will be possible to calculate the friction theoretically.
- **Visualization of slip planes**
 The slip planes were observed visually with a simple experiment in Chapter 3 (see Figure 3.5). The insight gained from using stereography to measure the displacement field over the entire leaf spring as the spring is deflected will be valuable and will serve as further confirmation of the different phases (i.e. solid beam - transition - layered beam)
- **Theoretical stiffness of leaf springs**
 Apply the equations presented in Appendix B to calculate the stiffness of other types of leaf springs such as leaf springs with blades having a parabolic thickness profile. It was shown in this study that the two stiffness regimes (solid beam and layered beam) of a multi-leaf spring can be theoretically calculated using the equations presented in

Appendix B. The theoretical calculation of the stiffness of the parabolic leaf spring can be investigated in future work.

The equation in Appendix B used to calculate the stiffness of the layered beam does not include any frictional effects, whereas the physical leaf spring has friction that influences the stiffness. Methods should be investigated which will be able to account for the frictional effect and enable the theoretical calculation of the hysteresis present in multi-leaf springs.

- Supports inducing continuous loaded length change
The combined elasto-plastic leaf spring model and the model accounting for changes in the loaded length should be used in future work to investigate the ability of the model to simulate a leaf spring in which the supports induce a continuous change in the loaded length as the leaf spring is deflected.
- Source of nonlinearity in parabolic leaf spring
It was mentioned in paragraph 3.2 in Chapter 3 that the parabolic leaf spring has some nonlinear behaviour in the layered beam region which the elasto-plastic leaf spring model is not able to capture. It was stated that the cause for the nonlinear behaviour is not exactly clear but it is believed to be due to the friction process. The source for the nonlinear behaviour should be investigated. Once the source has been determined it would make it possible to refine the elasto-plastic leaf spring model in order to capture this behaviour more accurately.

2.2.2. Neural network model

It was shown that a neural network is able to emulate the vertical behaviour of the multi-leaf spring. It was also shown that the neural network is not able to predict the correct response when given inputs that fall outside the range of the training set. It was shown in paragraph 4.1.2 of Chapter 3 that the neural network leaf spring model is dependent on the excitation frequency whereas it was shown in Chapter 2 that the physical multi-leaf spring's force-displacement characteristic was independent of the excitation frequency. From this it is postulated that the choice of input variables to the neural network might influence the ability of the network to generalize the behaviour and predict the correct response for inputs that fall outside the range of the training set. It is proposed that the use of different inputs to the neural network, and its affect on the ability of the neural network to predict the response for inputs outside the range of the training set, be investigated.

2.3. Chapter 4

After the validated leaf spring models, created in Chapter 3, the spring only model was the next step in the systematic approach. The elasto-plastic leaf spring model was integrated into a subsystem model of the spring only setup. The model showed that it was able to give good predictions of the forces that are transmitted to the chassis. The model of the spring only setup should be refined and extended to include the radius rod. This will then effectively model the in-service setup which is the next step in the systematic approach that was shown in Figure 4.1. The experimental characteristics have already been obtained to validate all the models up to and including the complete suspension system.

2.4. Chapter 5

This chapter presented a validation metric that can be used in a quantitative validation process. The validation metric is based on the simple relative error. The challenges associated with using the relative error on periodic signals around zero were addressed. The proposed modified percentage relative error validation metric was applied to several case studies and compared to two other validation metrics that were identified from a literature study. The results from the modified percentage relative error metric indicated that it is able to represent the true overall relative error between two signals. The $m\%RE$ validation metric should be extended to quantify model and experimental measurement uncertainties. The use of the relative error's characteristic (discussed in paragraph 2.2.1 in Chapter 5) to quantify the tendency of the model to over-or under predict should be investigated and incorporated into the $m\%RE$.

Bibliography

A

ASME standards (2006), “ASME V&V 10-2006 Guide for Verification and Validation in Computational Solid Mechanics”, The American Society of Mechanical Engineers, New York

ASTM Standard E 140-02 (2002), “Standard Hardness Conversion Tables for Metals. Relationship Among Brinell Hardness, Vickers Hardness, Rockwell Hardness, Superficial Hardness, Knoop Hardness, and Scleroscope Hardness”, *ASTM International*, West Conshohocken, PA, USA

B

Babuska, I. and Oden, J.T. (2004), “Verification and validation in computational engineering and science: basic concepts.”, *Comput. Methods Appl. Mech. Engrg.* 193:4057-4066

Bernard, J.E. and Clover, C.L. (1994), “Validation of Computer Simulations of Vehicle Dynamics”. *SAE Transactions*, 940231

C

Callister, W.D. (2003), “Material Science and Engineering - An Introduction”, 6th ed., Wiley, Hoboken, NJ

Cebon, D. (1986), “Simulation of the Response of Leaf Springs to Broad Band Random Excitation”, *Vehicle System Dynamics*, Vol. 15, No.6, pp. 375-392

Cole, D.J. and Cebon, D. (1994), “Predicting Vertical Dynamic Tire Forces of Heavy Trucks”, *Vehicle-Road Interaction, ASTM STP 1225*, B. T. Kulakowski, Ed., American Society for Testing and Materials, Philadelphia, pp. 27-35

Cosme, C., Ghasemi, A. and Gandevia, J. (1999), “Application of Computer Aided Engineering in the Design of Heavy-Duty Truck Frames”, *SAE Transactions*, 1999-01-3760

Czichos, H. (1978), “Tribology – A systems approach to the science and technology of friction, lubrication and wear”, Elsevier, New York

D

Dowling, N.E. (1999), “Mechanical behavior of materials – Engineering methods for deformation, fracture and fatigue”, 2nd ed., Prentice Hall, Upper Saddle River, NJ

Dreyfus, G. (2005), “Neural networks – Methodology and applications”, Springer-verlag, Heidelberg, New York

E

Edara, R. Shih, S., Tamini, N., Palmer, T. and Tang, A. (2005), “Heavy Vehicle Suspension Frame Durability Analysis Using Virtual Proving Ground”, *SAE Transactions*, 2005-01-3609

ELMadany, M.M. (1987), “Nonlinear ride analysis of heavy trucks”, *Computers & Structures*, Vol. 25, No. 1, pp. 69-82

Ekici, B. (2005), “Multi-response optimisation in a three-link leaf-spring model”, *Int. J. Vehicle Design*, Vol. 38, No.4, pp. 326-346

F

Fancher, P.S., Ervin, R.D., MacAdam, C.C. and Winkler, C.B. (1980), “Measurement and Representation of the Mechanical Properties of Truck Leaf Springs”, SAE Technical Paper 800905

Ferry, W.B., Frise, P.R., Andrews, G.T. and Malik, M.A. (2002), “Combining virtual simulation and physical vehicle test data to optimize durability testing”, *Fatigue & Fracture of Engineering Materials and Structures*, Vol. 25, Issue 12, pp.1127-1134

Figliola, R.S. and Beasley, D.E. (2006), “Theory and Design for Mechanical Measurements”, Fourth Edition, Wiley and Sons.

G

Geers, T.L. (1984), “An objective error measure for the comparison of calculated and measured transient response histories”, *The shock and vibration bulletin*, 54:99-107

Gere, J.M. (2004), “Mechanics of materials”, 6th ed., Brooks/Cole, Belmont, California

Ghazi Zadeh, A., Fahim, A. and El-Gindy, M. (2000), “Neuro-leaf spring”, *Heavy Vehicle Systems, A Series of the International Journal of Vehicle Design*, Vol. 7, No. 4, pp. 317-335

H

Hagan, M.T., Howard, B.D. and Beale, M. (1996), “Neural network design”, PWS publishing company, Boston, MA

Heydinger G.J., Garrot W.R., Chrstos J.P. and Guenther D.A. (1990), “A Methodology for Validating Vehicle Dynamics Simulations”, *SAE Technical Paper 900128*

Hoyle, J.B. (2004), “Modelling the static stiffness and dynamic frequency response characteristics of a leaf spring truck suspension”, *Proc. of IMechE, Part D: J. Automobile Engineering*, Vol. 218, pp. 259-278

Huhtala, M., Vesimaki, M. and Halonen, P. (1994), “Computer Simulation of Road-Vehicle Dynamic Interaction Forces of Three-and Four-Axle Trucks”, in Kulakowski, B.T. (Ed.): *Vehicle –Road Interaction*, pp.36-51, ASTM STP 1225, American Society for Testing and Materials, Philadelphia

J

Jayakumar, P., Alanoly, J. and Johnson, R. (2005), “Three-Link Leaf-Spring Model for Road Loads”, *SAE Technical Paper 2005-01-0625*

K

Kat, C. and Els, P.S. (2011), “Importance of correct validation of simulation models”, *Proc. ASME 2011 International Design Engineering Technical Conferences & Computers and Information in Engineering Conferences*, Aug. 29-31, Washington, DC, USA

Kyowa (2011), Available at <http://www.kyowa-ei.co.jp/english/products/gages/pdf/bridge.pdf>, [Accessed on 09 July 2011]

L

Li, Q. and Li, W. (2004), “A Contact finite element algorithm for the multileaf spring of vehicle suspension systems”, *IMEC-E Part D: J. Autom. Engrg.*, Vol. 218, pp. 305-314

M

- Merkle, A.P and Marks, L.D. (2007)**, “A predictive analytical friction model from basic theories of interfaces, contacts and dislocations”. *Tribology Letters*, Vol. 26, No.1, pp. 73-84
- Milliken, W.F. and Milliken, D.L. (2002)**, “Chassis Design: Principles and Analysis”, SAE, Warrendale, PA.
- Monroe (2011)** Monroe Shocks and Struts, [Online] available at <http://www.monroe.com.au/trade-corner/tech-info/suspension-systems/rear-suspensions.html> (Accessed on 11 Oktober 2011)
- Moon, I.d., Kim, G.t., Lim, J.h. and Hwang, Y. (2007)**, “A Flexible Multi-Body Dynamic Model for Analyzing the Hysteretic Characteristics and the Dynamic Stress of a Taper Leaf Spring”, *SAE Technical Paper 2007-01-0852*
- Müller, B., Reinhardt, J. and Strickland, M.T. (1995)**, “Neural networks – An Introduction“, 2nd ed., Springer-Verlag, Heidelberg, New York.

O

- Oberkampf, W.L. and Barone, M.F. (2006)**, “Measures of agreement between computation and experiment: Validation metrics”, *Journal of Computational Physics*, 217, pp.5-36
- Oberkampf, W.L. and Trucano, T.G. (2002)**, “Verification and validation in computational fluid dynamics”, *Progress in Aerospace Sciences*, Vol. 38 pp. 209-272
- Omar, M.A., Shabana, A.A., Mikkola, A., Loh, W and Basch, R (2004)**, “Multibody System Modeling of Leaf Springs”, *J. of Vibration and Control*, Vol. 10, No. 11, pp.1601-1638
- Oxford Dictionaries (2011)** Dictionary, [Online] available at <http://www.oxforddictionaries.com/definition/tribology?region=us> (Accessed on 19 September 2011)

P

- Prasade, U., Medepalli, S., Moore, D. and Rao, R.N. (2006)**, “Beam Element Leaf Spring Suspension Model Development and Assessment Using Road Load Data”, *SAE Technical Paper 2006-01-0994*

Q

Qin, P., Dentel, G. and Mesh, M. (2002), “Multi-leaf spring and Hotchkiss suspension CAE simulation”, *ABAQUS Users’ Conference*

R

Rill, G., Kessing, N., Lange, O. and Meier, J. (2003), “Leaf Spring Modelling for Real Time Applications”, *Proceedings of International Association of Vehicle System Dynamics (IAVSD) 18th Symposium*, Atsugi, Japan

Roy, C.J. and Oberkampf, W.L. (2011), “A comprehensive framework for verification, validation, and uncertainty quantification in scientific computing”, *Computer methods in applied mechanics and engineering*, 200:2131-2144

Russell, D.M. (1997a), “Error Measures for Comparing Transient Data: Part I: Development of a Comprehensive Error Measure”, *Proceedings of the 68th Shock and Vibration Symposium, Hunt Valley, MD*, pp. 175 – 184

Russell, D.M. (1997b), “Error Measures for Comparing Transient Data: Part II: Error Measures Case Study”, *68th Shock and Vibration Symposium, Hunt Valley, MD*, pp. 185 – 198

S

SAE Spring Design Manual (1996), 2nd ed., *Society of Automotive Engineers, Inc.*, 400 Commonwealth drive, Warrendale, PA

Sarin, H., Kokkolaras, M., Hulbert, G., Papalambros, P., Barbat, S. and Yang, R.-J. (2010), “Comparing Time Histories for Validation of Simulation Models: Error Measures and Metrics”, *J. Dynamic Systems, Measurement, and Control*, Vol. 132

Schwer, L.E. (2007), “Validation metrics for response histories: perspectives and case studies”, *Engineering with Computers*, 23:295-309

Sprague, M.A. and Geers, T.L. (2003), “Spectral elements and field separation for an acoustic fluid subject to cavitation”, *J. Computational Physics*, 184:149-162

Sprague, M.A. and Geers, T.L. (2006), “A spectral-element/finite-element analysis of a ship-like structure subjected to an underwater explosion”, *Computer methods in applied mechanics and engineering*, 195:2149-2167

Sugiyama, H., Shabana, A.A., Omar, M.A. and Loh, W. (2006), “Development of nonlinear elastic leaf spring model for multibody vehicle systems”, *Computer methods in applied mechanics and engineering*, Vol. 195, pp. 6925-6941

T

Tavakkoli, S., Aslani, F., Rohweder, D.S. and Savanur, S. (1996), “Analytical predictions of Leaf spring bushing loads using MSC/NASTRAN and MDI/ADAMS”, MSC conference proceedings, viewed 14 October 2011,
< http://www.mscsoftware.com/support/library/conf/wuc96/11b_asla.pdf>.

V

Van de Wetering Engineering (2001), “Owners Handbook”, Rosslyn, South Africa

W

West York Steel, (2009), Available at: <http://www.westyorkssteel.com/EN19.html> [Accessed on 14 October 2009]

Y

Yang, Y., Ren, W., Chen, L., Jiang, M. and Yang, Y. (2007), “Study on ride comfort of tractor with tandem suspension based on multi-body system dynamics”, *Applied mathematical modeling*, doi:10.1016/j.apm.2007.10.011

Appendix A

Six component load cell (6clc)

This appendix is concerned with the development of the six component load cell. It discusses the calibration of the uni-axial (tension-compression) load cells, the verification of the concept of the 6clc as well as the verification of the model of the 6clc that was created in ADAMS/Car. The verification is done by using the analytical equations that were derived. The validation of both the analytical and ADAMS/Car model against experimental measurements are presented. Paragraph A.1 discusses the calibration of the individual uni-axial load cells and paragraph A.2 discusses the verification and validation of the physical and virtual six component load cell.

A.1. Calibration of uni-axial load cells

The uni-axial load cell forms the basis of the 6clc. The 6clc is formed by connecting six uni-axial load cells between two parts in such a way that all six degrees of freedom between the two parts are removed. The uni-axial load cells are orientated such that each uni-axial load cell is only in tension or compression. Figure A.1 shows the two parts with the six uni-axial load cells connecting them. Figure A.2 shows one of the uni-axial load cells.

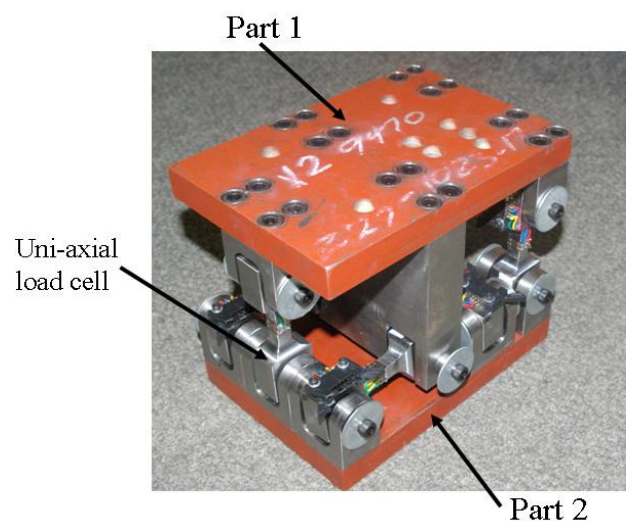


Figure A.1. Six component load cell

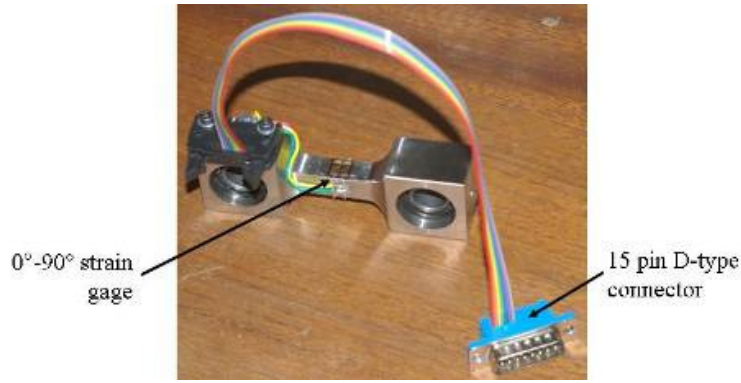


Figure A.2. Uni-axial load cell

The uni-axial load cell was designed to be able to handle 5000 kg without yielding and with a cross-sectional area that will give good sensitivity for the strain measurements. In order to measure the strain two 0°-90° strain gages were placed on opposite sides of the reduced cross-sectional area of the uni-axial load cell (see Figure A.2). A full bridge configuration was used as shown in Figure A.3. This configuration allows for temperature compensation, the cancellation of the thermal effect of the lead wires as well as cancelling bending. It is not expected that the uni-axial load cells will have any bending imposed on them as they will be connected to the two parts in the 6clc via spherical bearings.

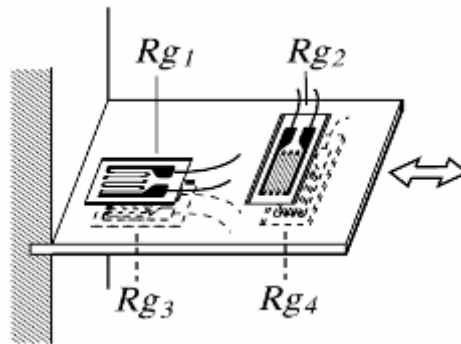


Figure A.3. Full bridge configuration used in uni-axial load cells (Kyowa, 2011)

The force is obtained from the uni-axial load cell by taking the measured strain (ϵ) and multiplying it by the Young’s Modulus (E) of the material and the cross-sectional area (A) of the uni-axial load cell (Eq.{A.1}). The cross-sectional area of each of the uni-axial load cells were measured with a micrometer. The cross-sectional areas of each of the uni-axial load cells are given in Table A.1, with the diagram in Figure A.4 indicating where Dim 1 and Dim 2 were measured. Note that the cross-sectional area of uni-axial load cell L1 is not included in the table. The measurement was not taken as the strain gages were on the load cell before the measurements of the cross-sectional area were taken.

$$F = \epsilon EA \tag{A.1}$$

Table A.1. Cross-sectional area of the uni-axial load cells

Uni-axial load cell	Dim 1 [mm]	Dim 2 [mm]	Cross-sectional area [m ²]
L2	10.37	10.37	0.00010754
L3	10.02	10.40	0.00010421
L4	9.81	9.79	0.00009604
L5	9.77	9.84	0.00009614
L6	9.93	9.82	0.00009751

L7	9.95	9.90	0.00009851
L8	9.73	9.76	0.00009496
L9	9.85	9.86	0.00009712
L10	9.89	9.86	0.00009752
L11	10.01	9.89	0.00009900
L12	9.77	9.77	0.00009545
L13	9.73	9.75	0.00009487

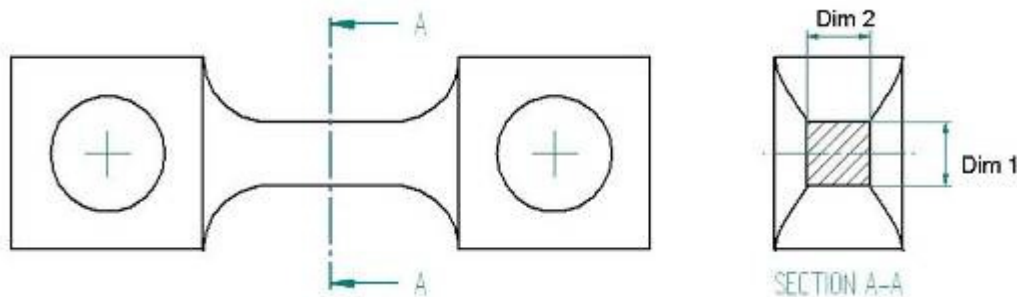


Figure A.4. Cross-sectional area of uni-axial load cell

Before the uni-axial load cells were calibrated the tensile strength of the material used to manufacture the uni-axial load cells were measured to make sure that the material used conformed to specification. The permitted force that can be applied without the load cell yielding was calculated using material data. It is important that the uni-axial load cell is not physically deformed as this may cause damage to the strain gages and affect the measurements obtained from the uni-axial load cells. The uni-axial load cells are made of EN19 steel (condition T). A hardness test was performed on two of the uni-axial load cells with four measurements taken on each. The hardness tester used gave the Vickers and Rockwell (C-scale) hardness as output. The Vickers harness (HV) values obtained from the test were converted to Brinell hardness (HB) by means of the ASTM Standard E 140-02 (2002). A test load of 294.2N was used with a dwell time of 5s.

The tensile strength was calculated from the Brinell hardness using Equation {A.2} (Callister, 2003). The results for the hardness test and the calculated tensile strength values are given in Table A.2. For sample 1 a mean tensile strength of 1017.7MPa with a standard deviation of 29.8MPa was obtained and for sample 2 a mean tensile strength of 1116.3MPa with a standard deviation of 26.7MPa was obtained. The mean tensile strengths that were obtained from the tests for the two samples show good agreement to typical tensile strength values of EN19 steel (condition T) (West York Steel, 2009).

$$TensileStrength(MPa) = 3.45 \times HB \quad \{A.2\}$$

Table A.2. Results of harness tests

	HV (Vickers hardness)	HRC (Rockwell hardness. C-scale)	HB (Brinell hardness)	Tensile strength [MPa]
Sample 1:				
Measurement 1	304.2	30.2	287.6	992.22
Measurement 2	306.4	30.5	290	1000.5
Measurement 3	311.9	31.2	295.4	1019.13
Measurement 4	323.5	32.6	307	1059.15
Mean				1017.7
Standard deviation				29.8

	HV (Vickers hardness)	HRC (Rockwell hardness. C-scale)	HB (Brinell hardness)	Tensile strength [MPa]
Sample 2:				
Measurement 1	331.6	33.5	315	1086.75
Measurement 2	338.3	34.2	320.6	1106.07
Measurement 3	344.8	34.8	325.4	1122.63
Measurement 4	351.8	35.7	333.3	1149.89
Mean				1116.3
Standard deviation				26.7

Each uni-axial load cell is calibrated separately against a reference load cell. The reference load cell was calibrated against a DH Budenburg dead-weight tester. The uni-axial load cell is placed in series with the reference load cell in a Schenck Hydropulse, as shown in Figure A.5, and calibrated.

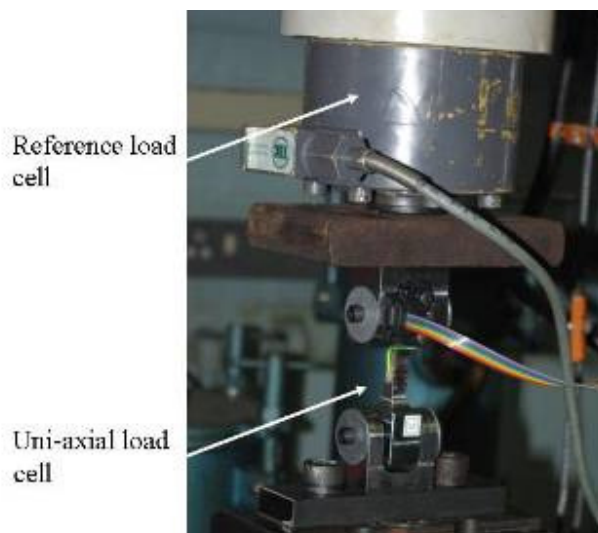


Figure A.5. Experimental setup for calibrating the uni-axial load cells

The calibration of the uni-axial load cells were performed by firstly subjecting all of them to a sinusoidal load with an amplitude of 22 300N around a mean of -22 300N and a frequency of 0.5Hz. They were subjected to ± 70 cycles. This was done as it was initially observed that when the uni-axial load cell was loaded and unloaded for a few cycles an offset between the uni-axial load cell and the reference load cell's force measurement was present (see Figure A.6). This was the case for all the uni-axial load cells. The uni-axial load cells can not be used if they are not able to return to the same initial force value after the loading has been removed. After investigating this phenomenon it was found that after subjecting them to a number of cycles this offset disappeared (see Figure A.7). It was concluded that there might be residual stresses left on the surface of the load cell from manufacturing and after a few cycles of loading and unloading these residual stresses are relieved. For this reason all the load cells were subjected to a cyclic loading in order to relieve these residual stresses. In hindsight it might have been beneficial to anneal the load cells before the strain gages were applied in order to remove residual stresses. However, the method used seems to effectively relieve the residual stresses.

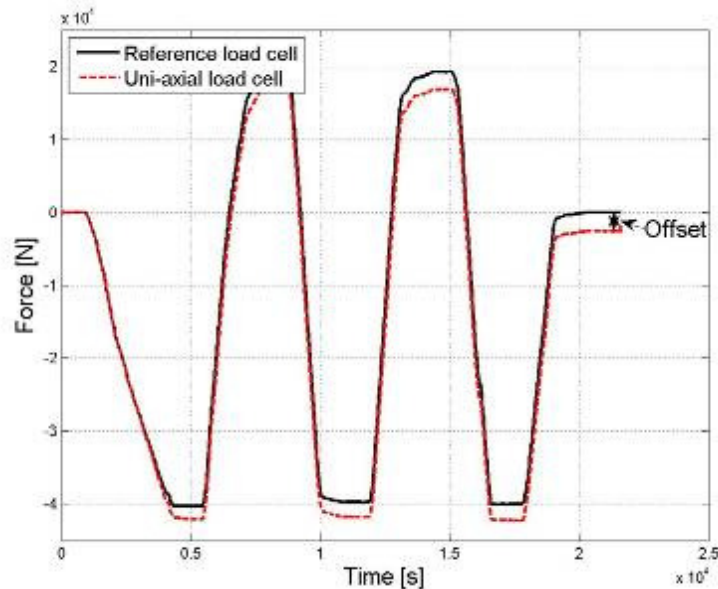


Figure A.6. Offset present in uni-axial load cell (Uni-axial load cell L13)

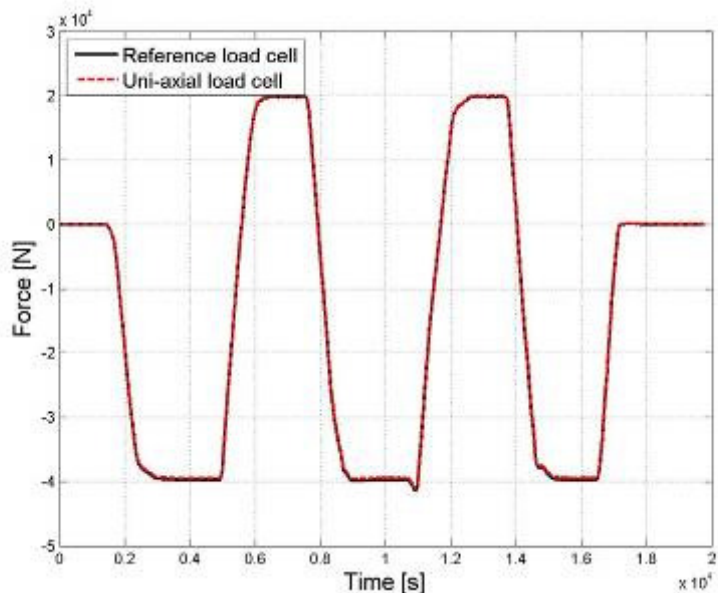
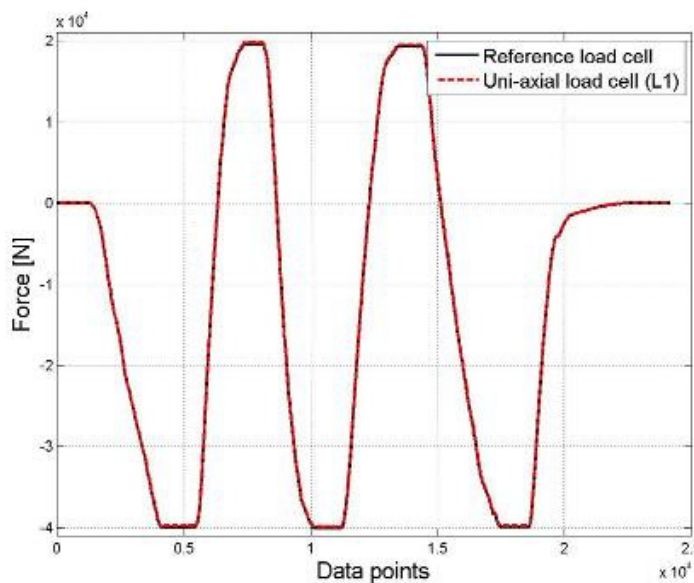


Figure A.7. Offset absent after cyclic loading (Uni-axial load cell L13)

After the residual stresses were relieved the uni-axial load cells were given a hand generated input that ranged from $-39\,639\text{N}$ to 19819.6N . This signal was used to calibrate the uni-axial load cells. This is also the signal that was used in Figure A.6 and Figure A.7. The uni-axial load cells were calibrated by comparing the force calculated from Eq.{A.1} against the force measured by the reference load cell. The maximum difference between these two signals is then minimized by adjusting the Young's modulus (E). The calibrated Young's modulus (E) which results in the best correlation between the uni-axial load cell's and reference load cell's force is given in Table A.3. It should be noted that the calibrated Young's modulus takes effects such as the misalignment of the strain-gages into account. The Young's modulus are adjusted as the value for this parameter is more uncertain in this case than the cross-sectional area that was used. Figure A.8 shows the correlation between the calibrated uni-axial load cell's and reference load cell's force measurements using the calibrated values for the Young's modulus. Similar results were obtained for the other twelve load cells. From these results it was concluded that the uni-axial load cells are calibrated and can now be used in the 6clc.

Table A.3. Calibrated Young's modulus

Uni-axial load cell	Calibrated Young's modulus (E) [GPa]
L1	207.09
L2	192
L3	200.41
L4	211.54
L5	211.34
L6	208.4
L7	210
L8	211.5
L9	211
L10	210.4
L12	211
L13	211.35
Mean	208
Standard deviation	5.9


Figure A.8. Calibrated uni-axial load cell (L1) compared to reference load cell

A.2. Verification and Validation of the physical and virtual 6clc

Twelve of the calibrated uni-axial load cells from paragraph A.1 is now incorporated into two 6clcs each using six uni-axial load cells. The two 6clcs will be referred to as the front 6clc and the rear 6clc. Figure A.9 shows the axis system that is used for both the front and rear 6clcs. All measurements and dimensions are relative to the centre of volume (cv) of the 6clc. The verification process will firstly establish whether the concept of the 6clc can indeed work and that it can measure the forces between the chassis and the suspension system. Secondly, the virtual 6clc created in ADAMS/Car will be verified. Analytical equations will be derived in order to verify the concept of the 6clc as well as to verify the ADAMS/Car model. After the concept of the 6clc and the ADAMS/Car model have been verified, both the analytical equations and the ADAMS/Car model will be validated against experimental measurements.



Figure A.9. 6clc axis system

Table A.4 shows the four load cases that were used in the verification and validation process. Table A.4 shows the load direction as well as the application point of the applied force relative to the cv of the 6clc for each load case.

Table A.4. Load cases used in verification process

	Load direction	Application point	Application point coordinates (Theoretical)
Load case 1	Vertical (negative z-direction)	Center (at the origin of the xy-plane)	[0, 0, 0.085]
Load case 2	Vertical (negative z-direction)	Off center	[0.0475, 0.04, 0.085]
Load case 3	Lateral (y-direction)	Off center	[0.035,-0.0175,0.115]
Load case 4	Longitudinal (negative x-direction)	Off center	[0.0575,-0.0175, 0.101]

A.2.1. Verification of 6clc

As mentioned, the verification process will establish whether the concept of the 6clc as well as whether the virtual 6clc created in ADAMS/Car is correct. This is done by deriving the equations which calculates the three forces and three moments due to the force applied to the 6clc. The reference point for these forces and moments is the centre of volume (cv) of the 6clc. The three forces and three moments acting at the centre of volume of the 6clc are referred to as the equivalent forces and moments. Similarly, a set of equations are derived to calculate the equivalent forces and moments using the forces in the uni-axial load cells. The results of these two sets of equations are then compared and are expected to give the same results for the equivalent forces and moments. The comparison between these two sets of equations will indicate whether the 6clc is able to measure the equivalent forces and moments correctly and whether the concept of the 6clc is feasible. The equation will also be used to verify the virtual 6clc.

A.2.1.1. Derivation of analytical equations

Figure A.10 shows a schematic of the 6clc indicating the position of the applied force which is used in the derivation of the equations. The figure also indicates the position and orientation of the six uni-axial load cells. The equations are derived by considering the free-body diagram of Part 1 in the zy-, zx-, and xy-planes, respectively. Summing the forces in the two directions

and the moments about the third direction for each plane, will result in a set of six equations from which the equivalent forces and moments can be calculated.

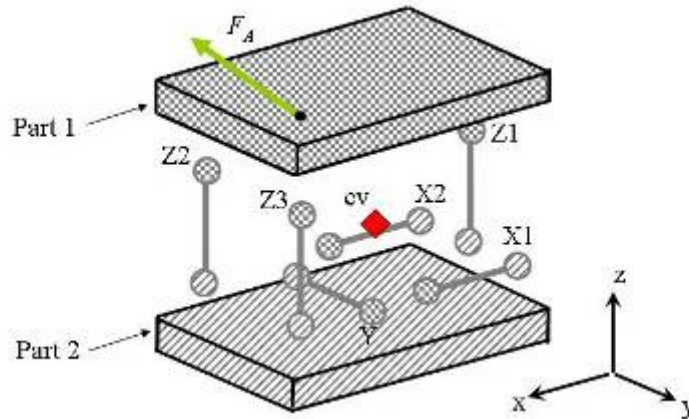


Figure A.10. Schematic of 6clc and the six uni-axial load cells it consists of

zy-plane:

Figure A.11 shows the free-body diagram of Part 1 in the zy-plane. Summing the forces in the y- and z-directions and the moment about the x-axis gives the following equations:

$$\begin{aligned} \sum F_z = 0: & \quad Z_1 + Z_2 + Z_3 = F_{Az} \\ \sum F_y = 0: & \quad Y = F_{Ay} \\ \sum M_x = 0: & \quad d_{Yz} Y - d_{Z_2y} Z_2 + d_{Z_3y} Z_3 = d_y F_{Az} - d_z F_{Ay} \end{aligned}$$

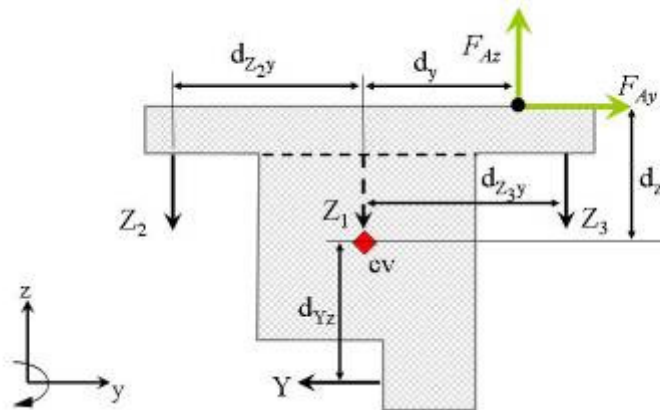


Figure A.11. Free body diagram of Part 1 in the zy-plane

zx-plane:

Figure A.12 shows the free-body diagram of Part 1 in the zx-plane. Summing the forces in the x- and z-direction and the moment about the y-axis gives the following equations:

$$\begin{aligned} \sum F_z = 0: & \quad Z_1 + Z_2 + Z_3 = F_{Az} \\ \sum F_x = 0: & \quad X_1 + X_2 = F_{Ax} \\ \sum M_y = 0: & \quad -d_{X_{12z}} (X_1 + X_2) + d_{Z_1x} Z_1 - d_{Z_2x} Z_2 - d_{Z_3x} Z_3 = d_z F_{Ax} - d_x F_{Az} \end{aligned}$$

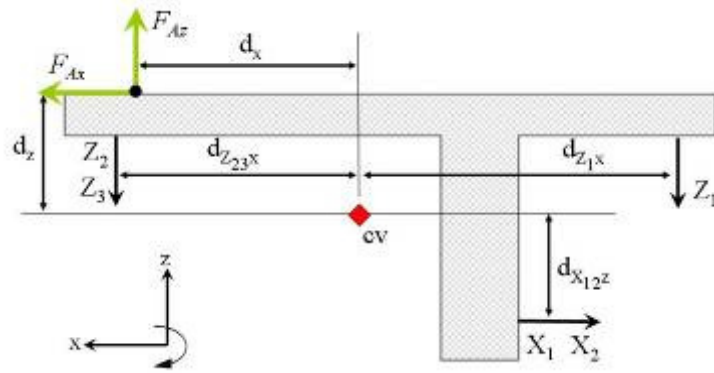


Figure A.12. Free body diagram of Part 1 in the zx-plane

xy-plane

Figure A.13 shows the free-body diagram of Part 1 in the xy-plane. Summing the forces in the x- and y-direction and the moment about the z-axis gives the following equations:

$$\begin{aligned} \sum F_x = 0: & \quad X_1 + X_2 = F_{Ax} \\ \sum F_y = 0: & \quad Y = F_{Ay} \\ \sum M_z = 0: & \quad -d_{x_1y}X_1 + d_{x_2y}X_2 + d_{yx}Y = d_xF_{Ay} - d_yF_{Ax} \end{aligned}$$

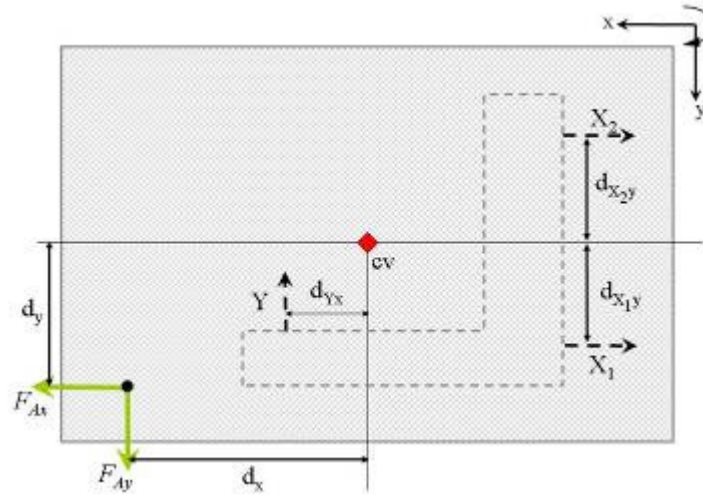


Figure A.13. Free-body diagram of Part 1 in the xy-plane

Combining the forces and moment equations derived from the zy-, zx- and xy-plane the following set of equations are obtained:

$$\begin{aligned} X_1 + X_2 &= F_{Ax} \\ Y &= F_{Ay} \\ Z_1 + Z_2 + Z_3 &= F_{Az} \\ d_{yz}Y - d_{z_2y}Z_2 + d_{z_3y}Z_3 &= d_yF_{Az} - d_zF_{Ay} \\ -d_{x_{12z}}(X_1 + X_2) + d_{z_1x}Z_1 - d_{z_23x}Z_2 - d_{z_{23x}}Z_3 &= d_zF_{Ax} - d_xF_{Az} \\ -d_{x_1y}X_1 + d_{x_2y}X_2 + d_{yx}Y &= d_xF_{Ay} - d_yF_{Ax} \end{aligned} \tag{A.3}$$

The left hand side of the set of equations in Eq.{A.3} is equal to the equivalent forces and moments due to the forces in the uni-axial load cells, whereas, the right hand side is equal to the equivalent forces and moments due to the applied force. It is therefore possible to write the set of equations into two sets calculating either the equivalent forces and moments from the applied force (Eq.{A.4}) or the equivalent forces and moments from the forces in the uni-axial load cells (Eq.{A.5}). The set of equations in Eq.{A.3} can also be used to calculate the forces in the uni-axial load cells due to an applied force (Eq.{A.6}).

Equivalent forces and moments calculated from applied force

In order to calculate the equivalent forces and moments from the applied force, Eq.{A.3} is simply rewritten as Eq.{A.4}. The applied force (F_A) and its application point (d_x, d_y, d_z) relative to the cv is known and the equivalent forces (F_x, F_y, F_z) and moments (M_x, M_y, M_z) can be calculated.

$$\begin{aligned}
 F_x &= F_{A_x} \\
 F_y &= F_{A_y} \\
 F_z &= F_{A_z} \\
 M_x &= d_y F_{A_z} - d_z F_{A_y} \\
 M_y &= d_z F_{A_x} - d_x F_{A_z} \\
 M_z &= d_x F_{A_y} - d_y F_{A_x}
 \end{aligned} \tag{A.4}$$

Equivalent forces and moments calculated from the forces in the uni-axial load cells

In order to calculate the equivalent forces and moments from the forces in the uni-axial load cells, Eq.{A.3} is simply rewritten as Eq.{A.5}. The forces in the uni-axial load cells (X_1, X_2, Y, Z_1, Z_2 and Z_3) are known and the equivalent forces (F_x, F_y, F_z) and moments (M_x, M_y, M_z) can be calculated.

$$\begin{aligned}
 F_x &= X_1 + X_2 \\
 F_y &= Y \\
 F_z &= Z_1 + Z_2 + Z_3 \\
 M_x &= d_{y_z} Y - d_{z_2_y} Z_2 + d_{z_3_y} Z_3 \\
 M_y &= -d_{x_{12_z}} (X_1 + X_2) + d_{z_1_x} Z_1 - d_{z_2 z_3_x} (Z_2 + Z_3) \\
 M_z &= -d_{x_{1_y}} X_1 + d_{x_{2_y}} X_2 + d_{y_x} Y
 \end{aligned} \tag{A.5}$$

Calculate force in uni-axial load cells due to applied force

The set of equations in Eq.{A.3} can be written in matrix form $Ax = b$, as shown in Eq.{A.6}.

$$\begin{bmatrix} 1 & 1 & 0 & 0 & 0 & 0 \\ 0 & 0 & 1 & 0 & 0 & 0 \\ 0 & 0 & 0 & 1 & 1 & 1 \\ 0 & 0 & d_{Yz} & 0 & -d_{Z2y} & d_{Z3y} \\ -d_{X12z} & -d_{X12z} & 0 & d_{Z1x} & -d_{Z23x} & -d_{z23x} \\ -d_{X1y} & d_{X2y} & d_{Yx} & 0 & 0 & 0 \end{bmatrix} \begin{Bmatrix} X_1 \\ X_2 \\ Y \\ Z_1 \\ Z_2 \\ Z_3 \end{Bmatrix} = \begin{Bmatrix} F_{Ax} \\ F_{Ay} \\ F_{Az} \\ d_y F_{Az} - d_z F_{Ay} \\ d_z F_{Ax} - d_x F_{Az} \\ d_x F_{Ay} - d_y F_{Ax} \end{Bmatrix} \quad \{A.6\}$$

Substituting $d_{X1y} = d_{X2y} = d_{Z2y} = d_{Z3y}$ with d_1

$$d_{Yx} = d_{X12z} = d_{Yz} \text{ with } d_2$$

$$d_{Z1x} = d_{Z23x} \text{ with } d_3$$

we can rewrite matrix A as follows:

$$A = \begin{bmatrix} 1 & 1 & 0 & 0 & 0 & 0 \\ 0 & 0 & 1 & 0 & 0 & 0 \\ 0 & 0 & 0 & 1 & 1 & 1 \\ 0 & 0 & d_2 & 0 & -d_1 & d_1 \\ -d_2 & -d_2 & 0 & d_3 & -d_3 & -d_3 \\ -d_1 & d_1 & d_2 & 0 & 0 & 0 \end{bmatrix}$$

The values for d_1 , d_2 and d_3 are obtained from the dimensions of the 6clc. Substituting the values of $d_1=0.045m$, $d_2=0.035m$ and $d_3=0.0825m$ into matrix A the determinant of the matrix can be calculated. The $\det(A) = 0.0013$ and implies that the system of linear equations has a unique solution because $\det(A) \neq 0$. This implies that Eq.{A.3} rewritten in the form of Eq.{A.6} can be used to calculate the forces in the uni-axial load cells due to the applied force.

A.2.1.2. Verification of 6clc concept

Comparing the results from Eq.{A.4} and Eq.{A.5} we can verify whether the 6clc can indeed measure the equivalent forces and moments correctly. Figure A.14 shows the results obtained from Eq.{A.4} and Eq.{A.5} when a force (F_A)¹ is applied to the 6clc. This figure shows that Eq.{A.4} and Eq.{A.5} does indeed give the same answers and implies that the concept is feasible. It should be noted that in order to get the results in Figure A.14 the force in the uni-axial load cells (X_1 , X_2 , Y , Z_1 , Z_2 and Z_3), used in Eq.{A.5}, was obtained from solving Eq.{A.6}. Note that both Eq.{A.4} and Eq.{A.6} uses the applied force (F_A) and its associated coordinates (d_x , d_y and d_z). This may lead to errors in the equations being disguised as the inputs equal the outputs, and vice versa. The second part of the verification procedure may help to identify problems with the equations. A model of the 6clc is created in ADAMS/Car. The same applied force¹ used to generate the results in Figure A.14 will be applied to the ADAMS/Car model. The reaction forces measured by the ADAMS/Car model will then be substituted into Eq.{A.5} in order to calculate the equivalent forces and moments that can be compared with the results of Eq.{A.4}. If the comparisons show good correlation

¹ For this example the applied force had the following characteristic: $F_{Ax} = 200 \sin(2\pi ft)$ N,

$F_{Ay} = 150 \sin(2\pi ft)$ N and $F_{Az} = 2000 \sin(2\pi ft)$ N. Applied at [0m, 0.001m, 0.085m].

then we will consider the analytical equations and the ADAMS/Car model, of the 6clc, verified. The next step will then be to validate the results from the analytical equations and the ADAMS/Car model against experimental measurements.

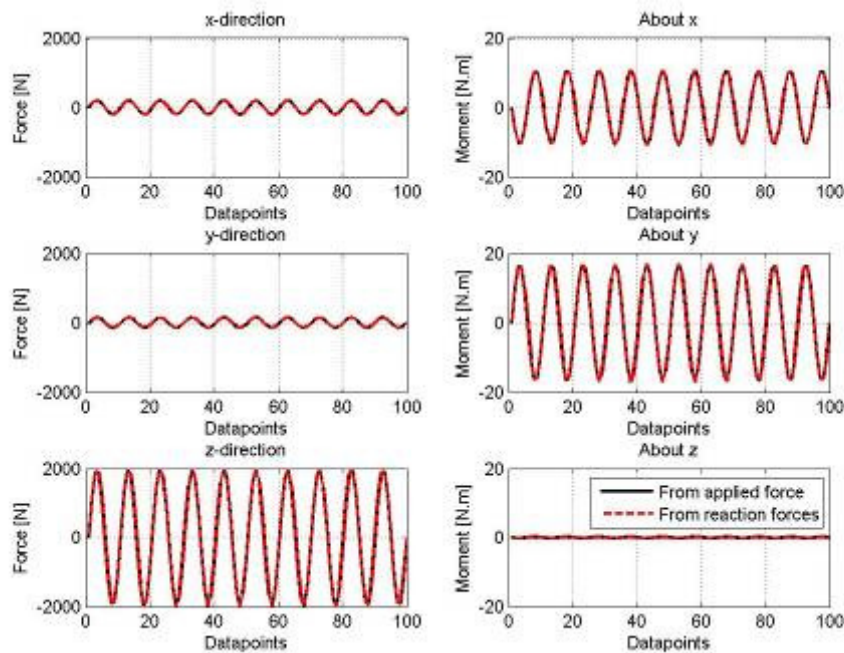


Figure A.14. Compare results from Eq. {A.4} and Eq. {A.5}

A.2.1.3. Verification of the 6clc ADAMS/Car model

This paragraph considers the verification of the ADAMS/Car model. The 6clc that is modelled in ADAMS/Car consists of:

- 15 Moving Parts (not including ground)
- 1 Cylindrical Joint
- 6 Spherical Joints
- 6 Translational Joints
- 6 Constant velocity Joints
- 1 Fixed Joint
- 1 Inplane Primitive Joint
- 7 Motions

The 6clc model has zero degrees of freedom. Figure A.15 shows the ADAMS/Car model of the 6clc. The force is applied to the 6clc model via three point-point actuators each representing the three components of the applied force. Each component can be given a specified force. The 6clc model measures the forces in the uni-axial load cells through the translational joints that are used to connect the two bodies representing the uni-axial load cells. The two bodies are connected to the two parts of the 6clc via a spherical joint at the one end and a constant velocity joint at the other end.

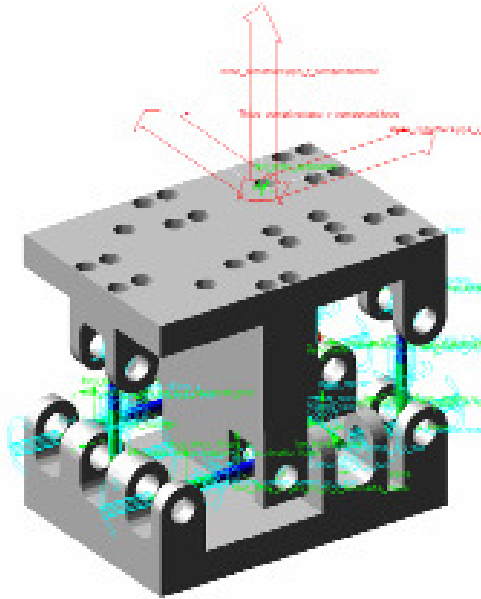


Figure A.15. ADAMS/Car model of 6clc

Before the 6clc model is subjected to the load cases that were shown in Table A.4 the ADAMS/Car model was analysed with no external force applied to it. The results obtained from the analytical equations and the ADAMS/Car model is shown in Table A.5. As expected the results of the analytical equations are zero for the force in the uni-axial load cells and for the equivalent forces and moments. The forces in the uni-axial load cell in the ADAMS/Car models, however, have non-zero values and therefore give non-zero values for the equivalent forces and moments. This difference is due to the mass of the two parts not being included in the analytical equation, whereas in the ADAMS/Car model the mass was included. It is expected that when the 6clc load cell is orientated such that the gravitational field acts in the negative z-direction, and has no force applied to it, that X_1 , X_2 , Y , F_x , F_y and M_z should be zero, but Table A.5 indicates that this is not the case. The non-zero values of these parameters are merely a result of the centre of mass of the 6clc not going through the centre of volume. The values for the forces in the uni-axial load cells shown in Table A.5 for the ADAMS/Car model will be subtracted from the ADAMS/Car measurements for X_1 , X_2 , Y , Z_1 , Z_2 and Z_3 . This is done as the measurements of X_1 , X_2 , Y , Z_1 , Z_2 and Z_3 in the physical 6clc load cell was zeroed when under its own mass.

Table A.5. Results from analysis with no load applied to 6clc

	Analytical Eq.{A.4} and Eq.{A.5} [N]	ADAMS/Car model [N]
Forces in uni-axial load cells		
X_1	0	1.6439e-007
X_2	0	-2.1334e-007
Y	0	2.5271e-007
Z_1	0	-42.1146
Z_2	0	-18.147
Z_3	0	-25.0167
Equivalent forces		
F_x	0	-4.8946e-008
F_y	0	2.5271e-007
F_z	0	-85.2783

	Analytical Eq. {A.4} and Eq. {A.5} [N]	ADAMS/Car model [N]
Equivalent moments		
M_x	0	-0.30914
M_y	0	0.086554
M_z	0	-8.1529e-009

Using Load case 1, we will check whether cross-sensitivity between the uni-axial load cells in the three directions exists. With Load case 1, X_1 , X_2 , Y , F_x , F_y and M_z is expected to be zero. The results from the analytical equations are indeed zero for X_1 , X_2 , Y , F_x , F_y and M_z whereas the results from the ADAMS/Car model is not. Table A.6 shows the maximum difference between the analytical and ADAMS/Car results.

From the results in Table A.6 it can be seen that as the magnitude of the vertical component of the applied force is changed the difference between the analytical and ADAMS/Car results become larger. This seems to indicate that there exists a small amount of cross-sensitivity of the uni-axial load cells in the different directions. However, the force present in the uni-axial load cells due to the cross-sensitivity is very small and will have a negligible effect on the accuracy of the 6clc model's measurements.

Table A.6. Maximum difference between analytical results and ADAMS/Car results (Load case 1)

	Load case 1 ($F_z = -100\text{N}$)	Load case 1 ($F_z = -1000\text{N}$)	Load case 1 ($F_z = -10000\text{N}$)
Forces in uni-axial load cells			
X_1	2.226e-7	2.226e-6	2.226e-5
X_2	3.727e-7	3.727e-6	3.727e-5
Y	4.673e-7	4.673e-6	4.673e-5
Z_1	3.173e-6	3.173e-6	5.098e-6
Z_2	5.17e-7	4.13e-6	4.595e-5
Z_3	3.304e-5	3.65e-5	7.085e-5
Equivalent forces			
F_x	1.5e-7	1.5e-6	1.5e-5
F_y	4.673e-7	4.673e-6	4.673e-5
F_z	3e-5	3e-5	3e-5
Equivalent moments			
M_x	1.468e-6	1.664e-6	3.621e-6
M_y	3e-6	3e-6	3e-6
M_z	1.043e-8	1.043e-7	1.043e-6

The analytical equations and the ADAMS/Car model are subjected to load cases 2 to 4 with the non-zero components of the applied force having the characteristic shown in Figure A.16. It is a ramp input with maximum amplitude of -4000N. The results for the different load cases are shown in Table A.7.

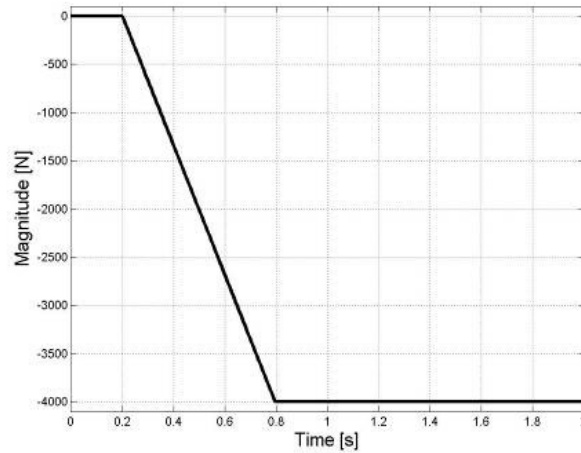


Figure A.16. Characteristic of the components of the applied force

Table A.7. Maximum difference between analytical results and ADAMS/Car results (Load case 2 to 4)

	Load case 2 $F_x = 0\text{N}$ $F_y = 0\text{N}$ $F_z = -4000\text{N}$	Load case 3 $F_x = 0\text{N}$ $F_y = -4000\text{N}$ $F_z = 0\text{N}$	Load case 4 $F_x = -4000\text{N}$ $F_y = 0\text{N}$ $F_z = 0\text{N}$	$F_x = -4000\text{N}$ $F_y = -4000\text{N}$ $F_z = -4000\text{N}$ (Same application point as Load case 2)
Forces in uni-axial load cells				
X_1	2.158e-6	2.551e-6	3.4e-5	3.47e-5
X_2	8.076e-8	1.416e-5	3.177e-5	4.5e-5
Y	1.377e-5	4.76e-6	2.612e-5	3.52e-5
Z_1	3.173e-6	3.173e-6	7.2e-6	9.5e-6
Z_2	7.837e-6	6.57e-6	1.2e-5	1.26e-5
Z_3	3.99e-5	3.27e-5	3.77e-5	3.3e-5
Equivalent forces				
F_x	2.239e-6	1.671e-5	2.29e-6	1.026e-5
F_y	1.377e-5	4.76e-6	2.612e-5	3.52e-5
F_z	3e-5	3e-5	3e-5	3e-5
Equivalent moments				
M_x	1.67e-6	1.65e-6	1.446e-6	1.446e-6
M_y	3e-6	3e-6	3e-6	3e-6
M_z	5.754e-7	6.89e-7	2.05e-6	2.35e-6

From the results shown in Table A.6 and Table A.7 it can be concluded that the ADAMS/Car model was constructed correctly and is able to measure the equivalent forces and moments applied to the virtual 6clc. The ADAMS/Car model as well as the analytical equations will now be validated against experimental results. This is done as comparing the results of the two models with one another only verifies that the models have been created correctly, but does not indicate whether either model is correct and can measure the force in the uni-axial load cells correctly, and infer the equivalent forces and moments. In the following paragraph we will discuss the validation of the 6clc models.

A.2.2. Validation of 6clc models

The 6clc ADAMS/Car model has been verified. The next step before the 6clc model can be used is to validate it. The validation will consist of qualitatively comparing the measurements of the physical 6clc and the “measurements” of the 6clc ADAMS/Car model. The analytical

equations will also be compared to the measurements of the physical 6clc measurements. In the comparisons the data referred to as the **Measured** data is obtained from the physical 6clc measurements. The forces in the uni-axial load cells (i.e. X_1 , X_2 , Y , Z_1 , Z_2 and Z_3) are obtained by taking the strain measurements of each uni-axial load cell and then using Eq.{A.2} to calculate the force. Once the measured force in each of the uni-axial load cells have been calculated Eq.{A.5} is used to calculate the equivalent forces and moments. The **Analytical** data refers to the data obtained by calculating the uni-axial load cell forces and the equivalent forces and moments due to the applied force. The forces in the uni-axial load cells are calculated using Eq.{A.6} and the equivalent forces and moments are calculated using Eq.{A.4}. The last set of data used in the comparisons is the data from the 6clc ADAMS/Car model which will be referred to as **acar**. The uni-axial load cells in the ADAMS/Car model was modelled such that the force measured by the uni-axial load cells is already in Newtons. Therefore, the uni-axial load cell forces obtained from the ADAMS/Car model can directly be substituted into Eq.{A.5} to calculate the equivalent forces and moments.

The experimental setup that was used to obtain the experimental data required for the validation process is shown in Figure A.17. An external force is applied to the 6clc via the actuator which will be referred to as the applied force. The force is applied to the actuator at a known location for the different load cases as was given in Table A.4. The applied force is measured by the load cell. The measured applied force is used in the analytical equations as well as applied to the ADAMS/Car model. The same load cases are used that was used in the verification process (see Table A.4). The validation results of the 6clc models for each of the load cases is given in the following paragraphs.

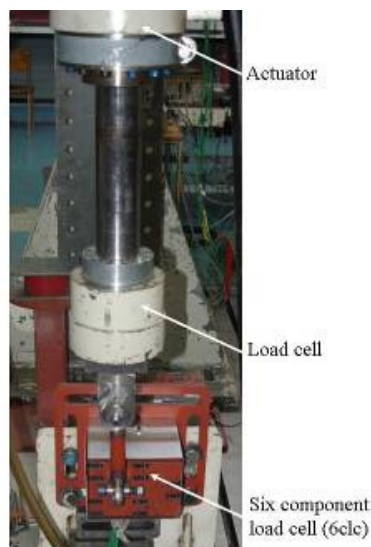


Figure A.17. Experimental setup of 6clc for Load case 3

A.2.2.1. Load case 1 and Load case 2

The force in the vertical direction was applied both at the origin of the xy-plane (Load case 1) as well as at an off-centre location (Load case 2). The interface between the actuator and the 6clc was a 32mm round tube that transferred the load to the 6clc. The midpoint of the round tube corresponded with the application point given in Table A.4. This assumed that the load, applied through the 32mm round tube, will be a perfect point load and that it will act at the mid point of the tube at the specified location. However, in the experimental setup it may happen that the load is actually applied at some other point within the circular envelope formed by the round tube (see Figure A.18). This implies that it may happen that the practical

application points differ from the theoretical application points and thus influence the results of the equivalent moments and forces calculated by Eq. {A.4}.

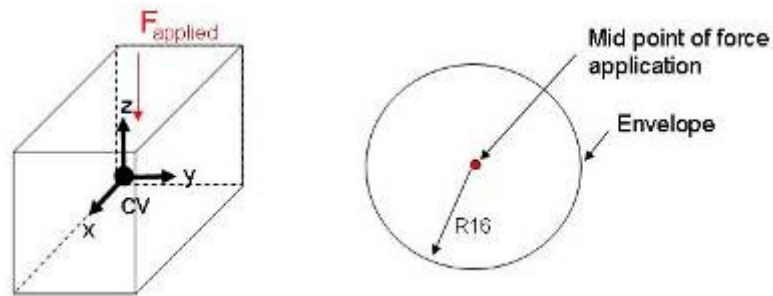


Figure A.18. Force application for Load case 1 and 2

Figure A.19 shows the comparison of the equivalent forces and moments between the two models and the physical 6clc when subjected to Load case 1. From this figure it can be observed that the equivalent vertical force measured on the physical 6clc and the two models show good agreement. However for the other two forces and all three moments there is not good agreement. It is difficult to distinguish between the results from the two models (Analytical and acar) in Figure A.19. This is because the results are equal. Figure A.20 and Figure A.21 show the correlation of the forces in the six uni-axial load cells. As can be expected for this load case the analytical equations and the ADAMS/Car model measures no forces in the lateral and longitudinal directions (see Figure A.20). The physical 6clc, however, does measure forces in the uni-axial load cells X_1 , X_2 and Y . The forces present in X_1 , X_2 and Y of the physical 6clc but which are not measured in the 6clc models, cause the deviation observed in the equivalent forces and moments.

From Figure A.19 it would seem that the two models measure the vertical force correctly, however, when the forces in the uni-axial load cells in the z direction are viewed (see Figure A.21) it can be observed that there is some deviation between the measured and predicted forces in the uni-axial load cells.

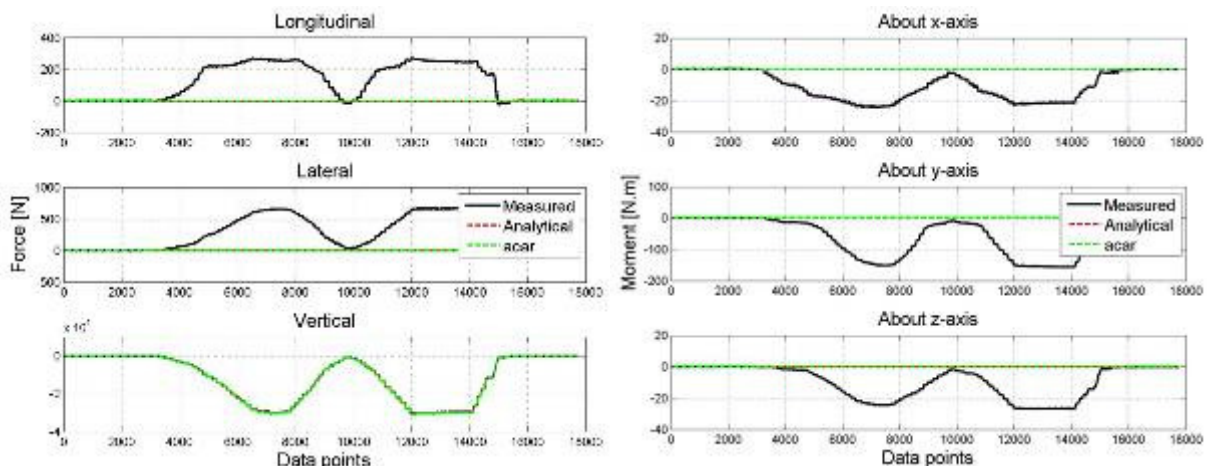


Figure A.19. Comparison of equivalent forces and moments (Load case 1)

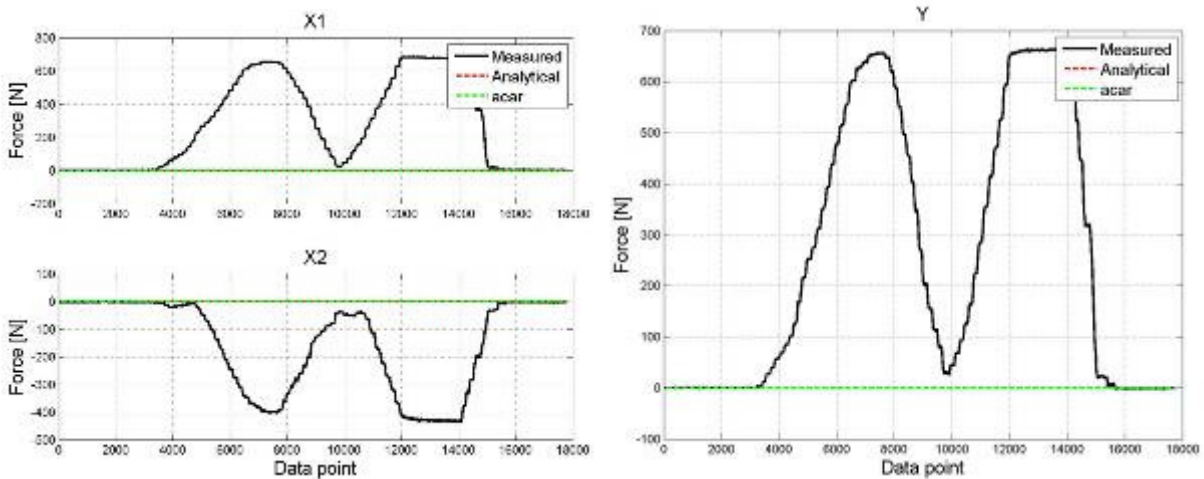


Figure A.20. Comparison of forces in uni-axial load cells orientated in the longitudinal and lateral direction (Load case 1)

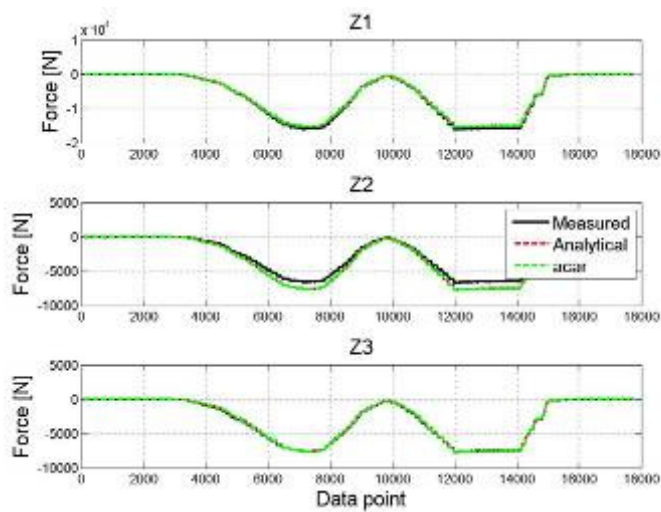


Figure A.21. Comparison of forces in uni-axial load cells orientated in vertical direction (Load case 1)

Figure A.22 shows the comparison of the equivalent forces and moments when the 6clc is subjected to Load case 2. It can be observed that the predicted equivalent vertical force from the two models has good correlation with the measured data. The equivalent moment around the x- and y-axis also shows good correlation. Once again the forces in the uni-axial load cells measured by the two models in the longitudinal and lateral direction are zero. Similar to the results obtained for Load case 1, the results show that the equivalent vertical force has good correlation between measured and predicted data, however, this is not true for the forces in the uni-axial load cells orientated in the z-direction, especially for Z_2 . This is shown in Figure A.23.

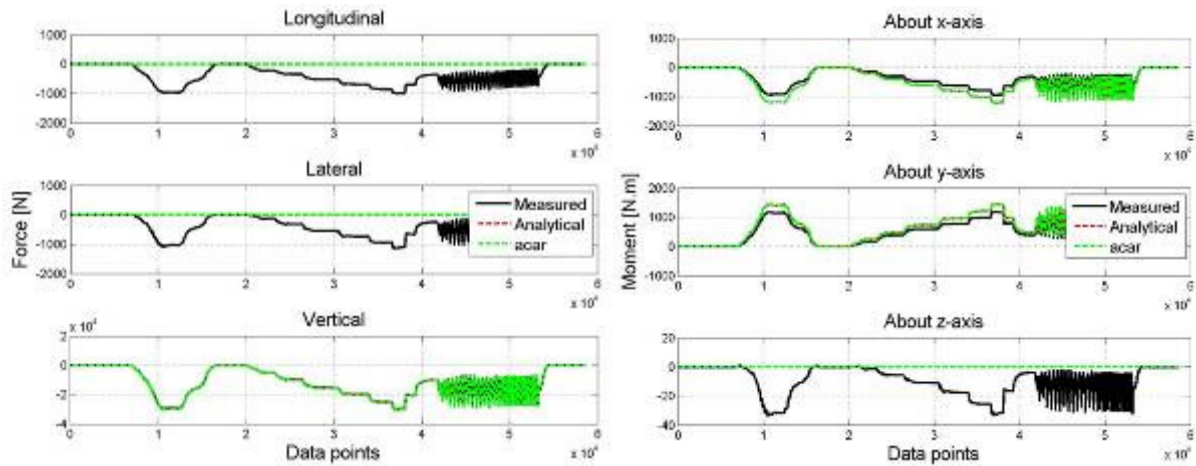


Figure A.22. Comparison of equivalent forces and moments (Load case 2)

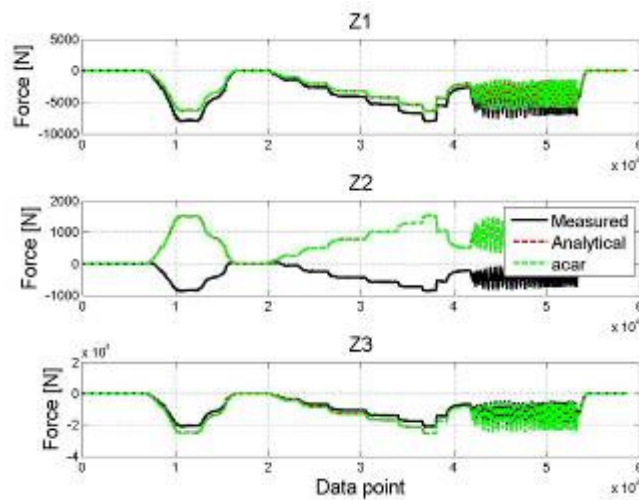


Figure A.23. Comparison of forces in uni-axial load cells orientated in the vertical direction (Load case 2)

A.2.2.2. Load case 3

In this load case the force is applied to the 6clc via a spherical joint and yoke. Figure A.24 shows the experimental setup and a schematic of the 6clc showing the orientation of the applied force in the 6clc's coordinate system.

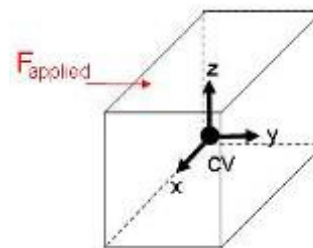


Figure A.24. Experimental setup for Load case 3

The equivalent lateral force and the moments about the x- and z-axis show good correlation between the measured and model data (see Figure A.25). The moment about the z-axis uses the forces in the uni-axial load cells X_1 , X_2 and Y . It is interesting to note that the comparison of the results from the two models and the measured force in the uni-axial load cell Y shows good correlation whereas X_1 and X_2 do not show good correlation as shown in Figure A.26. Even though the models do not give good predictions of X_1 and X_2 , good correlation is still obtained for the moment about the z-axis. This is most likely due to the models giving accurate measurements for Y and with the forces in Y being much higher than in X_1 and X_2 .

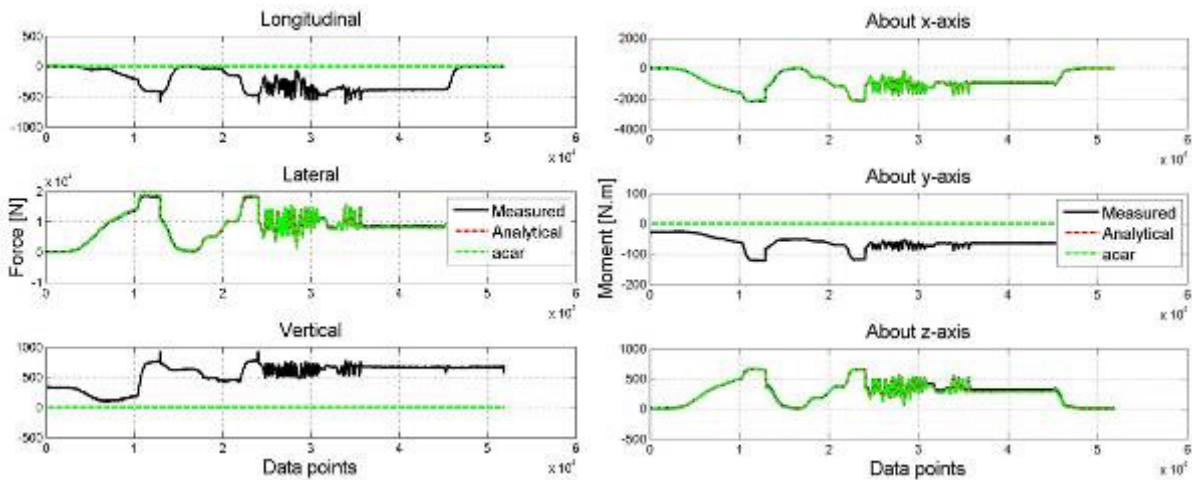


Figure A.25. Comparison of equivalent forces and moments (Load case 3)

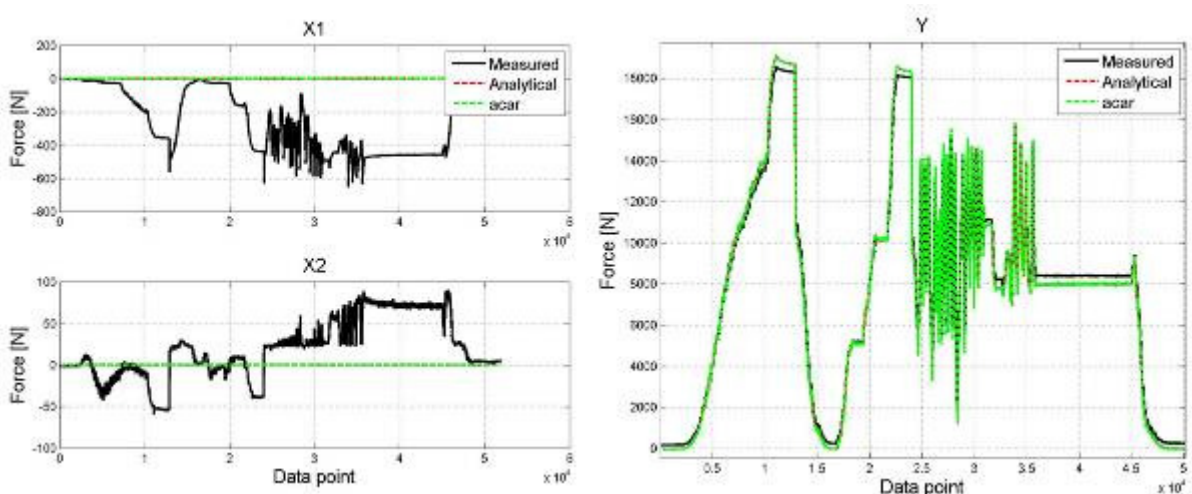


Figure A.26. Comparison of forces in uni-axial load cells orientated in the longitudinal direction (Load case 3)

A.2.2.3. Load case 4

In this load case the force is applied to the side of the yoke, which is attached to the 6clc, through the same 32mm tube that was used in Load case 1 and Load case 2. The experimental setup and a schematic of the 6clc showing the orientation of the applied force ($F_{applied}$) in the 6clc's coordinate system are shown in Figure A.27. Because the loading is applied through the 32mm round tube the same effect as described in Load case 1 and 2 can occur here.

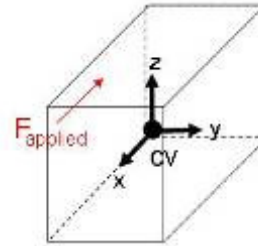


Figure A.27. Experimental setup for Load case 4

The equivalent longitudinal force and the moments about the y- and z-axis show good correlation between the measured and the results from the two models, as shown in Figure A.28. The moment about the z-axis uses the forces in the uni-axial load cells X_1 , X_2 and Y . The uni-axial load cell forces in X_1 and X_2 shows much better correlation between the measured and the models' results than the uni-axial load cell Y 's forces as shown in Figure A.29. Similar to what was observed in Load case 3, the models' prediction of the equivalent moment about the z-axis is good inspite of the deviation in their prediction of the uni-axial load cell Y 's force from the measured data. This is due to the good correlation of the models' forces in X_1 and X_2 and the higher forces present in X_1 and X_2 compared to the forces in Y .

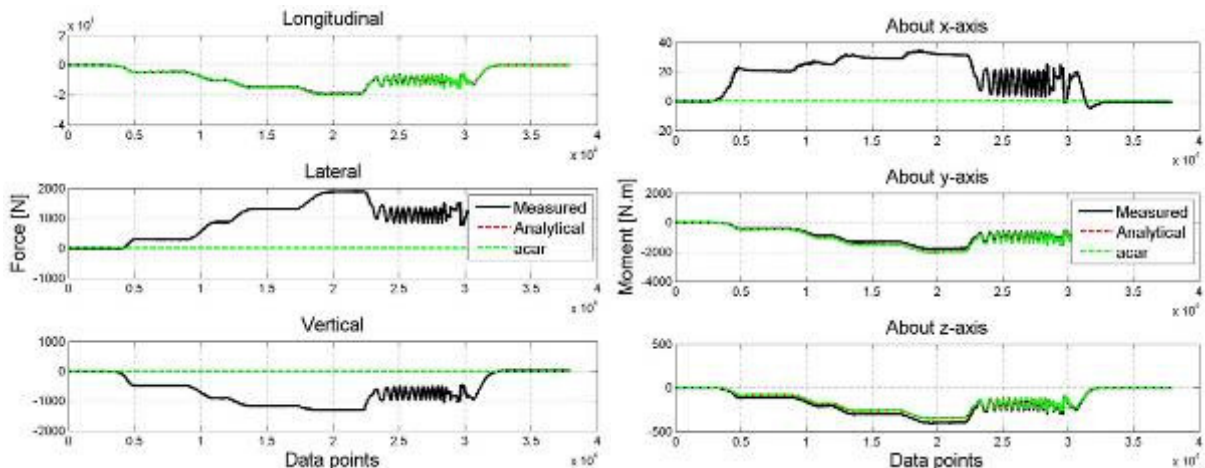


Figure A.28. Comparison of equivalent forces and moments (Load case 4)

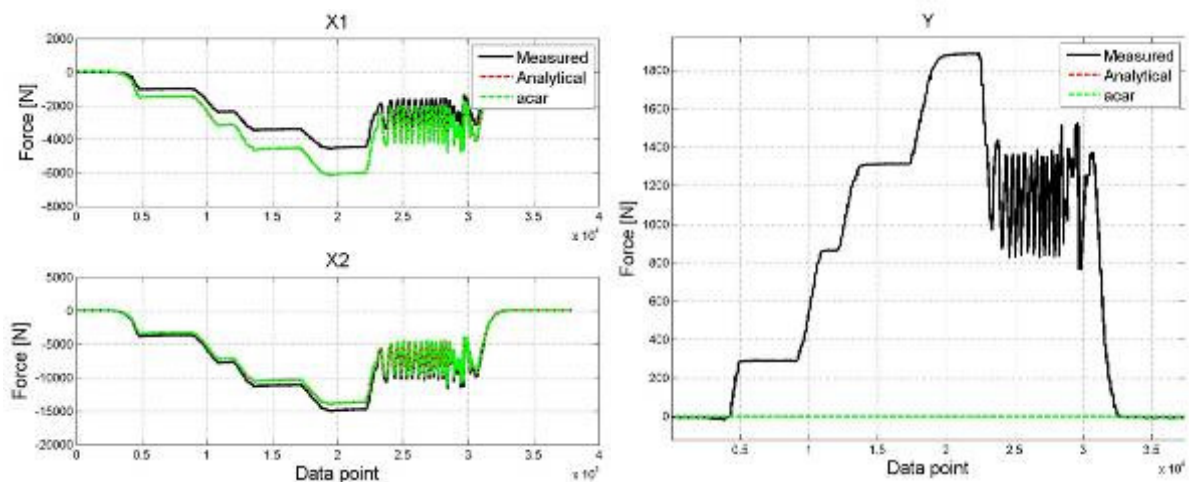


Figure A.29. Comparison of forces in uni-axial load cell orientated in the longitudinal and lateral direction (Load case 4)

It was observed in the previous paragraphs that for each load case good correlation was obtained for one of the equivalent forces and for two of the equivalent moments. For the other two equivalent forces and moment the analytical equations and ADAMS/Car model's measurements did not correlate well. It was mentioned that in some of the load cases the theoretical force application point may not actually coincide with the practical application point. This was mainly as a result of how the force was applied to the physical 6clc. This possible cause, along with three other possible causes, are listed below. One, or a combination of them, might be the cause for the deviation observed:

- The practical application point may differ from the theoretical application point
- The applied force may not be purely in one direction but might have another orientation,
- The physical 6clc had some play between the rod end of the uni-axial load cells and the bolts,
- The physical 6clc is not perfectly rigid whereas the models are.

A.2.3. Model refinement

From the validation results shown in paragraph A.2.2 it was concluded that four possible causes may be responsible for the deviation between the results of the equivalent forces and moments as well as the forces in the uni-axial load cells obtained from the physical 6clc and the two models. In this paragraph the two most likely causes will be investigated namely, the force orientation and the force application point.

In order to investigate the effect of the force orientation and its application point on the results, the orientation of the force as well as its application point will be calculated from the experimentally measured forces in the uni-axial load cells. After the orientation of the forces and its application point have been calculated from the experimental measurements, it will be used in the two models. This should improve the correlation as the physical and virtual 6clc should then be subjected to the same conditions. Considering Equation {A.3}, presented here for convenience as Eq.{A.7}, the left hand side of the equations contain the components of the applied force as well as the coordinates of its application point. The right hand side of the equations contain the forces in the uni-axial load cells as well as their location relative to the centre of volume.

$$\begin{aligned}
 F_{A_x} &= X_1 + X_2 \\
 F_{A_y} &= Y \\
 F_{A_z} &= Z_1 + Z_2 + Z_3 \\
 d_y F_{A_z} - d_z F_{A_y} &= d_{yz} Y - d_{z2y} Z_2 + d_{z3y} Z_3 \\
 d_z F_{A_x} - d_x F_{A_z} &= -d_{x1z} (X_1 + X_2) + d_{z1x} Z_1 - d_{z23x} (Z_2 + Z_3) \\
 d_x F_{A_y} - d_y F_{A_x} &= -d_{x1y} X_1 + d_{x2y} X_2 + d_{yx} Y
 \end{aligned}
 \tag{A.7}$$

All the values on the right hand side are known and it should therefore be possible to calculate the components and the application point of the applied force from the experimental measurements of the forces in the uni-axial load cells. The set of equations in Eq.{A.7} are unfortunately not linear independent. However, dividing the set of equations in Eq.{A.7} into two sets of equations consisting of the three forces and the three moment equations we can

solve for the three components of the applied force (F_{Ax} , F_{Ay} , F_{Az}) as well as its coordinates (d_x , d_y , d_z) as discussed in the following two paragraphs. Paragraph A.2.3.1 discusses the results when the experimentally calculated orientation of the applied force is used in the two models and paragraph A.2.3.2 discusses the results when the experimentally calculated application point is used.

A.2.3.1. Orientation of applied force

The components of the applied force are calculated from the experimental force measurements in the uni-axial load cells (X_1 , X_2 , Y , Z_1 , Z_2 and Z_3) using the three force equations in Eq.{A.7} shown here as Eq.{A.8}.

$$\begin{aligned} F_{A_x} &= X_1 + X_2 \\ F_{A_y} &= Y \\ F_{A_z} &= Z_1 + Z_2 + Z_3 \end{aligned} \quad \text{[A.8]}$$

The three components of the applied force, and therefore the orientation of the applied force, can easily be calculated using Eq.{A.8}. Using the experimentally calculated applied force orientation for Load case 1 in the analytical equations and the ADAMS/Car model gives the results shown in Figure A.30. An improvement in the correlation of the longitudinal and lateral equivalent forces can be seen from Figure A.30. The equivalent moments do not however show any improvement in the correlation between the data of the two models and the measured data. Unlike the results for Load case 1 shown in Figure A.30, the correlation between the results for Load case 3 shows great improvements for both the equivalent forces as well as the equivalent moments (see Figure A.31).

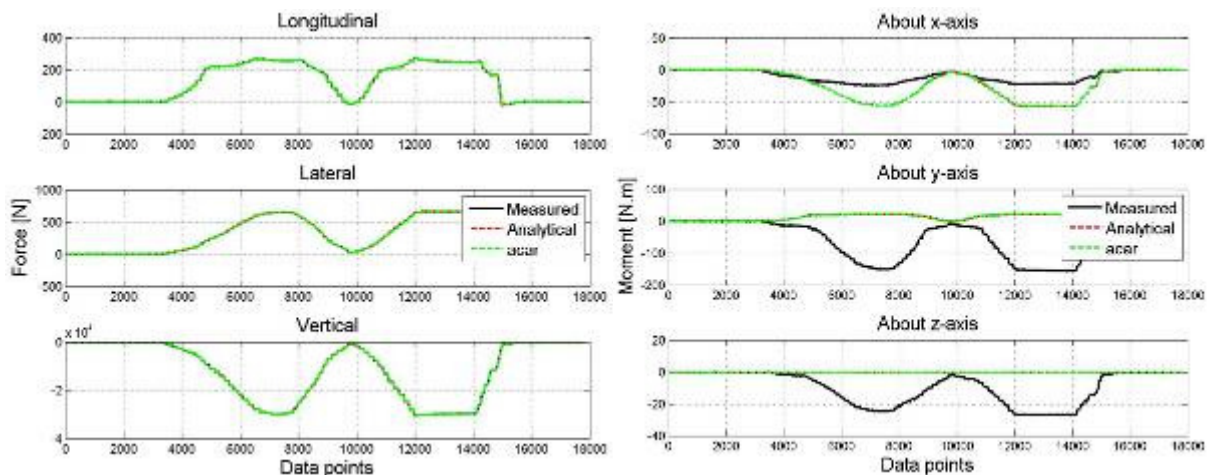


Figure A.30. Comparison of equivalent forces and moments (Load case 1 – Experimental loading)

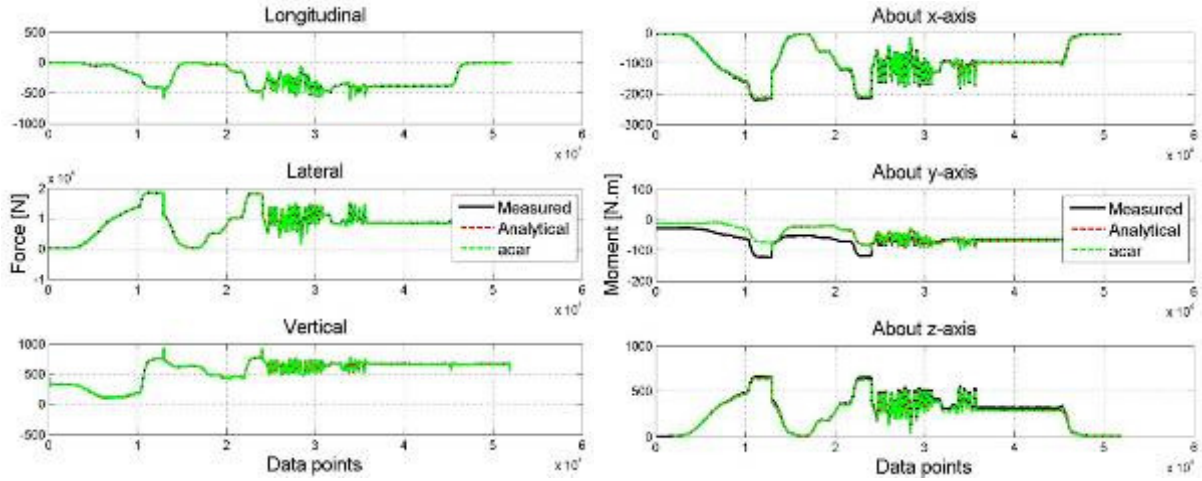


Figure A.31. Comparison of equivalent forces and moments (Load case 3 – Experimental loading)

The possibility that the orientation of the applied force between the physical 6clc and the two models differ was investigated. The components of the applied force were calculated from the experimental measurements of the force in the uni-axial load cells in the physical 6clc and were used as input to the analytical equations and the ADAMS/Car model. This showed improvement in the correlation of the equivalent forces for both Load case 1 and Load case 3. Improvement in the correlation of the equivalent moments was obtained only for Load case 3. The fact that good correlation is obtained for the equivalent forces but not for the equivalent moments seem to indicate that there might be an error in the application point of the applied force. This is investigated in the next paragraph.

A.2.3.2. Application point of applied force

In the previous paragraph the orientation of the applied force was calculated from experimental measurements. When this force orientation was used in the two models an improvement in the comparisons was observed. The effect of the application point on the correlation is now checked by calculating the application point from the experimental measurements and using these coordinates in the two models. The application point will be calculated using the three moment equations in Eq.{A.7} shown here as Eq.{A.9}. The three components of the applied force (F_{Ax} , F_{Ay} , F_{Az}) in Eq.{A.9} can be calculated using Eq.{A.8}. Eq.{A.9} therefore results in a set of three linear equations with three unknowns.

$$\begin{aligned}
 d_y F_{Az} - d_z F_{Ay} &= d_{yz} Y - d_{z2y} Z_2 + d_{z3y} Z_3 \\
 d_z F_{Ax} - d_x F_{Az} &= -d_{x12z} (X_1 + X_2) + d_{z1x} Z_1 - d_{z23x} (Z_2 + Z_3) \\
 d_x F_{Ay} - d_y F_{Ax} &= -d_{x1y} X_1 + d_{x2y} X_2 + d_{yx} Y
 \end{aligned} \tag{A.9}$$

The three moment equations in Eq.{A.9} can be written in the form $Ax = b$ as shown in Eq.{A.10}. As stated the variables in matrix A can be calculated from Eq.{A.8} and all variables in vector b is known as they have been measured experimentally. The determinant of matrix A is calculated to be zero ($\det(A) = 0$). This implies that matrix A is singular and it is not possible to invert it and we can therefore not solve for the application point coordinates d_x , d_y and d_z using Eq.{A.10}. If, however, either d_x , d_y , or d_z is known it is possible to calculate the other two variables using the set of equations in Eq.{A.9}.

$$\begin{bmatrix} 0 & F_{A_z} & -F_{A_y} \\ -F_{A_z} & 0 & F_{A_x} \\ F_{A_y} & -F_{A_x} & 0 \end{bmatrix} \begin{Bmatrix} d_x \\ d_y \\ d_z \end{Bmatrix} = \begin{Bmatrix} d_{y_z} Y - d_{z_2y} Z_2 + d_{z_3y} Z_3 \\ -d_{x_{12z}} (X_1 + X_2) + d_{z_{1x}} Z_1 - d_{z_{23x}} (Z_2 + Z_3) \\ -d_{x_{1y}} X_1 + d_{x_{2y}} X_2 + d_{y_x} Y \end{Bmatrix} \quad \{A.10\}$$

Considering the way the force is applied to the 6clc in the four load cases the following can be concluded. For Load case 1 and 2 d_z is well defined whereas d_x and d_y is not as it may be anywhere within the envelope discussed in paragraph A.2.2.1. The same situation is present in Load case 4 where d_x is assumed to be well defined whereas d_y and d_z is not as they may be anywhere within the envelope created by the 32mm tube. For Load case 3 the application point is supposed to be well defined in d_x , d_y and d_z as the actuator was attached to the 6clc via a spherical joint and yoke. This however may not guarantee that the practical application point coincides exactly with the theoretical point but it is assumed that the theoretical and practical application points for Load case 3 coincide.

When it is assumed that d_z is well defined for Load case 1 and Load case 2, d_y and d_x can be calculated using Eq.{A.9} from which the following equations are obtained for d_y and d_x :

$$d_y = \frac{d_{y_z} Y - d_{z_2y} Z_2 + d_{z_3y} Z_3 - d_z F_{A_y}}{F_{A_z}}$$

$$d_x = \frac{d_z F_{A_x} - (-d_{x_{12z}} (X_1 + X_2) + d_{z_{1x}} Z_1 - d_{z_{23x}} (Z_2 + Z_3))}{F_{A_z}}$$

F_{A_z} is calculated from Eq.{A.8}. The remaining moment equation can be used as a check, as d_x and d_y substituted into Equation {A.11}, should be equal to zero:

$$d_x F_{A_y} - d_y F_{A_x} - (-d_{x_{1y}} X_1 + d_{x_{2y}} X_2 + d_{y_x} Y) = 0 \quad \{A.11\}$$

For Load case 4 it is assumed that d_x is well defined and d_y and d_z can be calculated using Eq.{A.9} from which the following equations are obtained for d_y and d_z :

$$d_y = \frac{d_x F_{A_y} - (-d_{x_{1y}} X_1 + d_{x_{2y}} X_2 + d_{y_x} Y)}{F_{A_x}}$$

$$d_z = \frac{-d_{x_{12z}} (X_1 + X_2) + d_{z_{1x}} Z_1 - d_{z_{23x}} (Z_2 + Z_3) + d_x F_{A_z}}{F_{A_x}}$$

F_{A_x} is calculated from Eq.{A.8}. The remaining moment equation can be used as a check, as d_y and d_z substituted into Equation {A.12}, should be equal to zero:

$$d_y F_{A_z} - d_z F_{A_y} - (d_{y_z} Y - d_{z_2y} Z_2 + d_{z_3y} Z_3) = 0 \quad \{A.12\}$$

Table A.8 shows the application point calculated from the experimental measurements for Load cases 1, 2 and 4 calculated using the equations above. It also shows whether the adjustment falls within the envelope as well as the results from the test equations (Eq.{A.11} and Eq.{A.12}). The reader should note that the results of the test equations are given as a mean and a standard deviation because the application point may shift within the envelope as the force is applied and removed.

Table A.8. Application point

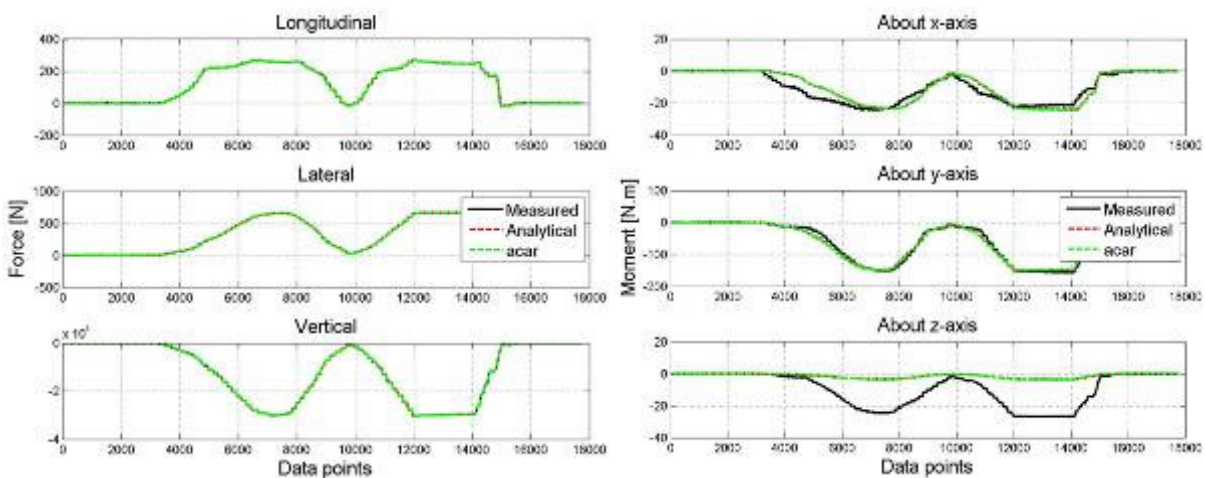
Load case	Application point: Theoretical	Application point: Calculated from measurements	Adjustment	Test equations	
				mean [N.m]	standard deviation [N.m]
1	[0, 0, 0.085]	[-0.0057,-0.00108, 0.085]	5.8mm < 16mm ⇒ within envelope	9.85	10.25
2	[0.0475, 0.04, 0.085]	[0.0421,0.0345, 0.085]	7.7mm < 16mm ⇒ within envelope	9.85	10.18
4	[0.0575 ,-0.0175, 0.101]	[0.0575 ,-0.0261,0.0955]	10.2mm < 16mm ⇒ within envelope	-83.6	67.5

Note: The coordinates shown in **orange** are the coordinates that are assumed to be known for the specific load case

From the results in Table A.8 it can be seen that the application point calculated from the experimental measurements falls within the envelope created by the 32mm tubing. The test equations are not satisfied with Load case 4 having the greatest deviation. This indicates that the application point that is calculated changes, within the envelope, as the force is applied. Although the test equation is not satisfied, the application point calculated from the experimental measurements will be used as they still fall within the envelope. The results for the two models, when using the experimentally calculated applied force orientation and application point, are shown next for all four load cases.

Load case 1 and 2

From Figure A.32 and Figure A.33 it can be observed that there is an improvement in the correlation of the equivalent moments as well as in the forces in the uni-axial load cells when the experimentally calculated application is used in the models. However, the correlation of the forces in the uni-axial load cells X_1 and X_2 are still not good. This is true for both Load case 1 and 2 (see Figure A.33 and Figure A.35). Similarly, the correlation of the equivalent moment about the z-axis is also not good for both Load case 1 and 2 (see Figure A.32 and Figure A.34). Except for the correlation of the two uni-axial load cell forces X_1 and X_2 and the equivalent moment about the z-axis, good correlation is obtained for all the other equivalent forces and moments and forces in the uni-axial load cells.


Figure A.32. Comparison of equivalent forces and moments (Load case 1 – Experimental loading and application point)

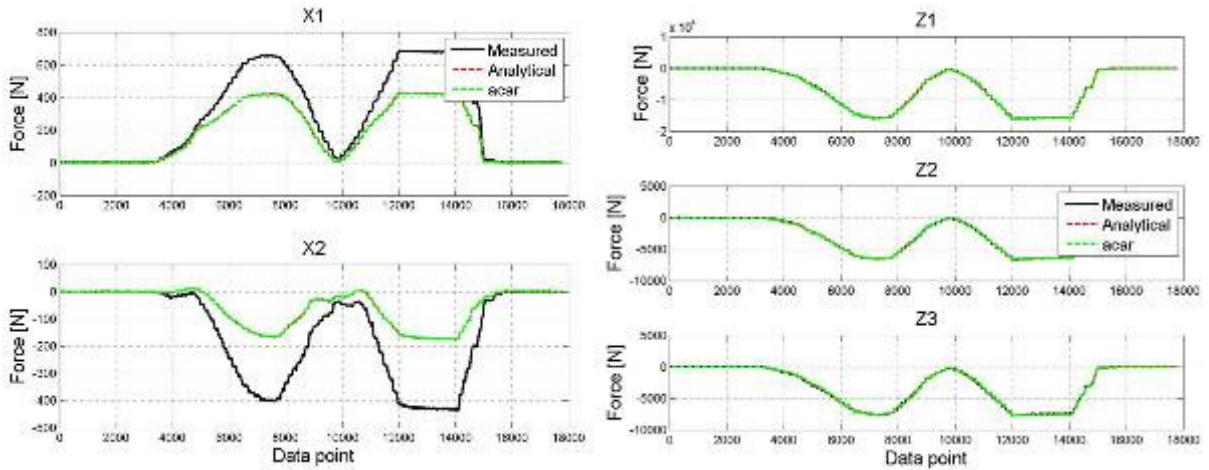


Figure A.33. Comparison of forces in uni-axial load cells orientated in the longitudinal and vertical direction (Load case 1 – Experimental loading and application point)

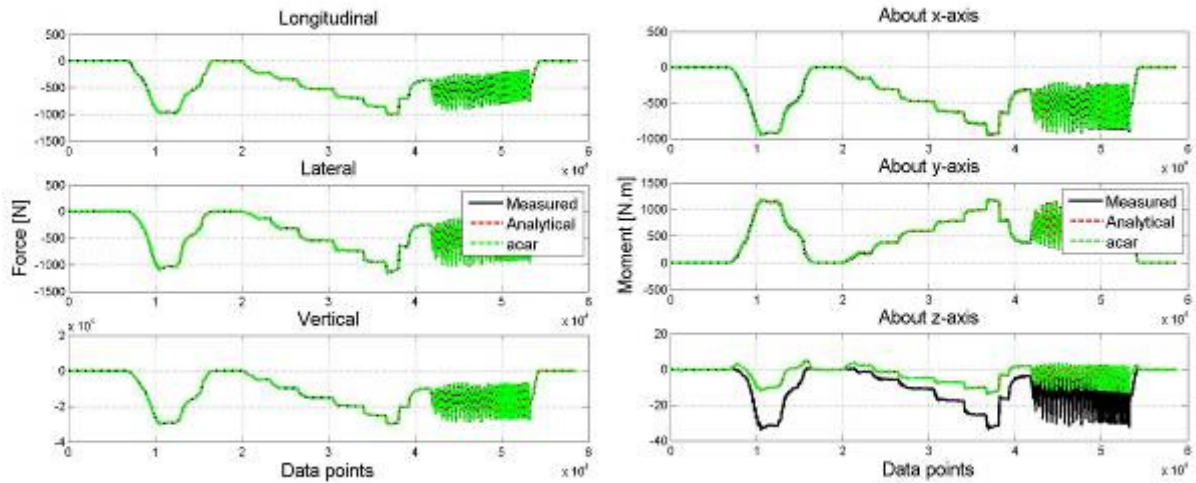


Figure A.34. Comparison of equivalent forces and moments (Load case 2 – Experimental loading and application point)

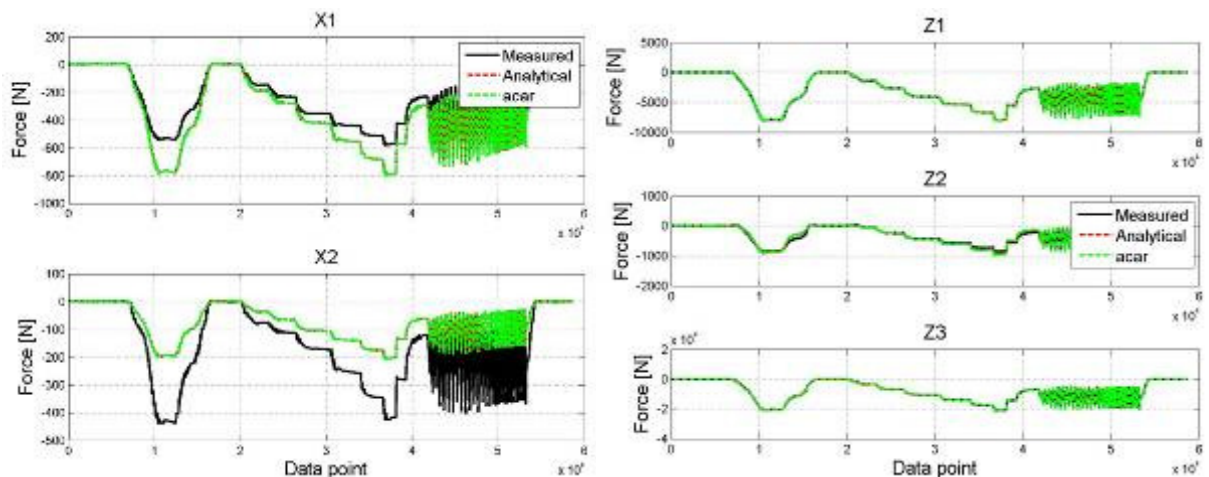


Figure A.35. Comparison of forces in uni-axial load cells orientated in the longitudinal and vertical direction (Load case 2 – Experimental loading and application point)

Load case 3

Figure A.36 and Figure A.37 show the correlation between the models and the measured data when the experimentally calculated applied force orientation is applied to the two models.

The application point is not calculated from the experimental measurements as the loading was applied via a spherical joint and yoke. It was therefore assumed that the practical application point should be in close agreement with the theoretical application point. Therefore the theoretical application point is used for Load case 3. The equivalent forces results show good correlation. The forces in the uni-axial load cells X_1 , X_2 and Z_1 do not show good correlation which leads to the deviations in the correlation of the equivalent moment about the y-axis.

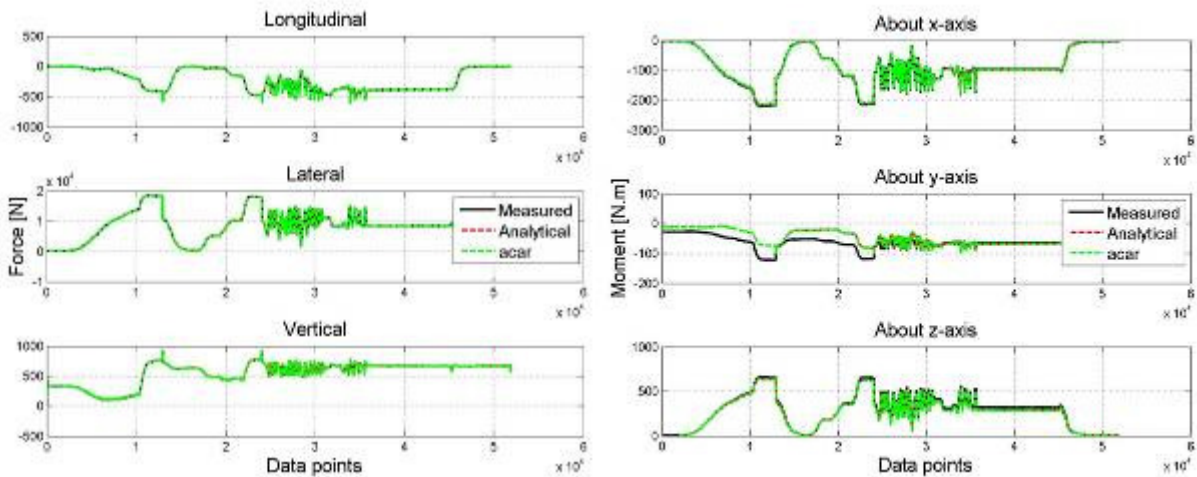


Figure A.36. Comparison of equivalent forces and moments (Load case 3 – Experimental loading and application point)

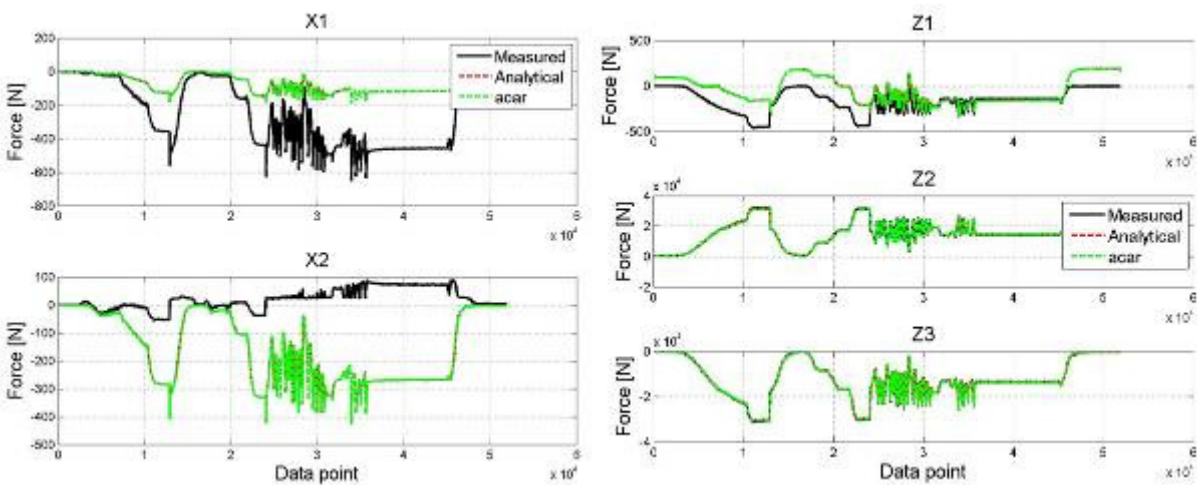


Figure A.37. Comparison of forces in uni-axial load cells orientated in the longitudinal and vertical direction (Load case 3 – Experimental loading and application point)

Load case 4

Figure A.38 and Figure A.39 show the correlation between the models and the measured data for Load case 4. The equivalent force results show good correlation. The forces in the uni-axial load cells Z_2 and Z_3 do not show good correlation which leads to the deviations in the correlation of the equivalent moment about the x-axis.

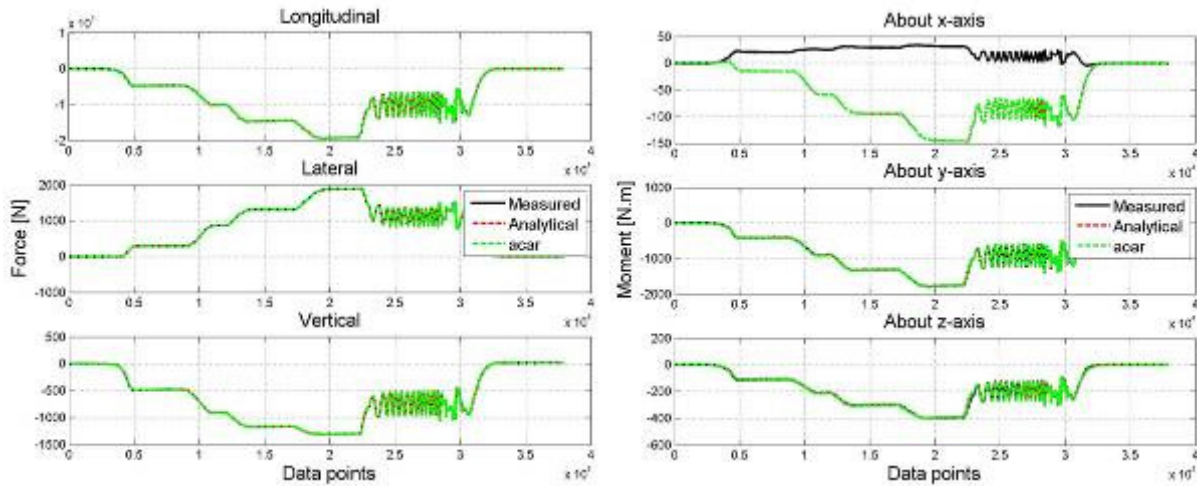


Figure A.38. Comparison of equivalent forces and moments (Load case 4 – Experimental loading and application point)

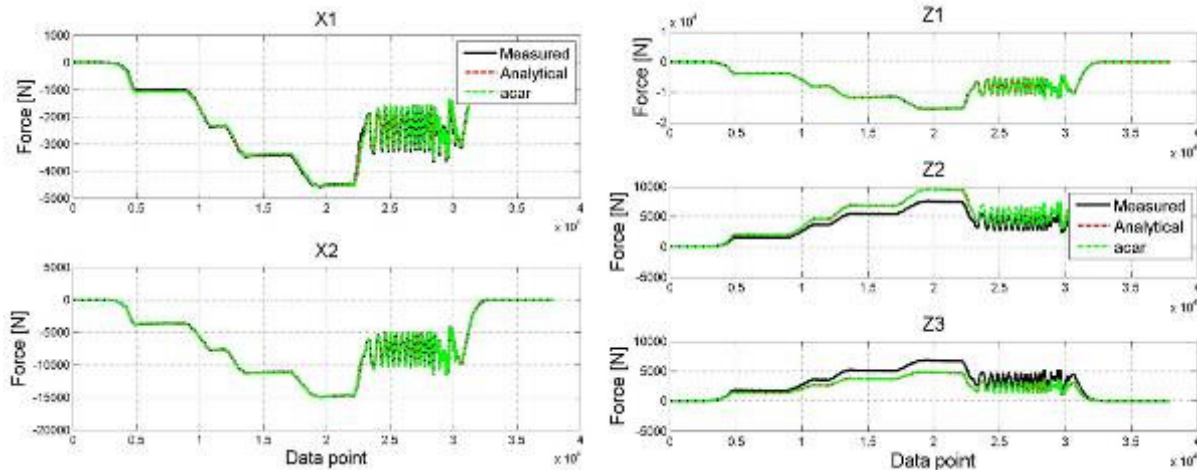


Figure A.39. Comparison of forces in uni-axial load cells orientated in the longitudinal and vertical direction (Load case 4 – Experimental loading and application point)

The force measurements from the two models were improved when the applied force and the application point, calculated from the experimental measurements, were used in the models. Good correlation is obtained between the physical 6clc and the two models' equivalent forces for all the load cases. The correlation for the equivalent moments are good but there are still some equivalent moments from the models that deviate from the experimental data. Possible causes for this may be due to the application point still not being exactly the same as the application point in the experimental setup.

A.2.4. Validation results for the rear 6clc

Paragraph A.2.2 and paragraph A.2.3 showed the validation results using the experimental measurements taken on the front 6clc. The two models will now be validated using the experimental measurements taken on the rear 6clc. Obtaining good results between the two models' "measurements", using the experimental measurements taken on the rear (physical) 6clc, and the experimental measurements will imply that the ADAMS/Car model can be used to model both the front and rear physical 6clcs.

The results for the four load cases (see Table A.4) are given in the following three paragraphs. The same ADAMS/Car model is used for the front and rear 6clc, the only difference is in the

practical application point that is used in the model. The experimentally calculated force orientation and application point are used in the two models. Table A.9 shows the application points used for the four load cases. For all the load cases, except for Load case 3, the experimentally calculated application point is used.

Table A.9. Application point (Rear 6clc)

Load case	Application point: Theoretical	Application point: Calculated from measurements	Adjustment	Test equations	
				mean [N.m]	standard deviation [N.m]
1	[0, 0, 0.085]	[-0.00465, 0.00327, 0.085]	5.7mm < 16mm ⇒ within envelope	-10.32	10.29
2	[0.0475, 0.04, 0.085]	[0.0472, 0.0356, 0.085]	4.4mm < 16mm ⇒ within envelope	-2.63	2.73
3	[0.035, -0.0175, 0.115]	N/A	N/A	N/A	N/A
4	[0.0575 , -0.0175, 0.101]	[0.0575 , -0.0133, 0.0951]	7.2mm < 16mm ⇒ within envelope	22.68	26.12

Note: The coordinates shown in **orange** are the coordinates that are assumed to be known in the specific load case

Load case 1 and Load case 2

Figure A.40 and Figure A.41 show the results for Load case 1 and Figure A.42 and Figure A.43 show the results for Load case 2. The results for both load cases show that the correlation between the models' and the physical 6clc's measured forces in the uni-axial load cells X_1 and X_2 is not good. This causes the correlation of the equivalent moment about the z-axis also not to be good. This is similar to the results obtained in paragraph A.2.3.2.

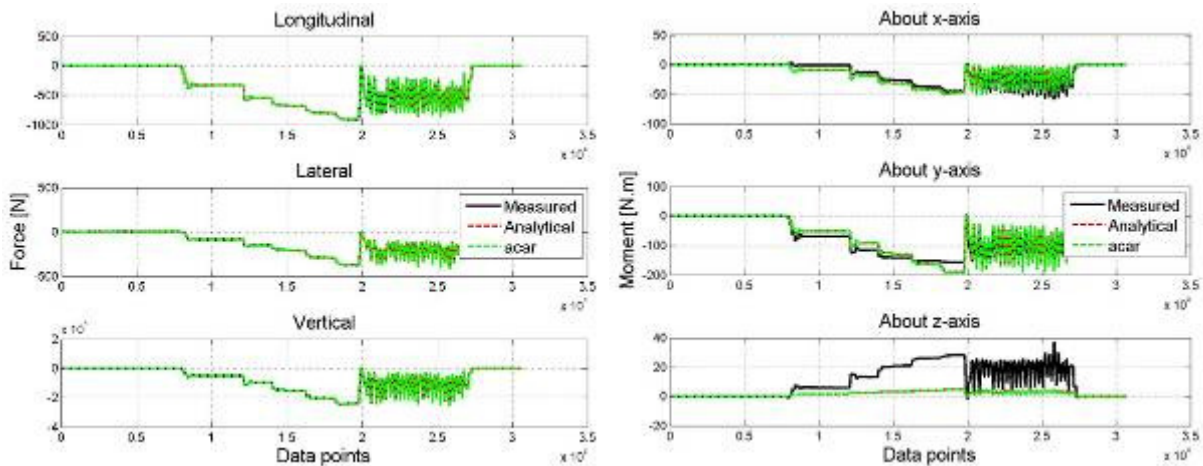


Figure A.40. Comparison of equivalent forces and moments (Load case 1 - Rear 6clc – Experimental loading and application point)

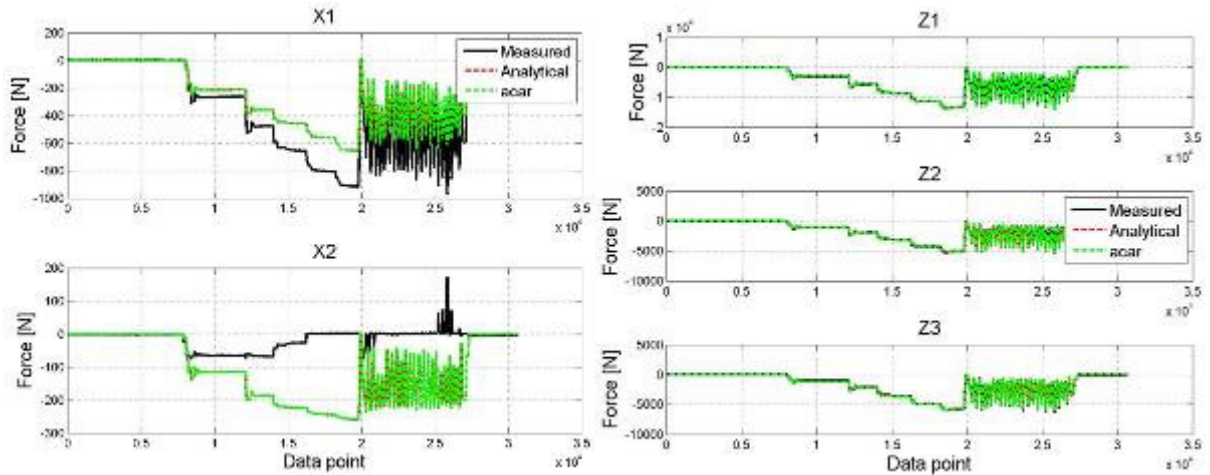


Figure A.41. Comparison of forces in uni-axial load cells orientated in the longitudinal and vertical direction (Load case 1 - Rear 6clc – Experimental loading and application point)

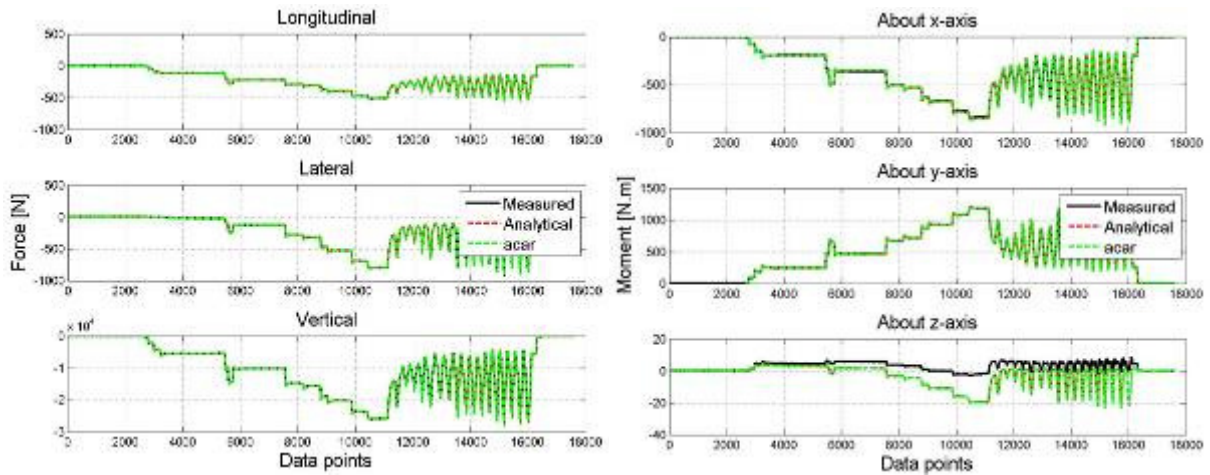


Figure A.42. Comparison of equivalent forces and moments (Load case 2 - Rear 6clc – Experimental loading and application point)

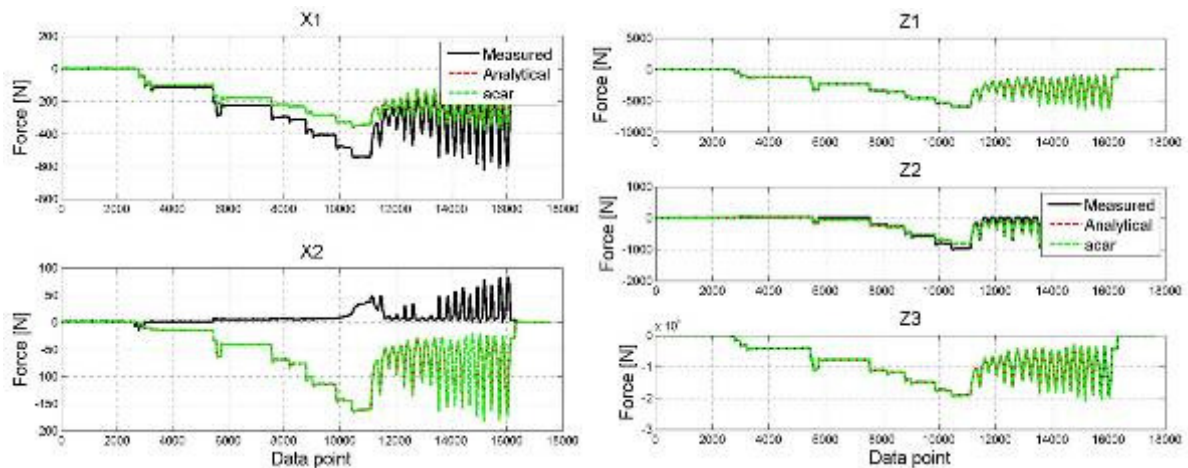


Figure A.43. Comparison of forces in uni-axial load cells orientated in the longitudinal and vertical direction (Load cell 2 - Rear 6clc – Experimental loading and application point)

Load case 3

The correlation of the forces in the uni-axial load cells X_1 , X_2 and Z_1 is not as good as the correlation for the other uni-axial load cell forces (see Figure A.44). Except for the equivalent

moment about the y-axis, the other two equivalent moments and all three equivalent forces show good correlation (see Figure A.45).

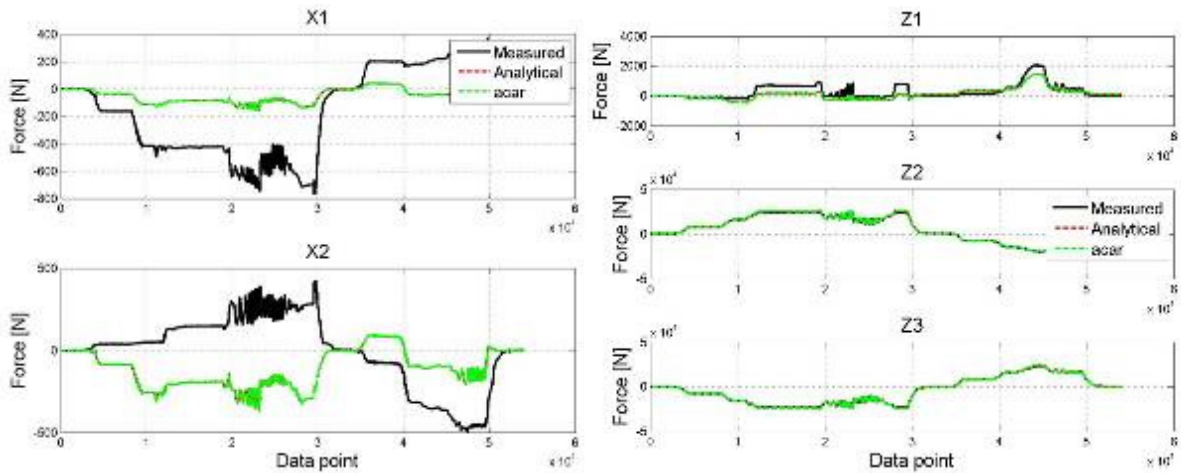


Figure A.44. Comparison of the forces in the uni-axial load cells orientated in the longitudinal and vertical direction (Load case 3 - Rear 6lc – Experimental loading and application point)

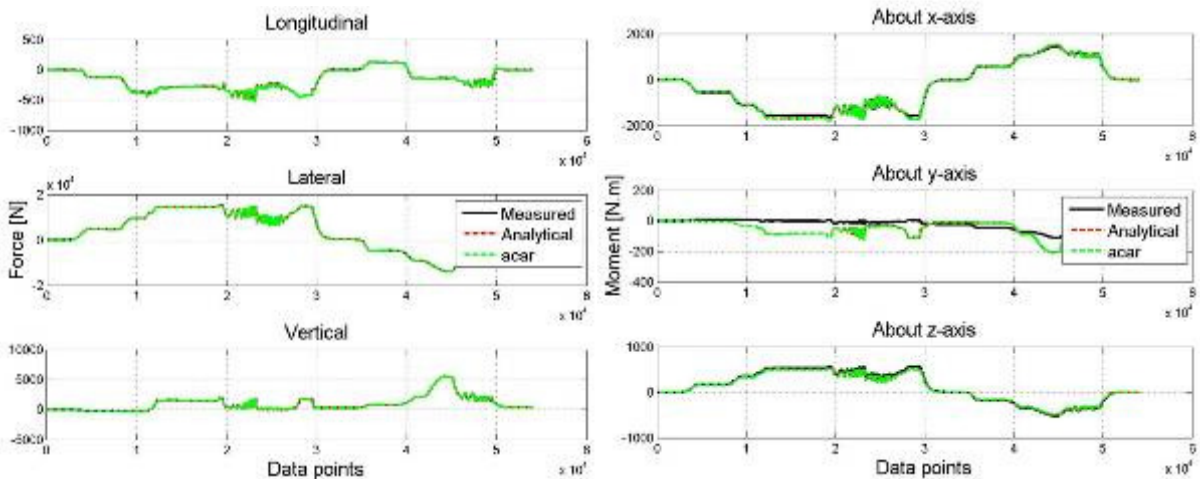


Figure A.45. Comparison of equivalent forces and moments (Load case 3 - Rear 6lc – Experimental loading and application point)

Load case 4

Figure A.46 and Figure A.47 show the results for Load case 4. Except for the forces in the uni-axial load cells Z_2 and Z_3 all the other uni-axial load cell forces show good correlation. The discrepancy between Z_2 and Z_3 causes the equivalent moment about the x-axis to deviate from the measured data. The other two equivalent moments and all three equivalent forces show good correlation.

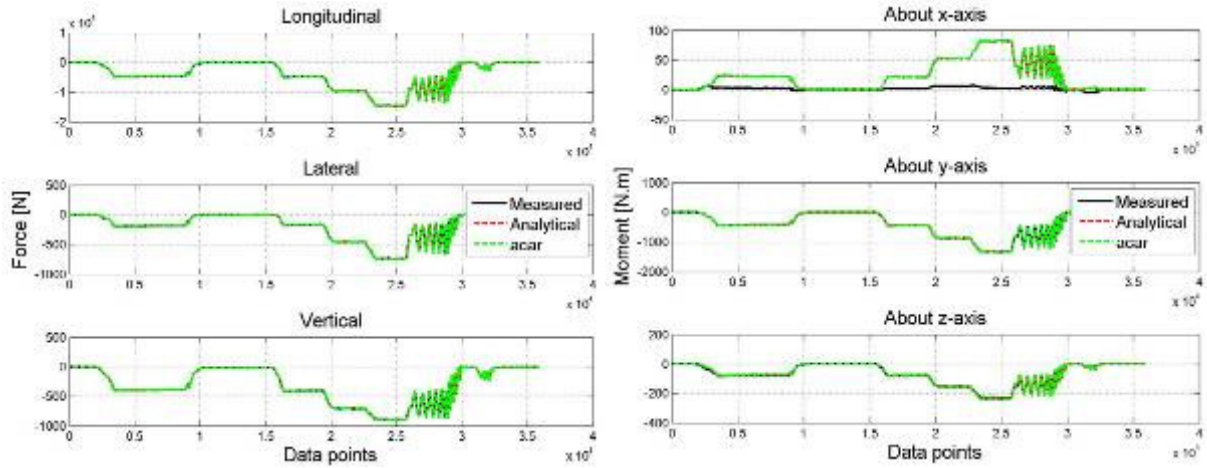


Figure A.46. Comparison of equivalent forces and moments (Load case 4 - Rear 6clc – Experimental loading and application point)

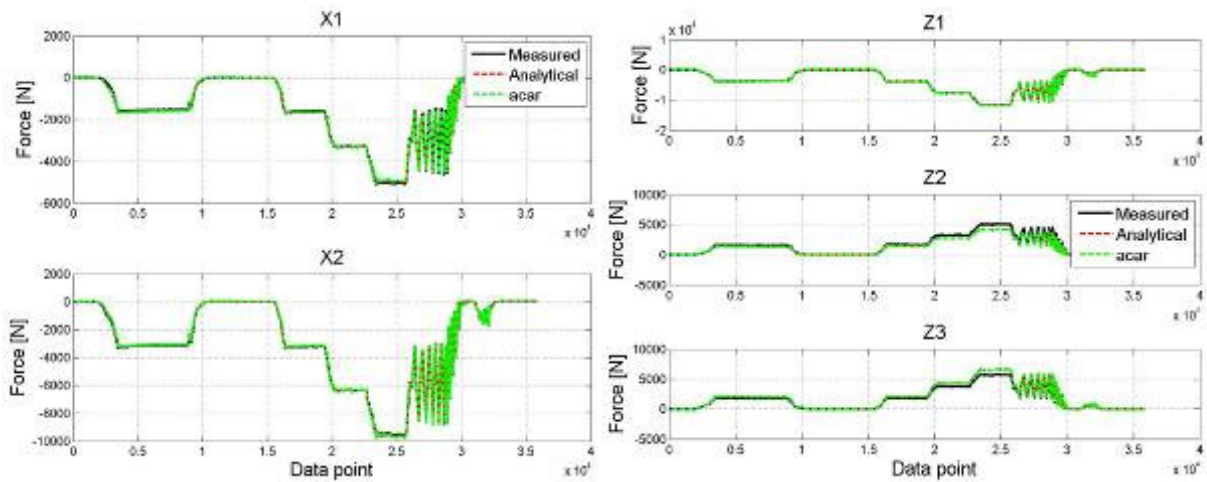


Figure A.47. Comparison of forces in uni-axial load cell orientated in the longitudinal and vertical direction (Load case 4 - Rear 6clc – Experimental loading and application point)

The validation results for the two models using the experimental measurements taken on the rear 6clc showed similar trends and correlation to that obtained when the measurements on the front (physical) 6clc were used.

A.3. Conclusion

Twelve uni-axial load cells were calibrated and integrated into two six component load cells. The analytical equations for the 6clc were derived which calculates the equivalent forces and moments acting on the load cell. Using the analytical equations the feasibility of the 6clc concept was verified. An ADAMS/Car model was created to represent the 6clc and was also verified using the analytical equations. The analytical equations and the ADAMS/Car model were validated against experimental measurements. The results showed good correlation between the two models and the measured data when the experimentally calculated force orientation and application point were used in the two models. Good correlation was obtained for all the equivalent forces for all four load cases. The correlation of the equivalent moments tends to have one of the equivalent moments that do not have good correlation. This may be due to the application point between the physical 6clc and the model not being exactly the same.

From the verification and validation results it can be concluded that both the physical as well as the virtual 6clc can be used to measure the equivalent forces and moments. It is however suggested that a more rigorous validation process is undertaken which concentrates on having a experimental setup which enables better control over the orientation and application point of the applied force.

Appendix B

Theoretical stiffness of the multi-leaf spring

This appendix investigates the use of beam theory to calculate the two stiffness regimes observed on the force-displacement characteristic of the multi-leaf spring. The two stiffness regimes are associated with the solid beam and layered beam behaviour discussed in paragraph 2.2 of Chapter 3. The appendix will first present the equations that can be used to calculate the stiffness of the two regimes. The two stiffness regimes of the multi-leaf spring are calculated using two methods, 1) the principle of superposition from beam theory (Gere, 2004) and, 2) the equations in the SAE Spring Design Manual (1996).

B.1. Calculating the theoretical stiffness

The stiffness of the two regimes of the multi-leaf spring is calculated by dividing the multi-leaf spring, shown in Figure B.1, into two cantilevers. It is assumed that the clamping in the clamped section is perfect meaning that this section acts like a solid beam without the possibility of slip between the individual blades. This result in the boundary condition shown in Figure B.1 and divides the leaf spring in a front and rear cantilever, The stiffness of the multi-leaf spring is calculated by first calculating the stiffness of the two cantilevers and then combining the cantilever stiffnesses to obtain the equivalent stiffness which represents the multi-leaf spring stiffness. As mentioned, two methods will be used to calculate the stiffness of the cantilever beams. The method of superposition, presented in paragraph B.1.1, is able to calculate the stiffness of both stiffness regimes whereas the second method using the equations in the SAE spring design manual (1996) is only able to calculate the stiffness of the regime associated with the layered beam behaviour.

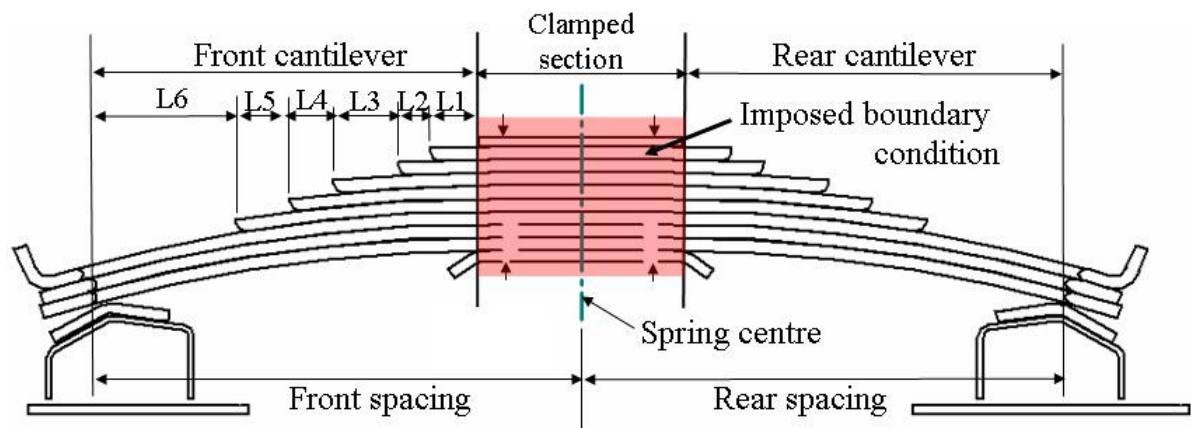


Figure B.1. Multi-leaf spring dimensions

Figure B.1 shows the dimensions for the multi-leaf spring. The lengths L1 to L5 represent the actual length and not the total length as the total length of each section is not in complete contact with the next blade. This is shown in Figure B.2.

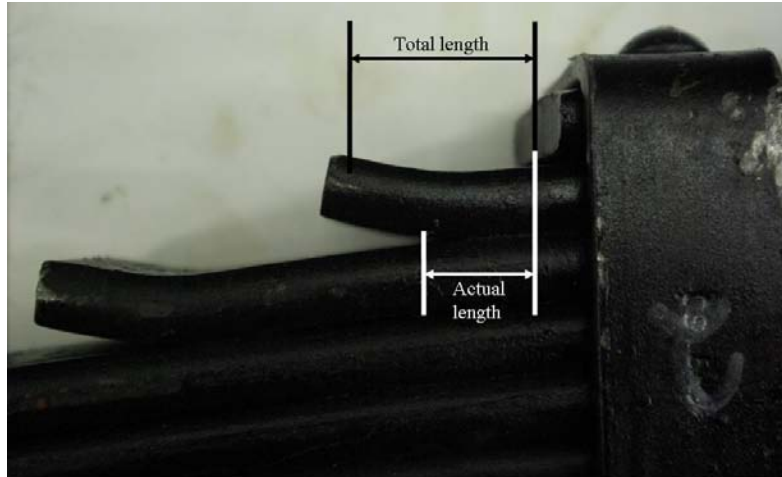


Figure B.2. Contact between blades at blade ends

B.1.1. Principle of superposition

The theoretical stiffness of the spring's two stiffness regimes is calculated using the principle of superposition (Gere, 2004). The principle of superposition is used as the cantilever beam is non-prismatic. As mentioned the multi-leaf spring is divided into two cantilever beams (see Figure B.1), a front cantilever and rear cantilever. The stiffness of the cantilevers is calculated as follows. The cantilever is divided into prismatic sections (see Figure B.3). Calculating the deflection of each section and summing them gives the total deflection at G. Equation {B.1} shows the calculation of the deflection at G.

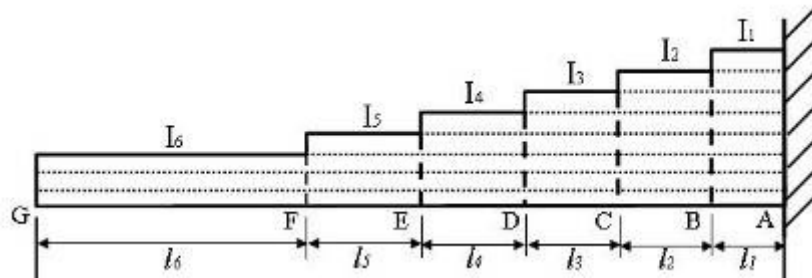


Figure B.3. Cantilever beam divided into sections with uniform cross section

$$\begin{aligned}
 \delta_G = & \delta_B + \theta_B l_2 + \delta_{C_2} + (\theta_B + \theta_C) l_3 + \delta_{D_2} + (\theta_B + \theta_C + \theta_D) l_4 + \delta_{E_2} \\
 & + (\theta_B + \theta_C + \theta_D + \theta_E) l_5 + \delta_{F_2} + (\theta_B + \theta_C + \theta_D + \theta_E + \theta_F) l_6 + \delta_{G_2}
 \end{aligned}
 \tag{B.1}$$

For $\delta_B; \delta_{C_2}; \delta_{D_2}; \delta_{E_2}; \delta_{F_2}; \delta = \frac{PL^3}{3EI} + \frac{ML^2}{2EI}$ {Case 4 and Case 6 in Gere (2004)}

$$\delta_{G_2} = \frac{PL^3}{3EI} \tag{Case 4 in Gere (2004)}$$

For $\theta_B; \theta_C; \theta_D; \theta_E; \theta_F; \theta = \frac{PL^2}{2EI} + \frac{ML}{EI}$ {Case 4 and Case 6 in Gere (2004)}

The deflections $\delta_B, \delta_{C_2}, \delta_{D_2}, \delta_{E_2}$ and δ_{F_2} are calculated using the equation given for δ and with the correct values for P, L, M, E and I substituted into the equation for each section. Similarly, the angles of rotation $\theta_B, \theta_C, \theta_D, \theta_E$ and θ_F are calculated using the equation given for θ and with the correct values for P, L, M, E and I substituted into the equation for each section. Substituting these equations into Equation {B.1}, and after some rearrangement, we obtain Equation {B.2} which is the stiffness (k) of the non-prismatic cantilever. Note that in this equation the following shorthand notation is used: $l_{62} = l_6 + l_5 + l_4 + l_3 + l_2$ etc.

$$k = \frac{P}{\delta_G} = E \left[\frac{l_1^3}{3I_1} + \frac{l_2^3}{3I_2} + \frac{l_3^3}{3I_3} + \frac{l_4^3}{3I_4} + \frac{l_5^3}{3I_5} + \frac{l_6^3}{3I_6} + \frac{l_{62}l_{61}l_1}{I_1} + \frac{l_{63}l_{62}l_2}{I_2} + \frac{l_{64}l_{63}l_3}{I_3} + \frac{l_{65}l_{64}l_4}{I_4} + \frac{l_{66}l_{65}l_5}{I_5} \right]^{-1} \quad \{B.2\}$$

As discussed in paragraph 2.2 of Chapter 3 we expect the multi-leaf spring to have two stiffness regimes in its force-deflection characteristic. To calculate the stiffness of the two regimes the area moments of inertias (I_1 - I_6) are calculated in one of two ways. For the instance where the beam is initially loaded or unloaded we assume that there is no slip between the blades (see paragraph 2.2 of Chapter 3). This causes the multi-leaf spring to act as a single non-prismatic beam (i.e. the spring is machined out of a solid billet and not made of stacked blades). For this instance the area moment of inertias are calculated as follows:

Multi-leaf spring considered as solid beam

$$I_i = \frac{bh_i^3}{12}$$

- with b = width of blade
 h = thickness of individual blade
 h_i = h x number of blades in section i
 i = section 1, 2, ..., 6

The other instance is when there is slip between the blades and the multi-leaf spring acts as a layered beam. In this case the blades are assumed to have no friction between them. The calculations of the area moments of inertias are as follows:

Multi-leaf spring considered as layered beam

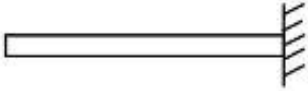
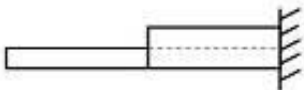
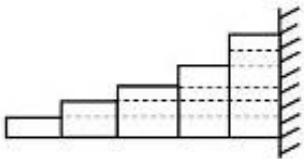
$$I_i = \frac{no l_i \times bh^3}{12}$$

- with b = width of blade
 h = thickness of individual blade
 i = section 1, 2, ..., 6
 $no l_i$ = number of blades in section i

Equation {B.2} was derived for an eight blade multi-leaf spring with three full-length blades as indicated in Figure B.3. Table B.1 gives the general equations for the calculation of the theoretical spring stiffness of a leaf spring with a prismatic and non-prismatic cross-section. A leaf spring with a prismatic cross-section will for example consist of a single full length blade. A leaf spring with a non-prismatic cross-section will obviously consist of full length and non-full length blades.

Note that the stiffness Equation {B.2}, and the equations given in table B.1, assume that the initial rotation of the cantilever beam is zero.

Table B.1. Equation for calculating stiffness of prismatic and non-prismatic cantilever beams

Prismatic cantilever	
Number of sections, $n = 1$	
$k = E \left[\frac{l^3}{3I} \right]^{-1}$	
Non-prismatic cantilevers	
Number of sections, $n = 2$	
$k = E \left[\sum_{i=1}^n \frac{l_i^3}{3I_i} + \frac{l_n(l_n + l_{n-1})l_{n-1}}{I_{n-1}} \right]^{-1}$	
Number of sections, $n > 2$	
$k = E \left[\sum_{i=1}^n \frac{l_i^3}{3I_i} + \sum_{i=1}^{n-2} \frac{l_i \sum_{j=i+1}^n l_j \sum_{k=1}^n l_k}{I_i} + \frac{l_n(l_n + l_{n-1})l_{n-1}}{I_{n-1}} \right]^{-1}$	

B.1.2. SAE spring design manual

The SAE Spring Design Manual (1996) gives the following equation for the stiffness of a uniform strength cantilever beam:

$$k = \frac{2E \sum I}{l^3} \cdot SF \tag{B.3}$$

- with
- E - Young's modulus
 - l - either for front cantilever (l_f) or rear cantilever (l_r)
 - SF - Stiffening factor. According to SAE Spring Design Manual (1996), for truck springs with untapered leaf ends and three full length blades $SF = 1.25$
 - $\sum I$ - total moment of inertia

This equation can only be used to calculate the stiffness of the beam when it is considered to be behaving as a layered beam, in other words for the condition where the individual blades are able to move relative to one another.

B.1.3. Calculating equivalent spring stiffness

In paragraph B.1.1 and B.1.2 we presented equations for the calculation of the stiffness of a cantilever beam. Seeing that the front and rear cantilever beam is in parallel the equivalent stiffness can be calculated by summing the stiffness of the front (k_a) and rear (k_b) cantilever beams:

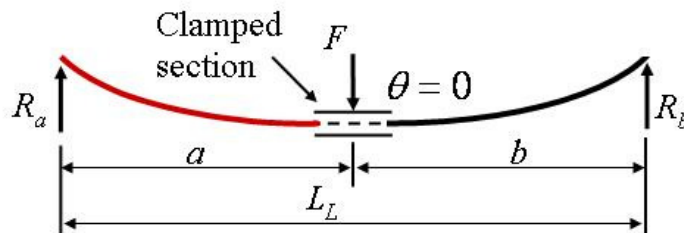
$$k_{eq} = k_a + k_b \quad \{B.4\}$$

The SAE spring design manual (1996) suggests using the following equation to combine the stiffnesses of the front and rear cantilevers:

$$k_{eq} = \frac{k_a k_b L^2}{k_a a^2 + k_b b^2} \quad \{B.5\}$$

The difference between Equation {B.4} and Eq.{B.5} will be shown by applying it to the two simple beams shown in Figure B.4. The figure shows two simply supported beams, one loaded symmetrically and the other one asymmetrically. Both beams are divided into a front and rear cantilever beam. In Figure B.4 the front cantilever is indicated in red and the rear cantilever in black. The clamped section is assumed to be infinitesimally small. The angle θ represent the initial angle of rotation of the two cantilever beams. For a symmetric loading of the beam the initial angle of the cantilevers are zero, whereas for a asymmetric load case the initial angle of rotation of the two cantilever beams is non-zero.

Symmetric loading: $a = b \Rightarrow \theta = 0$



Asymmetrical loading: $a \neq b \Rightarrow \theta \neq 0$

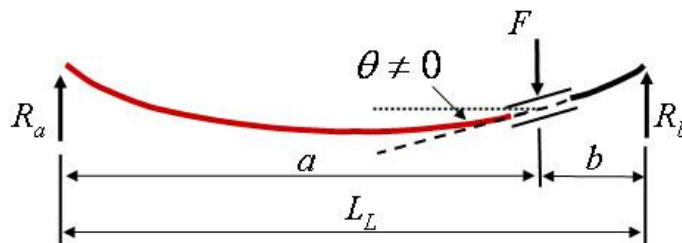


Figure B.4. Initial angle of rotation for symmetric and asymmetric loading

The stiffness of the two simple beams given in Figure B.4 will be calculated using the analytical equations for a simple beam. This will then be compared to the stiffness of the two beams that are calculated by dividing the simply supported beam into two cantilevers and then using Eq.{B.4} and Eq.{B.5}, respectively, to calculate the equivalent stiffness of the beam.

B.1.3.1. Symmetrical loading

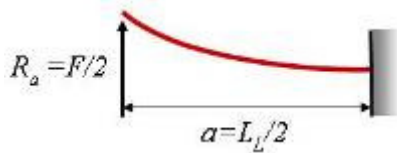
The stiffness of the symmetrically loaded simple beam can be calculated from Equation {B.6}. The equation for the deflection (δ) is at the point where the force is applied (Gere, 2004).

$$\delta = \frac{FL_L^3}{48EI}$$

$$k = \frac{48EI}{L_L^3} \quad [\text{N/m}] \quad \text{\{B.6\}}$$

The stiffness of the left and right cantilever beams are calculated using the equation given in Table B.1 for the prismatic cantilever beam. The calculation of the stiffness of the front and rear cantilever beams is given below:

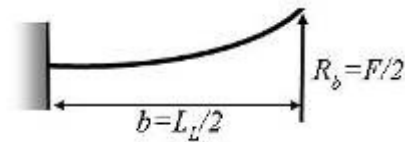
Left cantilever



The stiffness is calculated using the formulae for the prismatic beam given in Table B.1:

$$k_a = \frac{24EI}{L_L^3}$$

Right cantilever



The stiffness is calculated using the formulae for the prismatic beam given in Table B.1:

$$k_b = \frac{24EI}{L_L^3}$$

Using Eq.{B.4} to combine the stiffness of the two cantilevers we obtain the following equivalent stiffness:

$$\begin{aligned} k_{eq} &= k_a + k_b \\ &= \frac{24EI}{L_L^3} + \frac{24EI}{L_L^3} \\ &= \frac{48EI}{L_L^3} \end{aligned}$$

Using Eq.{B.5} to obtain the equivalent stiffness we get:

$$\begin{aligned} k &= \frac{k_a k_b L^2}{k_a a^2 + k_b b^2} \\ &= \frac{48EI}{L^3} \end{aligned}$$

Using either Eq.{B.4} or Eq.{B.5} we obtain the same stiffness as was calculated by the analytical equation for the stiffness of the simply supported beam with symmetric loading. The next paragraph will look at the same calculations but now applied to a simply supported beam with asymmetric loading.

B.1.3.2. Asymmetrical loading

The stiffness of the asymmetrically loaded beam (shown in Figure B.4) can be calculated from Equation {B.7}. The equation for the deflection (v) is at the point where the force is applied (Gere, 2004). It is assumed that $a \geq b$.

$$v = \frac{Pba}{6L_L EI} (L_L^2 - b^2 - a^2) \quad \{B.7\}$$

$$k = \frac{6L_L EI}{ba(L_L^2 - b^2 - a^2)} \quad \{B.8\}$$

Before the stiffness of the front and rear cantilever beams is calculated, the reaction forces (R_a and R_b) of the simply supported beam are calculated. The following two equations are obtained by summing all the forces in the vertical direction and summing the moments about the point where the force F is applied.

$$\begin{aligned} \sum F_z = 0: R_a + R_b &= F \\ \sum M_c = 0: aR_a - bR_b &= 0 \end{aligned}$$

Solving these two equations simultaneously by multiplying the force equation with a and subtracting the moment equation from the new force equation we obtain:

$$R_b = \frac{aF}{L_L}$$

Substituting R_b into the original force equation we obtain:

$$R_a = \frac{bF}{L_L}$$

Now that the two reaction forces (R_a and R_b) are known, the simple beam will be divided into two cantilever beams and their stiffnesses calculated. As was shown in Figure B.4 the point where the force F is applied will serve as the point for dividing the simple beam into two cantilevers. In calculating the stiffness of the two cantilever beams the slope of the beam at the force application point is required to calculate the correct deflection of each cantilever and infer the stiffness. Figure B.5 shows the calculation of the deflection at the end points of the simply supported beam (which are also the ends of the two cantilever beams) by using superposition. Figure B.5 shows that the deflection of the simply supported beam can be calculated by assuming that the two cantilevers have a zero initial angle of rotation. The deflection of the two cantilevers is calculated with the deflection, due to the angle of rotation of the undeformed cantilevers, added to obtain the deflection of the simply supported beam.

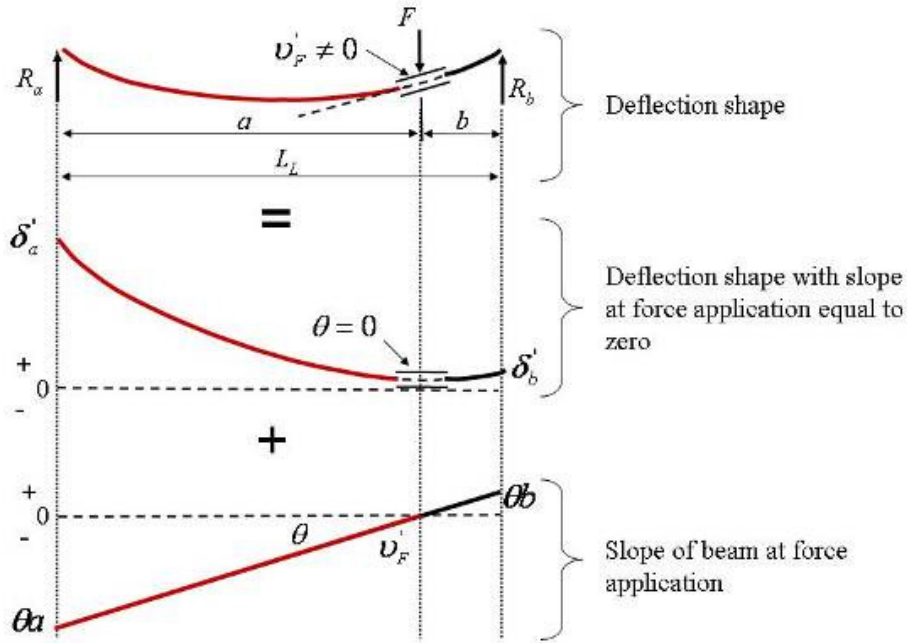
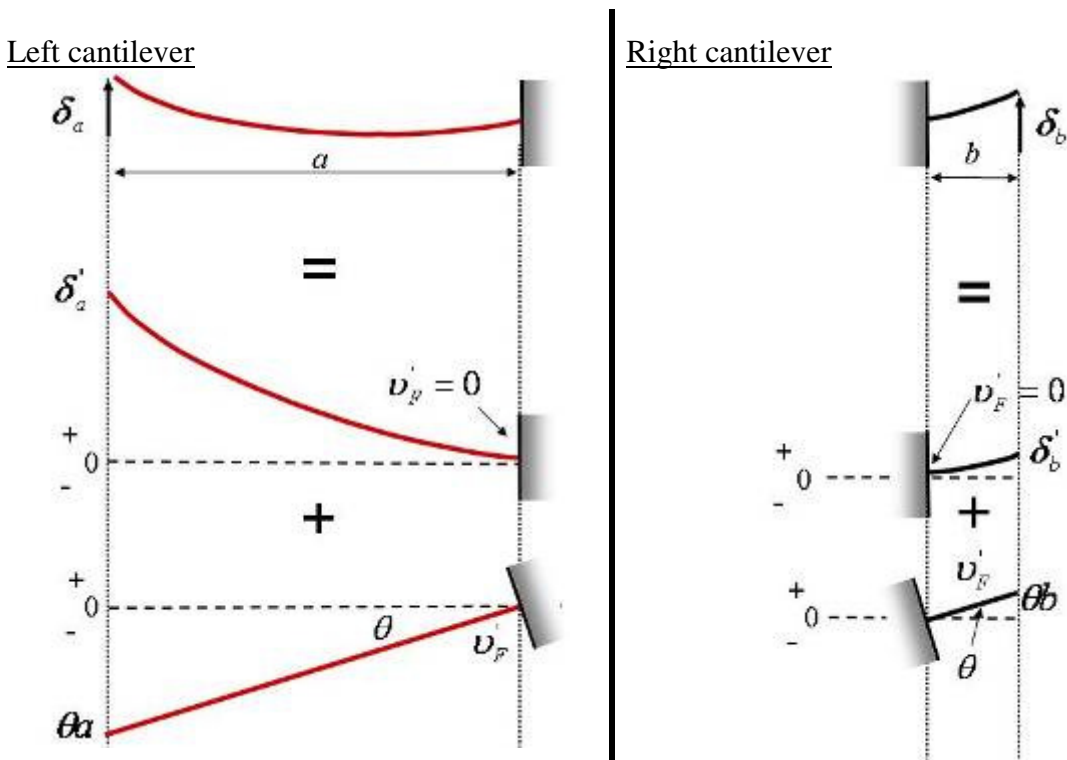


Figure B.5. Decomposition of deflection of simple beam

The deflection of the cantilevers, with the initial angle of rotation set to zero, is calculated with the deflection equation for a cantilever beam which was used to obtain the stiffness of the cantilever beam in Eq.{B.6}. The slope at the point of force application of the simple beam can be calculated with the following equation (Gere, 2004):

$$v'_F = -\frac{Fb}{6L_L EI} (L_L^2 - b^2 - 3a^2)$$

From this equation the angle of rotation can be calculated as $\theta = \tan^{-1} v'_F$. The stiffness of the two cantilevers using the method mentioned in Figure B.5 is shown below.



Deflection:

$$\begin{aligned}\delta_a &= \delta'_a - a\theta \\ &= \frac{R_a a^3}{3EI} - a\theta \\ &= \frac{bFa^3}{3EIL_L} - a\theta\end{aligned}$$

Stiffness:

$$\begin{aligned}k_a &= \frac{R_a}{\delta_a} \\ &= \frac{bF}{\frac{bFa^3}{3EI} - a\theta L_L}\end{aligned}$$

Deflection:

$$\begin{aligned}\delta_b &= \delta'_b + b\theta \\ &= \frac{R_b b^3}{3EI} + b\theta \\ &= \frac{aFb^3}{3EIL_L} + b\theta\end{aligned}$$

Stiffness:

$$\begin{aligned}k_b &= \frac{R_b}{\delta_b} \\ &= \frac{aF}{\frac{aFb^3}{3EI} + b\theta L_L}\end{aligned}$$

The stiffness of the front and rear cantilever beam calculated above can now be used in either Eq.{B.4} and Eq.{B.5} to calculate the equivalent beam stiffness. This equivalent beam stiffness can then be compared to the stiffness calculated from the Eq.{B.8}. In order to evaluate and compare the results from Eq.{B.4}, Eq.{B.5} and Eq.{B.8}, the following values for the parameters in these equations are used:

$$\begin{aligned}a &= 0.7\text{m} \\ b &= 0.3\text{m} \\ L_L &= 1\text{m} \\ F &= 1000\text{N} \\ E &= 207 \times 10^9 \text{Pa} \\ I &= 1.7 \times 10^{-8} \text{m}^4\end{aligned}$$

Table B.2 shows the results obtained from Eq.{B.4}, Eq.{B.5} and Eq.{B.8}. From these results it can be seen that the deflection calculated from the two cantilevers are equal to the deflection calculated from the simple beam Equation {B.7}. Similarly, the stiffness calculated using Equation {B.4} and Eq.{B.5} give the same answer as was calculated for the simple beam from Equation {B.8}.

Table B.2. Results from two cantilevers compared with results from simply supported beam

	Deflection [m]	Stiffness [kN/m]
Simple beam	0.004177	Using Eq.{B.8}
		239.4
Two cantilever beams	0.004177 ($\delta_a = \delta_b$)	Using Eq.{B.4}
		239.4
		Using Eq.{B.5}
		239.4

B.1.3.3. Conclusion

From the results obtained for the symmetric and asymmetric loaded simply supported beam it seems that the method of dividing the simply supported beam into two cantilevers, calculating their stiffness and then combining it with either Eq.{B.4} and Eq.{B.5} gives the same results as that calculated from the stiffness equation for the simply supported beam. However, it was

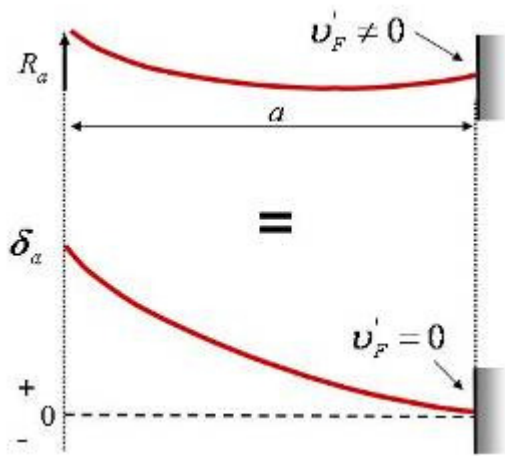
assumed at the beginning of the analysis that the clamped length is infinitesimally small. When the clamped length becomes longer the calculation of the slope of the beam may become increasingly more inaccurate as it deviates from the analytical deflection shapes of the simply supported beam. Therefore, it may become difficult to calculate the initial angle of rotation of the cantilever beams accurately. Not being able to include the initial angle of rotation in the calculation of the stiffness of the two cantilevers will lead to errors in the stiffness calculated. The following paragraph investigates the effect of the initial angle on the results of the stiffness calculations and how with the use of Eq.{B.5} this problem is circumvented.

B.1.3.4. Neglecting the initial angle of the cantilevers

With a longer clamp section the analytical equation for calculating the slope of the simply supported beam may become inaccurate. This implies that it may become difficult to calculate the initial angle of rotation of the cantilever beams and therefore make it difficult to calculate the stiffness accurately. The equations for calculating the stiffness of the two cantilevers, without including the initial angle of rotation, are given in Table B.3. The calculation of the deflection only includes the deflection due to the deformed cantilever with an initial angle of rotation set to zero. It neglects the second part of the deflection, the deflection due to the initial angle of rotation of the cantilever, which was discussion in Figure B.5.

Table B.3. Equations for calculating stiffness of cantilevers (Neglecting initial angle of rotation)

Left cantilever



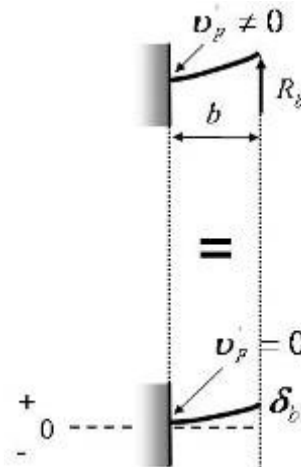
Deflection:

$$\delta_a = \frac{R_a a^3}{3EI} = \frac{bFa^3}{3EIL_c}$$

Stiffness:

$$k_a = \frac{R_a}{\delta_a} = \frac{3EI}{a^3}$$

Right cantilever



Deflection:

$$\delta_b = \frac{R_b b^3}{3EI} = \frac{aFb^3}{3EIL_c}$$

Stiffness:

$$k_b = \frac{R_b}{\delta_b} = \frac{3EI}{b^3}$$

From the equation given in Table B.3 it is clear that the deflection calculated for the two cantilevers will not be equal. The two cantilevers that are used to represent the simply supported beam are in parallel and should therefore experience the same deflection. Therefore from the results of the deflections it is clear that the exclusion of the initial angle of rotation of

the cantilever beams causes the incorrect calculation of the deflection. It is reasonable to expect that when the equivalent stiffness is calculated with either Eq.{B.4} and Eq.{B.5} that the incorrect simply supported beam stiffness will be obtained. Again Eq.{B.4}, Eq.{B.5} and Eq.{B.8} are evaluated and compared but with Eq.{B.4} and Eq.{B.5} using the front and rear cantilever stiffness calculated with the initial angle of rotation neglected. The equations are evaluated using the same values for the parameters as was used in paragraph B.1.3.2. The results are given in Table B.4.

Table B.4. Results from two cantilevers (initial angle of rotation neglected) compared with results from simply supported beam

	Deflection [m]	Stiffness [kN/m]
Simple beam	0.004177	Using Eq.{B.8}
		239.4
Two cantilever beams	$\delta_a = 0.009747$	Using Eq.{B.4}
		421.8
	$\delta_b = 0.00179$	Using Eq.{B.5}
		239.4

As expected the deflection of the two cantilevers differs, however, even though the deflection of the two cantilever beams is incorrect, the correct stiffness is obtained for the simple beam when using Eq.{B.5} to calculate the equivalent stiffness.

B.1.4. Validation of theoretical stiffness calculation

In paragraph B.1.1 and B.1.2 equations for the calculation of the stiffness of a cantilever beam were presented. It was shown that the stiffness of a simply supported beam can be calculated by dividing the beam into two cantilever beams, calculating their stiffness and using Eq.{B.5} to calculate the equivalent stiffness. This method was shown to work for a symmetrically loaded as well as asymmetrically loaded simply supported beam. This method, with the use of Eq.{B.5}, does not require that the initial angles of rotations of the two cantilever beams be included. This makes the method useful when considering multi-leaf spring which have large clamped section and therefore may cause difficulties in calculating the slope of the multi-leaf spring accurately with analytical equations. The main reason for not being able to accurately calculate the slope of the multi-leaf spring is that for certain configurations of the leaf spring (especially concerning the clamped section length) it deviates from the simply supported beam's deflection shape which is used to approximate the multi-leaf spring.

The method will now be used to calculate the stiffnesses of the two regimes observed in the force-displacement characteristics of the multi-leaf spring considered in this study. The method of superposition and the SAE spring design manual (1996) is used to calculate the stiffness of the regime associated with the layered beam behaviour. The stiffness of the regime associated with the solid beam behaviour is calculated only with the method of superposition. In order to calculate the theoretical stiffness of the multi-leaf spring, the leaf spring is divided into two cantilever beams as was shown in Figure B.1. The stiffness of the two cantilevers are calculated, for both the layered and solid beam states, and combined into the multi-leaf spring stiffness for the layered and solid beam states using Eq.{B.5}.

Figure B.6 shows the correlation between the theoretically calculated stiffness and the experimentally measured force-displacement characteristic of the multi-leaf spring. Note that

the theoretical calculated stiffnesses shown in Figure B.6 are significantly higher than the stiffnesses observed in the experimental force-displacement characteristic.

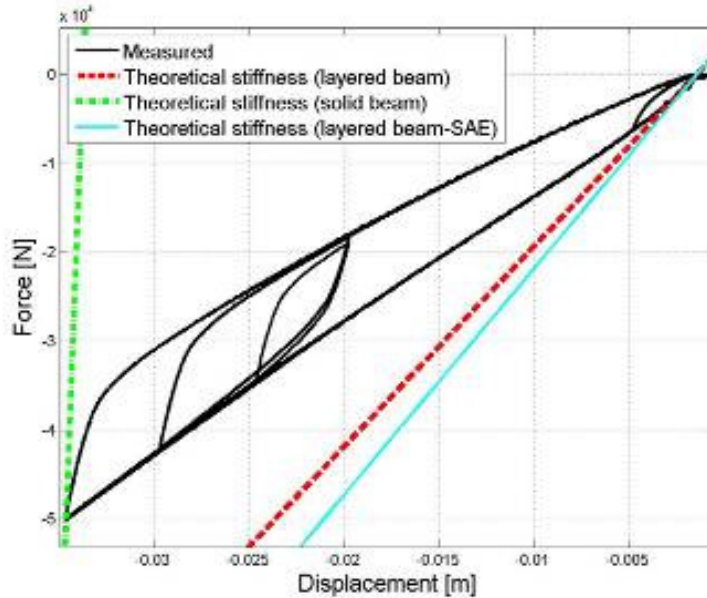


Figure B.6. Theoretical calculation of the two stiffness regimes

The deviation between the stiffness shown on the experimental and theoretically calculated force-displacement characteristics in Figure B.6 is large for both regimes. A possible cause for this might be from the assumption made in regards to the clamping in the clamped section. At the beginning of the Appendix it was assumed that the clamping in the clamped section is such that the individual blades within the clamped section are not able to move relative to one another implying that for this section the blades acted as a solid beam. This resulted in the system with the boundary conditions as was shown in Figure B.1. The imposed boundary conditions will definitely have an effect on the stiffness calculated for the leaf spring. The boundary condition effectively governs the effective length (or loaded length) of the leaf spring. As was shown in Chapter 2 the stiffness of a leaf spring is very sensitive to the loaded length. It was also shown in Chapter 2 that the stiffness of the leaf spring is sensitive to the preload of the U-bolts that are used to attach the axle to the leaf spring. The U-bolts are the components that apply the clamping force experienced in the clamped section. The sensitivity that was seen in the stiffness when changing the U-bolt preload was due to the boundary condition being changed. It is therefore expected that the theoretical stiffness will be just as sensitive to the boundary conditions of the clamped section as it will influence the loaded length used in the theoretical calculations. The effect of the clamping assumption and the resulting boundary condition on the theoretical stiffness calculation is investigated in more detail in the following paragraph.

B.2. Effect of the clamping assumption on the theoretical stiffness

It was mentioned that the assumption made with respect to the clamped section will influence the loaded length of the leaf spring and therefore affect the stiffness. Considering the equation for the stiffness of a prismatic cantilever beam given as Eq. {B.9} we can see that the stiffness

has a relation of $k \propto h^3$ and $k \propto \frac{1}{L^3}$.

$$k = \frac{Ebh^3}{4L^3} \quad \{B.9\}$$

From Eq.{B.9} it is clear that the stiffness has a high sensitivity to the thickness of the beam (h) and the length of the beam (L). Therefore, before we investigate the effect of the clamping assumption further we will confirm that the thickness used in the theoretical calculations is indeed the same as the thickness of the blades in the physical leaf spring. The thickness of each blade was measured at seven points spaced over the length of the blade. Table B.5 shows the measurements for the different blades and it can be seen that the thickness is rather uniform over the length of the blade; therefore the deviation in the theoretical stiffness observed in Figure B.6 is most probably not due to an incorrect thickness used in the theoretical stiffness calculations.

Table B.5. Blade thickness measurements

Measurements	1	2	3	4	5	6	7	Average	Std
Blade 8	14.1	14.1	14.1	14.1	14.1			14.1	0
Blade 7	14.05	14.1	14.05	14.05	14.1			14.07	0.0274
Blade 6	14	14	14	14.05	14.1			14.03	0.0447
Blade 5	14.15	14	14	14.05	14			14.04	0.0652
Blade 4	14	14	14	14.1	14.1			14.04	0.0548
Blade 3	14	14	14	13.95	13.95	13.8	13.8	13.93	0.09
Blade 2	13.8	13.9	14	13.95	14.05	14	13.9	13.94	0.084
Blade 1	14.1	14.05	14.1	13.95	14.05	13.9	13.9	14	0.089

The effect of the loaded length of the leaf spring on the stiffness is now investigated. The loaded length is a result of the assumption that is made for the type of clamping that is present in the clamped section. Considering the front cantilever the loaded length corresponds to the length of the cantilever (see Figure B.7). Figure B.7 shows the difference between the loaded length when the clamping in the clamped section is considered to be ideal and when there is no clamping. Up to now it has been assumed that the clamping is ideal. From Figure B.7 and Eq.{B.9} it is easy to deduct that the stiffness of the front cantilever using the assumption of ideal clamping will be higher than the stiffness of the cantilever for which no clamping is assumed.

The comparison in Figure B.6 showed that the theoretical stiffness, when ideal clamping is assumed, is higher than the stiffness observed on the experimental force-displacement characteristic. Therefore, when we assume that there is no clamping, the theoretical stiffness should be lower. The result of the theoretical stiffness, with the assumption of no clamping, is shown in Figure B.8. From this figure it can be seen that the theoretical stiffness is indeed lower and that it correlates well with the stiffness observed on the experimental force-displacement characteristic.

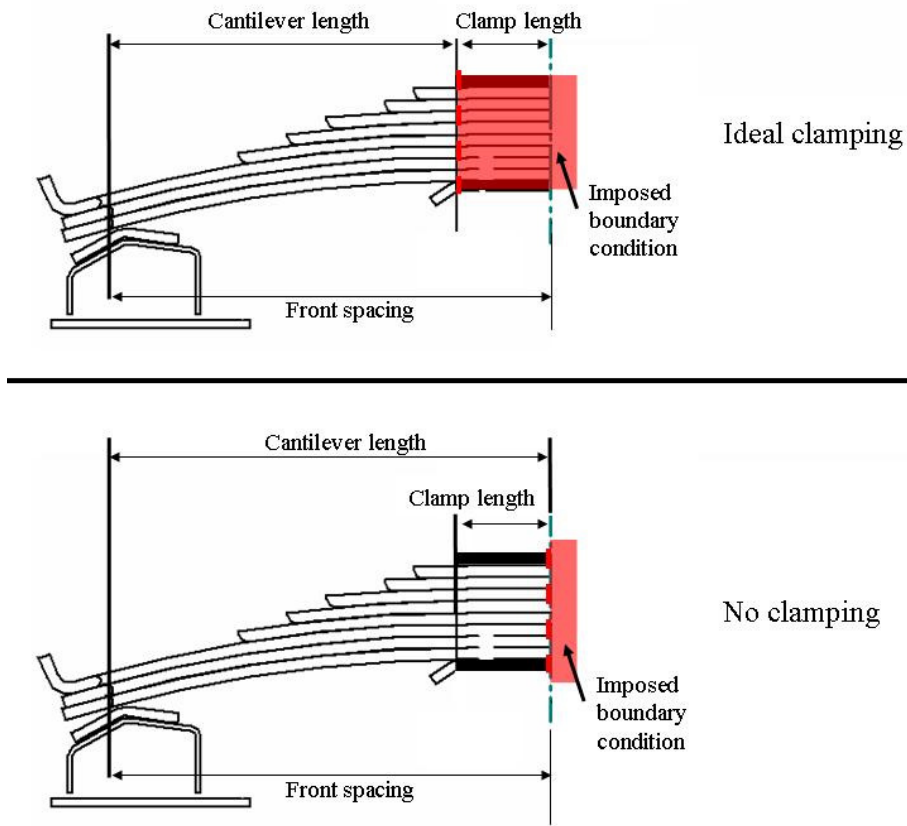


Figure B.7. Ideal vs. no clamping

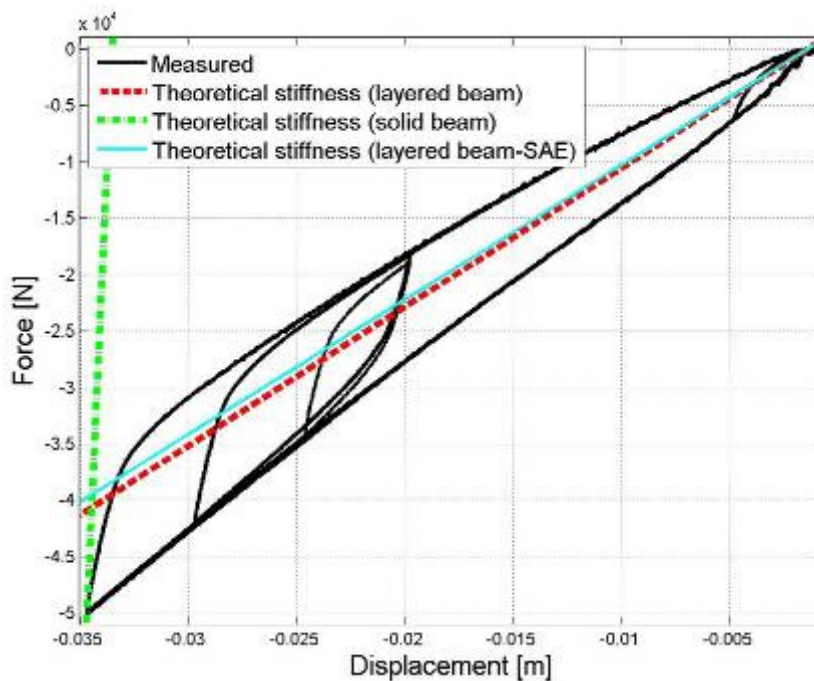


Figure B.8. Comparison between the measured force-displacement characteristic and the theoretically calculated stiffness assuming no clamping i.e. theoretical clamp length = 0m.

The theoretical stiffness of the two regimes was calculated using either the assumption of ideal clamping or no clamping. It should however be noted that the clamping may be between the ideal and no clamping assumption. The results from Figure B.8 seem to indicate that the

no clamping assumption is a good assumption in this case. It is expected that the more rigid the clamping is on the physical leaf spring the closer it will be to ideal clamping. With a less rigid (or less stiff) clamped section the clamping will be closer to the no clamping assumption.

B.3. Additional validation tests

Figure B.8 showed good correlation between the theoretical calculated stiffness and the stiffness observed on the experimental force-displacement characteristic of the multi-leaf spring. Comparisons of the theoretical and experimental stiffness of three additional leaf spring configurations will be presented. The theoretical calculations will be done for both the ideal clamping and no clamping assumption. The three additional tests were performed with the leaf spring having three full length blades. Each test used a different physical clamped length:

Test 1: 3 blade, clamped length = 0.076m

Test 2: 3 blade, clamped length = 0.22m

Test 3: 3 blade, clamped length = 0m

Additional to these three tests, a fourth test was performed with the original leaf spring (having three full length blades and 5 non-full length blades) and a clamp length of 0m but the test setup broke and the measured data was not useful. A detailed discussion of each of the tests is given in the following sections. Note that for calculation of stiffness using the SAE spring design manual (1996) a stiffening factor (SF) of 1.5 is used when all blades are full length.

B.3.1 Test 1: 3 blade, clamped length = 0.076m

Figure B.9 shows the experimental setup of the 3 blade, full length leaf spring. The five non-full length blades were rotated 90 degrees and created a clamped length of 0.076m. Figure B.10 shows the correlation between the theoretical and experimental stiffness for this configuration with the ideal clamping assumption. Figure B.11 shows the results for the no clamping assumption.

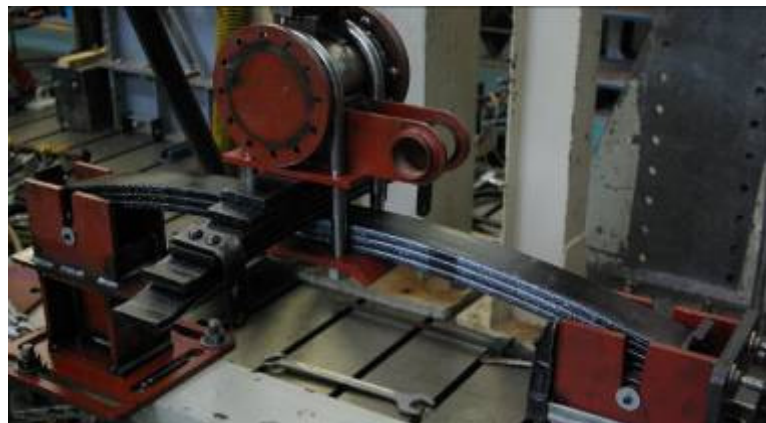


Figure B.9. Experimental setup of leaf spring with three full length blades and clamp length = 0.076m

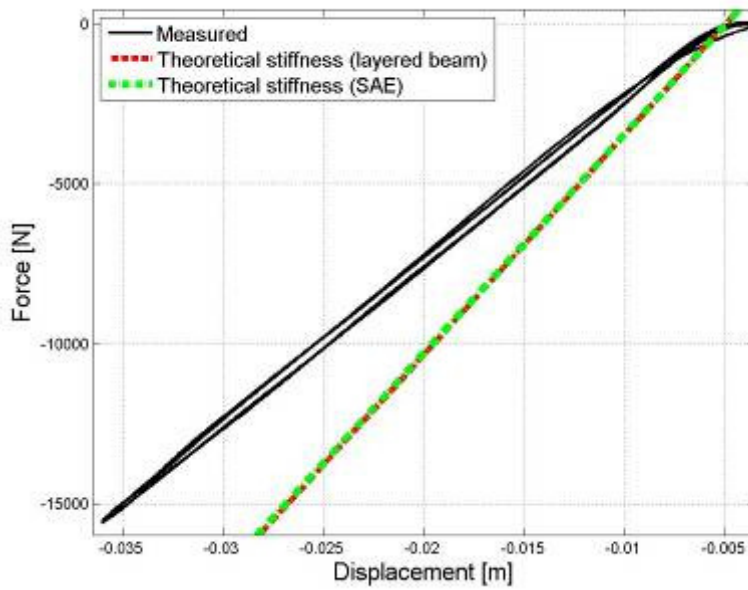


Figure B.10. Comparison between measured and theoretical stiffness for test 1 assuming ideal clamping

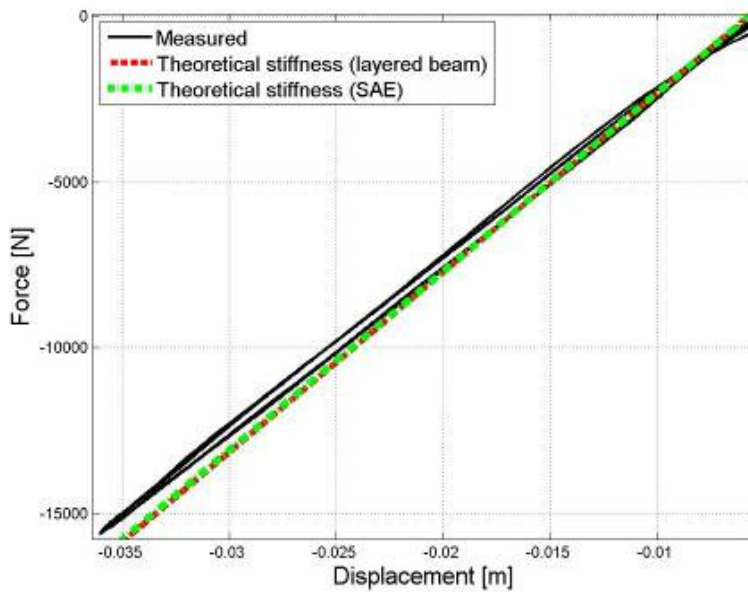


Figure B.11. Comparison between measured and theoretical stiffness for test 1 assuming no clamping

B.3.2 Test 2: 3 blade, clamped length = 0.22m

This test setup is shown in Figure B.12. When the theoretical stiffness, calculated using the ideal clamping assumption, is compared to the measured stiffness it is again observed that the theoretical stiffness is higher (see Figure B.13). Figure B.14(a) shows the correlation between the measured and theoretical stiffness when no clamping is assumed in the clamped section. With the assumption of no clamping being present in the clamped section the theoretical stiffness is lower than the measured stiffness. However, if a clamping is assumed that lies between the ideal and no clamping conditions the resulting theoretical stiffness correlates well with the measured stiffness (see Figure B.14(b)). The clamping between the ideal and no clamping conditions were simulated by setting the theoretical clamped length equal to 0.1m.

It was expected that if the no clamp assumption was used in the theoretical calculation of the stiffness will again show good correlation to the measured stiffness.

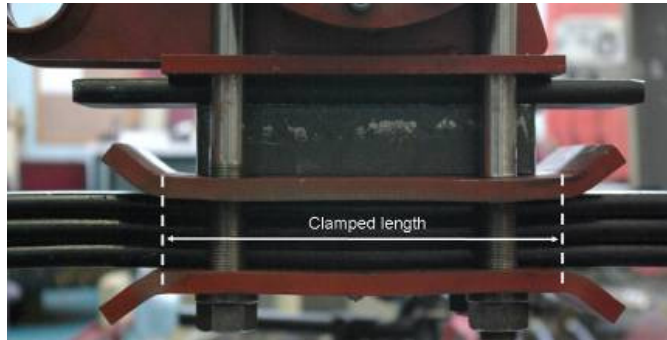


Figure B.12. Experimental setup of leaf spring with three blades and clamp length = 0.22m

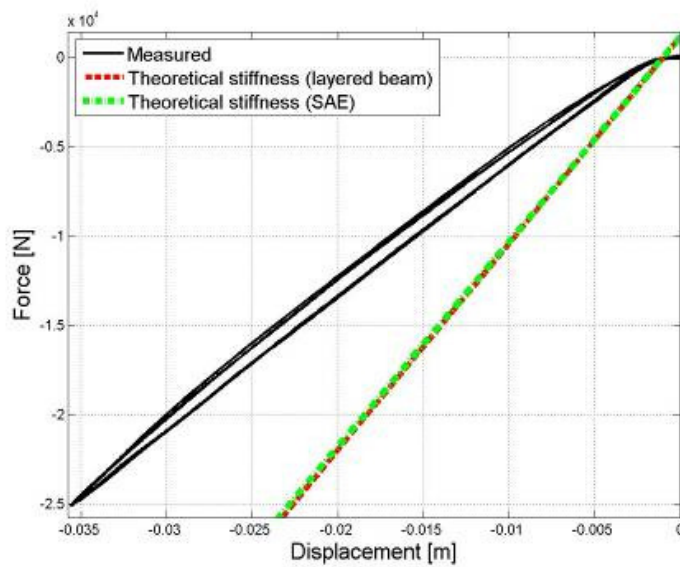


Figure B.13. Comparison between measured and theoretical stiffness for test 2 assuming ideal clamping

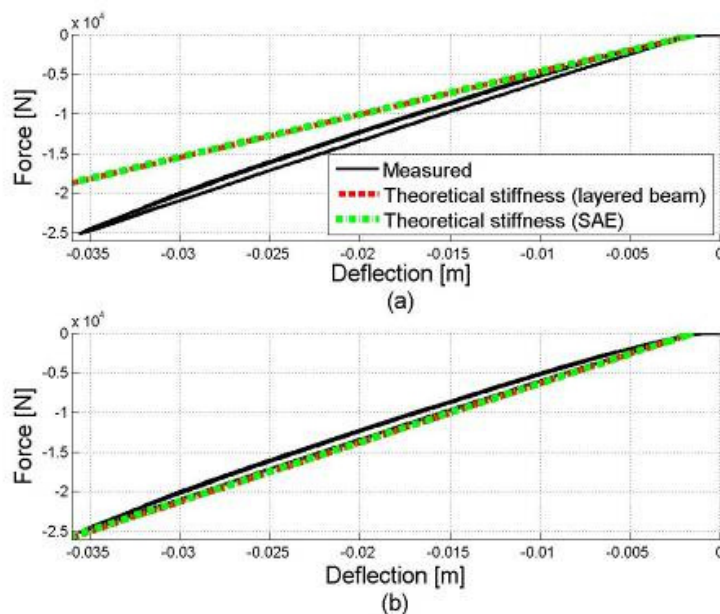


Figure B.14. Comparison between measured and theoretical stiffness for test 2 (a) Assumed no clamping . (b) Assumed clamping is between ideal and no clamping condition

However, when the setup shown in Figure B.12 is modelled in a different way, the theoretical stiffness obtained, with the no clamp assumption, is improved. The setup was modelled as three full-length prismatic blades. Instead, if the setup is modelled as shown in Figure B.15 the correlation obtained between the measured and theoretical stiffness is good when assuming a no clamping condition within the clamped section. The setup is modelled as having two sections. Section 1 has a length of 0.195m with the height being equal to the height of 8 blades. Section 2 is made up of three full length blades (see Figure B.15). In other words, the leaf spring effectively consisted out of three full length blades with five non-full length blades having equal length. The results using this model and the no clamping assumption are shown in Figure B.16 which correlate well with the measured stiffness. This shows that it is just as important to model the spring's cross-sectional area correctly as it is to model the boundary condition correctly.

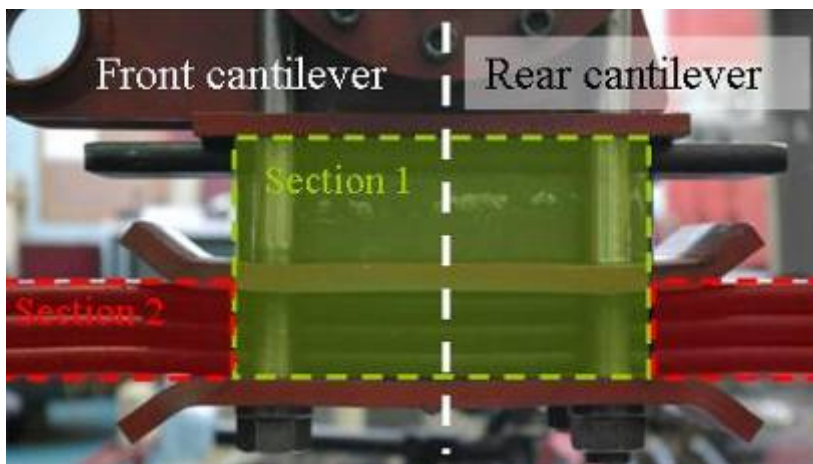


Figure B.15. Leaf spring modelled as having three full length blades and 5 non-full length blades having equal length

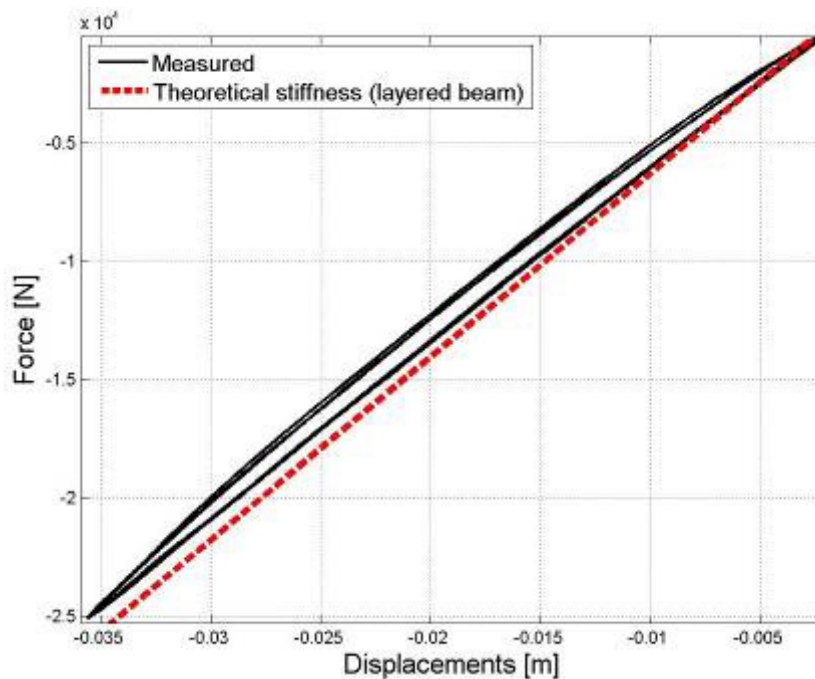


Figure B.16. Comparison between measured and theoretical stiffness for test 2 assuming no clamping and using the model shown in Figure B.15

B.3.3. Test 3: 3 blade, clamped length = 0m

Figure B.17 shows the experimental setup of the leaf spring with 3 full-length blades and a clamp length of 0. Figure B.18 shows the comparison between the theoretical and measured stiffness for this setup. The correlation is not as good as obtained for the test in paragraph B.3.1 and B.3.2 with the theoretical stiffness being higher than the measured stiffness. A possible reason for the physical spring being less stiff than the theoretical values may be due to the presence of the hole of the centre bolt. This was investigated by including the hole in the theoretical calculations to see whether this has any effect.



Figure B.17. Experimental setup of leaf spring with three full length blades and clamp length = 0m

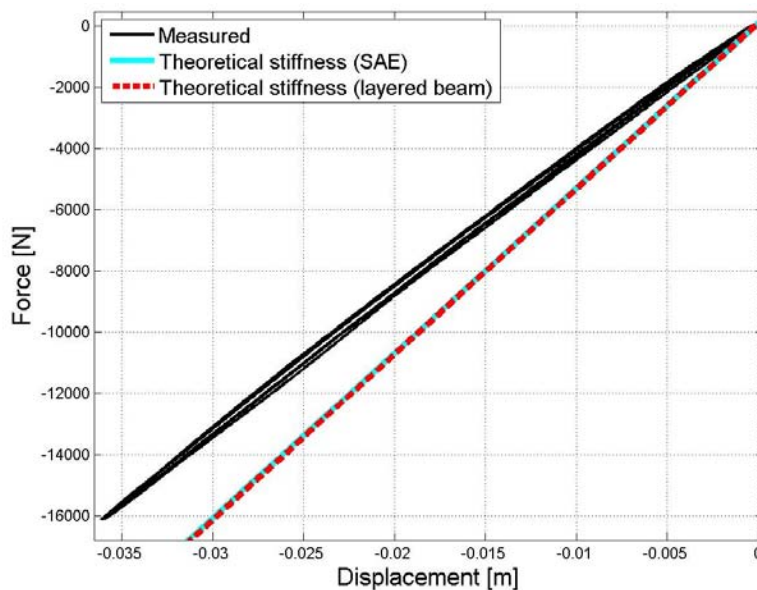


Figure B.18. Comparison between measured and theoretical stiffness for test 3

It is postulated that when including the effect of the hole in the theoretical calculation that the correlation shown in Figure B.18 will improve. The hole removes material and should thus decrease the stiffness of the blade as it leads to a smaller area moment of inertia (see Figure B.19). The hole was effectively treated as a square cut-out.



Figure B.19. Effect of hole on the area moment of inertia

Figure B.20 shows the comparison between the measured stiffness and the theoretical stiffness, calculated without and with the hole using the method of super position. From the figure it can clearly be observed that the hole does not have a big effect on the theoretical stiffness of the spring. The reason for the deviation between the theoretical and measured stiffness is not clear.

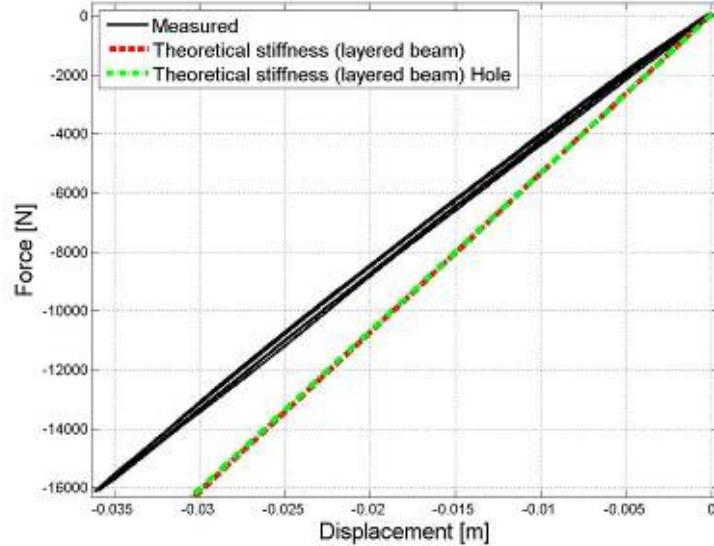


Figure B.20. Comparison between measured and theoretical stiffnesses (with and without hole) for test 3

B.4. Conclusion

The theoretical calculation of the stiffness of the two regimes in the force-displacement characteristic of the multi-leaf spring was investigated. It was shown that the stiffness regimes can be calculated using simple beam theory. The effect of the clamping assumption on the theoretical stiffness was shown. The clamping assumption influences the boundary conditions which is a similar effect that was obtained during the experimental characterisation in Chapter 2. It was shown in Chapter 2 that the stiffness of the spring is sensitive to the U-bolt preload which governs how the leaf spring is constrained and is analogue to the clamping assumption which governs the boundary condition. The sensitivity that was shown by the theoretical stiffness calculation with respect to the clamping assumption and the loaded length shows good agreement to what was observed during the experimental characterisation of the leaf spring.

The results in this appendix confirmed that the postulate of the two stiffness regimes being representative of a layered beam and solid beam behaviour is true. The results also indicate that the method can be used to theoretically calculate the stiffness of a multi-leaf spring. This method should be used on different leaf springs to confirm that it is generally applicable. It is suggested that the theoretical stiffness be used as a good estimator of the stiffness that can be expected for a specific leaf spring. The equation presented to calculate the stiffness of the layered leaf spring assumes that there is no friction present between individual blades. Future work should investigate ways to account for the friction between the blades in order to quantify the hysteresis loop. With the ability to account for the hysteresis and combining it with the theoretical stiffness of the two regimes will imply that the force-displacement characteristic can be calculated theoretically. This will be useful during early stages in the product development stage when physical leaf springs are not yet available or the configuration of the leaf spring is to be determined. This method will also enable the elastoplastic leaf spring to be parameterised theoretically